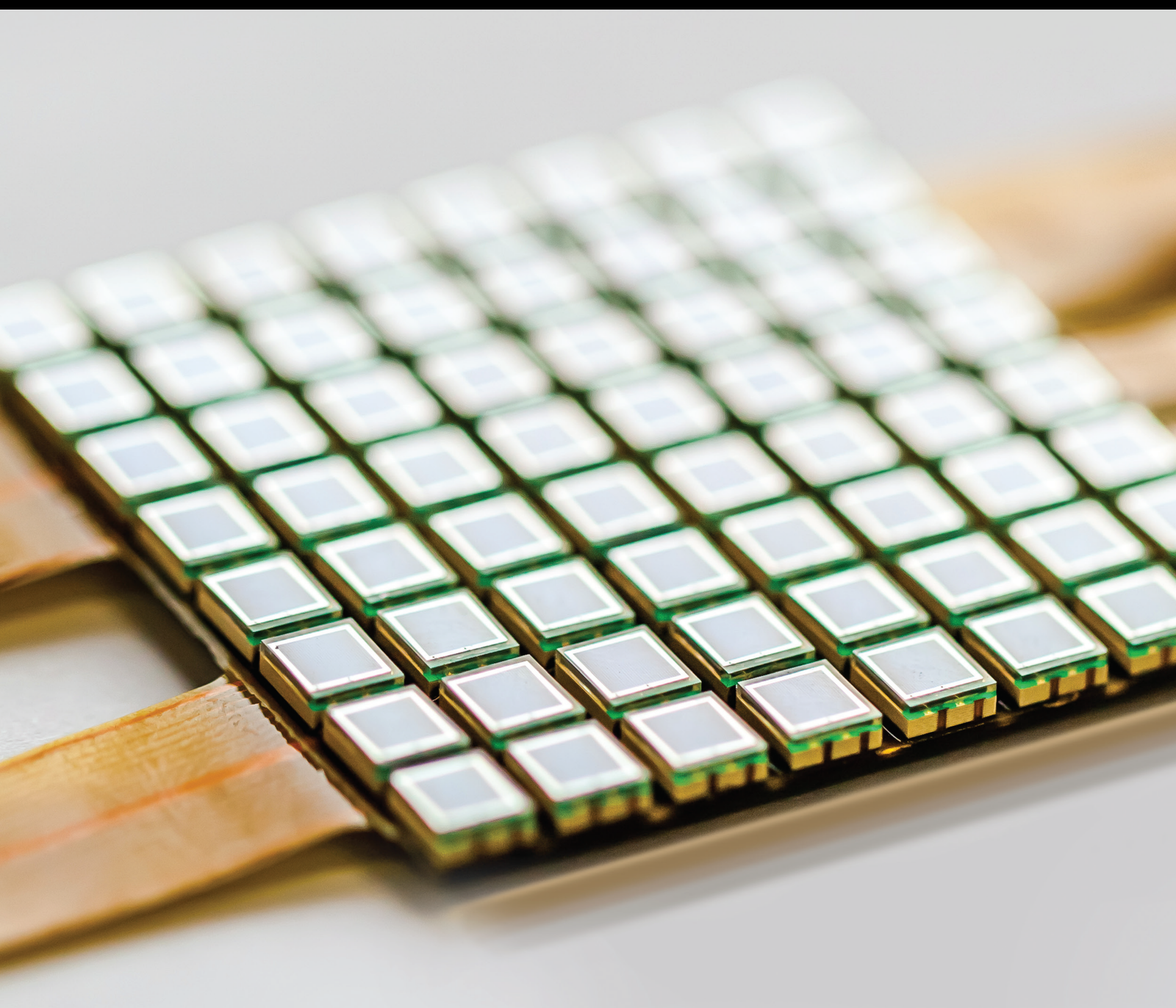# Intelligent Sensing and Artificial Intelligence in Industrial Systems

Lead Guest Editor: Kelvin Wong
Guest Editors: Simon Fong and Yu Lu

# Intelligent Sensing and Artificial Intelligence in Industrial Systems

# Intelligent Sensing and Artificial Intelligence in Industrial Systems

Lead Guest Editor: Kelvin Wong
Guest Editors: Simon Fong and Yu Lu

Ehsan Namaziandost (iD), Iran
Heinz C. Neitzert (iD), Italy
Sing Kiong Nguang (iD), New Zealand
Calogero M. Oddo (iD), Italy
Tinghui Ouyang, Japan
SANDEEP KUMAR PALANISWAMY (iD),
India
Alberto J. Palma (iD), Spain
Davide Palumbo (iD), Italy
Abinash Panda (iD), India
Roberto Paolesse (iD), Italy
Akhilesh Pathak (iD), Thailand
Giovanni Pau (iD), Italy
Giorgio Pennazza (iD), Italy
Michele Penza (iD), Italy
Sivakumar Poruran, India
Stelios Potirakis (iD), Greece
Biswajeet Pradhan (iD), Malaysia
Giuseppe Quero (iD), Italy
Linesh Raja (iD), India
Maheswar Rajagopal (iD), India
Valerie Renaudin (iD), France
Armando Ricciardi (iD), Italy
Christos Riziotis (iD), Greece
Ruthber Rodriguez Serrezuela (iD), Colombia
Maria Luz Rodriguez-Mendez (iD), Spain
Jerome Rossignol (iD), France
Maheswaran S, India
Ylias Sabri (iD), Australia
Sourabh Sahu (iD), India
José P. Santos (iD), Spain
Sina Sareh, United Kingdom
Isabel Sayago (iD), Spain
Andreas Schütze (iD), Germany
Praveen K. Sekhar (iD), USA
Sandra Sendra, Spain
Sandeep Sharma , India
Sunil Kumar Singh Singh (iD), India
Yadvendra Singh (iD), USA
Afaque Manzoor Soomro (iD), Pakistan
Vincenzo Spagnolo, Italy
Kathiravan Srinivasan (iD), India
Sachin K. Srivastava (iD), India
Stefano Stassi (iD), Italy

Danfeng Sun, China
Ashok Sundramoorthy, India
Salvatore Surdo (iD), Italy
Roshan Thotagamuge (iD), Sri Lanka
Guiyun Tian (iD), United Kingdom
Sri Ramulu Torati (iD), USA
Abdellah Touhafi (iD), Belgium
Hoang Vinh Tran (iD), Vietnam
Aitor Urrutia (iD), Spain
Hana Vaisocherova - Lisalova (iD), Czech
Republic
Everardo Vargas-Rodriguez (iD), Mexico
Xavier Vilanova (iD), Spain
Stanislav Vítek (iD), Czech Republic
Luca Vollero (iD), Italy
Tomasz Wandowski (iD), Poland
Bohui Wang, China
Qihao Weng, USA
Penghai Wu (iD), China
Qiang Wu, United Kingdom
Yuedong Xie (iD), China
Chen Yang (iD), China
Jiachen Yang (iD), China
Nitesh Yelve (iD), India
Aijun Yin, China
Chouki Zerrouki (iD), France

# Contents

*Research Article*

# Design of Intelligent Rehabilitation Evaluation Scale for Stroke Patients Based on Genetic Algorithm and Extreme Learning Machine

**Tongle Zhi ⓘD, Chengjie Meng ⓘD, and Linshan Fu ⓘD**

*Department of Neurosurgery, Yancheng First Hospital, Affiliated Hospital of Nanjing University Medical School, The First People's Hospital of Yancheng, Yancheng 224006, China*

Correspondence should be addressed to Chengjie Meng; mengchengjie2000@163.com

The rehabilitation of stroke patients is a long-term process. To realize the automation and quantification of upper limb rehabilitation assessment of stroke patients, an automatic prediction model of rehabilitation evaluation scale was established by extreme learning machine (ELM) according to Fugl-Meyer motor function assessment (FMA). Four movements in the shoulder and elbow joints of FMA were selected. Two acceleration sensors fixed on the forearm and upper arm of the hemiplegic side were used to collect the motion data of 35 patients. After preprocessing and feature extraction, the feature selection was carried out based on genetic algorithm and ELM, and the single-action model and comprehensive prediction model were established, respectively. The results show that the model can accurately and automatically predict the shoulder and elbow score of FMA, and the root mean square error of prediction is 2.16. This method breaks through the limitations of subjectivity, time-consuming and dependence on rehabilitation doctors in the traditional evaluation. It can be easily used in the assessment of long-term rehabilitation.

## 1. Introduction

With the improvement of living standards and the aging of population, the incidence rate of stroke is on the rise and tends to be younger. About 70% to 85% of the first stroke patients have hemiplegia [1]. According to statistics, 2 million 500 thousand stroke patients have added annually in China, 1 million 200 thousand to 1 million 500 thousand of them died from stroke-related diseases, and 7 million survived after stroke, of which 75% left with disability in varying degrees, 40% were severely disabled [2]. This high incidence rate, high mortality rate, and high disability rate bring heavy mental pressure and substantial financial burden to society and families.

Compared with the lower limbs, the upper limb movement is more refined, and the recovery is slow. Therefore, the rehabilitation of upper limb motor function after stroke has always been a significant problem. About one in five stroke patients can not achieve the complete recovery of upper limb function [3]. With the development of telemedicine technology, rehabilitation robot technology, and virtual reality technology, home-based rehabilitation has attracted more and more attention [4–8]. The literature reports that home-based rehabilitation can achieve the same effect as inpatient rehabilitation [9]. However, effectively monitoring and evaluating the progress and functional status of patients' home-based rehabilitation to help rehabilitation doctors further formulate individualized rehabilitation treatment plans has always been the bottleneck of the development of home-based rehabilitation.

At present, the Fugl-Meyer scale is the most widely used method to evaluate the motor function of stroke hemiplegia in the clinic. It requires patients to perform a series of movements. It depends on the evaluator's unarmed operation and observation to check the limb reflex state, flexion and extension cooperative movement, and selective separation movement in different recovery stages, which belongs to subjective evaluation. Many application studies show that

the scale is sensitive and reliable, but many items are. The assessment is time-consuming and requires the participation of therapists or rehabilitation doctors, which limits its application in home rehabilitation to a certain extent [10–12]. Therefore, the ideal evaluation method in home rehabilitation treatment is simple, objective, and quantitative automatic evaluation. The wireless body sensor network composed of multiple sensor nodes can realize the automation and quantification of motor function evaluation. Many studies abroad have used it for home monitoring of the elderly and patients with chronic diseases. Through the study of 169 stroke patients, Uswatte et al. [13, 14] found that the acceleration sensor can capture the clinical information reflecting the degree of upper limb motor dysfunction. Patel et al. [15] used acceleration sensors to automatically estimate the score of Wolf motor function test (WMFT-FAS). However, there are few reports on the combination of motion sensor and clinical evaluation scale in China.

To further automate and quantify the assessment of home based rehabilitation, we propose a method for achieving an automated assessment of the rugl Meyer scale using accelerometry sensors in the hope of more objectively and quantitatively reflecting the patient's upper extremity motor function status. The automatic algorithm can evaluate patients more quickly and accurately, and it is convenient to collect relevant data in order to change the treatment plan and make the treatment measures more active. Four movements were selected from the shoulder and elbow joints of the upper extremity Fugl-Meyer assessment (UE-FMA). The patient's movement data were collected with two acceleration sensors fixed to the forearm and upper arm of the patient's hemiplegic side. The automatic prediction model of the score of the shoulder and elbow joints of UE-FMA was established based on genetic algorithm and extreme learning machine.

## 2. Correlation Algorithm

*2.1. Extreme Learning Machine.* The extreme learning machine (ELM) is a single hidden layer feedforward neural network learning algorithm proposed by Huang et al. [16]. Its hidden layer node parameters (internal weight and bias) are randomly selected, and the external weight of the network obtains its least-squares solution by minimizing the square loss function. The determination process of network parameters does not need any iterative steps, which dramatically improves the operation speed (Figure 1). ELM algorithm is simple and easy, overcomes the disadvantages of slow training speed, and is easy to fall into local optimization of traditional neural network based on gradient descent method. Its network structure and working principle are as follows:

Given the training sample set $\{(x_i, t_i)\}_{i=1}^{N}$ and the number of hidden layer neurons L, there is $a_i, b_i, \beta_i$, so that:

$$f_L(x_j) = \sum_{i=1}^{L} \beta_i g(a_i x_j + b_i) = t_j \qquad (1)$$
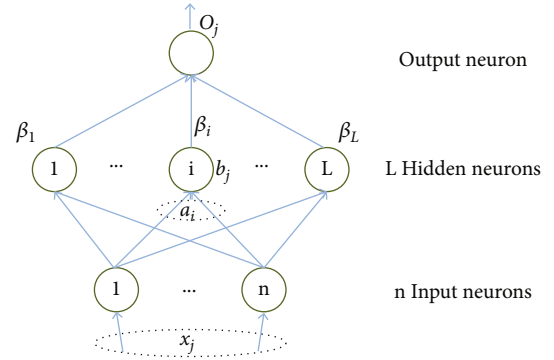


FIGURE 1: Structure diagram of single hidden layer feedforward neural network.

Where: $a_i, b_i$ are node parameters; $\beta_i$ represents the external weight connecting the $i$th hidden layer node and the network output, and g is the activation function.

Equation Equation (1) is written in matrix form as follows:

$$H\beta = T \qquad (2)$$

In which:

$$
H = H(a_1, \cdots, a_L, b_1, \cdots, b_L, x_1, \cdots, x_N)
$$
$$
= \begin{bmatrix} g(a_1 x_1 + b_1) & \cdots & g(a_L x_1 + b_L) \\ \vdots & \ddots & \vdots \\ g(a_1 x_N + b_1) & \cdots & g(a_L x_N + b_L) \end{bmatrix}_{N \times L}
$$

$$
\beta = \begin{bmatrix} \beta_1^T \\ \beta_L^T \end{bmatrix}_{L \times m}
$$

$$
T = \begin{bmatrix} t_1^T \\ t_N^T \end{bmatrix}_{N \times m}
$$

$$(3)$$

H is called hidden layer output matrix.

Considering the prediction error, equation (2) can be modified as:

$$H\beta = T + E \qquad (4)$$

Define the square loss function:

$$J = (H\beta - T)^T (H\beta - T) \qquad (5)$$

In this way, the training problem of ELM network parameters is transformed into the issue of minimizing the square loss function. It is necessary to find a set of optimal parameters to make J minimum. When the activation function g is infinitely differentiable, the hidden layer node parameters can be randomly selected at the beginning of

training, fixed in the training process. The external weight can be obtained by solving equations (6) by the least square method.

$$\widehat{\beta} = \arg\min \|H\beta - T\| = H^+ T \tag{6}$$

*2.2. Genetic Algorithm.* The genetic algorithm is an adaptive probability search method that simulates the natural genetic mechanism and biological evolution process. It has inherent, implicit parallelism and global optimization ability. It maps the problem to the string space, represents a potential solution set of the problem as a population, and the problem's solution as a chromosome, that is, an individual in the people, and eliminates the fittest based on the fitness function. The genetic algorithm realizes population evolution through a series of operators to produce new offspring. Standard genetic operators include selection operator, crossover operator, and mutation operator. The operation flow of the genetic algorithm consists of the following steps.

(1) Code: The solution data of solution space is expressed as genotype string structure data of genetic space. Different combinations of string data represent other solutions to the problem. The typical coding methods are binary coding, gray coding, and floating-point coding

(2) Population initialization: Determine the population size N, crossover probability $P_c$, mutation probability $P_m$, and termination evolution criterion, randomly generate N individuals as the initial population X(0), set the current evolution algebra k = 0 and the maximum evolution algebra T

(3) Calculate the fitness value: Fitness value represents the advantages and disadvantages of individuals or solutions. Different fitness functions are defined for various problems and the fitness value of $\{x_k^i\}_{i=1}^N$ of each individual in the k generation population is calculated according to the fitness function

(4) Genetic manipulation: The selection operator, crossover operator and mutation operator act on the current population in turn to realize evolution

Inspection termination conditions: If the genetic algebra satisfies the termination condition, the calculation is terminated, and the best individual in the current population is output as the final satisfactory solution; Otherwise, k = k + 1, go to step (3)

## 3. Materials and Methods

*3.1. Experimental Design and Data Acquisition.* A total of 35 stroke inpatients from the Department of Neurosurgery, Yancheng First Peoples' Hospital participated in the study. The ethics committee approved the experiment of our hospital. Table 1 shows the basic data of the patients.

The admission criteria are: 1) the clinical diagnosis meets the diagnostic criteria of stroke formulated by the fourth

TABLE 1: General information of research object.

| Information | Value |
| --- | --- |
| Sex, M/F | 19/16 |
| Age (year) | $68.6 \pm 13.1$ |
| Hemorrhage/infarction | 21/14 |
| Hemiplegic site, L/R | 11/24 |
| Time of onset (month) | $9.1 \pm 6.7$ |
| UE-FMA | $15.8 \pm 9.2$ |

national cerebrovascular conference of Chinese Medical Association in 1995, and is confirmed by cranial CT or MRI; 2) The onset time is no more than two years, and the upper limbs on the hemiplegic side have the ability of autonomous movement.

The exclusion criteria were: 1) those with cognitive impairment and unable to cooperate; 2) Accompanied by upper limb or trunk pain and affecting active movement.

Firstly, a rehabilitation physician with many years of clinical experience used UE-FMA to evaluate the subjects. UE-FMA includes 33 items, with a score of $0 \sim 2$ for each item, 0 for incomplete, 1 for partial completion, and 2 for smooth completion, including 15 items for shoulder and elbow joints, with a total of 30 points. The rehabilitation physician gives a score of 0, 1 or 2 by observing the completion of each task, and the sum of each score is the total score. Four movements of shoulder and elbow joints were selected: 1) Forward flexion of shoulder joint; 2) Abduction of shoulder joint; 3) Elbow flexion, forearm pronation and supination; 4) Hand touching the lumbar spine is used as a collection action (Figure 2). The selection of actions is based on the clinical experience of rehabilitation doctors and the standard examination method of bmrmstiwn six level evaluation method. The simplified Fugl-Meyer scale (S-FMA) developed by Hsieh et al. [17] is basically consistent with the actions selected in this study. The reliability and validity of S-FMA have been verified. This reflects the effectiveness of action selection in this study to a certain extent.

The wireless body sensor network system composed of two triaxial acceleration sensor nodes and one receiving node is used for data acquisition. The sensitivity of the acceleration sensor is $\pm 6$ g and the sampling rate is 40 Hz. During the acquisition process, two sensor nodes were fixed on the forearm and upper arm of the patient with hemiplegia,; The c-axis is parallel to the arm, as shown in Figure 1. For the four selected actions, the patient will do it for $1 \sim 2$ times under the guidance of the rehabilitation physician, and then start formal collection. Each action will be repeated $3 \sim 5$ times according to the patient's physical condition. The patient's action data collected by the acceleration sensor will be wirelessly transmitted to the PC client through ZigBee to complete the visualization and classified storage of the data.

*3.2. Fugl-Meyer Shoulder and Elbow Score Prediction Model.* After preprocessing, feature extraction, and feature selection, the original data is input into the ELM model. Firstly, the prediction model of a single action is established, and then the regression relationship between the prediction result of
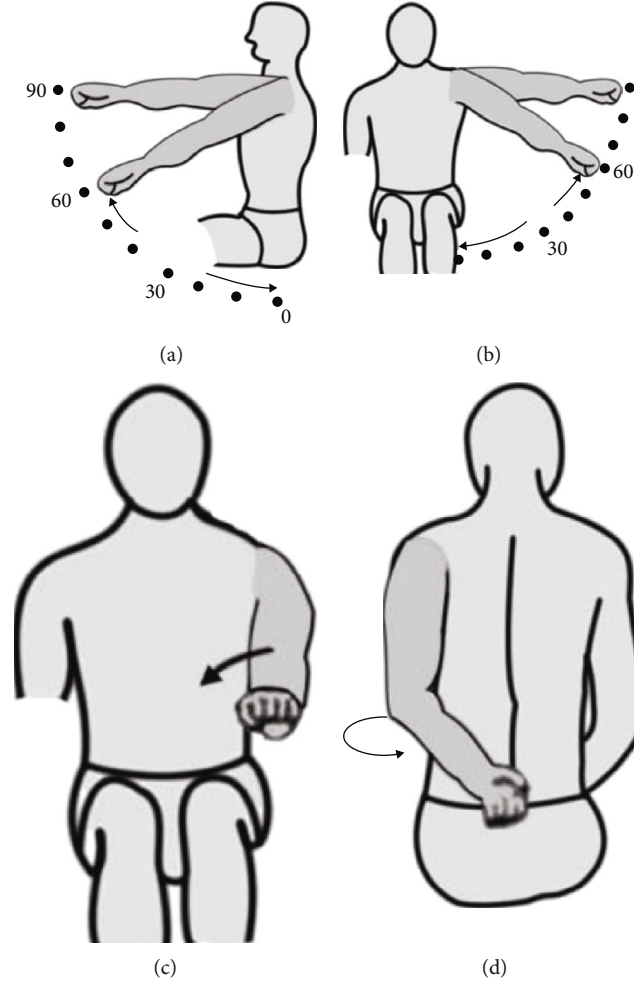
FIGURE 2: Brunnstrom eva luation action. A: forward flexion of shoulder joint. B: Abduction of shoulder joint. C: Elbow flexion, forearm pronation and supination. D: Hand touching the lumbar spine.

a single action and the score of the doctor is established to obtain the comprehensive prediction model. Figure 3 shows the overall process of the algorithm.

### 3.3. Feature Extraction.

The original collected signal is filtered by 9-point median filter to remove the interference caused by clothing friction, sensor looseness and wireless channel noise. Then, according to the experimental and theoretical analysis and previous experience, some statistical features (such as amplitude, mean value, root mean square, approximate entropy, etc.) and physical features (such as energy features, speed and angle) are extracted from the filtered signal. These features reflect the completion of the patient's upper limb movement to a certain extent, including the amplitude, speed, smoothness and coordination of the movement. All the extracted features are shown in Table 2.

AMP, RMS, JERK, MEAN and ApEn are calculated, respectively, on 6 channels (2 nodes and 3 axes of the acceleration sensor), and other features are calculated separately on each node of the acceleration sensor. The angle is the angle between $\chi$ axis and vertical direction. The approximate entropy is a measure of the complexity of time series, which can reflect the irregularity of motion. The velocity is the inte-

gral of acceleration to time. The calculation formulas of energy characteristics and root mean square value are as follows:

$$
\begin{aligned}
\mathrm{ENE} &= \sum_{i=1}^{n} \left( \left( x_i^2 + Y_i^2 + Z_i^2 \right)^{1/2} - 1 \right) \\
\mathrm{RMS} &= \left( \frac{1}{n} \sum_{i=1}^{n} X_i^2 \right)^{1/2}
\end{aligned}
\tag{7}
$$

Where n is the sequence length. X, Y and Z represent the quantity of fractional acceleration on the three axes.

### 3.4. Feature Selection.

All 42 features extracted are encoded into a binary string with a length of 42 composed of "0" and "1". Each binary bit represents a feature in the feature set, and this bit is 1, which represents the corresponding feature subset, 0 indicates that the corresponding feature is not in the selected feature subset. Set the initial population size N =50, the maximum number of iterations T =100, the crossover probability $P_c$=0.6, and the mutation probability $P_m$=0.01. ELM learning algorithm is introduced into the
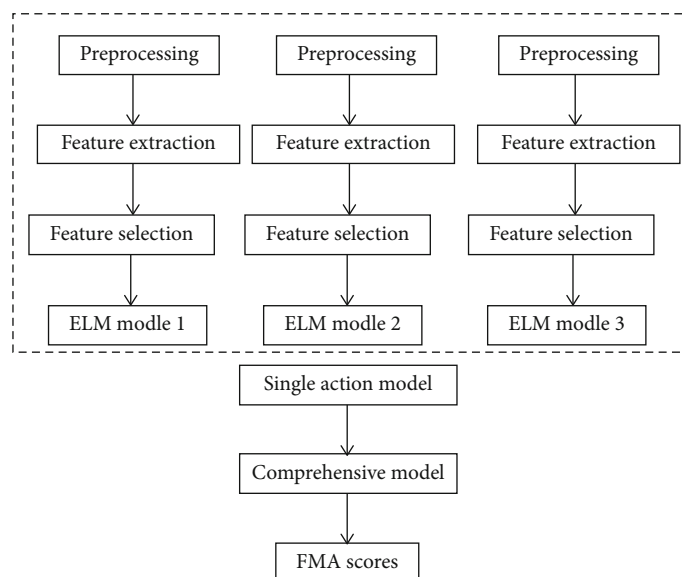
FIGURE 3: Flow chart based on genetic algorithm and extreme learning machine.

TABLE 2: Feature list of upper limb movement.

| Description | Number |
| --- | --- |
| Acceleration amplitude AMP | 2×3 |
| Root mean square value of acceleration RMS | 2×3 |
| Root mean square value of reciprocal acceleration JERK | 2×3 |
| MEAN acceleration MEAN | 2×3 |
| Acceleration approximate entropy ApEn | 2×3 |
| Energy characteristic ENE | 2 |
| Maximum speed Vmax | 2 |
| Speed average Vmean | 2 |
| Standard deviation of speed Vstd | 2 |
| Velocity approximate entropy VapEn | 2 |
| Angle max anglemax | 2 |

design of fitness function; The ELM prediction model is established based on the feature subset corresponding to $x_k^i$. The prediction error of the model is an important evaluation index of the individual fitness in the population. The smaller the prediction error, the higher the individual fitness value. 10 fold cross validation is used to estimate the prediction error. The design of fitness function is as follows:

$$\text{fitness}\left(x_k^i\right) = 1/Error\left(x_k^i\right) \qquad (8)$$

Where $Error(x_k^i)$ represents the result of 10 fold cross validation of prediction error of ELM model established for the feature subset corresponding to individual $x_k^i$. After the fitness function is determined, the evolution process is carried out according to the fitness value of each individual in the population. After repeated iterations of "selection, crossover and variation", individuals with large fitness value are continuously found until the termination condition is met, as shown in Figure 4. In genetic algorithm, the strategy of retaining the optimal fitness individual is adopted, that is, the individual with the highest fitness value is directly incorporated into the next generation population without "selection, crossover and mutation" operation.

## 4. Results and Discussion

The optimal feature set selected for each action is the independent variable, and the corresponding score is the dependent variable. After normalization, it is input into the ELM model. The sigmoidal function is selected as the activation function, and the number of hidden layer nodes is set to 10. First, use a single action to predict Fugl-Meyer's shoulder and elbow joints score, and then consider that Fugl-Meyer scale is a standard scale that has been clinically verified for many years, and there is not much correlation between its actions. Using the data of one action to predict the total score is bound to bring large errors, and the weighted average of the predicted results of the four movements alone can predict the shoulder and elbow score of UE-FMA more accurately. Therefore, for each patient, a regression relationship is established between the single action prediction results and the doctor's score to obtain the final comprehensive prediction model, and the comprehensive prediction results are compared with the single action prediction results. Figure 5 shows the prediction results of single action model and comprehensive model for 35 patients using leave one subject out cross validation (i.e. taking one patient as the test set and the rest as the training set in turn). It can be seen that the error of comprehensive prediction is relatively small and concentrated compared with single action prediction. Table 3 lists the root mean square error (RMSE) and standard deviation (STD) of the prediction errors of 35 patients. The RMSE values predicted by the four singl actions were nearly 10% of the total score (30 points). With the comprehensive prediction model, the predicted RMSE value can be reduced to 2.6 points, accounting for 7.2% of the total score,
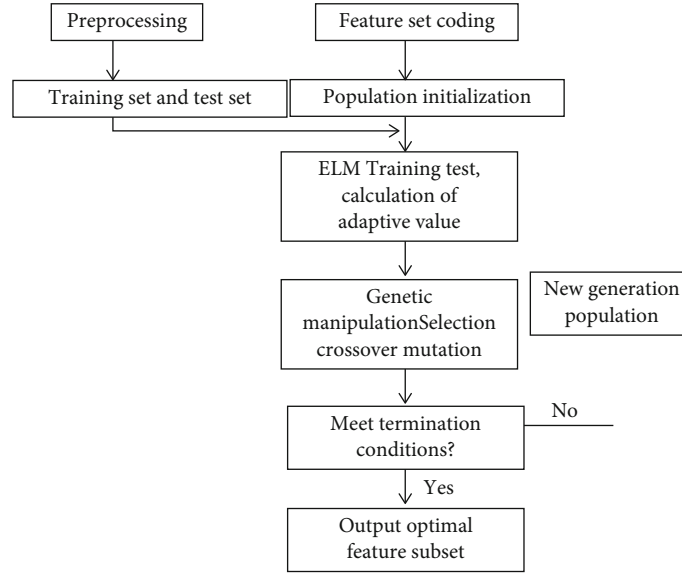
Figure 4: Feature selection process based on genetic algorithm and ELM.
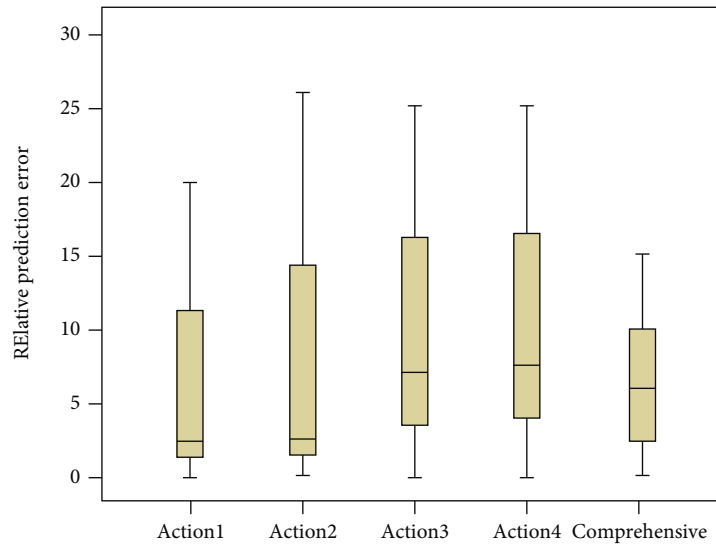


Figure 5: Single action prediction and comprehensive prediction results.

Table 3: Comparison between single and comprehensive prediction.

| Prediction model | RMSE | RMSE/total | STD |
|---|---|---|---|
| Action 1 individual prediction | 2.64 | 8.8 | 2.64 |
| Action 2 individual prediction | 2.83 | 9.4 | 3.32 |
| Action 3 individual prediction | 4.72 | 15.7 | 5.13 |
| Action 4 individual prediction | 3.89 | 13.0 | 4.24 |
| Composive prediction | 2.16 | 7.2 | 2.15 |

which is less than the prediction error of any single action. The standard deviation of the comprehensive prediction error is also the smallest, indicating that the comprehensive prediction model is more stable, which is consistent with Figure 5.

Hsueh et al. [18] determined that the minimum detectable change (MDC) of Fugl-Meyer upper limb motor function rating scale was 7.2 points, accounting for 10.9% of the total score. MDC is the minimum threshold to identify whether the change exceeds the random test error, and the random error is often caused by different evaluators' different understanding of the evaluation standard or different evaluation time and space. MDC reflects the allowable range of evaluation error of clinical application scale to a certain extent. The prediction error of the comprehensive prediction model proposed in this paper for the shoulder and elbow score of UE-FMA is 2.16 points, accounting for 7.2% of the total score. Within this range, it shows that the result is clinically acceptable.

Patel team [15, 19] has done a lot of research on the use of motion sensors in clinical evaluation, but they mainly

focus on the Wolf motor function test (WMFT); They uses six acceleration nodes to collect data, selects a single WMFT action, and establishes a multiple linear regression model to predict the shoulder and elbow score of Fugl-Meyer scale. The minimum prediction error is 2.35 points. The same acquisition device was used to select 8 WMFT actions to automatically predict the score of Fugl-Meyer scale. However, WMFT often requires high motor coordination ability, and needs specific tools to complete the test. It is rarely used in clinical practice in China, and it is difficult for patients to complete home rehabilitation. Our study directly selects actions from Fugl-Meyer scale, uses fewer sensor nodes to predict the shoulder and elbow score of Fugl-Meyer scale, and obtains more accurate prediction results. Compared with WMFT, the actions selected from Fugl-Meyer scale can be completed directly by patients without any additional experimental conditions, which is easier to realize in home rehabilitation evaluation.

In home rehabilitation or community rehabilitation, patients can accurately record the actual situation of upper limb motor function during training by wearing acceleration sensors, and feed back to remote rehabilitation doctors to help doctors formulate individualized and professional rehabilitation treatment plans, so as to maximize the recovery of upper limb motor function. It can also be used to evaluate the efficacy of different rehabilitation treatment techniques. However, there is still a lack of evaluation of wrist and hand function. In future work, sensors that can reflect the wrist and hand function state (such as bending sensor) will be used to collect wrist and hand movement data, and a model will be established to predict the score of Fugl-Meyer wrist and hand part, so as to more comprehensively and carefully reflect the whole upper limb movement function of the patient. In the future, other deep learning models will be used [20, 21].

## 5. Conclusions

This study combines the motion sensor with the clinical evaluation scale, and uses four actions to accurately and automatically predict the shoulder and elbow joints score of UE-FMA, breaking through the limitations of subjectivity and time-consuming in the traditional evaluation and the dependence on rehabilitation doctors or therapists. It was initially shown that the acceleration sensor can be used to automatically predict shoulder and elbow scores on the Fugl-Meyer upper extremity motor function rating scale, enabling automation, objectification, and quantitation of rehabilitation assessments.

## Data Availability

The data used to support the findings of this study are available from the corresponding author upon request.

## Conflicts of Interest

The authors declare no conflict of interest.

## References

[1] B. Jiang, H. Sun, X. Ru et al., "Prevalence, incidence, prognosis, early stroke risk, and stroke-related prognostic factors of definite or probable transient ischemic attacks in china, 2013," *Frontiers in Neurology*, vol. 8, p. 309, 2017.

[2] X. Yi, H. Luo, J. Zhou et al., "Prevalence of stroke and stroke related risk factors: A population based cross sectional survey in southwestern china," *BMC Neurology*, vol. 20, no. 1, 2020.

[3] K. L. Meadmore, E. Hallewell, C. Freeman, and A. M. Hughes, "Factors affecting rehabilitation and use of upper limb after stroke: views from healthcare professionals and stroke survivors," *Topics in Stroke Rehabilitation*, vol. 26, no. 2, pp. 94–100, 2019.

[4] K. J. Pascual, E. Vlasova, K. J. Lockett, J. Richardson, and M. Yochelson, "Evaluating the impact of personalized stroke management tool kits on patient experience and stroke recovery," *Journal of Patient Experience*, vol. 5, no. 4, pp. 244–249, 2018.

[5] R. G. Bellomo, T. Paolucci, A. Saggino et al., "The wereha project for an innovative home-based exercise training in chronic stroke patients: A clinical study," *Journal of Central Nervous System Disease*, vol. 12, 2020.

[6] L. Dodakian, A. L. McKenzie, V. Le et al., "A home-based telerehabilitation program for patients with stroke," *Neurorehabilitation and Neural Repair*, vol. 31, no. 10-11, pp. 923–933, 2017.

[7] K. O. Thielbar, K. M. Triandafilou, A. J. Barry et al., "Home-based Upper Extremity Stroke Therapy Using a Multiuser Virtual Reality Environment: A Randomized Trial," *Archives of Physical Medicine and Rehabilitation*, vol. 101, no. 2, pp. 196–203, 2020.

[8] S. Li, J. Zheng, and D. Li, "Precise segmentation of non-enhanced computed tomography in patients with ischemic stroke based on multi-scale u-net deep network model," *Computer Methods and Programs in Biomedicine*, vol. 208, article 106278, 2021.

[9] J. Langan, K. Delave, L. Phillips, P. Pangilinan, and S. H. Brown, "Home-based telerehabilitation shows improved upper limb function in adults with chronic stroke: a pilot study," *Journal of Rehabilitation Medicine*, vol. 45, no. 2, pp. 217–220, 2013.

[10] S. H. Ohn, W. K. Yoo, D. Y. Kim et al., "Measurement of synergy and spasticity during functional movement of the post-stoke hemiplegic upper limb," *Journal of Electromyography and Kinesiology*, vol. 23, no. 2, pp. 501–507, 2013.

[11] D. A. Cunningham, J. S. Knutson, V. Sankarasubramanian, K. A. Potter-Baker, A. G. Machado, and E. B. Plow, "Bilateral contralaterally controlled functional electrical stimulation reveals new insights into the interhemispheric competition model in chronic stroke," *Neurorehabilitation and Neural Repair*, vol. 33, no. 9, pp. 707–717, 2019.

[12] Y. L. Lin, K. A. Potter-Baker, D. A. Cunningham et al., "Stratifying chronic stroke patients based on the influence of contralesional motor cortices: An inter-hemispheric inhibition study," *Clinical Neurophysiology*, vol. 131, no. 10, pp. 2516–2525, 2020.

[13] G. Uswatte, W. L. Foo, H. Olmstead, K. Lopez, A. Holand, and L. B. Simms, "Ambulatory Monitoring of Arm Movement Using Accelerometry: An Objective Measure of Upper-Extremity Rehabilitation in Persons With Chronic Stroke," *Archives of Physical Medicine and Rehabilitation*, vol. 86, no. 7, pp. 1498–1501, 2005.

[14] G. Uswatte, C. Giuliani, C. Winstein, A. Zeringue, L. Hobbs, and S. L. Wolf, "Validity of Accelerometry for Monitoring Real-World Arm Activity in Patients With Subacute Stroke: Evidence From the Extremity Constraint-Induced Therapy Evaluation Trial," *Archives of Physical Medicine and Rehabilitation*, vol. 87, no. 10, pp. 1340–1345, 2006.

[15] S. Patel, R. Hughes, T. Hester et al., "A novel approach to monitor rehabilitation outcomes in stroke survivors using wearable technology," *Proceedings of the IEEE*, vol. 98, no. 3, pp. 450–461, 2010.

[16] G. B. Huang, Q. Y. Zhu, and C. K. Siew, "Extreme learning machine: Theory and applications," *Neurocomputing*, vol. 70, no. 1-3, pp. 489–501, 2006.

[17] Y. W. Hsieh, I. P. Hsueh, Y. T. Chou, C. F. Sheu, and G. Kwakkel, "Development and validation of a short form of the fugl-meyer motor scale in patients with stroke," *Stroke*, vol. 38, no. 11, pp. 3052–3054, 2007.

[18] I. Hsueh, M. J. Hsu, C. F. Sheu, L. Su, C. L. Hsieh, and J. H. Lin, "Psychometric comparisons of 2 versions of the fugl-meyer motor scale and 2 versions of the stroke rehabilitation assessment of movement," *Neurorehabilitation & Neural Repair*, vol. 22, no. 6, pp. 737–744, 2008.

[19] S. Patel, H. Park, P. Bonato, L. Chan, and M. Rodgers, "A review of wearable sensors and systems with application in rehabilitation," *Journal of NeuroEngineering and Rehabilitation*, vol. 9, no. 1, 2012.

[20] Z. Tang, Y. Li, X. Chai, H. Zhang, and S. Cao, "Adaptive nonlinear model predictive control of nox emissions under load constraints in power plant boilers," *Journal of Chemical Engineering of Japan*, vol. 53, no. 1, pp. 36–44, 2020.

[21] H. Gao, C. Wu, D. Huang, D. Zha, C. Zhou, and The Third People's Hospital of HeFei, Heifei 230000, China, "Prediction of fetal weight based on back propagation neural network optimized by genetic algorithm," *Mathematical Biosciences and Engineering*, vol. 18, no. 4, pp. 4402–4410, 2021.

Hindawi

## Research Article
# The Effect of Enhanced Multislice Spiral Computed Tomography Scan in Nursing

## Yan Wang, Binyan Qian, and Jidong Peng [ID]

*Department of Radiology, Ganzhou People's Hospital, 341000 Jiangxi, China*

Correspondence should be addressed to Jidong Peng; jidongpeng2021@163.com

*Purpose.* Side effects such as local pain and tissue swelling will affect the effect of enhanced multislice spiral computed tomography (CT) scan. The aim of this study was to explore the effect of imaging nursing in enhanced CT scan for heart patients. *Method.* We selected 86 heart patients to receive enhanced multislice spiral CT scan as the research objects and randomly divided them into the test group and the control group. Imaging nursing and traditional nursing intervention was taken to compare the nursing effects of the two groups. *Results.* The incidence of unpleasant mood in the test group was 9.3%, which was significantly lower than that in the control group. The nursing satisfaction of the test group was 97.7%, which was much higher than the 79.1% of the control group. At the same time, the visual analogue scale (VAS) score of the test group and the incidence of contrast agent extravasation were significantly lower than those of the control group. *Conclusion.* The use of imaging nursing for heart patients with enhanced multislice spiral CT scan can reduce the patient's unhealthy mood and improve nursing satisfaction, and the nursing effect is ideal.

## 1. Introduction

Multislice spiral computed tomography- (CT-) enhanced scanning is commonly used in clinical practice [1–4], which belongs to computer scanning technology. The clinical advantages [5–7] include clear images, short scanning time, and qualitative and positioning diagnoses and are widely used in clinical examinations. In CT-enhanced scanning, water-soluble contrast agents need to be injected intravenously.

We commonly used contrast agents which include non-ionic contrast agents and ionic contrast agents. The former has relatively few adverse reactions, but the price is higher, and the latter is cheap but easy adverse reactions may be taken seriously during the examination. Thus, corresponding nursing measures should be applied to the heart patients.

The clinically enhanced CT scan of heart patients requires intravenous infusion of water-soluble contrast agents to ensure that the X-ray absorption rate of the patient's diseased tissues is increased [8–10], which can increase the density of normal tissues and diseased tissues

and the difference in show efficiency. Multislice spiral CT enhanced scanning on heart patients can easily lead to related leakage of the contrast agent [11–16], which will lead to low patient compliance and decreased satisfaction.

The contrast-enhanced imaging examination is mainly based on a plain scan [17, 18], and then, the diseased tissue can be qualitatively diagnosed through the difference of contrast agent density. Contrast-enhanced scanning requires high-pressure injection when the contrast agent is injected. However, due to individual differences in heart patients, some heart patients will ooze out after the injection of the contrast agent. The contrast agent itself will have a certain impact on the local skin tissue of the patient, mainly local pain and tissue swelling.

With the rapid development of enhanced imaging examinations, enhanced imaging examinations have been widely used in medical imaging diagnosis and differential diagnosis, which can improve the detection rate of lesions and the accuracy of diagnosis. However, if the exudation is severe, serious consequences such as tissue necrosis and limb dysfunction may occur. Therefore, predictive nursing interven-
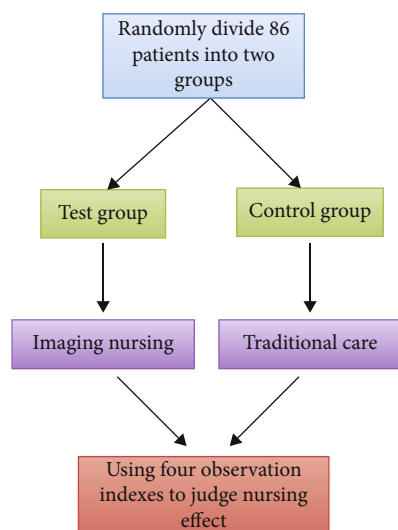
Figure 1: The specific structure of the control experiment.

tion is particularly important.

As the success or failure of contrast agent injection for enhanced imaging examination will directly affect the density identification of diseased tissues and normal tissues, the care before and after the enhanced imaging examination is one of the important links to ensure accurate and effective image information. Therefore, the aim of this study was to explore the effect of imaging nursing in an enhanced CT scan for heart patients.

## 2. Materials and Methods

*2.1. General Information.* According to the established control experiment structure, this paper studies the imaging nursing effect of enhanced scanning with multislice spiral CT. The experimental structure is shown in Figure 1.

The 86 heart patients with enhanced imaging examination in our hospital were randomly divided into two groups. The number of cases in each group is 43. The age of the test group was 20-73 years, the average age was $44.9 \pm 7.3$ years, and the male to female ratio was $24 : 19$. The control group was 21 to 70 years old, with an average age of $44.0 \pm 6.4$ years old, and the ratio of males to females was $20 : 23$. The comparison of the two groups of samples showed no significant difference ($t = 0.608$, $P = 0.545$). The specific situation is shown in Figure 2.

*2.2. Method*

*2.2.1. Control Group.* A total of 43 cases were treated with traditional care. After the scan, the heart patients were evaluated psychologically. Traditional nursing includes basic nursing, treatment and medication, rehabilitation guidance, health education, psychological nursing, and other nursing work.

*2.2.2. Test Group.* A total of 43 cases were treated with imaging care. The specific steps are as follows [19, 20].

The first step is to measure and record the patient's blood pressure, height, weight, etc. before the examination, which helps to choose the contrast agent and determine the amount of contrast agent. The nurse should carefully read the examination application form and patiently ask the patient's condition and allergy history to determine whether it is suitable for CT-enhanced examination. If the patient needs an abdominal examination, fasting can avoid intestinal substances affecting the examination results. Barium meal examinations have been carried out recently, and CT-enhancement examinations can only be carried out after 1 week. Before the examination, check whether the patient has residual barium meal. If residual, use diatrizoate meglumine at a dose of 1000 ml 2 hours before the examination. And then, we use 500 ml to exclude heart patients with allergies and asthma from other substances, exclude heart patients with contraindications, and strictly control the examination of high-risk heart patients.

In the second step, the patient may have emotions such as fear and anxiety due to the examination. Before the examination, the nurse should guide the patient's psychology, explain the knowledge of the contrast agent, and encourage the patient to actively cooperate with the examination.

The third step is to strictly abide by the relevant operating regulations during the scan to avoid liquid leakage. The nurse should make a reasonable choice of the injection position according to the actual situation. During the puncture process, strictly perform aseptic operations and select the venous lumens of the extremities. After completing the puncture and doing a good job of drug injection, place the puncture arm to a comfortable position and instruct the patient to rest for 0.5 to 1 hour and relax. If it is painful, the nurse should inject analgesic drugs according to the patient's pain.

In the fourth step, after the scan, the nurse should assist the patient to get out of bed and instruct the patient to drink plenty of water, which can accelerate the excretion of drugs. All kinds of first aid supplies are prepared in the CT-enhanced scanning room to actively respond to unforeseen adverse reactions. If the patient is mildly allergic and needs to drink plenty of water and rest and if the patient is moderately allergic, the intravenous channel needs to be established quickly and injected with 10 mg dexamethasone, if necessary, 0.5~1 mg epinephrine, and rescue preparations will be made. Well, if the patient is severely allergic, he should be rescued immediately, the emergency department shall be notified, and the relevant cooperation work will be done to treat the patient in the shortest time.

*2.3. Observation Indicators*

*2.3.1. Incidence of Unpleasant Mood.* The negative emotions we studied include tension, uneasiness, and anxiety.

*2.3.2. Nursing Satisfaction.* Questionnaires were distributed to heart patients to count nursing satisfaction. The survey results were divided into 3 levels: very satisfied (V), generally satisfied (G), and not satisfied (N). The calculation formula
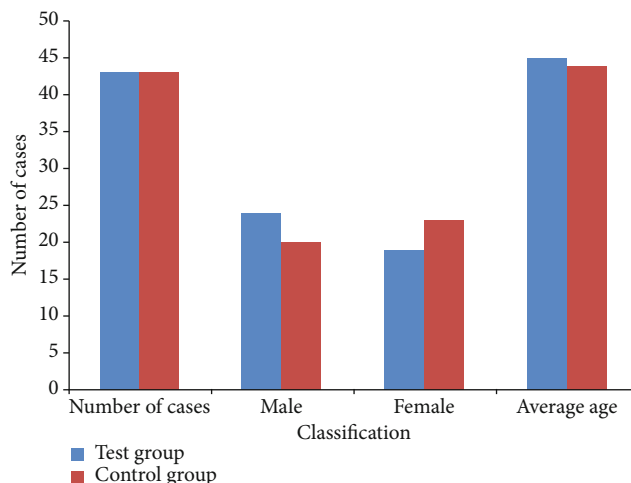
FIGURE 2: Details of sample data.



(a)

(b)

(c)
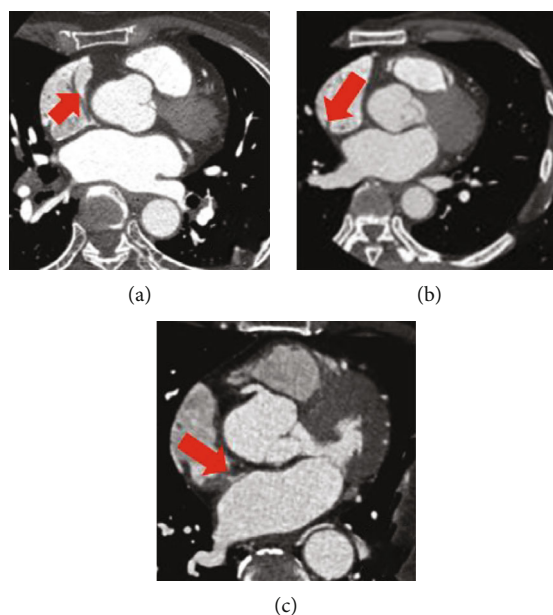
FIGURE 3: Multislice spiral CT image of a heart disease patient.

of nursing satisfaction is as follows:

$$N = \frac{V + G}{T} \times 100\%. \qquad (1)$$

In Equation (1), $N$ represents nursing satisfaction, $V$ represents very satisfactory, $G$ represents general satisfaction, and $T$ represents the total number of cases.

*2.3.3. Visual Analogue Scoring Method.* This paper uses the visual analogue scale (VAS) [21–24] to assess the patient's pain level. The total score is 10 points. The higher the VAS score is, the more severe the pain.

*2.3.4. Incidence of Contrast Media Extravasation.* The calculation of the incidence of contrast agent extravasation is actually the ratio of the number of cases of contrast agent extravasation to the total number of cases.

*2.4. Statistical Processing.* SPSS 26.0 software processes the data, counts for chi-square statistics, and measures data for $t$ test. $P < 0.05$ indicates that the difference is meaningful.

## 3. Results

*3.1. CT Images.* Figure 3 shows part of the multislice spiral CT images of 86 heart patients with heart disease. The red arrow points to the part of the heart disease. The patient can be cared for more accurately through imaging. Imaging nursing and traditional nursing intervention is applied to examine the difference in treatment and diagnosis.

*3.2. Comparison of Incidence of Unpleasant Mood.* The incidence of unpleasant mood in the test group was significantly lower; compared with the control group, the difference was significant ($P < 0.05$). The specific situation of the
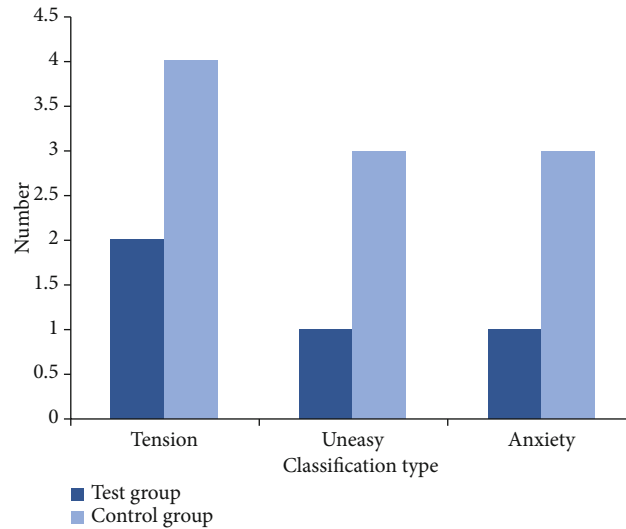
FIGURE 4: The specific situation of unpleasant emotions.

occurrence of unpleasant mood is shown in Figure 4, and the incidence of unpleasant mood and the results of statistical processing are shown in Table 1.

3.3. *Comparison of Nursing Satisfaction.* The nursing satisfaction of heart patients in the test group was significantly improved compared with the control group, and the difference was significant ($P = 0.007$). The specific situation of nursing satisfaction is shown in Figure 5, and the nursing satisfaction and statistical processing results are shown in Table 2.

3.4. *Comparison of VAS Score.* The VAS pain scores of the test group and the control group are shown in Table 3. The scores of the test group are significantly lower than those of the control group, which proves that the nursing effect of the multislice spiral CT-enhanced scanning is more effective than traditional nursing.

3.5. *Comparison of Incidence of Contrast Agent Extravasation.* It can be seen from Figure 6 that the incidence of contrast agent extravasation in the test group is lower than that in the control group ($P = 0.042$), and imaging nursing has a great advantage in contrast agent extravasation.

## 4. Discussion

In the process of enhanced scanning with multislice spiral CT, heart patients need to be injected intravenously with a water-soluble organic iodine contrast agent. The X-ray absorption rate of the diseased tissue is increased. Compared with the normal tissue, the difference is obvious. The display

TABLE 1: Comparison of incidence of unpleasant mood.

| Type | Test group | Control group |
|---|---|---|
| Incidence of unpleasant mood | 9.3% | 23.3% |
| $\chi^2$ value | 3.071 | |
| $P$ value | 0.039 | |

rate of the disease is greatly improved. The contrast is significantly enhanced.

However, due to the invasiveness of the examination and the use of contrast agents and because the heart patients do not understand the relevant knowledge, they are prone to different levels of unhealthy emotions, and patient care should be strengthened. During the nursing process, nurses should pay attention to the psychological fluctuations of heart patients, do a good job of diversion, actively implement various nursing countermeasures, prompt heart patients to actively cooperate with the examination, deepen heart patients' understanding of relevant knowledge, and prompt heart patients to successfully complete the examination [25–27]. Heart patients are provided with symptomatic treatment, which will ultimately significantly improve patient treatment effects.

Clinical studies have shown that the accuracy of CT-enhanced scanning will be directly affected by the sharpness of the image. In addition to the scanning technology, the image quality is also related to the patient's mental state. Therefore, before, during, and after the enhanced multislice spiral CT scan of the patient, individualized nursing intervention should be taken to help the patient relax and maintain a good emotional state, to pay attention to observe
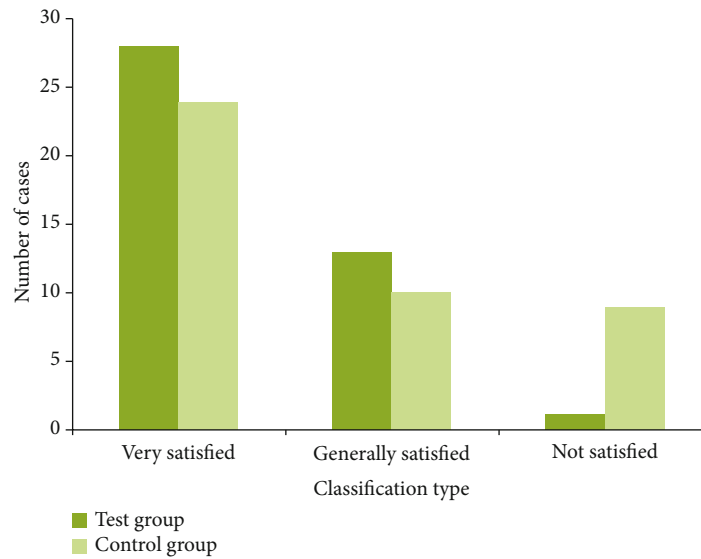
FIGURE 5: Details of nursing satisfaction.

TABLE 2: Comparison of nursing satisfaction.

| Type | Test group | Control group |
|---|---|---|
| Nursing satisfaction | 97.7% | 79.1% |
| $\chi^2$ value | | 7.242 |
| $P$ value | | 0.007 |

TABLE 3: VAS pain score of test group and control group.

| Group | VAS score |
|---|---|
| Test group | $1.2 \pm 0.5$ |
| Control group | $3.0 \pm 0.8$ |
| $\chi^2$ value | 12.512 |
| $P$ value | <0.001 |
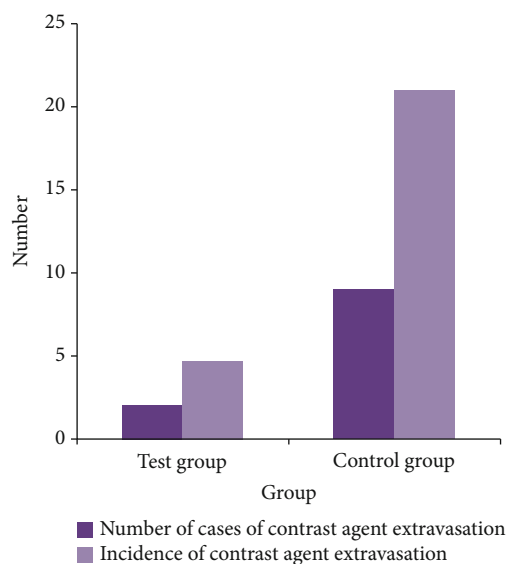


FIGURE 6: Comparison of the incidence of contrast agent extravasation.

whether there are adverse reactions, and to do a good job of coping. The purpose of nursing is to improve the clarity of scanned images and patient satisfaction. For prediction of the optimized nursing effect, a deep learning platform [28] can be utilized to enhance the nursing intervention.

## 5. Conclusion

According to the experiments in this paper, the incidence of unpleasant emotions in the test group was significantly lower, and the data comparison between the groups was <0.05. The results suggest that the clinical application value of imaging nursing is higher and can be referred to clinically. In addition, the VAS pain score of the test group was lower than that of the control group, and the incidence of contrast agent extravasation was also significantly lower than that of the control group.

In summary, multislice spiral CT enhanced scan heart patients have an ideal effect and high feasibility. It can significantly alleviate heart patients' unpleasant mood and reduce the incidence of contrast agent leakage. As such, our study is clinically worth promoting.

## Data Availability

The data used to support the findings of this study are available from the corresponding author upon request.

## Conflicts of Interest

The authors declare that they have no conflicts of interest.

## References

[1] F. Cademartiri, G. Luccichenti, and A. V. Lugt, "Sixteen-row multislice computed tomography: basic concepts, protocols, and enhanced clinical applications," *Seminars in Ultrasound CT and MRI*, vol. 25, no. 1, pp. 2–16, 2004.

[2] H. Bruder, T. Flohr, and S. Schaller, "Imaging method for a multi-slice spiral CT scan with 3D reconstruction, and a computed tomography unit for carrying out this method," vol. 21, no. 3, pp. 75–79, 2004.

[3] Y. Jin-Gang, P. Wei-Bin, and Y. Rui-Gen, "Multi-slice spiral CT single-phase enhanced scanning in the pancreas," *Chinese Journal of Medical Imaging Technology*, vol. 22, no. 9, pp. 1380–1382, 2006.

[4] H. Scheffel, P. Stolzmann, M. J. Wilhelm et al., "Conventional radiography and computed tomography of cardiac assist devices," *European Radiology*, vol. 14, no. 5, pp. 186–190, 2009.

[5] A. S. Lowe and C. L. Kay, "Recent developments in CT: a review of the clinical applications and advantages of multidetector computed tomography," *Imaging*, vol. 18, no. 2, pp. 62–67, 2006.

[6] S. Kappler, T. Hannemann, and E. Kraft, "First results from a hybrid prototype CT scanner for exploring benefits of quantum-counting in clinical CT," vol. 57, no. 9, pp. 8313–83130, 2012.

[7] T. Masaryk, R. Kolonick, T. Painter, and D. B. Weinreb, "The economic and clinical benefits of portable head/neck CT imaging in the intensive care unit," *Radiology Management*, vol. 30, no. 2, pp. 50–54, 2008.

[8] C. Y. Shu, L. H. Gan, C. R. Wang, X. L. Pei, and H. B. Han, "Synthesis and characterization of a new water-soluble endohedral metallofullerene for MRI contrast agents," *Carbon*, vol. 44, no. 3, pp. 496–500, 2006.

[9] L. Nebuloni, G. A. Kuhn, and R. Müller, "A comparative analysis of water-soluble and blood-pool contrast agents for in vivo vascular imaging with micro-CT," *Academic Radiology*, vol. 20, no. 10, pp. 1247–1255, 2013.

[10] F. L. Weitl, M. Sovak, T. M. Williams, and J. H. Lang, "Studies in the design of x-ray contrast agents. Synthesis, hydrophobicity, and solubility of some iodoresorcyl bis(beta-glucosides)," *Journal of Medicinal Chemistry*, vol. 19, no. 12, pp. 1359–1362, 1976.

[11] M. Hamon, G. G. L. Biondi-Zoccai, P. Malagutti et al., "Diagnostic performance of multislice spiral computed tomography of coronary arteries as compared with conventional invasive coronary angiography: a meta-analysis," *Journal of the American College of Cardiology*, vol. 48, no. 9, pp. 1896–1910, 2006.

[12] S. Achenbach, S. Ulzheimer, and U. Baum, "Noninvasive coronary angiography by retrospectively ECG-gated multislice spiral CT," *ACC Current Journal Review*, vol. 10, no. 3, pp. 44–44, 2001.

[13] M. Kachelrie, S. Ulzheimer, and W. A. Kalender, "ECG-correlated image reconstruction from subsecond multi-slice spiral CT scans of the heart," *Medical Physics*, vol. 27, no. 8, pp. 1881–1902, 2000.

[14] M. Vembar, M. J. Garcia, D. J. Heuscher et al., "A dynamic approach to identifying desired physiological phases for cardiac imaging using multislice spiral CT," *Medical Physics*, vol. 30, no. 7, pp. 1683–1693, 2003.

[15] S. Schaller and T. Flohr, "Spiral interpolation algorithm for multislice spiral CT. I. Theory," *Medical Imaging IEEE Transactions on*, vol. 19, no. 9, pp. 822–834, 2000.

[16] W. A. Kalender, T. Flohr, S. Schaller, J. Krause, and T. Fuchs, "Spiral interpolation algorithms for multislice spiral CT–part II: measurement and evaluation of slice sensitivity profiles and noise at a clinical multislice system," *IEEE Transactions on Medical Imaging*, vol. 19, no. 9, pp. 835–847, 2000.

[17] L. Bin, G. Fengling, and S. Chuan, "Analysis of the application value of plain CT scan and contrast-enhanced scan in the diagnosis of hypopharyngeal carcinoma and clinical manifestation of its adjacent structure," *The Practical Journal of Cancer*, vol. 86, no. 5, pp. 543–548, 2018.

[18] M. B. I. Lobbes, U. C. Lalji, P. J. Nelemans et al., "The quality of tumor size assessment by contrast-enhanced spectral mammography and the benefit of additional breast MRI," *Journal of Cancer*, vol. 6, no. 2, pp. 144–150, 2015.

[19] T. Shinjo and R. Kagami, "Radiological imaging change in a malignant bowel obstruction patient treated with octreotide," *Supportive Care in Cancer*, vol. 17, no. 6, pp. 753–755, 2009.

[20] K. P. Mcguire, E. S. Hwang, and A. Cantor, "Surgical patterns of care in patients with invasive breast cancer treated with neoadjuvant systemic therapy and breast magnetic resonance imaging: results of a secondary analysis of TBCRC 017," *Annals of Surgical Oncology*, vol. 22, no. 1, pp. 75–81, 2015.

[21] R. C. B. Aitken, "A growing edge of measurement of feelings [abridged]," *Proceedings of the Royal Society of Medicine*, vol. 62, no. 10, pp. 989–993, 1969.

[22] K. Taxis, B. Dean, and N. Barber, "The validation of an existing method of scoring the severity of medication administration errors for use in Germany [J]," *Pharmacy World & Science*, vol. 24, no. 6, pp. 236–239, 2002.

[23] L. C. Loh, S. H. Puah, C. V. Ho et al., "Disability and breathlessness in asthmatic patients-a scoring method by repetitive inspiratory effort," *Journal of Asthma Research*, vol. 42, no. 10, pp. 853–858, 2005.

[24] A. T. Casey, J. M. Bland, and H. A. Crockard, "Development of a functional scoring system for rheumatoid arthritis patients with cervical myelopathy," *Annals of the Rheumatic Diseases*, vol. 55, no. 12, pp. 901–906, 1996.

[25] Q. Dan, M. A. Xiaolian, and O. Room, "The effect and influence of humanistic care in the whole process on the nursing of patients in the operating room," *China Continuing Medical Education*, vol. 46, no. 5, pp. 127–129, 2019.

[26] M. Nakabayashi, K. Teranishi, and M. Niikura, "A change in the degree of the mental health condition of mother with infants: the follow-up survey until an infant was 18 months from 4 months," *Japanese journal of maternal health*, vol. 46, pp. 655–665, 2006.

[27] D. Jian-Ping, "Obstetrics and gynecology. Episiotomy postoperative nursing countermeasure analysis," *World latest medicine Information*, vol. 124, no. 5, pp. 46–49, 2016.

[28] Z. Tang, G. Zhao, and T. Ouyang, "Two-phase deep learning model for short-term wind direction forecasting," *Renewable Energy*, vol. 173, pp. 1005–1016, 2021.

*Research Article*

# Model and Verification of Medical English Machine Translation Based on Optimized Generalized Likelihood Ratio Algorithm

**Peng Yu** [ID] [1] **and Youyu Zhu** [ID] [2]

[1]*School of Foreign Languages, Chaohu University, Chaohu, Anhui 238024, China*
[2]*School of Basic Medical Sciences, Anhui Medical University, Hefei 230032, China*

Correspondence should be addressed to Youyu Zhu; zhuyy0103@126.com

Phrase identification plays an important role in medical English machine translation. However, the phrases in medical English are complicated in internal structure and semantic relationship, which hinders the identification of machine translation and thus affects the accuracy of translation results. With the aim of breaking through the bottleneck of machine translation in medical field, this paper designed a machine translation model based on the optimized generalized likelihood ratio (GLR) algorithm. Specifically, the model in question established a medical phrase corpus of 250,000 English and 280,000 Chinese words, applied the symbol mapping function to the identification of the phrase's part of speech, and employed the syntactic function of the multioutput analysis table structure to correct the structural ambiguity in the identification of the part of speech, eventually obtaining the final identification result. According to the comprehensive verification, the translation model employing the optimized GLR algorithm was seen to improve the speed, accuracy, and update performance of machine translation and was seen to be more suitable for machine translation in medical field, therefore providing a new perspective for the employment of medical machine translation.

## 1. Introduction

Affected by the raging novel coronavirus the world over, medical English translation has become an active and important communication medium in the fight against the epidemic among the countries. In recent years, the number of machine translation applications has witnessed a boom due to the fact that education and technology develop at the fastest speed that we have ever seen [1]. These applications, however, are mainly concentrated in the translation of such fields as cultural exchanges, economy, politics, and academic literature. Less attention was seen to be paid to the special field, for example, medical English translation in question. Moreover, existing machine translation technology did exhibit some drawbacks when applied to the field of medical translation. For instance, there are terms representing categories and concepts in medicine, whose semantic relationship is complicated within these phrases, posing

problems for the phrase identification in current machine translation. Accordingly, the accuracy of the identification in machine translation is seen to fail to meet the standards of medical translation. As we all know, phrase identification plays a crucial role in machine translation. Notably, one of the difficulties of the current English-Chinese machine translation is the resolution of phrase ambiguity [2]. Furthermore, medical terms usually display a high degree of ambiguity in both English and Chinese languages, which makes the syntactic analysis in machine translation extremely complicated. But this ambiguity, to a large extent, can only to be solved by phrase identification, and thus, machine translation is inseparable from phrase identification. Along this line of consideration, the core issue affecting the quality of machine translation is the machine's performance to deal with ambiguities based on employing appropriate phrase identification. To be specific, structural ambiguity is one of the most complex ones, and previous

researchers studied this phenomenon from multiple angles and proposed a variety of methods for phrase identification and disambiguation [3].

Joty et al. [4] applied a rule-based algorithm to phrase identification via calling the rules in question to obtain correct labeling, trying to establish a complete and accurate set of labeling rules. This algorithm could accurately describe the certain phenomenon between part of speech collocations. However, it was not seen to be a satisfying solution to structural ambiguity of the phrases since the language coverage of the rules was limited, the compilation and the maintenance of the huge rule base were overwhelming, and the priority and the conflict between the rules were not easy to be settled.

Banik et al. [5] used statistical algorithm for phrase identification. The algorithm was described to collect the language information in the training corpus via statistical methods. To be specific, the information of the language in statistical algorithm was used as an automatically "summed up" language phenomenon and was applied to the test corpus to obtain the correct part-of-speech tagging [6–9]. Evidently, this algorithm considered the dependence among parts of speech from a macro perspective, which was seen to cover most language phenomenon, thus possessing an overall higher accuracy and stability. Comparatively, the accuracy of statistical algorithm in describing the phenomenon of determining part of speech collocation was not as good as that of the rule-based algorithm.

Hybrid algorithm was also employed by the researchers for phrase identification. The hybrid method, as the name implied, referred to the combination of rule-based algorithm and statistical algorithm. Namely, its part-of-speech tagging model combined those of the two algorithms, which was regarded as the most effective tagging method based on the statistical algorithm tagging mode via the rule-based algorithm. Nevertheless, hybrid algorithms still could not resolve structural ambiguities to a large extent. In summary, in these automatic phrase identification algorithms, some structures that were extremely simple in artificial translation could not yet be accurately identified.

After reviewing the above literature, it is not difficult to find that the intelligent identification of phrases is to recognize and summarize the phrases in the sentence, to mark their part of speech and syntax, and automatically to combine and translate them against the corpus, eventually obtaining the corresponding translation results. Evidently, nowadays, there are quite many English translation model designs, most of which were designed based on word-sense disambiguation and semantic role labeling. To a certain extent, they could partly meet the needs of users. However, medical translation is different from other general translation activities. It has higher requirements for accuracy and professionalism. Therefore, common part-of-speech identification technologies could hardly meet the requirements of medical English translation.

As mentioned in the foregoing sections, intelligent phrase identification was regarded as the core of medical English translation since it could facilitate the selection of translation samples and the precise alignment of parallel corpus. Furthermore, the use of phrase intelligent identification technology could effectively remove structural ambiguity. Along this line of consideration, the present paper used a machine translation model on the basis of an optimized likelihood ratio (GLR) algorithm [10]. To be specific, the algorithm in question constructed a medical phrase corpus of approximately 250,000 English and 280,000 Chinese words labeled, making the phrases searchable. These phrases, like those of vocabulary, were made to possess such features as subcategories, morphology, semantics, and other characteristics. In effect, these features were mainly reflected by the central word of a phrase. Accordingly, the part-of-speech identification result was obtained while recognizing the short syntactic structure, and the ambiguity of the English-Chinese structure in the part-of-speech identification was corrected in accordance with the syntactic function of the parsing linear table. Finally, the recognized content was obtained, and the actual range of the position of the phrase in translation was therefore determined. Therefore, the model based an optimized GLR was assumed to alleviate the structural ambiguity in the current medical translation to a certain extent and to improve the accuracy of phrase identification.

## 2. Intelligent Modes Based on Optimized GLR

*2.1. Construction of Medical English Intelligent Translation Model.* The machine translation model based on the bilingual corpus is seen to make its translation more accurate via the identification of phrases, thus contributing more help to translators. Therefore, corpus, especially bilingual corpus, is increasingly gaining attention and application in current intelligent translation models. To be specific, accurately labeling the English-Chinese bilingual phrase corpus and storing it in the corpus would, to a large extent, improve the accuracy and efficiency of the phrase identification algorithm in the machine translation process, which would serve as an effective auxiliary tool for translators to improve translation quality and efficiency [11–13]. Corpus, however, is a multiangle, multilevel, and multidomain research tool, whose classification is intricate and still seems to be an open question. In spite of that, the English-Chinese bilingual medical phrase corpus is homogenous, that is, it only collected the same type of content. Accordingly, this type of corpus would be more accurate and professional when applied to machine translation in specific fields, and meanwhile, the probability of ambiguity in semantic identification would also be reduced.

Notably, the following three aspects were considered in the construction of the English-Chinese bilingual medical corpus in question. First is the field of the corpus. Medical field is regarded as an important one of machine translation applications. Communication in medicine, as we know, is often carried out among hospitals, firms, and individuals using different languages, especially English and other languages. Therefore, a certain demand for machine translation cannot be avoided in such an information-explosion era. From a linguistic point of view, medical English is unique in stylistic features, i.e., obvious syntactic and morphological

features, such as rich terminology, rigorous long sentence structure, and standardized wording. Moreover, its written medical tests are stylized. Thus, these features make it more suitable for the research and application of machine translation. Second are the size, the genre, and the style of the corpus. Due to the limited time and manpower, the scale of the English-Chinese bilingual medical phrase corpus in this paper was positioned at 15,000 sentence pairs, with the genre of the corpus being medical language and with the style being written and spoken language. Third is the collection and the sorting of corpus. The collection and arrangement of corpus was composed of five processes: corpus collection, clauses, English-Chinese alignment, deduplication, and proofreading, separately. To be specific, the source of the corpus was from publicly issued books and electronic journals, and the corpus itself was in terms of sentence-level parallel. Moreover, the original corpus collected initially was paragraphs, and then, the phrases of which were divided into sentences. The division of sentences, however, was mainly in terms of English ones. Furthermore, in the English-Chinese alignment stage, Chinese sentences were matched to their English counterparts, and after the alignment of English and Chinese, the duplicates were removed. Therefore, there were no repeated English sentences in the corpus. Furthermore, the final process was proofreading, while other aspects remained the original appearance of the corpus. Thus, the authenticity of the corpus was assured.

Accordingly, the phrase corpus of medical translation model constructed in this paper contained 250,000 English words and 280,000 Chinese counterparts, which could meet the needs of constructing 10,000 sentences and 5000 phrases. As is shown in Table 1, the medical phrase corpus was homogeneous, mainly focusing on medical-related professional terms, and could be translated between English and Chinese in various medical fields such as clinical, pharmacy, and imaging. To be specific, the English phrase corpus and that of Chinese were marked separately, meanwhile distinguishing the tenses of different phrase corpus. Evidently, the corpus processing method was composed of three parts: data, level, and processing mode, separately. Specifically, the type of data was text format, and the level of part of speech and alignment were selected. Additionally, the processing method adopted direct interaction between human and machine, carrying out a series of operations of translation and promoting the authenticity and accuracy of phrase corpus translation. The specific corpus information is shown in Table 1.

*2.2. The Optimized Algorithm Employed in the Model.* As mentioned in the foregoing sections, phrase-level syntax analysis was the core of the intelligent identification algorithm of machine translation, while the GLR algorithm was a commonly used algorithm in part-of-speech identification [14]. To be specific, this algorithm was the one that identified context-independent languages via the analysis tables of "action" and "goto." Furthermore, each table entry contained multiple shifts or reduction actions in which each entry and each exit of the stack existed in terms of the state symbol pair. However, when there was ambiguity between

advancement and statute, the GLR algorithm would apply the graph structure stack technology to copying the analysis stack, allowing each analysis stack to complete an action in the analysis table, while retaining multiple possibilities to generate multiple identification results. Then, an independent analysis would be carried out on these identification results. Particularly, when an error occurred in one of the analysis stacks, this analysis stack was discarded and other analysis results were output [15, 16].

Therefore, when a machine translation model using the GLR algorithm was applied to the translation in medicine, the following problems would arise. First, the number of identification results given by the GLR algorithm was uncertain, and there would be overlapping data in the identification results, which affected the accuracy of the identification results and thus hindered the quality of translation. Second, in the results of the GLR algorithm, each chunk was not seen to be compatible with one another, that is to say, phrases, unlike those of vocabulary, did not have semantic, morphological, and subcategory characteristics. Finally, the central word of the syntax structure was not specified in the results of the GLR algorithm.

To avoid the problems mentioned above, this paper, however, used a GLR algorithm that had been expanded and optimized. Specifically, this algorithm in question employed a context-independent grammatical form in the system and expanded its start symbol $S$ and production formula $P$. Moreover, it analyzed the structure of the phrase via phrase, which effectively reduced the probability of overlapping data points. Its algorithm form was a quaternion, as shown in

$$G = (V_N, V_T, S, \alpha). \tag{1}$$

In Equation (1), $V_N$ represented a nonterminal symbol set, which was a nonempty finite set; $V_T$ represented a terminal symbol set, which was likewise a nonempty finite one, and the elements in $V_T$ and $V_N$ did not overlap. $S$ stood for the start symbol set, an element in $V_N$, and a syntactically recognizable phrase symbol set. $\alpha$ represented the set of productions. Assuming that $P$ was any action in $\alpha$ and $P \in V_N$, the production (2) could be obtained:

$$P \longrightarrow \{\theta, C, \beta, \gamma\}. \tag{2}$$

In Equation (2), $\theta$, $C$, $\beta$, and $\gamma$ represented the right symbol string, center symbol, restriction condition, and target conversion mode of the action, respectively. Among them, $\theta$ and $C$ belonged to both $V_T$ and $V_N$, and $\gamma$ could belong to both $V_T$ and $V_N$. The improved GLR algorithm stipulated that the top symbol of the linear table of the identification result was consistent with $\theta$, the restriction condition $\beta$ should be true, and the center symbol $C$ should be a numeric value, not a null value. Only the identification result that met the above three criteria was the result of phrase part-of-speech identification.

*2.3. The Process of Algorithm Designed in the Model.* In current English-Chinese machine translation algorithms, the part-of-speech identification result of the phrase corpus was usually output as the final result of translation, which

TABLE 1: Corpus information of English-Chinese bilingual medical phrases.

| Element | Nature | Content |
| --- | --- | --- |
| Corpus composition | Scale | 250,000 English words 280,000 Chinese words, |
| | Scale of use | Clinical, pharmacy, imaging, inspection, etc. |
| | Style | Spoken and written |
| | Tense | Past, present, future |
| Corpus processing | Data | Text |
| | Level | Part of speech, alignment |
| | Processing | Man-machine communication |
| Corpus application | Scale | Medical English translation |

mainly relied on the part-of-speech analysis of the corpus. However, the identification in question did not improve the structural ambiguity between English and Chinese languages, and thus, it hindered the accuracy of the translation results. Therefore, it was difficult to meet the high-accuracy and high-precision requirements of medical English translation.

Along this line of consideration, it was essential to correct the results of identification in the process of machine translation [17–19]. Therefore, this paper further considered the correction of the results of the identification and identified phrase actions via the analytic linear table in the process of performing part-of-speech analysis against the optimized GLR algorithm. In addition, errors of the identification would be analyzed via such pointers as advancement, specification, acceptance, termination, error, and correction due to the fact that the analytic linear table also owned the function of syntactic identification. These errors were finally to be corrected by searching the marked content in the phrase corpus. The detailed phrase correction algorithm flow is shown in Figure 1.

In Figure 1, there were 6 actions involved in the entire algorithm, namely, advancement, statute, acceptance, terminator, error, and correction. Moreover, the relationship between advancement and statute could be evidently observed in which lay the similarities and essential differences. On the one hand, the similarity was that the two functions were similar both of which were to replace the position of the terminator in the analytical linear table. On the other hand, the difference between them was that the advancement referred to putting the current state and symbols on the stack and moving down the analysis pointer. However, statute referred to reinvoking the constraint condition function to check the rule condition. If the conditions were met, each subnode would be popped from the symbol stack to form a nonterminal syntactic structure tree. At the same time, the identification pointer of the central word was pointed to the corresponding central one, eventually generating the translation of the current nonterminal character in accordance with the mode of translation. Conversely, if the conditions were not met, the terminator pointer was directly placed. Specifically, terminator replacement meant that if the terminator pointer was not placed, the current system terminator was mapped to the analysis table termina-

tor via the symbol mapping function; if the termination pointer was entered, the current system terminator was directly mapped to the analysis table terminator.

It should be pointed out that before the terminator replacement the type of pointer was required to be identified in the optimized and expanded GLR algorithm. To be specific, suppose that it was a statute pointer and then whether the constraint function of the pointer belonged to the phrase corpus should be checked; if not, the termination pointer was directly placed. The terminator generally appeared at the backup point with structural ambiguity. Therefore, when it was queried, a phrase structure tree would be formed, and the central symbol would be check whether it was placed on the correct sentence structure. If it was not correct, then the algorithm in question would call up error pointer to correct the identification result of the part of speech. As shown in the figure, there were multiple phrase identification outputs in the entire correction process of the algorithm, and one acceptance pointer only output one identification result. However, when multiple identification results appeared at the same time, the correction process would write them into the same node of the phrase structure tree, and the receiving pointer then would automatically treat it as one identification result.

## 3. Model Design Verification

In order to detect the actual effect of the medical English-Chinese translation model on the basis of the optimized GLR algorithm, relevant evaluations were carried out in the research. Furthermore, the main performance indicators of the evaluation included the accuracy of the translation results, the translation speed, and the update ability, separately. Specifically, the evaluation team of the experiment was composed of 5 English-Chinese translation machines, 5 professional medical translators, and professional scorers. Among them, 5 English-Chinese translation machines chose rule-based algorithm, statistical algorithm, hybrid algorithm, GLR algorithm, and optimized GLR algorithm, respectively. Moreover, 5 professional medical translators all owned more than 10 years' experience in medical translation and worked together as a team, negotiating, and forming the only version of the tested material.
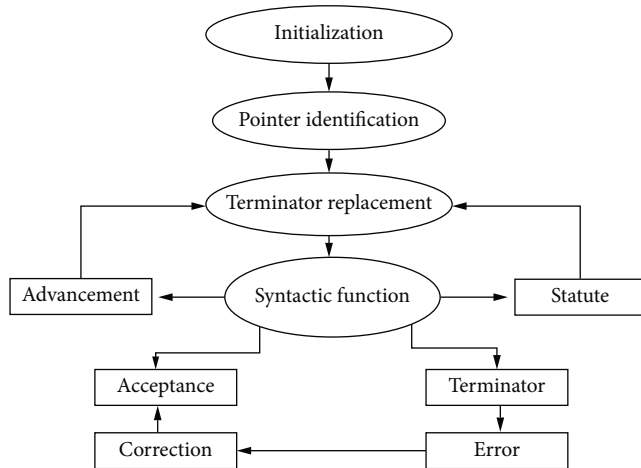
FIGURE 1: Intelligent identification algorithm correction flow.



FIGURE 2: Results of different English-Chinese translation algorithms.

In our paper, 5 English-Chinese machine translators translated the designated 70 medical terms and 70 randomly chosen medical English sentences in the evaluation process. Likewise, professional medical translators translate the same 70 phrases and 70 randomly chosen sentences. Then, the scorers would score the results of the machine translators, respectively, in accordance with certain rules. Specifically, the score would be given according to such rules as translation accuracy, translation speed, and update performance. To put it concretely, the translation accuracy was scored based on the clarity and accuracy of the translation, and the total score was 100 points. Furthermore, the translation speed was based on the total identification time multiplied by the weight, and then, the sum was divided by the number of phrase identification. The update capability, however, depended on the total update time multiplied by the weight, and then, the sum was divided by the number of phrase identification. Additionally, the weight of each score was the translation accuracy of 0.6, the translation speed of 0.2, and the update performance of 0.2.

## 4. Results and Discussion

The detailed experimental results are shown in Figures 2 and 3.

From the results in Figure 2, the machine translation based on the optimized GLR algorithm was seen to be the best of its kind in terms of translation accuracy, translation speed, and update performance. Furthermore, as the comprehensive evaluation results showed in Figure 3, the optimized GLR algorithm ranked the highest with a score of 94.4, while the statistical algorithm ranked the lowest with a score of 79.4. However, the hybrid algorithm was not much different from the optimized GLR algorithm in the final test score. The main gap between the two was centered on the score in update performance. Combined with Figures 2 and 3, it is obvious that the optimized GLR algorithm had obvious performance advantages over other algorithms, which was seen to be more suitable for medical translation.
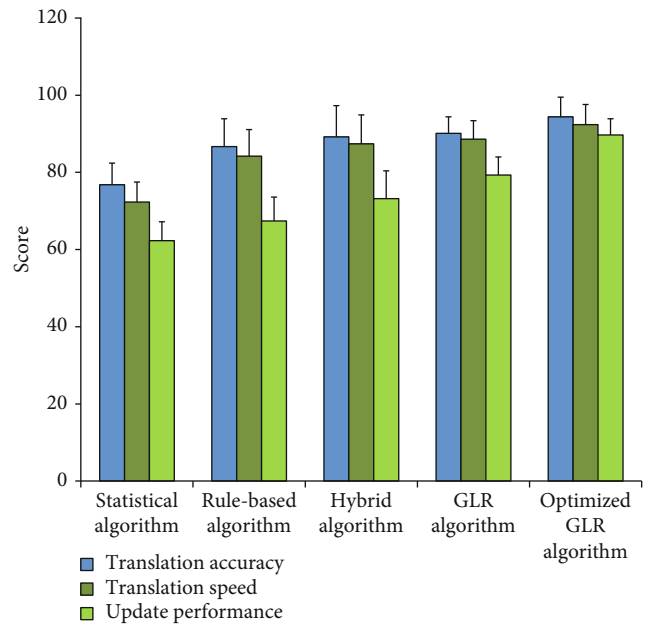
In order to test the performance of removing the structural ambiguity among different algorithms in real cases, this paper also employed a Chinese sentence that is related in medicine. "Tóutòng zhīqián de zhèngzhuàng yǒu kěnéng shì yóu dànǎo bùfèn qūyù gōngxiě shùnjiān jiǎnshǎo suǒ dǎozhì de" was selected for translation, and the results were compared among the translation model based on rule-based algorithm, statistical algorithm, hybrid algorithm, GLR algorithm, optimized GLR algorithm, and artificial translation. The results are shown in Table 2.

It can be found from Table 2 that translations based on statistical algorithms, rule-based algorithms, hybrid algorithms, and GLR algorithms were basically correct from a grammatical perspective, but from a semantic point of view, they were not very complete. In particular, the translation results of statistical algorithms were ambiguous, and the translation results were not very accurate. In addition, of the 5 algorithms, four did not translate the Chinese word "zheng zhuang," symptom, into English. Evidently, only the optimized GLR algorithm translated it into English. From the comparison of the semantics of the translation results, only the machine translation based on the optimized GLR algorithm was the closest to the artificial translation. Therefore, compared with the machine translation of other algorithms, it can be clearly seen that the machine translation result of the optimized GLR algorithm was more accurate in part-of-speech identification, the translation result was the closest to the artificial result, and the identification accuracy reached more than 96. This showed that the optimized GLR algorithm was more suitable for machine translation.
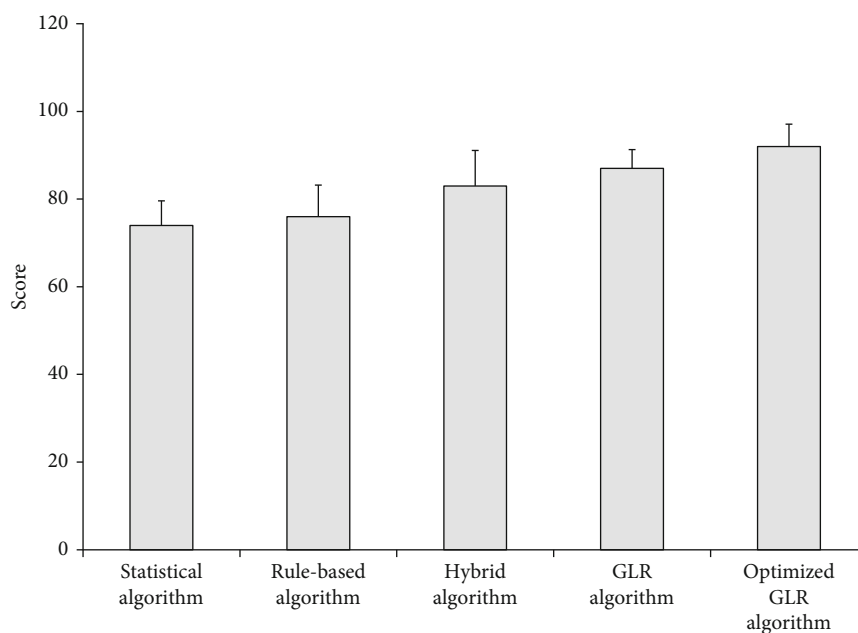
FIGURE 3: Comparison of comprehensive test scores of different English-Chinese translation algorithms.

TABLE 2: Results of translation examples.

| Method | Content |
|---|---|
| Statistical algorithm | The headache aforementioned has possibility that it is caused by the brain's parts of blood supply reducing suddenly. |
| Rule-based algorithm | The headache before may be caused by an instantaneous reduction in blood supply to parts of the brain. |
| Hybrid algorithm | It is likely that the headache may be caused by a sudden reduction in blood supply to parts of the brain. |
| GLR algorithm | The headache before is probably caused by an instantaneous reduction in blood supply to parts of the brain. |
| Optimized GLR algorithm | It is possible that the symptoms before the headache may be caused by an instantaneous reduction in blood supply to parts of the brain. |
| Artificial translation | It is possible that the symptoms preceding the headache result from a transient decrease in blood supply to areas of the brain. |

## 5. Conclusion

In order to improve the performance of machine translation in medicine field, this article designed an intelligent medical English translation model via expanding and optimizing the traditional GLR algorithm, which was seen to be capable of removing the structural ambiguity of English and Chinese medicine terms. The algorithm in question constructed the phrase structure through the phrase center point and endowed a phrase with such characteristics of a word as semantics, morphology, and subcategory, thus improving the accuracy of the phrase identification. Particularly, when this algorithm was applied to machine translation in medicine, correction pointer was added in the identification process. Therefore, when structural ambiguities were encountered, the syntactic function of parsing linear tables was to be used to correct the English and Chinese structural ambiguities in the results of part-of-speech identification. Notably, this algorithm largely changed the low accuracy of phrase part-of-speech identification among traditional algo-

rithms and improved the accuracy of machine translation's performance in medicine. The results of the evaluation showed that, compared with other algorithms, the translation model on the basis of the optimized GLR algorithm was more accurate in identification, faster in translation speed, and stronger in update performance. Accordingly, it was seen to be more suitable for medical English machine translation. An intelligent medical English translation model based on deep learning algorithms [20–22] may be developed in future implementations.

## Data Availability

The data used to support the findings of this study are available from the corresponding author upon request.

## Conflicts of Interest

The authors declare no conflict of interest.

# References

[1] J. Downie and A. Dickson, "Unsound evaluations of medical machine translation risk patient health and confidentiality," *JAMA Internal Medicine*, vol. 179, no. 7, pp. 1001-1002, 2019.

[2] A. Panayiotou, A. Gardner, S. Williams et al., "Language translation apps in health care settings: expert opinion," *JMIR mHealth and uHealth*, vol. 7, no. 4, article e11316, 2019.

[3] S. van de Velde, L. Macken, K. Vanneste et al., "Technology for large-scale translation of clinical practice guidelines: a pilot study of the performance of a hybrid human and computer-assisted approach," *JMIR Medical Informatics*, vol. 3, no. 4, article e33, 2015.

[4] S. Joty, F. Guzmán, L. Màrquez, and P. Nakov, "Discourse structure in machine translation evaluation," *Computational Linguistics*, vol. 43, no. 4, pp. 683–722, 2017.

[5] D. Banik, A. Ekbal, and P. Bhattacharyya, "Statistical machine translation based on weighted syntax–semantics," *Sadhana*, vol. 45, no. 1, p. 191, 2020.

[6] C. C. Chua, T. Y. Lim, L. K. Soon, E. K. Tang, and B. Ranaivo-Malançon, "Analogical-based translation hypothesis derivation with structural semantics for english to malay example-based machine translation," *Advanced Science Letters*, vol. 24, no. 2, pp. 1263–1267, 2018.

[7] C. C. Chua, T. Y. Lim, L.-K. Soon, E. K. Tang, and B. Ranaivo-Malançon, "Meaning preservation in example-based machine translation with structural semantics," *Expert Systems with Applications*, vol. 78, pp. 242–258, 2017.

[8] K. Welnitzová and D. Munková, "Sentence-structure errors of machine translation into Slovak," *Topics in Linguistics*, vol. 22, no. 1, pp. 78–92, 2021.

[9] K. Rajan, A. Zielesny, and C. Steinbeck, "Stout: smiles to iupac names using neural machine translation," *Journal of Cheminformatics*, vol. 13, no. 1, p. 34, 2021.

[10] M. A. Stoto, R. D. Fricker, A. Jain et al., "Evaluating statistical methods for syndromic surveillance," in *Statistical Methods in Counterterrorism: Game Theory, Modeling, Syndromic Surveillance, and Biometric Authentication*, pp. 141–172, Springer, New York, NY, 2006.

[11] N. Önder, "Compiling a written corpus of english as an academic lingua franca: medical research articles of turkish academics," *Boğaziçi Üniversitesi Eğitim Dergisi*, vol. 29, 2012.

[12] I. Taavitsainen, T. Hiltunen, A. Lehto et al., "Late modern English medical texts 1700–1800&58; a corpus for analysing eighteenth-century medical English," *ICAME Journal*, vol. 38, no. 1, pp. 137–153, 2014.

[13] E. E. Sweany, "Unsettling comparisons," *English Language Notes*, vol. 58, no. 2, pp. 83–100, 2020.

[14] D. Vivek and P. Balasubramanie, "An expressive phrases identification supported with feature prediction consuming unstructured data collection," *Multimedia Tools and Applications*, vol. 79, pp. 1–16, 2020.

[15] M. Barash and A. Okhotin, "Generalized lr parsing algorithm for grammars with one-sided contexts," *Theory of Computing Systems*, vol. 61, no. 2, pp. 581–605, 2017.

[16] A. Okhotin, "Lr parsing for conjunctive grammars," *Grammars*, vol. 5, no. 2, pp. 81–124, 2002.

[17] M. Murata, M. Utiyama, K. Uchimoto, H. Isahara, and Q. Ma, "Correction of errors in a verb modality corpus for machine translation with a machine-learning method," *Acm Transactions on Asian Language Information Processing*, vol. 4, no. 1, pp. 18–37, 2005.

[18] N. Ehsan and H. Faili, "Grammatical and context-sensitive error correction using a statistical machine translation framework," *Software: Practice and Experience*, vol. 43, no. 2, pp. 187–206, 2013.

[19] J. E. Denny and B. A. Malloy, "The IELR(1) algorithm for generating minimal LR(1) parser tables for non-LR(1) grammars with conflict resolution," *Science of Computer Programming*, vol. 75, no. 11, pp. 943–979, 2010.

[20] Z. Tang, G. Zhao, and T. Ouyang, "Two-phase deep learning model for short-term wind direction forecasting," *Renewable Energy*, vol. 173, no. 72, pp. 1005–1016, 2021.

[21] K. K. L. Wong, "Bridging game theory and the knapsack problem: a theoretical formulation," *Journal of Engineering Mathematics*, vol. 91, no. 1, pp. 177–192, 2015.

[22] K. K. Wong, "A geometrical perspective for the bargaining problem," *PLoS One*, vol. 5, no. 4, article e10331, 2010.

*Research Article*

# Bearing Faulty Prognostic Approach Based on Multiscale Feature Extraction and Attention Learning Mechanism

## Yiqing Zhou [ID],[1] Jian Wang,[1] and Zeru Wang[2]

[1]*Computer Integrated Manufacturing System (CIMS) Research Center, College of Electronics and Information Engineering, Tongji University, Shanghai 201804, China*
[2]*CAD Research Center, College of Electronics and Information Engineering, Tongji University, Shanghai 201804, China*

Correspondence should be addressed to Yiqing Zhou; 1710334@tongji.edu.cn

Recently, researches on data-driven faulty identification have been achieving increasing attention due to the fast development of the modern conditional monitoring technology and the availability of the massive historical storage data. However, most industrial equipment is working under variable industrial operating conditions which can be a great challenge to the generalization ability of the normal data-driven model trained by the historical storage operating data whose distribution might be different from the current operating datasets. Moreover, the traditional data-driven faulty prognostic model trained on massive historical data can hardly meet the real-time requirement of the practical industry. Since the hierarchical feature extraction can enhance the model generalization ability and the attention learning mechanism can promote the prediction efficiency, this paper proposes a novel bearing faulty prognostic approach combining the U-net-based multiscale feature extraction network and the CBAM- (convolutional block attention module-) based attention learning network. First, time domain conditional monitoring signals are converted into the two-dimensional gray-scale image which can be applicable for the input of the CNN. Second, a CNN model based on the U-net structure is adopted as the feature extractor to hierarchically extract the multilevel features which can be very sensitive to the faulty information contained in the converted image. Finally, the extracted multilevel features containing different representations of the raw signals are sent to the designed CBAM-based attention learning network for high efficiency faulty classification with its unique emphasize discrimination characteristic. The effectiveness of the proposed approach is validated by two case studies offered by the CWRU (Case Western Reserved University) and the Paderborn University. The experimental result indicates that the proposed faulty prognostic approach outperforms other comparison models in terms of the generalization ability and the speed-up properties.

## 1. Introduction

With the advent of the large-scale manufacturing of the modern industry, the prognostic and health management (PHM) of the manufacturing equipment has been becoming increasingly important. Bearings, regarded as the key component of the industrial machine, play a significant role in the health status of the whole equipment whose failure might directly result in total collapse. Therefore, the accurate and effective prediction of the bearing fault can not only save the periodical maintenance cost but also improve the reliability of the whole equipment. Traditional faulty prognostic approach can be mainly categorized into three schemes:

signal-based approach, physical analyzing-based approach, and pattern recognition-based approach. The signal-based approach, especially the vibration signal-based approach, can be the most commonly used one in the faulty prediction of the industrial mechanical components. By using the time domain, frequency domain, and the time-frequency analysis, the vibration-based faulty prognostic approach can be very sensitive to the machine faulty symptom. Hong and Dhupia [1] proposed a vibration-based faulty prognostic model by analyzing the kurtosis of strong impact circle of the vibration spectrum. Borghesani et al. [2] established a vibration-based faulty prognostic model by analyzing the relationship between the Kurtosis, square envelop spectrum and cepstrum

prewhitening. A novel band demodulation approach is proposed for the faulty prognostic of the rolling bearings. Apart from the vibration-based approach, the temperature-based approach and oil analysis-based faulty prognostic approach can also be very effective [3–5]. The signal-based faulty prognostic approach is totally based on the understanding of the target monitoring signal whose prediction accuracy can be limited to the priori domain expertise knowledge. Moreover, the manual feature extraction and alarming threshold setting of different target signal can be labour cost [6].

In addition to the signal-based approach, the physical analyzing-based approach has also been studied in recent literature. The physical analyzing approach aims at establishing the physical equation based on the material characterization. Xu et al. [7] analyzed the degradation situation of the aluminium-steel joint by analyzing the profile effects of the underwater friction stir welding tool pin on the on the properties of aluminium steel joint. Xu et al. [8] established a composite material fatigue analyzing evaluation based on the analysis of the dispersion wave characteristics of laminated composite nanoplate.

To overcome the above issue existed in the signal- and physical analyzing-based approach, the pattern recognition-based approach, usually realized by the deep learning model, is proposed for the faulty prognostic tasks. The deep learning models can replace the manual feature extraction with its power automatic learning ability of representative features and the nonlinear input-output mapping relationship in complex system with its deep nonlinear network structure [9–11]. As one of the most effective deep learning models, the convolution neural network model has shown its promising ability in hierarchical feature learning and intelligent faulty prognostic [12–18]. The CNN-based faulty prognostic approaches have achieved comparatively higher accuracy than the signal-based approaches; however, there still exists some points needed to be considered.

(1) It is assumed that the training datasets and the testing datasets are collected under the same operating situation; however, in the real industrial environment, the operation condition such as the bearing rotating speed and the load of the equipment can be variable in different time segments. The performance of traditional CNN-based faulty prediction approach can be vulnerable when the load condition vary. How to boost the model generalization ability remains a challenge

(2) In the traditional CNN-based faulty prediction approach, only the last feature layer, which is highly related to the specific task or datasets, is used for the faulty prognostic task. However, some generalized characteristics are contained in the low-level hidden layers which are not well preserved in the high-level feature. How to jointly use these multilevel features remain a problem

Since the low-level features reserved in the hidden layers are universal and similar for different but related distributed datasets or tasks, the multiscale hierarchical feature learning has been studied in recent literature [19–23]. Ding and He [20] combined the second max pooling layer with the last convolution layer as the categorical feature image for spindle bearing fault diagnosis. Sun et al. [21] connected both the third and the fourth convolution layer into the last hidden layer of the CNN network so that the model generalization ability can be enhanced. Lee and Nam [22] incorporated several low-level features with the extracted high-level feature. The concatenated feature vector is fed into a SVM detector for the prediction. In order to fully utilize the hierarchical features learned by the CNN model, Xu et al. [23] extracted the feature image of two pooling layers and one fully connected layer from the CNN model. These features are fed to the ensemble learning model of three random forests for final prediction.

Since these literature directly extract multiple feature layers from the traditional CNN and send them to the classifier for faulty prognostic, it is questionable whether the traditional CNN network has enough hierarchical feature learning ability and whether it is appropriate to directly use the multilevel features for practical faulty classification problem. The following two points need to be further considered.

(1) In current literature, the multilevel and multiscale features are extracted from the traditional CNN network such as the most commonly used LeNet-5, but the network itself has limited hierarchical feature learning ability which hinders the model generalization ability somewhat

(2) In current literature, the extracted multilevel feature images are directly used for the faulty classification tasks. Nevertheless, there exists some abundant features contained in these extracted feature images which has less relationship to the prognostic task. These abundant features greatly increase the computation cost, and the highly related features might be concealed by them, thus causing reduction of the prognostic efficiency and the prognostic accuracy

Dealing with the above two issues, this paper takes full advantage of the powerful hierarchical feature learning ability of the U-net CNN and the discriminative feature selection ability of the attention learning network. The major contributions of this research are as follows: considering the first issue listed above, an improved CNN based on U-net structure is designed as the hierarchical feature extractor network which has already been proved about its powerful hierarchical feature learning ability in the medical image area; considering the second issue listed above, a designed attention learning network based on several CBAM- (convolutional block attention model-) based attention learning blocks is used for the faulty classification with its unique discriminative feature selection mechanism for eliminating the redundant features; the rest structure of this paper is organized as follows: Section 2 briefly reviews the related theory and the methodology used in this paper; Section 3 presents the overall flowchart and the technical detail of the proposed faulty prognostic method; Section 4 presents the experimental result including the ablation study and the comparison
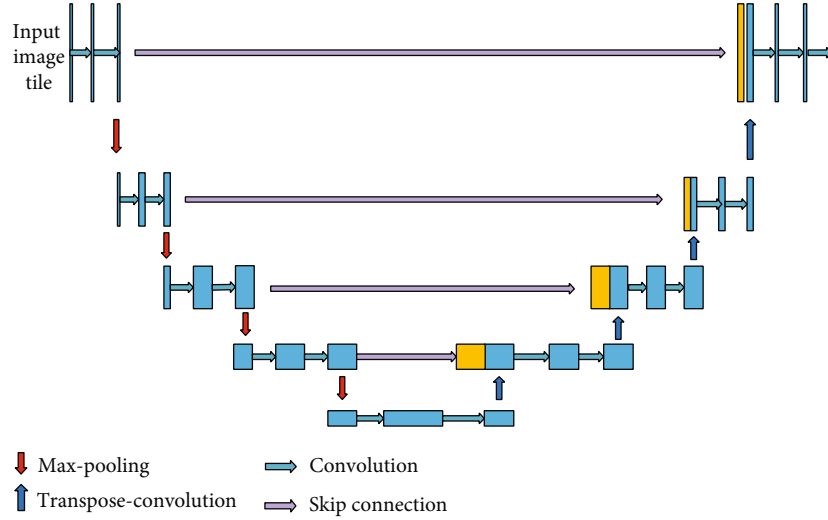
FIGURE 1: The conventional U-net structure.

experiment with other traditional prognostic approaches; finally, the conclusion and future work of this paper are presented in Section 5.

## 2. Related Theory and Methodology

*2.1. Multiscale Feature Extraction and U-Net.* As a typical representation of deep learning model, the convolution neural network can automatically learn the structured and representative features from the raw datasets through layer-to-layer propagation scheme. Since the convolution neural network can learn multiscale hierarchical features of raw data, researches on making full use of features in the multilayers of the CNN have achieved considerable attention which has been proved to have better generalization ability [21]. There are some famous CNN models such as LeNet-5 [24], Alex-Net [25], VGG-Net [26], Google-Net [27] and U-Net [28], among which the CNN model based on U-Net structure has shown its great advantage in hierarchical feature learning.

U-Net, as a new structure of CNN, has already been frequently applied into the task of image classification, segmentation, detection, and tracking in the medical imaging and biochemical area due to its powerful hierarchical feature learning ability [29]. Gao et al. [30] proposed an improved U-net-based image segmentation method for the blood vessel segmentation. In order to combine complementary magnetic resonance image protocols to reconstruct the high-quality image, Lei et al. [31] proposed a Dense-UNet to reconstruct T2-weighted image (T2WI) using both T1-weighted image (T1WI) and undersampled T2WI. Nazem et al. [32] proposed an improved 3D version of the U-net model based on the dice loss function to predict the binding sites of new proteins accurately. Dogan et al. [33] proposed a two-phase hybrid approach combining the Mask R-CNN and the 3D U-net for high-accuracy automatic segmentation of pancreas in CT imaging. Chae et al. [34] proposed a resid-

ual U-Net combined with an attention learning module for the image segmentation of the pressure ulcer (PU) region.

To the best of our knowledge, it is the first time that the "U-net" is used as a feature extractor in the area of equipment faulty prognostic. Normally, the U-net-based CNN network consists of two parts, the max-pooling period in the left and the upconvolution period in the right which jointly construct the "U" structure as shown in Figure 1. It usually consist of four kinds of operations, namely, convolution, max-pooling, transpose-convolution, and skip connection.

*2.1.1. Convolution Operation.* The convolution layer consists of a series of feature maps which is obtained through the convolution operation between the convolution kernel and the input as shown in

$$X_\alpha^j = f\left(\sum_{\beta=1}^n W_{\alpha,\beta}^j * X_\beta^{j-1} + b_\alpha^j\right). \tag{1}$$

$X_\alpha^j$ denotes the $\alpha_{\text{th}}$ output feature map of the $j_{\text{th}}$ layer; $X_\beta^{j-1}$ denotes the $\beta_{\text{th}}$ input feature map of the $(j-1)_{\text{th}}$ layer; $W_{\alpha,\beta}^j$ denotes the convolution kernel between the feature map $X_\alpha^j$ and the feature map $X_\beta^{j-1}$. The $f(*)$ denotes the activation function. In order to increase the nonlinearity of CNN, the rectifier linear units (Relu) is adopted in this paper due to its excellent performance. The ReLu function can be expressed as shown in

$$X_a^j = \max\left(0, X_a^{j'}\right). \tag{2}$$

*2.1.2. Max-Pooling Operation.* In order to release the model parameter size as well as the overfitting problem, the pooling operation is executed along with the convolution operation. Since the convolution kernels for the same feature map share the same weight and bias, a max-pooling layer is added to
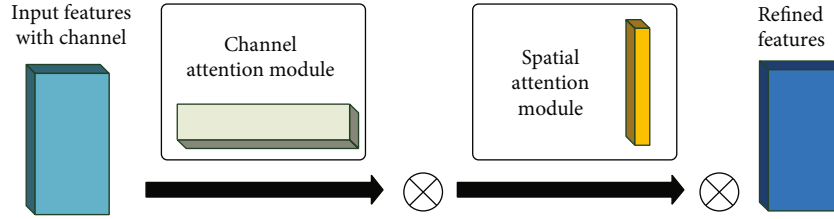
FIGURE 2: The structure of the CBAM attention mechanism.

each convolution layer, producing lower resolution feature maps through subsampling operations. The max-pooling function can be defined as illustrated in

$$X_a^{S_1*S_2} = \max\left(X_a^{S_1'*S_2'} : S_1 \le S_1' < S_1 + \lambda, S_2 \le S_2' < S_2 + \lambda\right), \tag{3}$$

where the $X_a^{S_1*S_2}$ and $X_a^{S_1'*S_2'}$ denote the $S_1 * S_2$ pixel in the $a_{th}$ feature map before and after max-pooling operation. The parameter $\lambda$ denotes the stride size of the pooling window whose value should be larger than 1. The max-pooling operation decreases the size of the feature maps and subsamples the highest resolution proportion of the input feature image which greatly reduce the parameter number of the CNN model.

*2.1.3. Transpose Convolution.* In order to obtain the feature image which has the same size as the input image, the transpose convolution operation is applied along with the max-pooling process. During the transpose convolution process, the domain interpolation is the most commonly used technology as shown in

$$X_a^{I*I} = \text{Deconv}\left(X_a^{i*i}\right),$$
$$I = \frac{i + 2p - k}{s} + 1, \tag{4}$$

where the $X_a^{i*i}$ denotes the $i * i$ pixel value in the $a_{th}$ feature map before the transpose convolution operation and $X_a^{I*I}$ denotes the $I * I$ pixel value in the $a_{th}$ feature image after the transpose convolution operation; the parameter $S$ denotes the stride step of the transpose convolution, and the parameter $p$ denotes the zero padding. The kernel size of the transpose convolution kernel is $k * k$.

*2.1.4. Skip Connection.* The U-net is a typical encoding-decoding structure. The encoding process is realized by the max-pooling operation while the decoding process is realized by the transpose convolution operation. In order to compensate the information loss during the max-pooling process, the U-net utilizes the concatenation layer to realize the feature fusion of the two symmetrical feature images located in the max-pooling and transpose processes, respectively, which is called skip connection. The "skip connection" enhances the hierarchical feature learning ability of the U-net without resolution loss.

*2.2. Attention Learning and CBAM.* The attention learning is first inspired by the cognitive neuroscience. When dealing with a certain task, people will pay more attention to the important issue while paying less attention to the unimportant ones. Based on this notion, the attention mechanism is first proposed by Treisman and Gelade in 1980s [35]. The attention mechanism is aimed at assigning different weights to different proportions of the input based on the contribution of the different input proportions to the output. It has already been successfully applied into the area of natural language processing, machine translation, pattern recognition, and large equipment maintenance due to its powerful ability of extracting discriminative features [36].

Chen et al. [37] proposed an attention-based deep learning framework for machine's RUL prediction. In his paper, the proposed approach first exploits the LSTM network to learn representative sequential features from raw sensory data, then the attention learning network is utilized to learn the importance of the sequential features and assign larger weights to more important ones. Chen et al. [38] applied a spatial-temporal convolution neural network with convolution block attention module for microexpression recognition. First image sequences were input to a medium-sized convolution neural network (CNN) to extract visual features. Afterwards, it learned to allocate the feature weights in an adaptive manner with the help of a convolutional block attention module. Since microexpressions only occur in parts of the human face, the attention mechanism helps to focus on specific facial regions, learning and acquiring the important features. Xiong et al. [39] proposed an attention augmented multiscale network (AAMN) for single-image superresolution (SISR), employing an attention driven strategy to guide feature selection and aggregation among multiple branches. Leng et al. [40] proposed a context-aware attention network combining the context learning module and the attention transfer module. The context learning module is first utilized to capture the global contexts. Then, the attention transfer module is proposed to generate attention maps that contain different attention regions, benefiting for extracting discriminative features.

Currently, there are two most commonly used attention learning mechanism, namely, SENET (sequential and excitation network) and CBAM (convolutional block attention model) [37]. The SENET applies the attention module to channel dimension while the CBAM applies the attention module not only on the channel dimension but also the spatial dimension of the image.

The idea of the CBAM attention mechanism was first proposed by Woo et al. [36]. The CBAM consists of channel
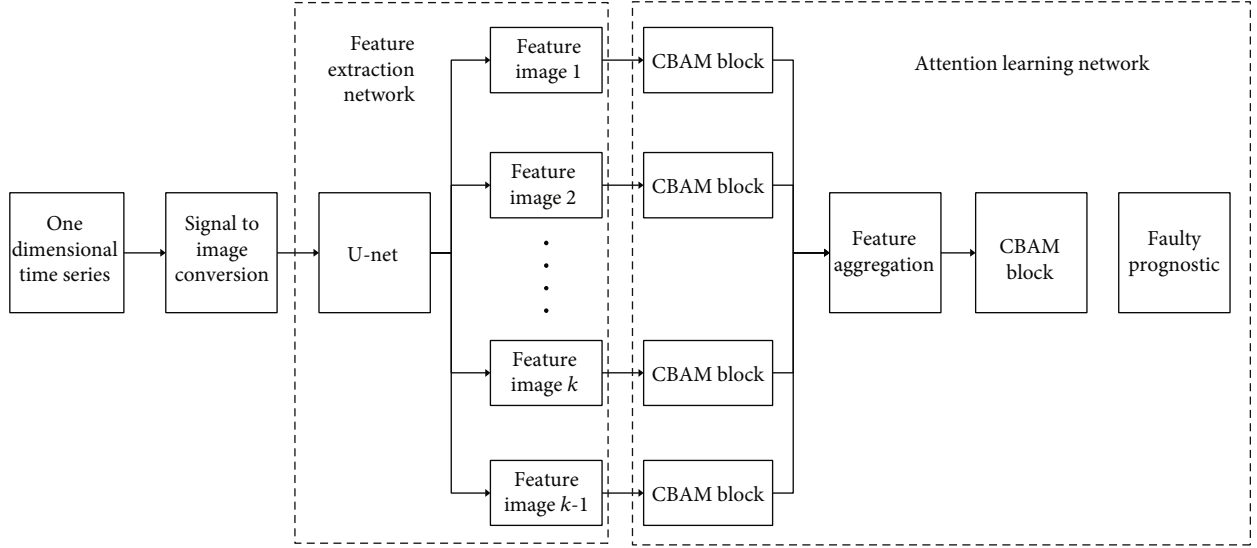
FIGURE 3: Framework of the hybrid model based on U-net and CBAM attention mechanism.

attention process and spatial attention process as shown in Figure 2. The overview of the channel-spatial process of the CBAM is illustrated in

$$M' = M_C(M) \otimes M, M \in R^{C*H*W},$$
$$M'' = M_S\left(M'\right) \otimes M', \tag{5}$$

where $M$ represents the input image of the CBAM module with the channel number of $C$, the height of $H$, and the width of $W$. The mark $\otimes$ represents the element-wise multiplication, $M'$ represents the feature image multiplying the channel attention map, and $M''$ represents the result of the spatial attention map multiplying $M'$ which is regarded as the output of the CBAM module.

2.2.1. Channel Attention Process. Usually, the input image can be transferred to a feature matrix through the convolutional layer. The channel number of the obtained feature matrix is the same as the kernel number of the convolutional layer with the common value of 256 or 512. Since some channels are not so useful to the information transference, it is necessary to apply channel attention on these channels. The attention weighting process is illustrated in

$$M_C(F) = \sigma(\text{MLP}(\text{AvgPool}(F))) + \text{MLP}(\text{MaxPool}(F))$$
$$= \sigma\left(W_1\left(W_0\left(F_{\text{avg}}^C\right)\right) + W_1\left(W_0\left(F_{\text{max}}^C\right)\right)\right), \tag{6}$$

where the $F_{\text{avg}}^C$ and $F_{\text{max}}^C$ denote the average pooling operation and the max pooling operation applied on the channel dimension of the feature matrix. $W_0 \in R^{C/r*C}$ and $W_1 \in R^{C*C/r}$ denote the activation operation of the shared multilayer perceptron with activation function of rectified linear unit (Relu) with the size of $R^{C/r*1*1}$, where $r$ denotes the compression ratio. The parameter $\sigma$ denotes the sigmoid activation.

2.2.2. Spatial Attention Process. Similar as the channel attention process, the spatial attention is aimed at applying the importance weighting on spatial dimension of the feature matrix as shown in

$$M_S(F) = \sigma\left(f^{R*R}([\text{AvgPool}(F); \text{MaxPool}(F)])\right)$$
$$= \sigma\left(f^{R*R}\left(\text{Concat}\left(F_{\text{avg}}^s; F_{\text{max}}^s\right)\right)\right), \tag{7}$$

where the average pooling and the max pooling are also applied for the information evaluation. The parameter $f^{R*R}$ denotes the convolutional layer with the kernel size of $*R$ and the spatial attention weighting is finally normalized by the sigmoid activation.

2.3. Proposed Combination Model Based on U-Net and CBAM Mechanism. Although the hierarchical feature extraction network can provide the multilevel characteristics of the input image, the input image has been largely expanded to some extent. Therefore, it is necessary to use the attention learning network to capture the sensitive proportion of these input feature images and eliminate the abundant proportion. This paper proposes a hybrid model based on the U-net and the CBAM-based attention learning blocks, compromising the hierarchical feature extraction of the U-net, the attention learning of the CBAM blocks, and the effectiveness of the combination. The overall framework is illustrated in Figure 3.

Firstly, the one-dimensional time series signal has been converted into the two dimensional gray-scale image, which is then decomposed by the U-net into several multilevel feature images hierarchically, representing the hierarchical characteristics of the input signal.

Secondly, multiple CBAM attention learning blocks are used to optimize the decomposed features, selecting the faulty sensitive features from the redundant ones. The complexity of the hierarchical feature images are greatly reduced, thus promoting the prediction efficiency.
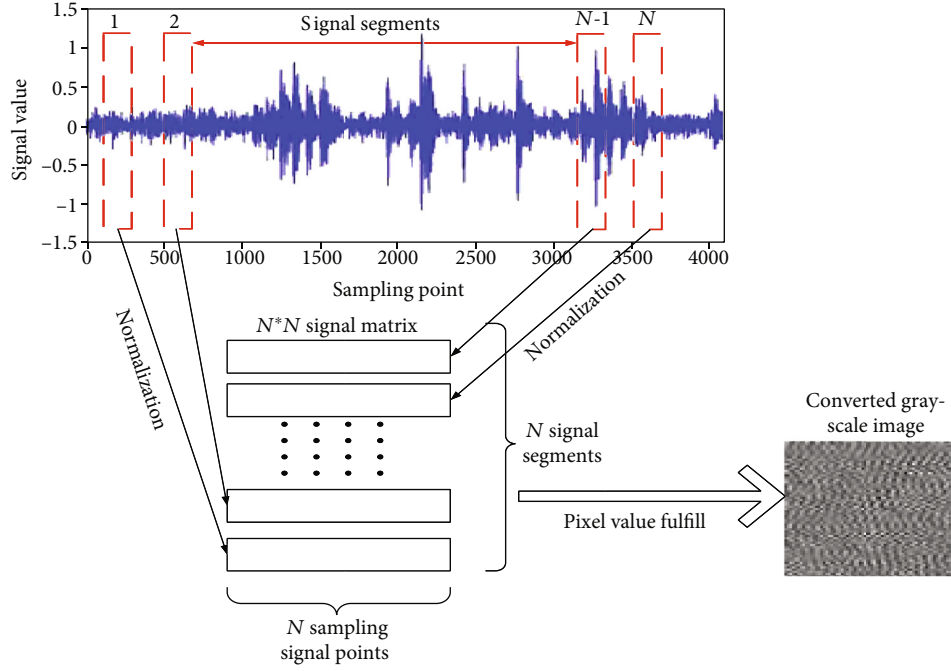
FIGURE 4: The schematic diagram of the "$N * N$" signal to image conversion method.
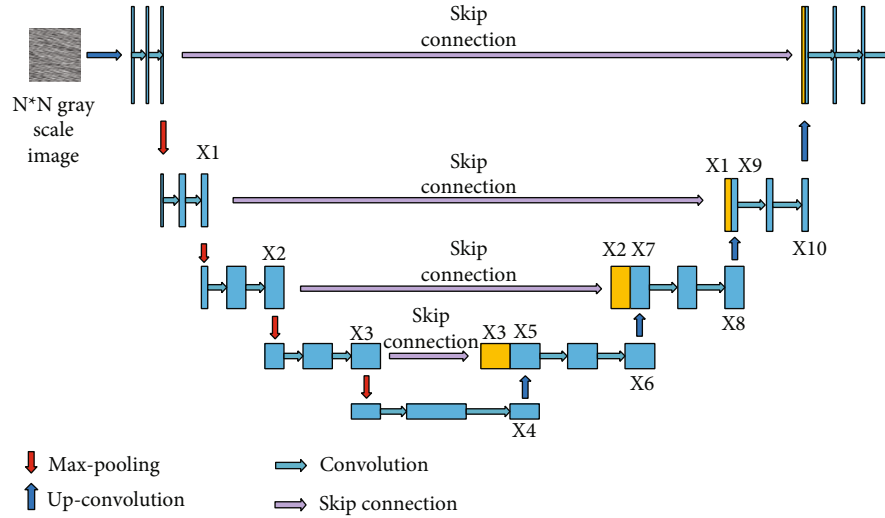


FIGURE 5: The structure of the proposed U-net feature extraction model.

Finally, the outputs of the CBAM attention learning blocks are aggregated, and the second CBAM block is applied on the categorical feature image. The categorical feature optimized by the CBAM attention learning is sent to the Softmax layer for final faulty prognostic as shown in

$$P\left(y^{(i)} = j \mid C^{(i)}; \theta\right) = \frac{\exp\left(\theta_j^T * C^{(i)}\right)}{\sum_{j=1}^K \exp\left(\theta_j^T * C^{(i)}\right)},$$

$$y = \text{argmax}_j p\left(y^{(i)} = j \mid C^{(i)}; \theta\right),$$

(8)

where $C^{(i)}$ denotes the optimized categorical feature image used for faulty prognostic; $i = 1, 2, ..n$ denotes the number of the training data; $j = 1, 2, ..k$ denotes the dimension of the output layer which is equal to the faulty type number. $\theta$ denotes the parameters of the Softmax layer.

## 3. Proposed Faulty Prognostic Procedure

3.1. Data Preprocessing. Generally speaking, the condition monitoring data collected from the front-end industrial equipment includes one-dimensional time series data and two-dimensional image data. The 2D image data can be used directly for the faulty prognostic task by using the pattern
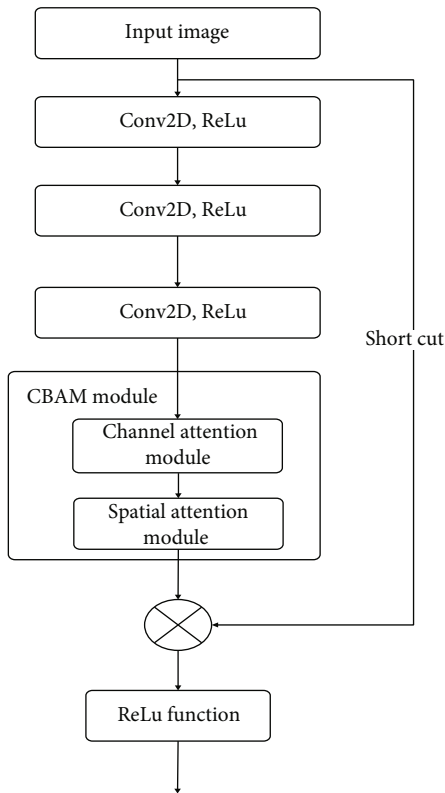
FIGURE 6: The flowchart of the proposed ResNet-CBAM attention learning network.

recognition techniques. In this paper, we use the "$N * N$" signal to image conversion technique proposed in literature [41] to convert the 1D time series vibration signal data into the 2D image data; the converted image is used as the input of the U-net convolution neural network. The specific schematic diagram of the $N * N$ "signal to image" conversion process is illustrated in Figure 4.

First, we randomly choose $N$ signal segments from the raw signal containing $N$ sampling points in each segment equally. Since the maximum value of the pixel length of the gray image is less than 255, the selected $N^2$ sampling points are normalized into the value ranging from 0~255 by using Equation (9) and the $N * N$ signal matrix is constructed. Finally, the normalized pixel value of the signal matrix is fulfilled for the construction of the gray-scale image.

$$\text{Pixel}(i, j) = 255 * \text{round} \\ \cdot \left( \frac{\text{value}((i - 1) * N + j) - \min(\text{value})}{\max(\text{value}) - \min(\text{value})} \right). \quad (9)$$

In Equation (9), the round function transforms the sampling signal value to the gray scale pixel value by using the round function "round($*$)". The $\text{Pixel}(i, j)$ denotes the converted pixel value of the corresponding signal value$(i, j)$ where the min (value) denotes the minimum value of sampling data point among the selected $N^2$ sampling data point while the max (value) denotes the maximum value among the $N^2$ data

points. The above "signal to image" conversion method used in this paper is simple, and it has been proved to be effective in literature [41] due to its less requirement of the domain expertise and signal processing knowledge. The converted gray-scale image is a 2D representation of the raw signal which can effectively retain the details and characteristics of the raw signals.

### 3.2. Proposed Feature Extraction Network and Attention Learning Block

*3.2.1. Proposed U-net-Based Feature Extraction Network.* In this paper, a U-net-based convolution neural network is designed as the hierarchical feature extraction network. The whole feature extraction network consists of 10 layers, namely, X1~X10, among which the feature images of X1~X4 denote the max-pooling process of the U-net while the feature images of X5~X10 denote the upconvolution process of the U-net as shown in Figure 5.

Since the feature layers of the transposed process of the U-net can better represent the hierarchical characteristics of the input data which contains less outside noise, the feature layers of X6, X8, and X10 from the low, middle, and high levels, respectively, are used as the extracted hierarchical features, representing the global and specific characteristics of different health conditions, thus contributing different knowledge to the feature extraction task.

*3.2.2. Proposed ResNet-CBAM Attention Learning Block.* In this paper, the designed CBAM attention learning network is compiled with the three-layer ResNet CNN as shown in Figure 6. First, the ResNet-based CNN is used to extract the spatial and channel features of the input feature images. Then, the CBAM attention learning block is used for the attention weighting of the channel dimensions and the spatial dimensions of the input images in an adaptive way. The advantage of the proposed ResNet-CBAM attention learning block is that there will not be feature loss and gradient disappearance before the input images are processed by the CBAM module.

*3.2.3. Proposed Prognostic Procedure.* The proposed prognostic procedure is illustrated in Figure 7. First, the one-dimensional time series data is converted to the two-dimensional gray-scale image by using the "$N * N$" image conversion approach. Second, the U-net-based hierarchical feature extraction network is applied and the multilevel feature images of X6, X8, and X10 are extracted as the multi-input of the attention learning network. Third, the three designed ResNet-CBAM-based attention learning blocks are applied on the three extracted multilevel feature images which are then fused through shaping into the same size and channel concatenation. Finally, the concatenated categorical feature image is optimized by the second ResNet-CBAM attention learning block, and the final faulty prognostic result can be calculated through Softmax prediction. The novel Pareto-optimal strategy based on spatial game theory which is proposed by Wong [42–43] is utilized as the parameter optimization strategy of the proposed hybrid
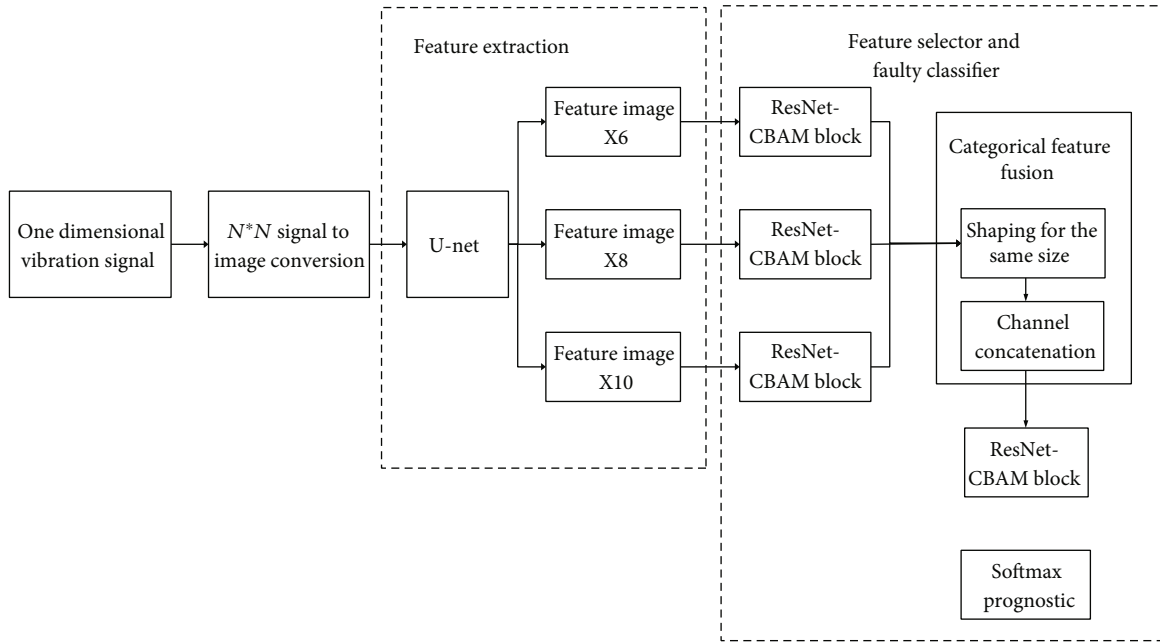
FIGURE 7: The framework of the proposed prognostic procedure.

---

**Algorithm: General procedure of the proposed approach**

Input: Given the one-dimensional time series bearing vibration data samples of different faulty diameters under different working loads, the architecture and parameters of the proposed U-net and the designed CBAM attention learning model.
Output: The prediction result and the testing accuracy.
**Step 1: Generate the training datasets and the testing datasets**
    1.1: Obtain the gray scale images of the one dimensional time series samples of the vibration signal by using the $N * N$ signal-to-image conversion method.
    1.2: Categorized the gray scale images into the training datasets Xs and the testing datasets Xt.
**Step 2: Construct the U-net hierarchical feature extractor for multilevel feature extraction**
    2.1: Construct the U-net hierarchical feature extractor as shown in Figure 5 and input the training datasets of Xs.
    2.2: Train the U-net hierarchical feature extractor by using unsupervised training.
    2.3: Extract the multilevel feature images of X6, X8, and X10 in the upconvolution process of the U-net.
**Step 3: Construct the attention learning mechanism for the further feature optimization**
    3.1: Construct the ResNet-CBAM-based attention learning network as shown in Figure 7 and apply it for the further feature optimization of the feature images X6, X8, and X10, respectively.
    3.2: Applying shaping and concatenation process for the construction of categorical feature.
    3.3: Applying ResNet-CBAM feature extraction network for the second feature optimization of the categorical feature in procedure 3.2.
**Step 4: Output the faulty prognostic result using flatten, dense, and Softmax prediction**
    4.1: Applying flatten, dense processing for the output in procedure 3.3.
    4.2: Applying Softmax prediction using Equation (8) for calculating the final faulty prognostic result.
    4.3: Optimizing the parameter of the proposed approach through minimizing the loss function in Equation (12) by using spatial game theory-based Pareto-optimal strategy.
    4.4: Repeat the procedures from 2.1 to 4.3 and finish the training procedure.
**Step 5: Evaluate the proposed methodology**
Evaluate the performance of the proposed methodology on testing datasets Xt and output the testing accuracy of the proposed approach.

ALGORITHM 1: The general procedure of the proposed methodology.

---

faulty prognostic model. The general procedure of the proposed approach is illustrated in Algorithm 1.

*3.3. Performance Metrics.* In order to evaluate the prediction accuracy as well as the prediction efficiency of the proposed

approach, the "accuracy" metric, the "accuracy gain" metric, and the function of the "average accuracy gain" are used in this paper.

Equation (10) denotes the definition of the "accuracy" function which has been widely used in the accuracy

evaluation of the classifying problem including the faulty classification task mentioned in this paper.

$$\text{acc}(f\,;D) = \frac{1}{m}\sum_{i=1}^{m}\Pi(f(\widehat{x}_i) = y_i),$$

$$\begin{cases}\Pi(f(\widehat{x}_i) = y_i) = 1, \text{if } f(\widehat{x}_i) = y_i, \\ \Pi(f(\widehat{x}_i) = y_i) = 0, \text{if } f(\widehat{x}_i) \neq y_i,\end{cases} \tag{10}$$

where $m$ denotes the number of the training or testing samples per epoch; $f(\widehat{x}_i)$ denotes the prognostic value obtained by model, and $y_i$ denotes the true label.

Equation (11) denotes the definition of the accuracy gain (AG) and the average accuracy gain (AAG) which has been frequently used to evaluate the speed-up properties of the prediction model [44].

$$AG_i = ACC_i^{Model1} - ACC_i^{Model2},$$

$$AAG_{N_{epoch}} = \frac{\sum_{i=0}^{N_{epoch}}\left(ACC_i^{Model1} - ACC_i^{Model2}\right)}{N_{epoch}}, \tag{11}$$

where the $ACC_i^{Model1}$ and $ACC_i^{Model2}$ denote the achieved accuracy of model 1 and model 2, respectively, after the $i_{th}$ epoch; $AG_i$ denotes the accuracy gain of model 1 over model 2 after the $i_{th}$ epoch; $AAG_{N_{epoch}}$ denotes the average accuracy gain of model 1 over model 2 within the epoch range of $N_{epoch}$; the indicator $AG_i$ evaluates the model speed-up properties from the microperspective while the indicator $AAG_{N_{epoch}}$ evaluates the model speed-up properties from the macroperspective.

The loss function is defined as shown in Equation (12), where $I(\ast)$ denotes the indicator function and $N$ denotes the number of the training samples.

$$H(y, P) = -\sum_{i=1}^{N} I\left(y^{(i)} = j\right) \ast \log\left(P\left(y^{(i)} = j \mid C^{(i)}\,;\theta\right)\right). \tag{12}$$

## 4. Methodology Evaluation

In order to evaluate the effectiveness of the proposed approach, two case studies are adopted with two bearing datasets from the reliance electric motor and electromechanical drive system, respectively. The experimental environment of this paper is Intel Xeon 5238 CPU@2.1 Hz x 2, 1 T SSD, 4xTesla T4 GPU, 256 G running memory.

### 4.1. Case Study 1: Bearing Faulty Prognostic for Reliance Electric Motor

*4.1.1. Data Description and Experimental Set-Up.* Performance of the proposed approach is evaluated on the bearing fault datasets provided by the CWRU (Case Western Reserve University) bearing data center [45]. The vibration signal data is collected from the drive-end of a 2-hp reliance electric motor as shown in Figure 8.
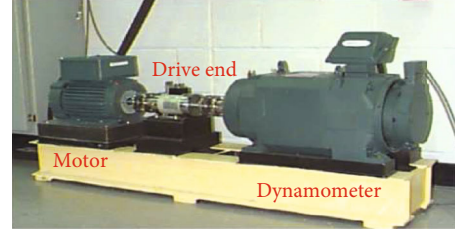


FIGURE 8: The testing rig 2-hp reliance electric motor.

TABLE 1: The details of the two bearing datasets.

| Machine operating status type | Class label | Dataset I number of training (loads: 0-3)/ testing (loads: 0-3) samples | Dataset II number of training (loads: 0-2)/ testing (loads: 3) samples |
|---|---|---|---|
| Normal | 0 | 400/400 | 300/100 |
| Faulty diameter 0.007 | 1 | 400/400 | 300/100 |
| Faulty diameter 0.014 | 2 | 400/400 | 300/100 |
| Faulty diameter 0.021 | 3 | 400/400 | 300/100 |
| Faulty diameter 0.028 | 4 | 400/400 | 300/100 |

The accelerator sensors are installed on the inner race, ball, and the outer race, respectively. In this case study, only the data collected from the inner race are collected and analyzed. The vibration data is sampled at the frequency of 12 kHz under different rotating speed of 1730 rpm, 1750 rpm, 1772 rpm, and 1797 rpm. There are totally five statuses of the inner race including one normal status and four different faulty severity statuses of the diameters 0.007, 0.014, 0.021, and 0.028, respectively. Therefore, five operating statuses are included in the datasets.

In this experiment, two datasets including the training datasets and the testing datasets in each are generated, respectively. In dataset $I$, for each health condition, 100 samples with 4096 data points in each sample are randomly selected under each load condition in the training datasets. That is to say, there are 400 samples of a single health condition with the load condition of 0, 1, 2, and 3. Therefore, there are totally 2000 samples of five health conditions altogether. Meanwhile, 2000 samples are randomly selected in the same way for the testing datasets. In dataset II, the training and testing samples are selected under different loads where 1500 samples with five operating statuses are randomly selected under the load condition of 0, 1, and 2 as the training datasets, while the testing datasets consist of 500 samples of five operating status under the load condition of 3. More details of the two datasets, namely, dataset I and dataset II, are listed in Table 1.
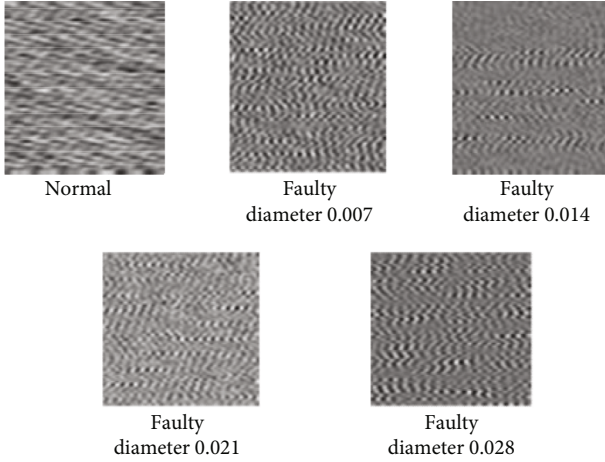
FIGURE 9: Converted image of the five health conditions under load 0.

TABLE 2: The detailed structure of the U-net model.

| Layer name | Configuration | Kernel/pooling/transpose size |
| --- | --- | --- |
| Input | $64 * 64$ | |
| X1 | $128@32 * 32$ | $128@3 * 3$ |
| X2 | $256@16 * 16$ | $256@3 * 3$ |
| X3 | $512@8 * 8$ | $512@3 * 3$ |
| X4 | $1024@4 * 4$ | $1024@3 * 3$ |
| X5 | $512@8 * 8$ | $2 * 2$ |
| X6 | $512@8 * 8$ | $512@3 * 3$ |
| X7 | $256@16 * 16$ | $2 * 2$ |
| X8 | $256@16 * 16$ | $256@3 * 3$ |
| X9 | $128@32 * 32$ | $2 * 2$ |
| X10 | $128@32 * 32$ | $128@3 * 3$ |

*4.1.2. Results and Discussion.* The raw vibration signal is converted to the $N * N$ gray-scale image by using the $N * N$ conversion approach. Since each sample contains 4096 signal points, the scale size of the gray scale image is set to the size of $64 * 64$. The converted gray-scale image of five operating status under load 0 are shown in Figure 9. It can be found that there is naked-eye distinguishable differences among these converted gray-scale images, which is applicable for the input of the U-net.

The converted ($64 * 64$) gray-scale images are used as the input of the U-net-based hierarchical feature extraction network with the specific configuration as shown in Table 2, where the feature layers of X6 ($512@8 * 8$), X8 ($256@16 * 16$), and X10 ($128@32 * 32$) are extracted, respectively.

In order to demonstrate the generalization ability and the faulty sensitivity of the proposed U-net hierarchical feature extractor, the *t*-distributed stochastic neighbor embedding (*t*-SNE) technology, regarded as a novel technology which visualizes high-dimensional data by giving each data-point a location in a two- or three-dimensional map [46], is used here for the visualized evaluation of the U-net hierarchical feature extractor. As shown in Figures 10(a)–

10(f), the two-dimensional visualizations of the feature images X6, X8, and X10 are illustrated under the test set of dataset I (loads 0~3) and the test set of dataset II (load 3), where different colors represent different health conditions.

Firstly, it can be found that the vast majority of the samples belonging to the same conditions are well gathered while separated for different health conditions. Therefore it can be concluded that the extracted multilevel features of the U-net feature extractor can be very sensitive for the faulty information contained in the gray-scale image. By the comparison analysis in Figures 10(a)–10(f), it is worth mentioning that the majority of samples belonging to the same health condition can be well gathered in the test set of both datasets, and there is no obvious difference in terms of the classification result. Since the operation conditions of the training and testing datasets are the same in dataset I while different in dataset II, it can be further proved that the U-net-based CNN has powerful generalized feature extraction ability which can be less influenced by the load condition variation.

In addition, the two-dimensional visualization view of the extracted multilevel features of X6, X8, and X10 are different from each other, indicating that the different feature level can contribute different knowledge to the faulty prognostic tasks. Therefore, it can be concluded the U-net-based CNN has powerful hierarchical feature learning ability which represent the information of the different health conditions from multiple aspects.

The visualization view of the representative feature images of X6, X8, and X10 is illustrated in Figure 11. It can be found that the three extracted multilevel feature images can be well distinguished from each other under the five different health statuses of the testing set of dataset I, indicating the proposed U-net hierarchical feature extractor being sensitive to the faulty information contained in the gray-scale feature image.

The extracted hierarchical features in layer X6, X8, and X10 are sent to the designed ResNet-CBAM attention learning block separately, and the designed ResNet-CBAM attention learning network is applied two times not only on the multilevel feature images but also on the ($8 * 8$) concatenated categorical feature images. The visualization of the attention learning result of the health condition of faulty diameter 0.007 under load 0 is illustrated as shown in Figures 12(a)–12(d); it should be noted that there is obvious discriminative concentration on these extracted multilevel feature images and the concatenated categorical feature image, thus, assigning larger weights to the important features and promoting the prognostic efficiency as well as the prognostic accuracy. Therefore, it can be concluded that it is necessary to apply the CBAM attention learning block not only on the extracted multilevel features of X6, X8, and X10 but also on the concatenated categorical feature used for faulty prognostic.

The optimized categorical feature image is sent to the Softmax layer for final faulty prognostic. The maximum epoch number is set to 60, and the average accuracy of the last 10 epochs from the $50^{th}$ to the $60^{th}$ epoch is defined as the final convergence accuracy (FCA) in this paper; the

(a)  (b)  (c)

- Healthy
- Faulty diameter 0.007
- Faulty diameter 0.014
- Faulty diameter 0.021
- Faulty diameter 0.028

(d)  (e)  (f)
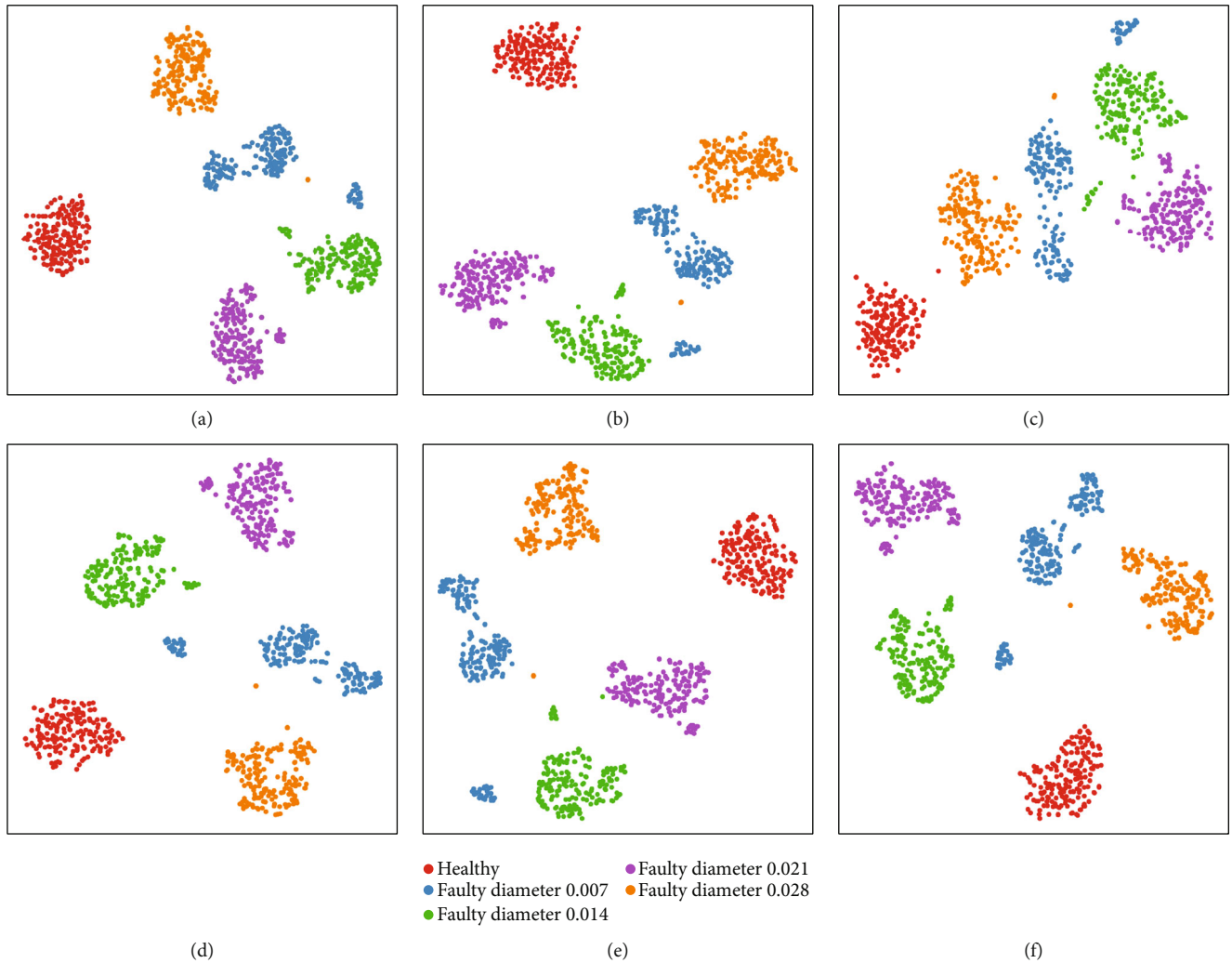
FIGURE 10: Visualization of the testing result of the multilevel features via t-SNE: (a) X6 (dataset I: loads 0-3); (b) X8 (dataset I: loads 0-3); (c) X10 (dataset I: loads 0-3); (d) X6 (dataset II: load 3); (e) X8 (dataset II: load 3); and (f) X10 (dataset II: load 3).

optimizer is Adam with the learning rate of 0.005. The prediction accuracy of the training and validation curves of two datasets are illustrated in Figure 13. It can be clearly seen that both the training and testing accuracy can reach almost 100% after the $60^{th}$ epoch in dataset I. In dataset II, the final convergence accuracy of the training result can also reach nearly 100%, and the testing accuracy can reach nearly 93%,which can be also comparatively high. Since the training and the testing datasets are collected under the same load in dataset *I* while different in dataset II, it can be proved that the proposed faulty prediction approach can achieve perfect prognostic accuracy as well as generalization ability.

*4.1.3. Ablation Experiment.* To evaluate the speed-up property promotion of introducing the attention mechanism to the proposed faulty prognostic framework, an ablation experiment of the different combinations of the U-net and the attention learning mechanism is evaluated on the two datasets of the case study. Specifically, we implement the proposed approach: the U-net+Softmax (US), the U-net+categorical attention+Softmax (UCAS) and the U-net+multi-
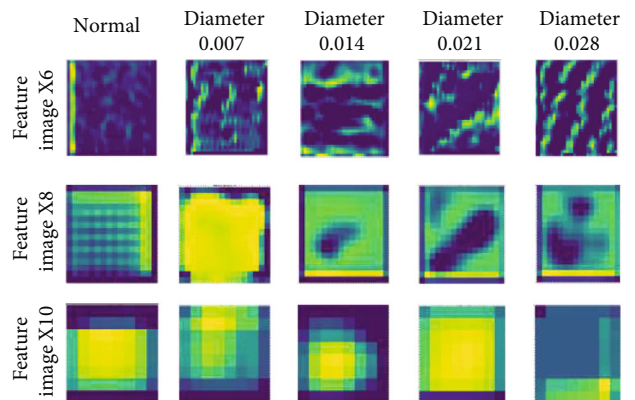


FIGURE 11: The visualization view of the extracted multilevel features under the testing set of dataset I.

scale attention+Softmax (UMAS). The "U-net+Softmax", which has no attention learning process, is used as the benchmark model, and the performance metrics of accuracy gain and the average accuracy gain is adopted for the

(a)

(b)

(c)

(d)
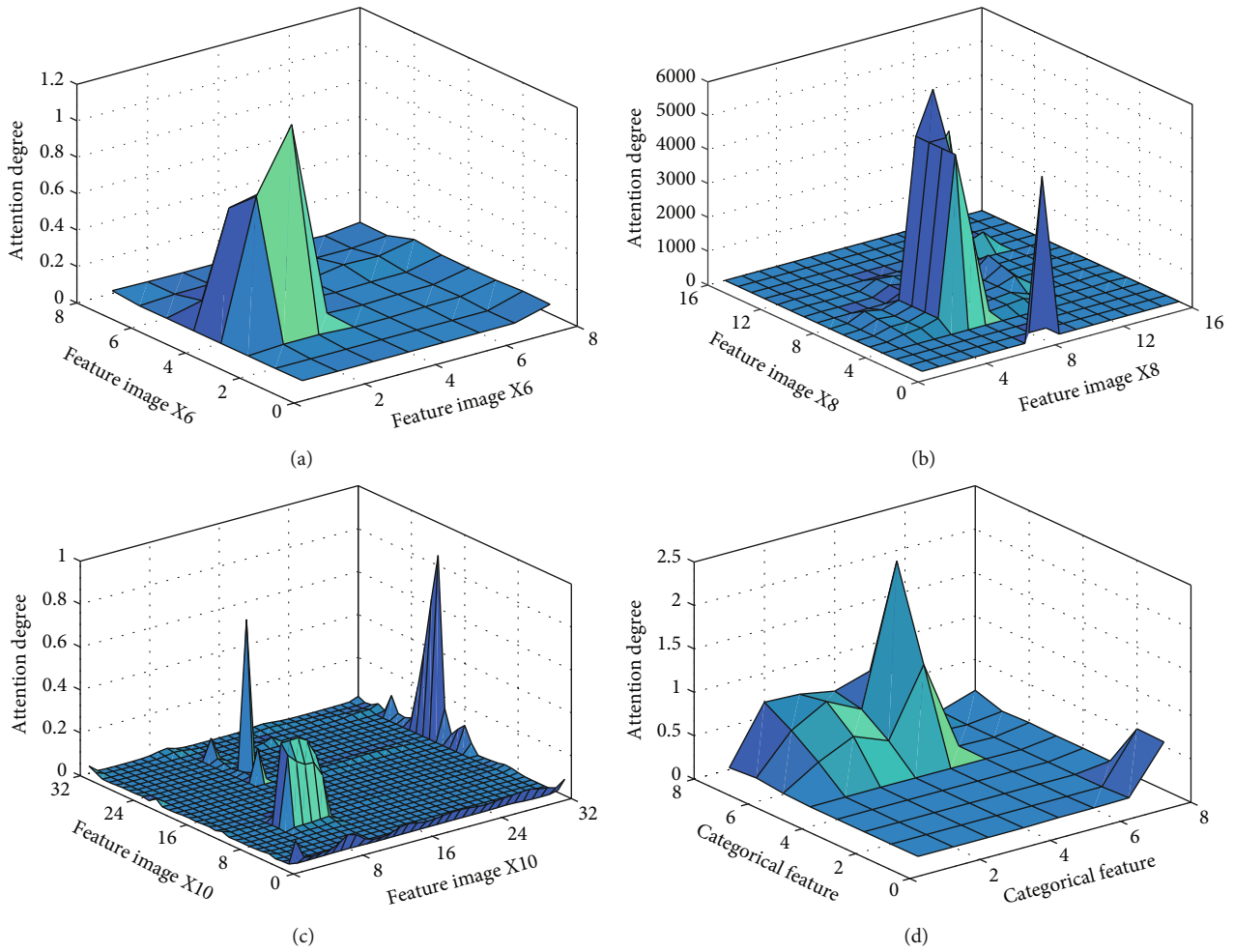
FIGURE 12: Visualization of the attention learning result of the optimized feature image of faulty diameter 0.007 under load 0: (a) feature image X6 (8 ∗ 8); (b) feature image X8 (16 ∗ 16); (c) feature image X10 (32 ∗ 32); (d) categorical feature image (8 ∗ 8).



(a)

(b)
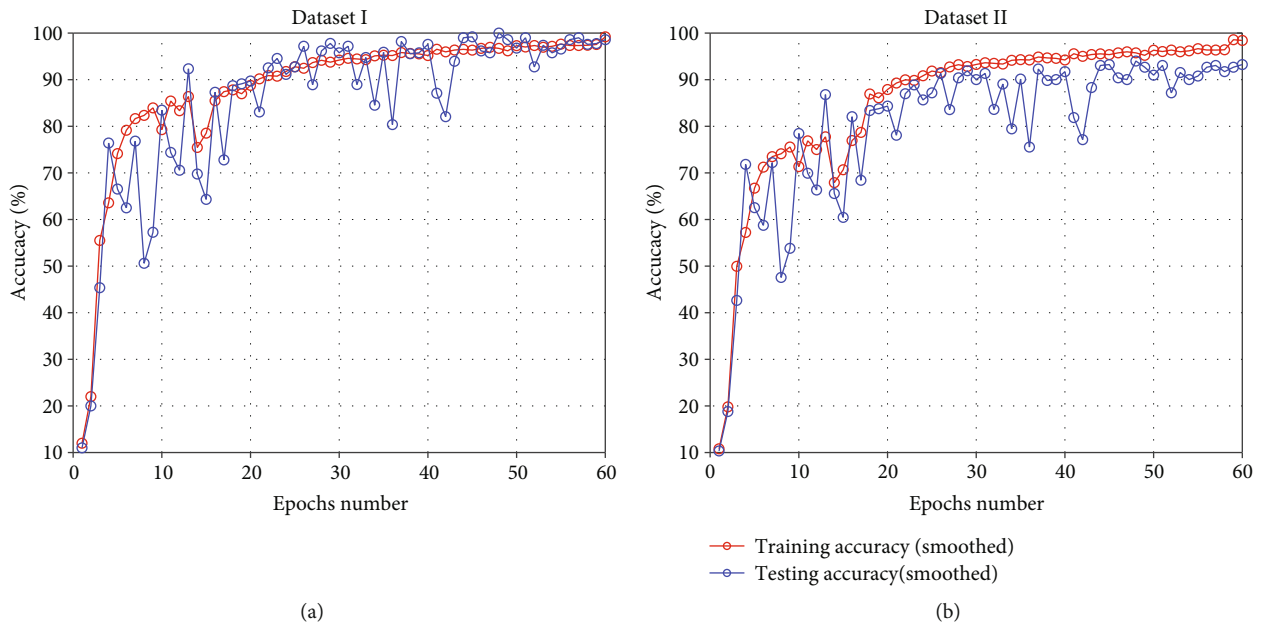
FIGURE 13: The training/testing accuracy curve of the proposed faulty prediction model: (a) dataset *I*; (b) dataset II.
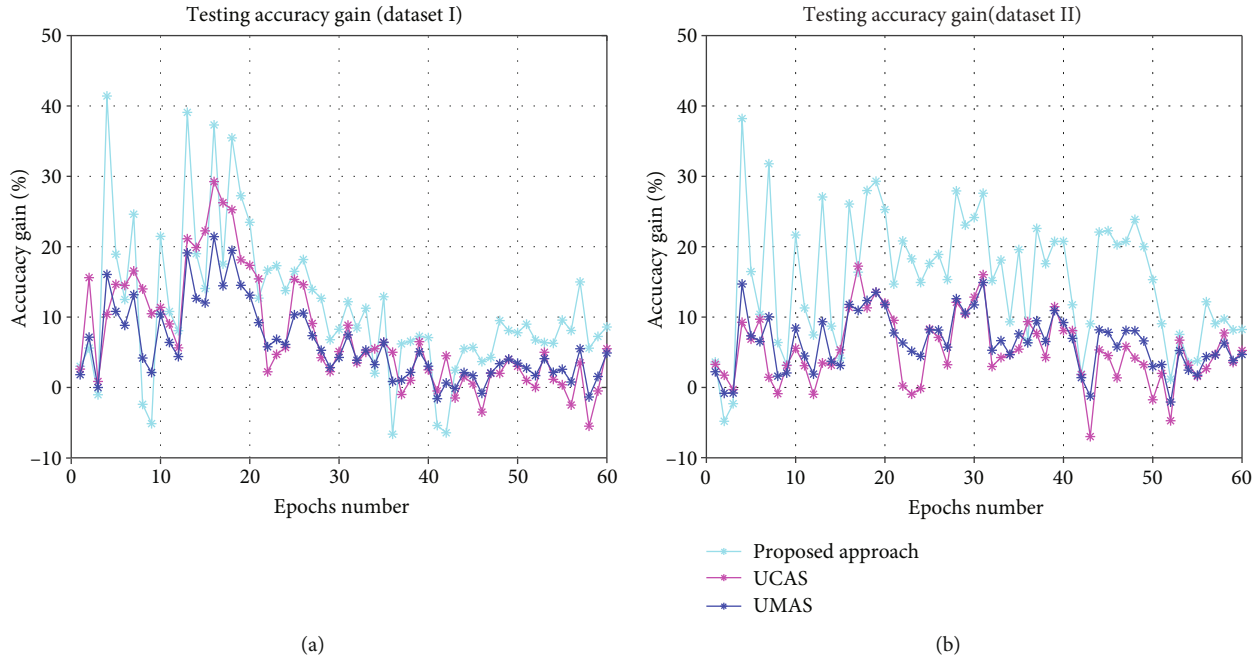
FIGURE 14: The accuracy gain of the three ablation models with attention learning mechanism: (a) testing accuracy gain of dataset I; (b) testing accuracy gain of dataset II.

TABLE 3: Mean value of the final convergence accuracy and the average accuracy gain of the testing result on two datasets.

| Model | Dataset I testing | | Dataset II testing | |
| --- | --- | --- | --- | --- |
| | FCA | AAG | FCA | AAG |
| Proposed approach | 98.59% | 11.2% | 93.24% | 15.36% |
| U-net+categorical attention+Softmax | 95.50% | 7.45% | 90.25% | 5.23% |
| U-net+multiscale attention+Softmax | 94.89% | 5.97% | 89.68% | 6.42% |
| U-net+Softmax | 90.00% | 0% | 85.50% | 0% |

evaluation of the model speed-up properties promoted by the attention learning network. As shown in Figure 14, the proposed model which has two times attention learning process significantly outperform the US model especially in the first 30 epochs in terms of the testing accuracy gain of both datasets, which is very important for the real-time requirement of the practical industry during the infant stage. Moreover, the ablation models of the UCAS and UMAS, which have only one attention learning process on the categorical feature and the multiscale features, respectively, also have certain accuracy gain promotion compared with the US model, indicating the effectiveness of the introduction of the attention learning mechanism in promoting prediction efficiency.

The ablation experiment is executed 10 times, and the mean values of the average final convergence accuracy (FCA) and the average accuracy gain (AAG) are illustrated in Table 3, where the proposed approach outperforms the other three ablation models in both metrics.

*4.1.4. Comparison Experiment.* To further evaluate the speed-up properties of the attention learning network and the generalization ability of the U-net CNN-based hierarchical feature extractor, the comparison analysis introduces the

proposed approach; the three ablation models as well as some hybrid prediction models based on the hierarchical feature extractor of the classical LeNet-5 CNN, namely, LeNet-5+Random forest (L-RF), LeNet-5+SVM(L-SVM), and LeNet-5+Softmax(LS) for comparison. Similar as the ablation experiment, the model of the U-net+Softmax is set as the benchmark model, and the accuracy gain curves of the multiple hybrid prediction approaches are illustrated in Figure 15, where the approaches with the attention learning mechanism has superior accuracy gain over the US model while the models without attention learning mechanism has inferior accuracy gain over US model, indicating the prognostic efficiency promotion of the attention learning.

The comparison experiments are conducted 10 times on both datasets just the same as the ablation experiment. It can be clearly seen from Table 4 that the proposed approach achieves the highest final convergence accuracy and the most superior average accuracy gain on the testing result of both datasets. Moreover, it should be noted that the models with the U-net feature extractor network significantly outperform other traditional LeNet-5 CNN-based model especially on the final convergence accuracy of dataset II when compared with the performance on dataset *I*. Therefore, it can be concluded that the models with the

Figure 15: The accuracy gain of the three ablation models with attention learning mechanism and the LeNet-5-based traditional hybrid models used for comparison: (a) testing accuracy gain of dataset I; (b) testing accuracy gain of dataset II.

Table 4: The comparison result with other traditional approaches.

| Model | Dataset I testing | | Dataset II testing | |
|---|---|---|---|---|
| | FCA | AAG | FCA | AAG |
| Proposed approach | 98.58% | 11.2% | 93.24% | 15.36% |
| U-net CNN+categorical attention+Softmax (UCAS) | 95.5% | 7.45% | 90.25% | 5.23% |
| U-net+multiscale attention+Softmax (UMAS) | 94.89% | 5.97% | 89.68% | 6.42% |
| U-net+Softmax (US) | 90.00% | 0% | 85.50% | 0% |
| LeNet-5 CNN+random forest (L-RF) | 83.53% | -11.03% | 79.71% | -6.01% |
| LeNet-5 CNN+SVM (L-SVM) | 82.66% | -6.96% | 77.1% | -5.83% |
| LeNet-5 CNN+Softmax (LS) | 82% | -7.51% | 70.73% | -8.09% |
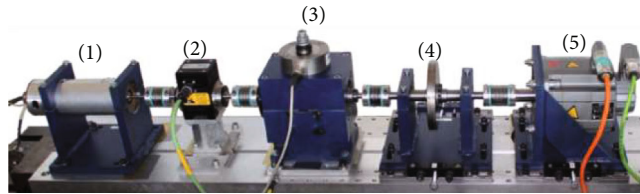


Figure 16: The testing rig of the Paderborn mechanical drive system.

designed U-net-based hierarchical feature extraction network has much better generalization ability compared with classical LeNet-5 CNN feature extractor network.

### 4.2. Case Study 2: Bearing Faulty Prognostic for Electromechanical Drive System

*4.2.1. Data Description and Experimental Set-Up.* Performance of the proposed approach is evaluated on the bearing fault datasets provided by the Paderborn University [47]. The testing rig is illustrated in Figure 16 which consists of

an electric motor (1), a torque-measurement shaft (2), a rolling bearing test (3), a flywheel (4), and a load motor (5). The experiment uses the motor current signal of the electromechanical drive system for bearing diagnostics which is collected under four operating conditions with different operating parameters settings as shown in Table 5. There are totally four different statuses of the electromechanical drive system, namely, inner-ring damage, outer-ring damage, combined damage, and the healthy status. All the samples with 4096 data sampling points are randomly selected from the conditional monitoring data. Different from the

TABLE 5: The operating parameters of the four operating conditions.

| Loads | Rotational speed [rpm] | Load torque $[N*m]$ | Radial force [N] | Name of setting |
|---|---|---|---|---|
| 0 | 1500 | 0.7 | 1000 | N15_M07_F10 |
| 1 | 900 | 0.7 | 1000 | N09_M07_F10 |
| 2 | 1500 | 0.1 | 1000 | N15_M01_F10 |
| 3 | 1500 | 0.7 | 400 | N15_M07_F04 |

TABLE 6: The description of the evaluated datasets.

| Machine operating status type | Class label | Dataset I number of training (loads: 0-3)/ testing (loads: 0-3) samples | Dataset II number of training (loads: 0-2)/ testing (loads: 3) samples |
|---|---|---|---|
| Healthy | 1 | 400/400 | 300/100 |
| Outer-ring damage | 2 | 400/400 | 300/100 |
| Inner-ring damage | 3 | 400/400 | 300/100 |
| Combined damage | 4 | 400/400 | 300/100 |
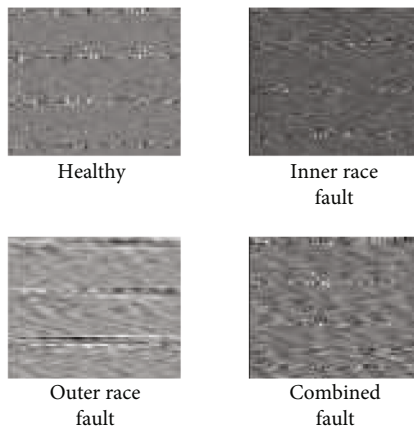


FIGURE 17: The converted gray-scale image of the four health conditions under load 0.

component faulty intensity classification of case study I, the faulty classification task in case study II involves multiple components. The arrangement of the training and testing datasets are illustrated in Table 6.

*4.2.2. Results and Discussion.* In this experiment, the 4096 continuous signal points are converted to the $64*64$ gray-scale image the same as case study one. The conversion result of the four operating statuses under load 0 are illustrated in Figure 17. It can be concluded that these images corresponding to different health conditions can also differ from each other, and it should be easy to classify them which further proves the effectiveness of the "$N*N$" signal to image conversion method.

The same as the case study one, the converted gray-scale images are used as the input of the U-net feature extractor

and the multilayer features extracted from the U-net are used as the input of the attention learning network for faulty classification within the maximum epoch range of 60. The prediction result is illustrated in Figure 18. It can be seen that the training and the testing accuracy of the 60th epoch can reach nearly 100% on both datasets which can be comparatively higher than case study one. The reason should be that the classification task is only within the same component of inner-race faulty in case study one while including different components in case study two, which has more distinguishable faulty symptom.

*4.2.3. Ablation Analysis.* The AG curves illustrated in Figure 19 show the effectiveness of the attention learning network where the proposed approach, the UCAS, and the UMAS have obvious accuracy advantage over the U-net+-Softmax within the same epoch range during the infant stage, indicating the effectiveness of the attention learning mechanism being also valid in case study two. The mean value of the average accuracy gain and the final convergence accuracy are illustrated in Table 7, where the proposed approach outperforms the other three ablation models in terms of both metrics in case study two.

*4.2.4. Comparison with Other Approaches.* Figure 20 and Table 8 show the accuracy gain curve; the mean final convergence accuracy and mean average accuracy gain of the proposed approach, the three ablation models and the traditional hybrid prediction models based on LeNet-5 hierarchical feature extractor network, where the model with the U-net feature extractor has better generalization ability; and the model with the attention learning mechanism has better speed-up properties especially during the infant stage, showing the great potential of the U-net, the attention learning network, and the proposed combination.

## 5. Conclusion and Future Work

*5.1. Main Contribution of the Proposed Paper.* In this paper, a novel bearing faulty prediction approach based on the U-net-based hierarchical feature extractor network and the ResNet-CBAM-based attention learning network is proposed. The main contributions of this paper can be summarized as follows:

(1) Introducing the $N*N$ "signal to image" conversion approach, the $N*N$ data to image approach can be simple but effective which can relax the dependencies on the domain expertise knowledge of signal processing

(2) Proposing a U-net CNN-based multilevel feature extractor network which has powerful generalized and hierarchical feature extraction ability. The extracted multilevel features can distinguish the different health conditions under the complex operational conditions and represent the different health conditions from multiple aspects, contributing different knowledge to the prognostic tasks

(a)                                                                                                                                    (b)
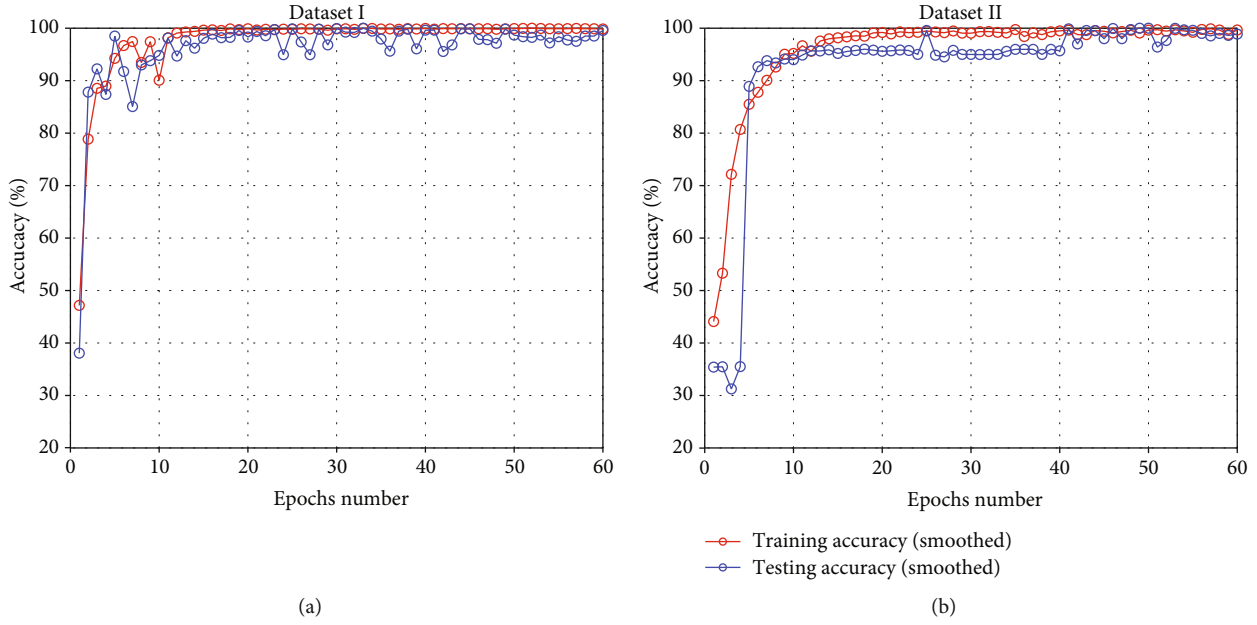
FIGURE 18: The training/testing accuracy curve of the proposed faulty prediction model: (a) dataset I; (b) dataset II.



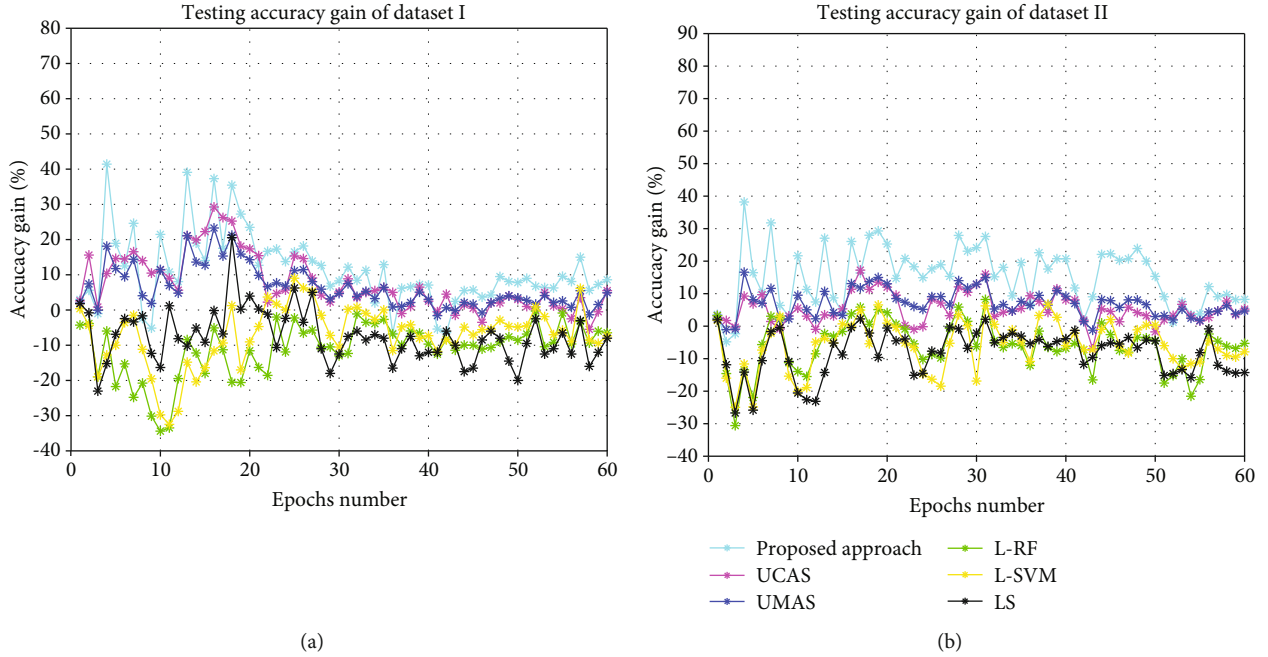(a)                                                                                                                                    (b)
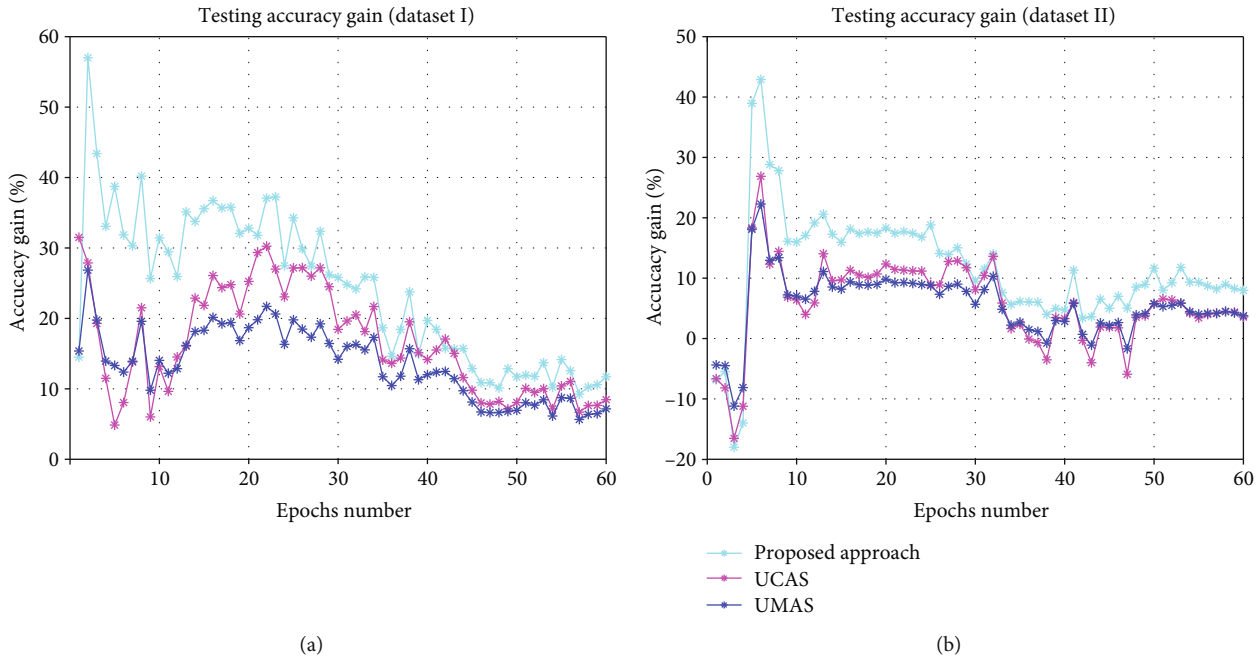
FIGURE 19: The accuracy gain of the three ablation models with attention learning mechanism: (a) testing accuracy gain of dataset I; (b) testing accuracy gain of dataset II.

TABLE 7: The comparison result of the ablation experiment.

| Model | Dataset I testing | | Dataset II testing | |
|---|---|---|---|---|
| | FCA | AAG | FCA | AAG |
| Proposed approach | 99.56% | 24.17% | 98.87% | 11.49% |
| U-net+categorical attention+Softmax | 96.31% | 16.52% | 94.47% | 5.78% |
| U-net+multiscale attention+Softmax | 95.01% | 13.57% | 94.68% | 5.52% |
| U-net+Softmax | 87.85% | 0% | 90.9% | 0% |
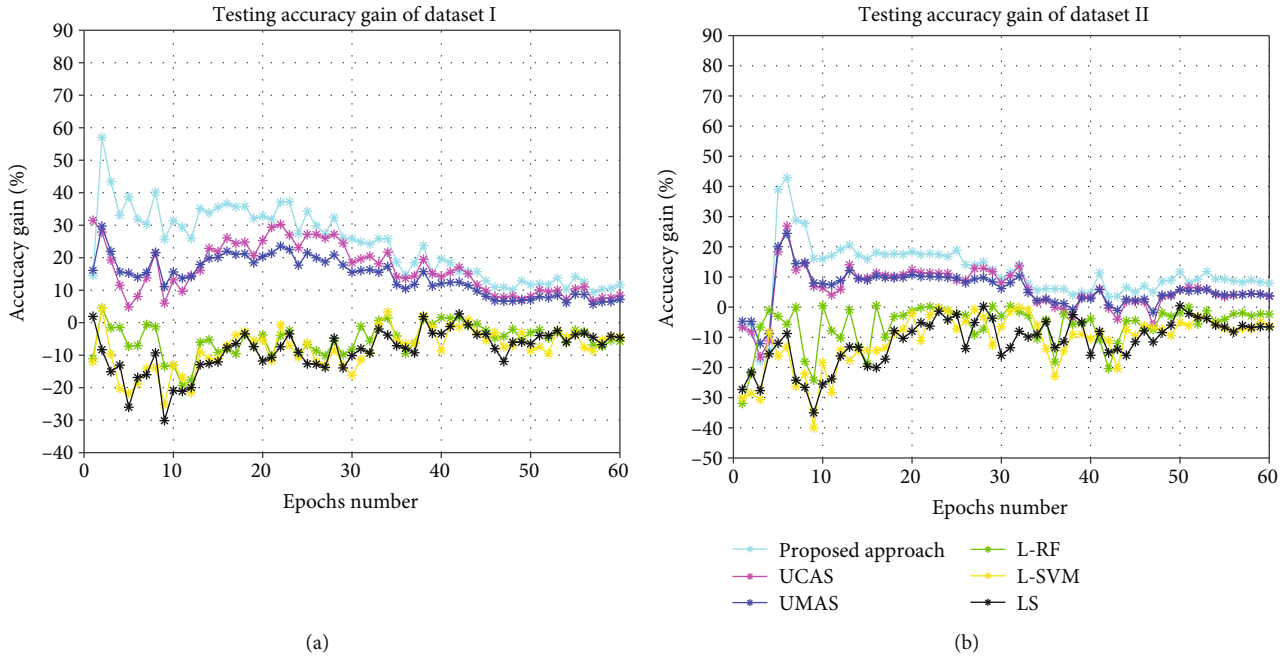
FIGURE 20: The accuracy gain of the three ablation models with attention learning mechanism and the LeNet-5 based traditional hybrid models used for comparison: (a) testing accuracy gain of dataset I; (b) testing accuracy gain of dataset II.

TABLE 8: The comparison result with other traditional approaches.

| Model | Dataset I | | Dataset II | |
|---|---|---|---|---|
| | FCA | AAG | FCA | AAG |
| Proposed approach | 99.56% | 24.17% | 98.87% | 11.49% |
| U-net CNN+categorical attention+Softmax (UCAS) | 96.31% | 16.52% | 94.47% | 5.78% |
| U-net+multiscale attention+Softmax (UMAS) | 95.01% | 13.57% | 94.68% | 5.52% |
| U-net+Softmax (US) | 87.85% | 0% | 90.9% | 0% |
| LeNet-5 CNN+random forest (L-RF) | 82.14% | -5.1% | 85.51% | -6% |
| LeNet-5 CNN+SVM (L-SVM) | 83.5% | -7.95% | 84.64% | -10.96% |
| LeNet-5 CNN+Softmax (LS) | 83.3% | -8.46% | 84.35% | -11.31% |

(3) Applying the designed ResNet-CBAM-based attention learning network for the feature selection of the extracted features. The ResNet-CBAM block is applied two times not only on the multilevel feature images but also on the categorical feature image. There is obvious discriminative concentration on the extracted features, and the proposed hybrid model can achieve certain prediction accuracy within the limited epoch range, enhancing the model speed-up properties

(4) Proposing the combination framework of the U-net and the ResNet-CBAM attention learning network. The U-net is used as the feature extractor, and the attention learning network is used as the feature selector and faulty classifier. Both the generalization ability and the speed-up properties of the model have been improved

The proposed approach is validated on two case studies, namely, offered by the CWRU (Case Western Reserved Uni-

versity) and the Paderborn University. Both case studies prove the effectiveness of the generalization ability of the U-net and the speed-up properties of the attention learning network. Moreover, the proposed approach is validated on the ablation experiment and the comparison experiment which further proves the effectiveness of introducing the proposed combination of the U-net and the attention learning network.

5.2. Future Work of the Proposed Paper. Although the proposed approach has made some achievements, there are still two items needed to be considered. Firstly, the complexity of the U-net-based hierarchical feature learning network as well as the attention learning network should be taken into account. In the future, the parameter scale of the proposed approach should be shortened which can be applicable for the model deployment of the edge-computing devices. Moreover, the proposed bearing faulty classification approach should be expected to be widely used in the faulty classification of other similar prognostic scene such as the gearbox, the milling equipment, and the gas pump system.

## Data Availability

## Conflicts of Interest

## Acknowledgments

## References

[1] L. Hong and J. S. Dhupia, "A time domain approach to diagnose gearbox fault based on measured vibration signals," *Journal of Sound and Vibration*, vol. 333, no. 7, pp. 2164–2180, 2014.

[2] P. Borghesani, P. Pennacchi, and S. Chatterton, "The relationship between kurtosis- and envelope-based indexes for the diagnostic of rolling element bearings," *Mechanical Systems and Signal Processing*, vol. 43, no. 1-2, pp. 25–43, 2014.

[3] M. C. Garcia, M. A. Sanz-Bobi, and J. del Pico, "SIMAP: intelligent system for predictive maintenance: application to the health condition monitoring of a windturbine gearbox," *Computers in Industry*, vol. 57, no. 6, pp. 552–568, 2006.

[4] D. Coronado and K. Fisher, *Condition Monitoring of Wind turbines: State of the Art, User Experience and Recommendations*, VGB Research Foundation,VGB-Nr.383; Fraunhofer-IWES Bremer haven, Germany, 2015.

[5] M. Asgarpour and J. Sørensen, "Bayesian based diagnostic model for condition based maintenance of offshore wind farms," *Energies*, vol. 11, no. 2, p. 300, 2018.

[6] G. Xu, M. Liu, Z. Jiang, W. Shen, and C. Huang, "Online fault diagnosis method based on transfer convolutional neural networks," *IEEE Transactions on Instrumentation and Measurement*, vol. 69, pp. 1–12, 2019.

[7] X. Xu, C. Zhang, H. A. Derazkola, M. Demiral, A. M. Zain, and A. Khan, "UFSW tool pin profile effects on properties of aluminium-steel joint," *Vacuum*, vol. 192, no. 8, article 110460, 2021.

[8] X. X. C. Zhang, H. A. Derazkola, M. Demiral, A. M. Zain, and A. Khan, "Dispersion of waves characteristics of laminated composite nanoplate," *Steel and Composite Structures*, vol. 40, no. 3, pp. 355–367, 2021.

[9] Z. Liu, Z. Jia, C. M. Vong, S. Bu, J. Han, and X. Tang, "Capturing high-discriminative fault features for electronics-rich analog system via deep learning," *IEEE Transactions on Industrial Informatics*, vol. 13, no. 3, pp. 1213–1226, 2017.

[10] H. Li, J. Chen, H. Lu, and Z. Chi, "CNN for saliency detection with low-level feature integration," *Neuro Computing*, vol. 226, pp. 212–220, 2017.

[11] Z. Tang, G. Zhao, and T. Ouyang, "Two-phase deep learning model for short-term wind direction forecasting," *Renewable Energy*, vol. 173, pp. 1005–1016, 2021.

[12] H. Shao, H. Jiang, X. Zhang, and M. Niu, "Rolling bearing fault diagnosis using an optimization deep belief network," *Measurement Science and Technology*, vol. 26, no. 11, article 11500, 2015.

[13] M. He and D. He, "Deep learning based approach for bearing fault diagnosis," *IEEE Transactions on Industry Applications*, vol. 53, no. 3, pp. 3057–3065, 2017.

[14] Y. Qi, C. Shen, D. Wang, J. Shi, X. Jiang, and Z. Zhu, "Stacked sparse autoencoder-based deep network for fault diagnosis of rotating machinery," *IEEE Access*, vol. 5, pp. 15066–15079, 2017.

[15] S. Haidong, J. Hongkai, L. Xingqiu, and W. Shuaipeng, "Intelligent fault diagnosis of rolling bearing using deep wavelet auto-encoder with extreme learning machine," *Knowledge-Based Systems*, vol. 140, pp. 1–14, 2018.

[16] M. Xia, T. Li, L. Xu, L. Liu, and C. W. de Silva, "Fault diagnosis for rotating machinery using multiple sensors and convolutional neural networks," *IEEE/ASME Transactions on Mechatronics*, vol. 23, no. 1, pp. 101–110, 2018.

[17] K. B. Lee, S. Cheon, and C. O. Kim, "A convolutional neural network for fault classification and diagnosis in semiconductor manufacturing processes," *IEEE Transactions on Semiconductor Manufacturing*, vol. 30, no. 2, pp. 135–142, 2017.

[18] L. Wen, L. Gao, and X. Li, "A new deep transfer learning based on sparse auto-encoder for fault diagnosis," *IEEE Transactions on Systems, Man, and Cybernetics: Systems*, vol. 49, no. 1, pp. 136–144, 2019.

[19] X. Min, L. Teng, X. Lin, L. Liu, and C. W. de Silva, "Fault diagnosis for rotating machinery using multiple sensors and convolutional neural networks," *IEEE/ASME Transactions on Mechatronics*, vol. 23, no. 1, pp. 101–110, 2017.

[20] X. Ding and Q. He, "Energy-fluctuated multiscale feature learning with deep ConvNet for intelligent spindle bearing fault diagnosis," *IEEE Transactions on Instrumentation and Measurement*, vol. 66, no. 8, pp. 1926–1935, 2017.

[21] Y. Sun, X. Wang, and X. Tang, "Deep learning face representation from predicting 10, 000 classes," in *IEEE Conference on Computer Vision & Pattern Recognition*, pp. 1891–1898, Columbus, OH, USA, 2014.

[22] J. Lee and J. Nam, "Multi-level and multi-scale feature aggregation using pre-trained convolutional neural networks for music auto-tagging," *IEEE Signal Processing Letters*, vol. 24, no. 8, pp. 1208–1212, 2017.

[23] G. Xu, M. Liu, Z. Jiang, D. Söffker, and W. Shen, "Bearing fault diagnosis method based on deep convolutional neural network and random forest ensemble learning," *Sensors*, vol. 19, no. 5, p. 1088, 2019.

[24] Y. LeCun, "LeNet-5, convolutional neural networks," 2015, http://yann.lecun.com/exdb/lenet.2015.

[25] A. Krizhevsky, I. Sutskever, and G. E. Hinton, "Imagenet classification with deep convolutional neural networks," *Advances in Neural Information Processing Systems*, vol. 25, pp. 1097–1110, 2012.

[26] K. Simonyan and A. Zisserman, "Very deep convolutional networks for large-scale image recognition," 2014, https://arxiv.org/abs/1409.1556.

[27] C. Szegedy, L. Wei, Y. Jia et al., "Going deeper with convolutions," in *Proceedings of the IEEE conference on computer*

*vision and pattern recognition*, pp. 1–9, Boston, MA, USA, 2014.

[28] O. Ronneberger, P. Fischer, and T. Brox, "U-net: convolutional networks for biomedical image segmentation," in *International Conference on Medica image computing and computer-assisted intervention*, pp. 234–241, Munich, Germany, 2015.

[29] F. Zhao, Z. Wu, L. Wang et al., "Spherical deformable U-net: application to cortical surface parcellation and development prediction," *IEEE Transactions on Medical Imaging*, vol. 40, no. 4, pp. 1217–1228, 2021.

[30] H. Gao, T. Qiu, C. Yuanting, M. Zhou, and X. Zhang, "Blood vessel segmentation of fundus images based on improved U network," in *2019 Chinese Automation Congress (CAC)*, pp. 4017–4021, Hangzhou, China, 2019.

[31] X. Lei, Y. Chen, W. Chang et al., *Ultra-Fast T2-Weighted MR Reconstruction Using Complementary T1-Weighted Information*, Springer, Cham, Switzerland, 2018.

[32] F. Nazem, F. Ghasemi, A. Fassihi, and A. M. Dehnavi, "3D U-Net: a voxel-based method in binding site prediction of protein structure," *Journal of Bioinformatics and Computational Biology*, vol. 19, no. 2, p. 2150006, 2021.

[33] R. O. Dogan, H. Dogan, C. Bayrak, and T. Kayikcioglu, "A two-phase approach using mask R-CNN and 3D U-Net for high-accuracy automatic segmentation of pancreas in CT imaging," *Computer Methods and Programs in Biomedicine*, vol. 207, article 106141, 2021.

[34] J. Chae, K. Y. Hong, and J. Kim, "A pressure ulcer care system for remote medical assistance: residual U-Net with an attention model based for wound area segmentation," 2021, https://arxiv.org/abs/2101.09433.

[35] A. M. Treisman and G. Gelade, "A feature-integration theory of attention," *Cognitive Psychology*, vol. 12, no. 1, pp. 97–136, 1980.

[36] S. Woo, J. Park, J. Lee, and I. S. Kweon, "Cbam: convolutional block attention module," in *Proceedings of the 15th European Conference on Computer Vision*, pp. 3–19, Munich,Germany, 2018.

[37] Z. Chen, M. Wu, R. Zhao, F. Guretno, R. Yan, and X. Li, "Machine remaining useful life prediction via an attention based deep learning approach," *IEEE Transactions on Industrial Electronics*, vol. 68, 2021.

[38] B. Chen, Z. Zhang, N. Liu, Y. Tan, X. Liu, and T. Chen, "Spatiotemporal convolutional neural network with convolutional block attention module for micro-expression recognition," *Information*, vol. 11, no. 8, p. 380, 2020.

[39] C. Xiong, X. Shi, Z. Gao, and G. Wang, "Attention augmented multi-scale network for single image super-resolution," *Applied Intelligence*, vol. 51, no. 2, pp. 935–951, 2021.

[40] J. Leng, Y. Liu, and S. Chen, "Context-aware attention network for image recognition," *Neural Computing and Applications*, vol. 31, no. 12, pp. 9295–9305, 2019.

[41] L. Wen, X. Li, L. Gao, and Y. Zhang, "A new convolutional neural network-based data-driven fault diagnosis method," *IEEE Transactions on Industrial Electronics*, vol. 65, 2018.

[42] K. K. Wong, "A geometrical perspective for the bargaining problem," *PLoS One*, vol. 5, no. 4, article e10331, 2010.

[43] K. Wong, "Bridging game theory and the knapsack problem: a theoretical formulation," *Journal of Engineering Mathematics*, vol. 91, no. 1, pp. 177–192, 2015.

[44] X. Dong, H. H. Wu, Y. Yan, and L. Qian, "Hierarchical transfer convolutional neural networks for image classification," in *2019 IEEE International Conference on Big Data (Big Data)*, pp. 2817–2825, Los Angeles, CA, USA, 2019.

[45] K. Loparo, "Case Western Reserve University bearing data centre website," 2012, http://csegroups.case.edu/bearingdatacenter/pages/download-data-file.

[46] S. Shi, "Visualizing data using GTSNE," 2021, https://arxiv.org/abs/2108.01301.

[47] C. Lessmeier, J. K. Kimotho, D. Zimmer, and W. Sextro, "Condition monitoring of bearing damage in electromechanical drive systems by using motor current signals of electric motors: a benchmark data set for data-driven classification," in *European Conference of the Prognostics and Health Management Society*, pp. 83–100, Bilbao, Spain, 2016.

*Research Article*

# Composition Regulation and Microstructure Characterization of $Fe_{100-x}Ga_x$ Films in the Manufacturing Industry

**Zhi Shen** [1,2] **Jian-Wu Yan,**[1,2] **Kang Jin,**[3] **Kai Fu,**[2] **and Ying-Li Zhou**[4]

[1]*School of Mechanical Engineering, Nanchang Institute of Technology, Nanchang 330099, China*
[2]*Jiangxi Province Key Laboratory of Precision Drive and Control, Nanchang 330099, China*
[3]*Beijing Research Institute of Mechanical & Electrical Technology Ltd., Beijing 100083, China*
[4]*Beijing National Innovation Institute of Lightweight Ltd., Beijing 100083, China*

Correspondence should be addressed to Zhi Shen; nickshen009@163.com

$Fe_{100-x}Ga_x$ giant magnetostrictive films (GMF) are attracting ever increasing attention for their potential application to manufacturing integrated magnetostrictive displacement sensors. However, it is difficult to fabricate $Fe_{100-x}Ga_x$ thin films with different compositions at will. The influence of compositions on alloy phases, grain sizes, film surface roughness, and magnetic domains of the films and magnetization of magnetron sputtered $Fe_{100-x}Ga_x$ films was investigated. Changing the ratio of the pure iron slice areas to alloy target areas, the desired film composition was achieved by the improved Mosaic method. The morphologies, magnetic domain structure, microstructure, and compositions of $Fe_{100-x}Ga_x$ films revealed by SEM, EDS, XRD, MFM, VSM, and TEM. The results show that there are <1 1 0> texture in magnetron sputtered $Fe_{100-x}Ga_x$ films. The sharp peak attributed to the $A_2$ microstructure suggests that the film is crystalline. The magnetic domain structure of $Fe_{100-x}Ga_x$ films presents a network form, and the domain width decreases with the decrease of gallium content. It is also found that the magnetic domains of the films are not uniform. The TEM result shows that there are some strip patterns in the films, and the diffraction ring is discontinuous because of the structure extinction. For a suitable candidate of microdevice applications in MEMS, the optimum composition film should be $Fe_{83.25}Ga_{16.75}$ film.

## 1. Introduction

$Fe_{100-x}Ga_x$ giant magnetostrictive films (GMF) are attracting ever increasing attention for their potential application to manufacturing integrated magnetostrictive displacement sensors [1–3]. So, $Fe_{100-x}Ga_x$ films are the suitable candidate of other magnetostrictive materials, e.g., Terfenol-D and Fe-Ga alloy, because of its superior synthetic properties [4]. $Fe_{100-x}Ga_x$ films for microsensor and microactuator development are possible [5].

Magnetron sputtering is a commonly technology used to prepare giant magnetostrictive films [6, 7]. Magnetron sputtering has the advantages of fast deposition rate, strong adhesion between coating and substrate, compact, and uniform coating.

Film grain size will be small and as well as surface roughness will be decrease when the substrates were maintained at lower temperature. This is beneficial to improve the performance of thin films. Basumatary et al. report the microstructure and magnetic properties of $Fe_{100-x}Ga_x$ films deposited at different deposited temperatures [5]. The grain size and surface roughness increase with the increasing of substrate temperature. The films deposited at higher substrate temperatures were found to saturate at lower magnetic field as compared to the room temperature deposited film. X-ray diffraction and TEM results revealed the presence of disordered $A_2$ phase in the films.

Preparing thin films is crucial to developing microdevices. The thin-film physical, mechanical, and chemical properties depend on how the film structure is organized, which is closely related to film composition [8, 9].

Single-metal-target and single-alloy-target sputtering are often used to fabricate various alloy thin films [10, 11].

However, traditional elemental-target co-sputtering cannot be used to prepare $Fe_{100-x}Ga_x$ films because gallium shows a low melting point. As a sputtering target, it is difficult to exist stably above room temperature. In addition, it is expensive and difficult to develop a series of $Fe_{100-x}Ga_x$ alloy targets because smelting $Fe_{100-x}Ga_x$ is a little difficult. There are some technology problems when $Fe_{100-x}Ga_x$ alloy targets prepared by melting, which means it is difficult to tune compositions of $Fe_{100-x}Ga_x$ films precisely at will.

So-called mosaic targets, *i.e.*, targets whose matrices consist of one metal and whose inserts consist of others, have recently been used to develop methods of magnetron-sputtering multicomponent thin films [12].

Such effective methods rely on several components being limited to fabricate numerous multicomponent alloy thin films. However, the traditional mosaic target must be drilled in order to embed the second material on the surface of the matrix target, which will produce gap on the target, affect the electromagnetic field uniformity, and affect the sputtering process. Against this background, Yan et al. report a composite or improved mosaic targets to tune $Fe_{100-x}Ga_x$ film compositions [13].

The way to do that is pure-iron patch is magnetically attracted to the surface of the $Fe_{100-x}Ga_x$ alloy target that can be a minitarget, and the $Fe_{100-x}Ga_x$ alloy target was another sputter target whose sputter area is reduced. Iron slices cover $Fe_{100-x}Ga_x$ alloy target surface, shielding it from $Ar^+$ bombardment, so the iron slices are bombarded instead of its increased surface area, assuming all other sputtering conditions are the same. Hence, the sputtered $Fe_{100-x}Ga_x$ films will be composite of a small amount of iron atoms come from the iron target and $Fe_{100-x}Ga_x$ alloy come from the $Fe_{100-x}Ga_x$ alloy target.

This, in essence, is equivalent to increasing the iron content in the target material, which subsequently increases the iron content in the sputtered film. Further, increasing the sputter area per unit of time increases the probability that the iron slices will be bombarded with argon ions so that more iron atoms are sputtered onto the target. The sputtering principle how to influence on film compositions must be further discussed.

In the process of magnetron sputtering, electrons collide with argon atoms and ionize a large number of argon ions and electrons, and the electrons fly to the substrate. A large number of target atoms are sputtered out by argon ions under the action of electric field, and the neutral target atoms (or molecules) are deposited on the substrate.

However, the nonuniform distribution of the magnetic field on the target surface leads to the nonuniform etching on the target surface, and the argon ion bombards the target surface selectively, and the intensity of bombardment is high in some places and weak in others; therefore, a deep circular groove is formed on the round target surface, which is located at the quarter of the diameter of the target surface. Therefore, the location of the pure patch on the target should be in the etching region in order to effectively control the composition of the sputtering film.

Films with high effective saturation magnetostriction constant and low stress fabricated by magnetron sputtering when argon pressure is suitable [14]. Liu et al. reported that the modified-$DO_3$ phase and the (100) texture play a positive role in magnetostrictive properties of $Fe_{77}Ga_{23}$ ribbons [15]. Some investigations reported that preparation methods affect magnetic properties of Fe-Ga films [16].

It is of great theoretical value to study the microstructure of magnetic domains, which is the basic physical parameter of magnetic materials. Magnetic domains or defects in ferromagnetic materials can be identified by magnetic imaging.

The domain structures of TbFe and Terfenol-D magnetostrictive thin films were investigated by Shih et al. [17] and Song et al. [18]. Sun et.al reported the magnetic properties and domain structures of FeSiB prepared by RF-sputtering method [19]. However, up to now, the domain structure of $Fe_{100-x}Ga_x$ films has been seldom reported.

It is well known that the magnetic domain structure affects magnetic properties of $Fe_{100-x}Ga_x$ films. MFM is an effective instrument to observe the magnetic structure of magnetic films. The MFM can give the magnetic domain image and surface roughness, come from the interaction between magnetic charges of the sample surface and magnetic probe.

In order to enhance these material analyses and optimize the concentration as well as better understand the influence of compositions on microstructure, deep learning [20] may be applied to assist in our study. Some advanced technologies [21, 22] in other fields can also be used for reference to develop new sensing technologies. It is centered on the simple mosaic targets to prepare $Fe_{100-x}Ga_x$ films in this paper. The purpose is composition regulation and microstructure characterization of $Fe_{100-x}Ga_x$ films.

## 2. Materials and Methods

A direct current (DC) magnetron sputtering equipment (JZCK-600F) was adopted to deposit films. The sputtering chamber base pressure was $2 \times 10^{-4}$ Pa, and 0.6 Pa argon (99.99% pure) was used during sputtering. 90 W sputtering power and 70 minutes sputtering time were chosen. The vertical distance between the target and the substrate was 100 mm. The substrates were maintained at room temperature.

In the experiment, some polished glasses were chosen as the substrates to deposit films. Its surfaces were cleaned by ultrasonic before sputtering. The thickness of films can be calculated by the weighing method [23]. The average value is taken as the thickness of films to reduce errors in the experiment.

$Fe_{84}Ga_{16}$ alloy target was used to prepare $Fe_{100-x}Ga_x$ films. The diameter of target is 60 mm, and its thickness is 3 mm. Some pure iron slices were absorbed to the etching area of round $Fe_{84}Ga_{16}$ alloy target by magnetron force, which is located at the quarter of the diameter of the target surface. The purity of iron slices used in the experiment was 99.99% and distributed uniformly on the target. The desired film composition was achieved by changing the ratio of the pure iron slice areas to alloy target areas (i.e., the area ratio, $R$).

The surfaces of $Fe_{100-x}Ga_x$ films were coated with gold. Scanning electron microscopy (SEM, Quanta 200) was used to characterize the surface morphologies of the gold-coated $Fe_{100-x}Ga_x$ films. The average composition and distributions of elements on the surfaces of $Fe_{100-x}Ga_x$ films were determined by an energy dispersive spectroscopy (EDS, Oxford energy-scattering spectrometer).

Bruker AXS D8 ADVANCE X-ray diffractometer (XRD) was used to analyze the film phase. X-ray tube target is Cu target, voltage is 40.0 (kV), and current is 30.0 (mA). Divergence slit is 1.00000 (deg), scatter slit is 1.00000 (deg), and receiving slit is 0.30000 (mm). Scan speed is 7.0000 (deg/min), sampling pitch is 0.0200 (deg), and preset time is 0.17 (sec).

The magnetic domain structure of $Fe_{100-x}Ga_x$ films was observed by a magnetic force microscopy (MFM, Micro-Nano D5A); the scan rage is 5 micron meter~10 micron meter.

The specimens no. (a) and no. (f) were deposited on polished glass; then, the films were removed from the glass and observed by a Jeol-2010F transmission electron microscope (TEM).

A YP07 vibrating sample magnetometer (VSM) was adopted to test magnetic hysteresis loop of $Fe_{100-x}Ga_x$ films.

A theoretical equation can be used to calculate film compositions. The theoretical formula of film composition can be deduced as follows [23].

According to the sputtering principle, the total material which sputtering on the substrate surface can be expressed as follows:

$$Q \approx \frac{k_1 Q_0}{qH}, \tag{1}$$

where $k_1$ is the constant value, $q$ is the sputtering pressure, and $H$ represents the target-substrate distance. $Q_0$ is the magnitude of target sputtering which can be approximated as:

$$Q_0 \approx \left(\frac{I_+}{e}\right) St \left(\frac{M}{N}\right), \tag{2}$$

where $I_+$ is the current of target ion, $e$ is the charge of an electron, $S$ is the sputtering rate, $t$ is the sputtering time, $M$ is the atomic weight of sputtered materials, and $N$ is the Avogadro constant. Generally speaking, the discharge current $I_S$ may be close to $I_+$ when sputtering, and there is a formula as follows:

$$S \propto V_s, \tag{3}$$

where $V_S$ is the discharge voltage. However, the relationship between $Q_0$ and $A$ (the area of target material) can be expressed within the scope of sputtering as follows:

$$Q_0 \propto A. \tag{4}$$

Therefore, $Q_0$ can be approximated as:

$$Q_0 \approx k_2 V_s I_s t A, \tag{5}$$

where $k_2$ is the constant of target material. According to formulas (1) and (5), the total of sputtered material can be represented as:

$$Q \approx \frac{k_1 k_2 V_s I_s t A}{qH} = \frac{k V_s I_s t A}{qH}. \tag{6}$$

From this expression, it can be seen that the total amount of sputtered materials from metal substrate is in direct proportion to electric energy ($V_S I_S t$) consumed on the device and the areas of target material ($A$). And it is inversely proportional to the sputtering pressure and the vertical distance between the target and the substrate.

Therefore, for mosaic target sputtering, the total amount of sputtered materials from the substrate can be approximated as:

$$Q \approx Q_{Fe} + Q_{Fe\text{-}Ga}. \tag{7}$$

Combined formulas (6) and (7), it can be given as follows:

$$Q \approx \frac{(k_{Fe} V_{Fe} I_{Fe} A_{Fe} + k_{Fe\text{-}Ga} V_{Fe\text{-}Ga} I_{Fe\text{-}Ga} A_{Fe\text{-}Ga}) t}{qH}. \tag{8}$$

Considering that sputtering power can be calculated by formula (9), it can be expressed by formula (10).

$$P = V_S I_S, \tag{9}$$

$$Q \approx \frac{(k_{Fe} P_{Fe} A_{Fe} + k_{Fe\text{-}Ga} P_{Fe\text{-}Ga} A_{Fe\text{-}Ga}) t}{qH} = Q_{Fe} + Q_{Fe\text{-}Ga}, \tag{10}$$

where $k_{Fe}$ is a coefficient related to iron element target sputtering, $k_{Fe-Ga}$ is a coefficient in relation to $Fe_{100-x}Ga_x$ target sputtering, $P_{Fe}$ and $P_{Fe-Ga}$ severally denote sputtering powers of iron element target and $Fe_{100-x}Ga_x$ targets, $A_{Fe}$ and $A_{Fe-Ga}$, respectively, signify the areas of iron element target and uncovered $Fe_{100-x}Ga_x$ targets. In the mosaic target sputtering, iron slices are attached on the $Fe_{100-x}Ga_x$ targets, and they have the same target seats, so it can be considered that $P_{Fe}$ is equal to $P_{Fe-Ga}$, and they all equal sputtering power ($P$).

Thus, $Q$ can be approximated as follows:

$$Q \approx \frac{(k_{Fe} A_{Fe} + k_{Fe\text{-}Ga} A_{Fe\text{-}Ga}) P t}{qH} = Q_{Fe} + Q_{Fe\text{-}Ga}. \tag{11}$$

In the experiment, iron content in the $Fe_{100-x}Ga_x$ films derives from two aspects. On the one hand, it is from pure iron slices. On the other hand, it comes from uncovered $Fe_{100-x}Ga_x$ targets. However, gallium content only stems from the $Fe_{100-x}Ga_x$ target. Thus, the relative contents of
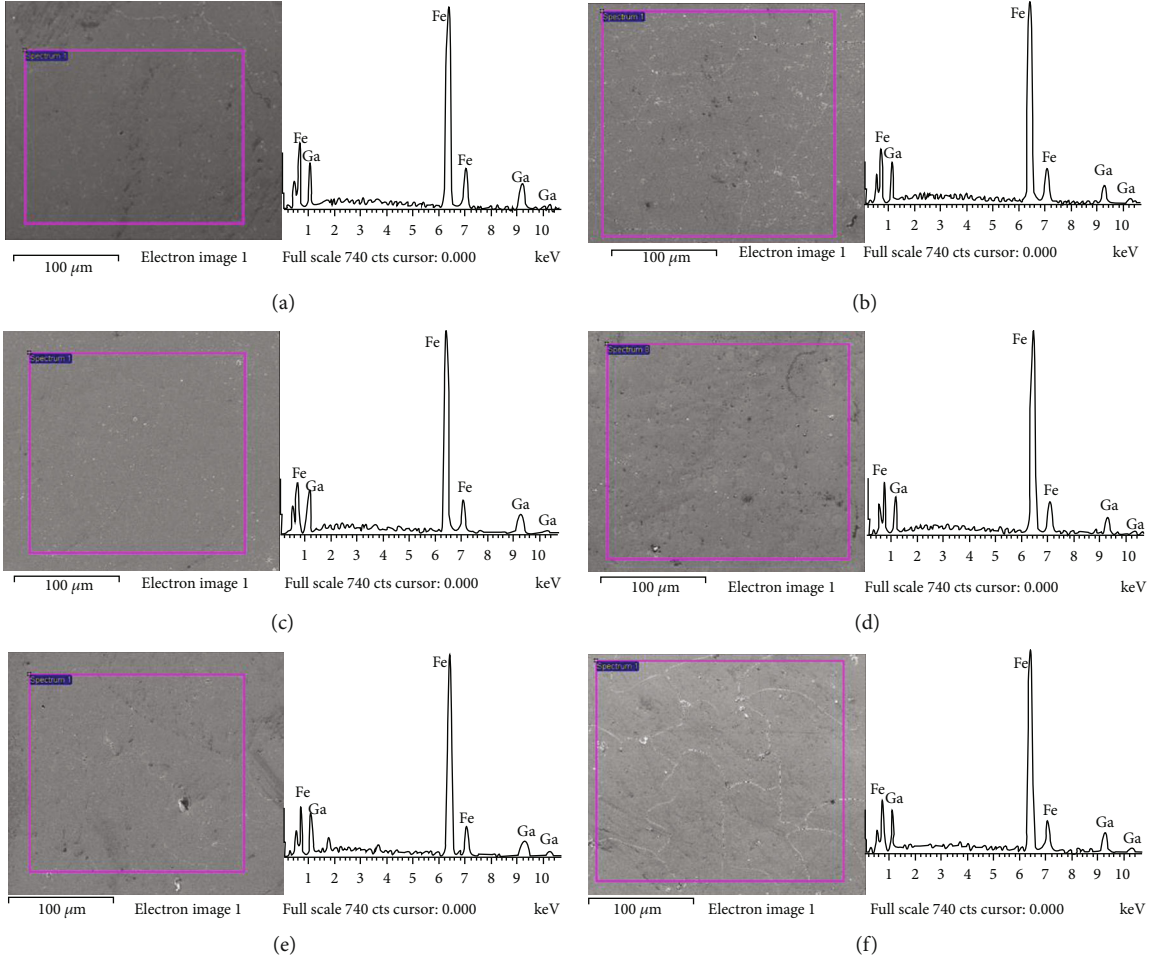
FIGURE 1: EDS results of as-deposited $Fe_{100-x}Ga_x$ films: $(a_1, a_2)$ $R = 0$, $(b_1, b_2)$ $R = 0.014$, $(c_1, c_2)$ $R = 0.028$, $(d_1, d_2)$ $R = 0.042$, $(e_1, e_2)$ $R = 0.056$, and $(f_1, f_2)$ $R = 0.070$.

iron and gallium of $Fe_{100-x}Ga_x$ films can be expressed as formula (12) and formula (13).

$$M_{Fe}\% = \frac{Q_{Fe} + Q_{Fe\text{-}Ga} \cdot m_{Fe}\%}{Q}, \quad (12)$$

$$M_{Ga}\% = \frac{Q_{Fe\text{-}Ga} \cdot m_{Ga}\%}{Q}, \quad (13)$$

where $m_{Fe}\%$ and $m_{Ga}\%$, respectively, mean iron and gallium content in the sputtered films from $Fe_{100-x}Ga_x$ targets uncovered with iron, and $M_{Fe}\%$ and $M_{Ga}\%$ separately represent the actual content of iron and gallium in the sputtered films.

Formulas (14) and (15) are given by means of substituting expression (11) into formulas (12) and (13).

$$M_{Fe}\% = \frac{k_{fe}A_{fe} + k_{fe\text{-}Ga}A_{fe\text{-}Ga} \cdot m_{Fe}\%}{k_{fe}A_{fe} + k_{fe\text{-}Ga}A_{fe\text{-}Ga}}, \quad (14)$$

$$M_{Ga}\% = \frac{k_{fe\text{-}Ga}A_{fe\text{-}Ga} \cdot m_{Ga}\%}{k_{fe}A_{fe} + k_{fe\text{-}Ga}A_{fe\text{-}Ga}}, \quad (15)$$

where $m_{Fe}\%$ and $m_{Ga}\%$ represent the content of iron and gallium in the pure $Fe_{100-x}Ga_x$ targets sputtering, separately.

On the basis of formulas (14) to (17), formulas (18) and (19) can be easily inferred.

$$A_{Fe\text{-}Ga} = A_{Target} - A_{Fe}, \quad (16)$$

$$R = \frac{A_{Fe}}{A_{Target}}, \quad (17)$$

$$M_{Fe}\% = \frac{k_{Fe}R + k_{Fe\text{-}Ga}(1 - R)m_{Fe}\%}{k_{Fe}R + k_{Fe\text{-}Ga}(1 - R)}, \quad (18)$$

$$M_{Ga}\% = \frac{k_{Fe\text{-}Ga}(1 - R)m_{Ga}\%}{k_{Fe}R + k_{Fe\text{-}Ga}(1 - R)}. \quad (19)$$

To calculate the correlation coefficients $k_{Fe}$ and $k_{Fe\text{-}Ga}$, experimental data measured by EDS can be applied to formulas (18) and (19). And then, the calculation values of iron content and gallium content can be calculated when different $R$ values were chosen. Conversely, we can use this formula to calculate the area ratio $R$ when we want to sputter a thin film of a certain composition and thus determine how many pieces of iron are needed.

TABLE 1: EDS results of as-deposited $Fe_{100-x}Ga_x$ films.

| Specimen no. | a | b | c | d | e | f |
|---|---|---|---|---|---|---|
| $R$, area ratio of iron slices to alloy targets | 0 | 0.014 | 0.028 | 0.042 | 0.056 | 0.070 |
| Fe content in films, at.100% | 83.25 | 83.61 | 84.35 | 84.58 | 84.95 | 85.48 |
| Ga content in films, at.100% | 16.75 | 16.39 | 15.65 | 15.42 | 15.05 | 14.52 |

This model can be used to implement the preparation of thin films with different compositions, accurately predict, and precisely tune the composition of thin films.

## 3. Results and Discussion

*3.1. EDS Analysis of $Fe_{100-x}Ga_x$ Films.* The thickness of $Fe_{100-x}Ga_x$ films was about $1\,\mu m$. Morphologies and EDS spectra of as-deposited $Fe_{100-x}Ga_x$ films are shown in Figure 1. The area ratio of iron slices and alloy targets was defined as $R$. The relationship between the ratio $R$ and the iron content and gallium content in $Fe_{100-x}Ga_x$ films is demonstrated in Table 1 and Figure 2. It can be observed that iron content in $Fe_{100-x}Ga_x$ films increases with increasing the value $R$ and approximately linearly related.

However, the experimental results show that the compositions of specimen no. (a) are not the same to the compositions of the target. When the film of specimen no. (a) was prepared by magnetron sputtering, pure iron patches were not attached to the Fe84Ga16 alloy target. Why is the content of iron in the film lower than that in the target?

The composition of the films depends on the sputtering rate of the atoms, and the sputtering rate depends on the threshold energy and the sputtering power of the target. The content of the elements with high sputtering rate is higher in the sputtering film. The sputtering rate of gallium is higher than that of iron, which results in this phenomenon.

The compositions of $Fe_{100-x}Ga_x$ films depend on the alloy target compositions when a single alloy sputtering targets is used for magnetron sputtering. Nevertheless, it relies on sputtering cases of every target when composite or mosaic targets were used for sputtering. It hinges on the area ratio between the slices and the target employing the slice-style mosaic target for sputtering.

This can be explained by the surface free energy theory. The iron atom has a radius of $1.24\,\text{Å}$, the outer electron 3d64s2.Ga has a radius of $1.4\,\text{Å}$, and the outer electron is 4s2p1. The iron atom's outermost electron, 4s2, is saturated and has a smaller radius than the gallium atom. As a result, the outermost electrons of gallium are more easily lost than those of Fe and require lower energy to ionize, so the excitation voltage is lower than that of Fe.

At the same time, since the surface binding energy of iron is higher than that of gallium and the binding force between the atoms is greater, the kinetic energy of iron atoms or clusters from the surface of iron target to be sprayed by ionized gas ions is higher than that of gallium target; that is, a higher discharge voltage is required. Therefore, the discharge voltage of magnetron sputtering and the surface binding energy (Es) of target increase. The greater
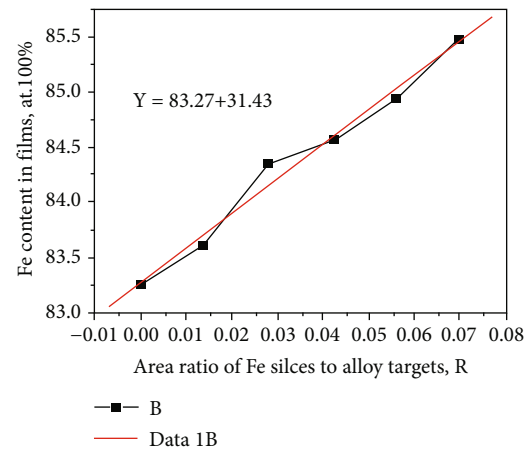


FIGURE 2: The relationship between the area ratio $R$ and content of iron element in $Fe_{100-x}Ga_x$ films.
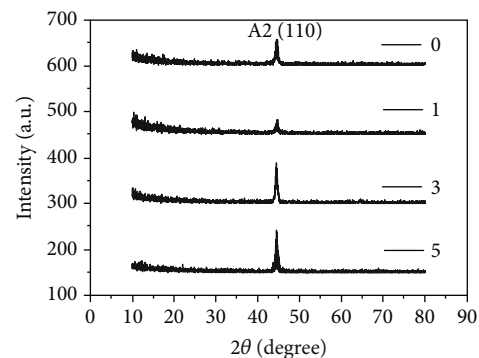


FIGURE 3: X-ray diffraction patterns of as-deposited $Fe_{100-x}Ga_x$ films.

the sputtering yield of an element, the higher the content of the element in the film.

*3.2. XRD Analysis of Fe-Ga Alloy Films.* Figure 3 shows XRD patterns of $Fe_{100-x}Ga_x$ films. The results show that there are <1 1 0> texture in magnetron sputtered $Fe_{100-x}Ga_x$ films. The sharp peak attributed to the $A_2$ microstructure suggests that the film is crystalline. However, the XRD peak of $A_2$ in $Fe_{100-x}Ga_x$ films is weak.

The experimental conditions are the incident light intensity, the sample area, the counting time per step, the opening size of the detector end, etc. When the experimental conditions are the same, the volume percent content of a phase in the sample is related to the intensity of its diffraction peak. Under the conditions determined by the Absorption Lorentz factor and the temperature factor, the content of a phase in the sample is directly proportional to the intensity of its

(a)

(b)

(c)

(d)

(e)

(f)
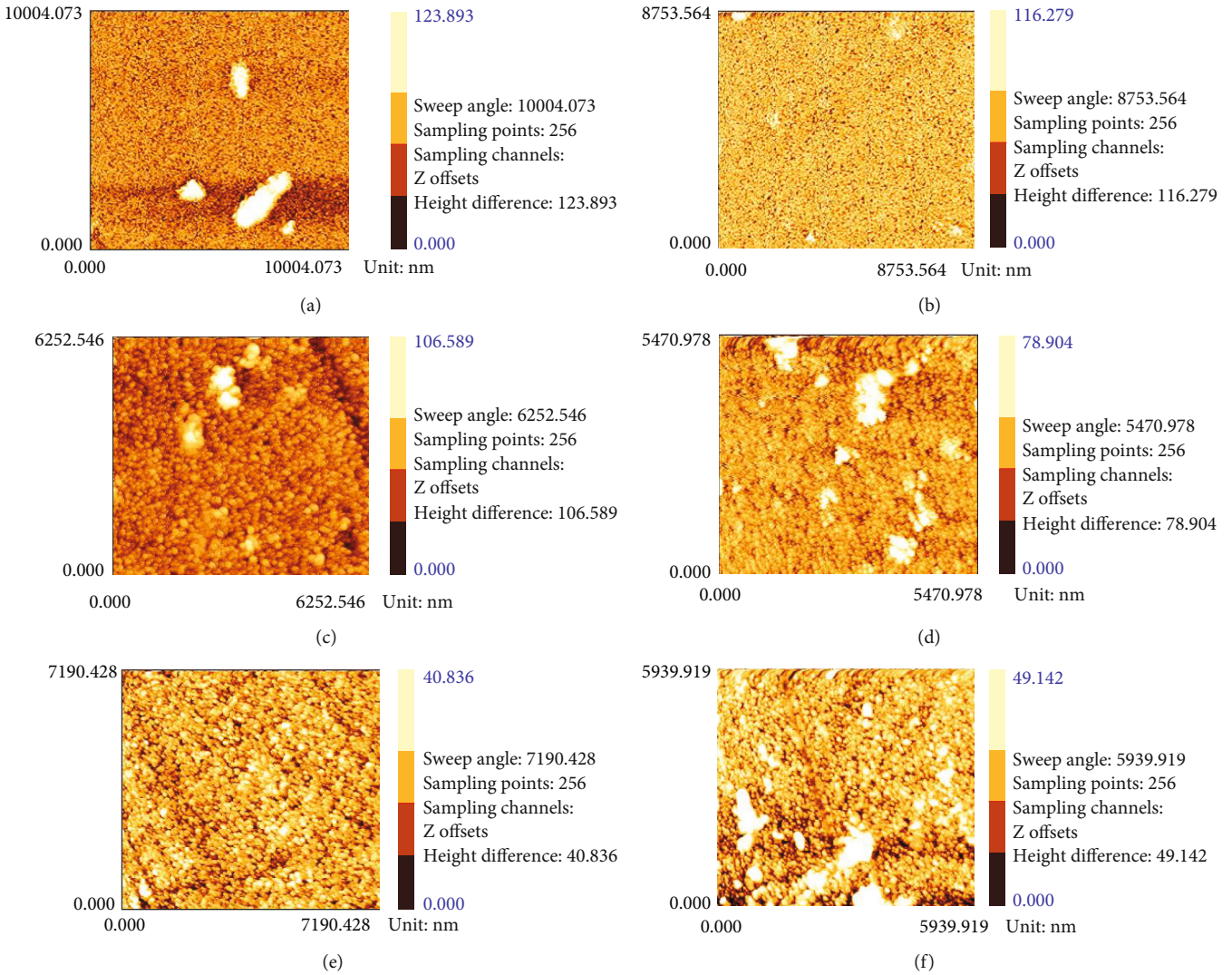
FIGURE 4: Domain structure of $Fe_{100-x}Ga_x$ films.

diffraction peak. In addition, the degree of crystal development and the preferred orientation of crystal plane also affect the intensity of characteristic diffraction peak.

Under the experimental conditions, there is only one $A_2$ (110) strong diffraction peak in Figure 3, which indicates that the sample has preferred orientation; all films are in polycrystalline form with <1 1 0>crystallographic texture perpendicular to the film plane.

The diffraction peak intensity was related to the film microstructure. In order to obtain fine grain and microstructure, the thin films were prepared by low sputtering energy, multiple sputtering, and 5 minutes interval. Therefore, the substrate temperature will not be too high. Then, the crystallization process can not be completed because of the weak diffusion ability of atoms.

Under this experimental condition, mixed structures, including crystalline and amorphous structures, will be formed. Most of the stress in the alloy film can be removed if heat treatment is carried out in the subsequent process. Driven by temperature gradient and residual stress, the

atoms in the films may migrate and segregate. When the annealing temperature reaches a certain critical value, the atoms in the film will be formed with large area arranged in order.

In general, a variety of phase structures, such as $A_2$ structure and $DO_3$ structure, may be formed during the preparation of $Fe_{100-x}Ga_x$ films. However, there is no obvious evidence of $DO_3$ phase formation from the abovementioned testing process. It has been reported in the literature that the formation of $DO_3$ phase depends mainly on the thickness of the film [14, 24]. The reason why the $DO_3$ phase was not found in the study may be that the peak value was too weak to be detected. Kumagai reported that when the content of gallium in Fe-Ga alloy varies from 15% to 30%, the $A_2$, $DO_3$, $L1_2$, $B_2$, and $DO_{19}$ phase structures appear under different preparation conditions [25]. At room temperature, when gallium content in Fe-Ga alloy exceeds its solubility, gallium atoms will exist in the form of clusters, while the main body of Fe-Ga material still retains the Bcc phase of alpha iron; the BCC phase gradually changed to $DO_3$ phase,

(a)

(b)

(c)

(d)

(e)

(f)
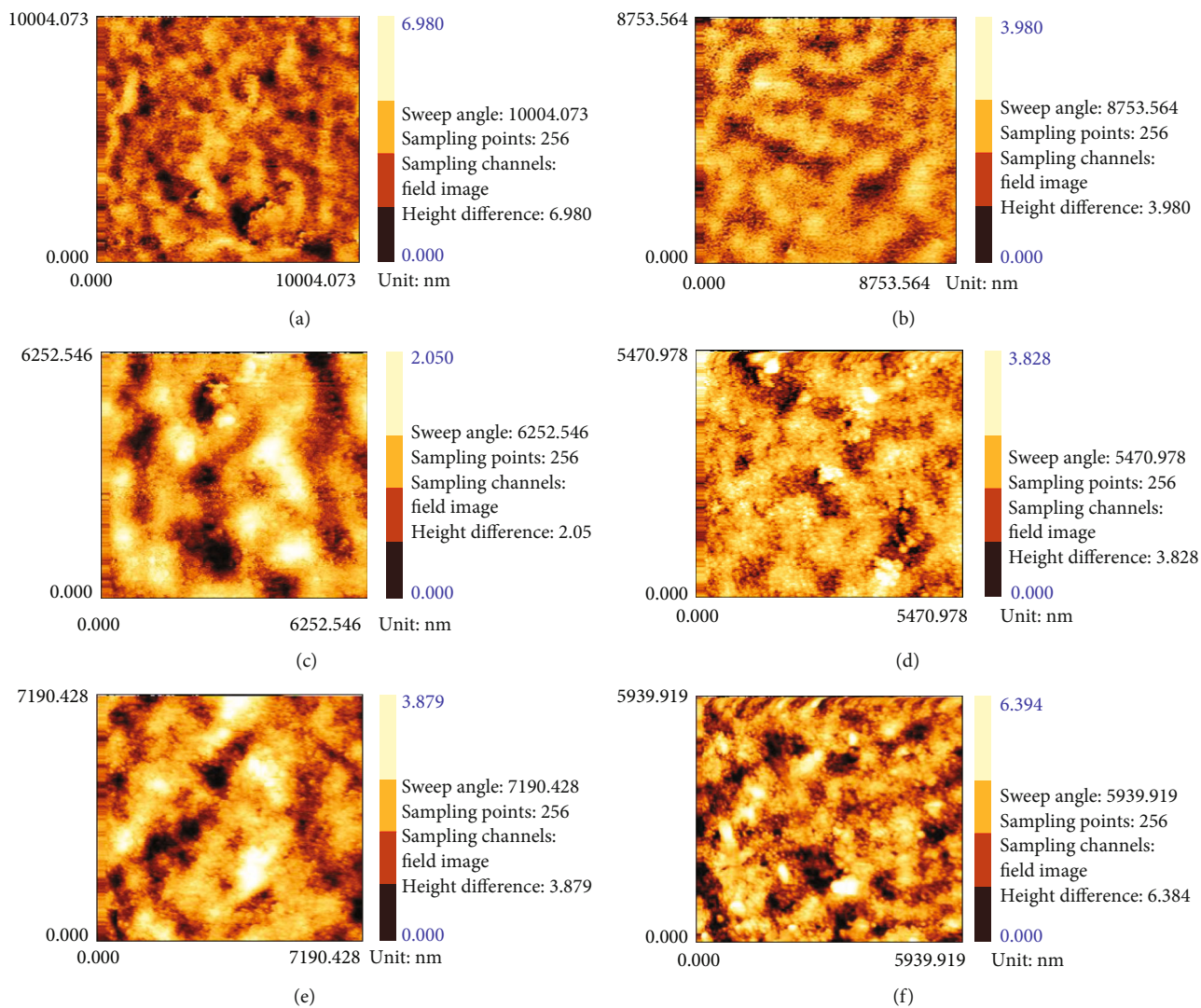
FIGURE 5: AFM image of $Fe_{100-x}Ga_x$ films.
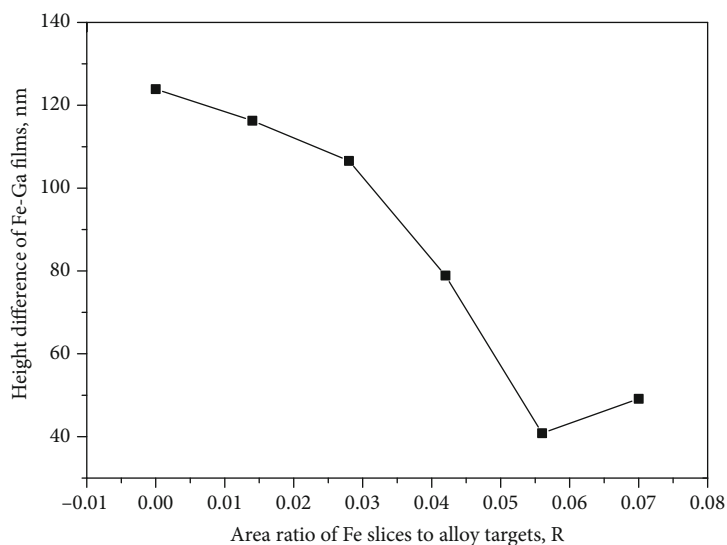


FIGURE 6: Height difference of the $Fe_{100-x}Ga_x$ films.

s = 0_005
Cal: 0.010269 nm/pix
17:32:25 3/21/2014
TEM mode: Imaging

1 nm
HV = 200.0 kV
Direct mag: 1000000 x
AMT camera system

Camera:, exposure (ms): 300 X 1 Gain: 8, Bin: 1
Gamma: 1.05, No Sharpening, normal contrast

s = 0_002
17:17:59 3/21/2014
TEM mode: Diffraction

0.2 (1/A)
HV = 200.0 kV
Cam len: 0.3000 m
AMT camera system

Camera:, Exposure (ms): 300 X 1 Gain: 8, Bin: 1
Gamma: 0.70, No Sharpening, normal contrast

(a)

88_008
Cal: 0.016574 nm/pix
18:44:26 3/21/2014
TEM mode: Imaging

5 nm
HV = 200.0 kV
Direct mag: 600000 x
AMT camera system

Camera:, exposure (ms): 300 X 1 Gain: 8, Bin: 1
Gamma: 1.00, No Sharpening, normal contrast

88_002
18:20:26 3/21/2014
TEM mode: diffraction

0.2 (1/A)
HV = 200.0 kV
Cam len: 0.3000 m
AMT camera system

Camera:, Exposure (ms): 300 X 1 Gain: 2, Bin: 1
Gamma: 0.55, No Sharpening, normal contrast

(b)

FIGURE 7: TEM image and TEM diffraction image of as-deposited Fe-Ga alloy films: (a) $R = 0$; (b) $R = 0.07$.

which was unfavorable to increase the magnetostrictive coefficient [26].

Under the experimental conditions in this paper, the gallium content in $Fe_{100-x}Ga_x$ films varies from 14.52 to 16.75, and the sputtering temperature is enough low; therefore, no $DO_3$ phase appears.

### 3.3. Domain Structure and Microstructures of Fe-Ga Films.
Figure 4 shows that the domain structure was network form, and the domain width of $Fe_{100-x}Ga_x$ films was varied. The magnetic properties of $Fe_{100-x}Ga_x$ films are usually tested by the domain microstructure, and the domain width is an important variable of the domain microstructure.

In Figure 4, the black and white regions are caused by the attractive and repulsive forces between the sample and the magnetic probe. A network form with different resolution and contrast of domain microstructure can be observed.

Additionally, it can be found that the domain width decreases with the decrease of gallium content. The major influence factor is compositions of $Fe_{100-x}Ga_x$ films. The different of compositions leads to different lattice constants of $Fe_{100-x}Ga_x$ films and then the different lattice constant causes
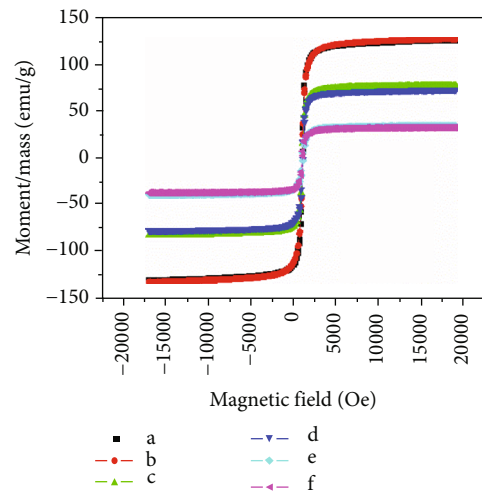


FIGURE 8: In-plane magnetization vs. magnetic field of $Fe_{100-x}Ga_x$ films with different iron contents.

of different domain widths and different magnetic domain microstructures, thus affecting the magnetostriction properties of $Fe_{100-x}Ga_x$ films.

TABLE 2: Magnetic results of as-deposited $Fe_{100-x}Ga_x$ films.

| Specimen no. | a | b | c | d | e | f |
|---|---|---|---|---|---|---|
| Coercivity (Hci), Oe | 45.112 | 51.864 | 53.684 | 55.116 | 54.977 | 53.831 |
| Magnetization (Ms), emu/g | 127.47 | 129.13 | 79.740 | 74.914 | 36.613 | 34.696 |

It is also found that the magnetic domains become more and more irregular with the decrease of gallium content, which indicates that the magnetic domains of the films are not uniform.

The signal detected by the instrument is the magnitude of the magnetic gradient component in the vertical direction of the membrane surface. When the cantilever oscillates near the surface with its resonance frequency, the resonance frequency of the cantilever will change with the force gradient of the surface in the range of $1 \sim 50$ Hz. The instrument used in the experiment detects the change of resonance frequency by means of phase measurement and obtains the distribution of surface force gradient.

As shown in Figure 4, the range of the pin-point phase angle values is shown on the right side of the figure and the corresponding contrast between light and dark in the image. Since MFM can only detect the magnetic gradient component in the vertical direction, the following definitions are made for the different contrasts in the magnetic image: the brighter regions represent the same direction of magnetic moment and the same direction of needle magnetization, which is the positive direction. The darker regions represent the negative direction of the magnetic moment, which is opposite to that of the tip.

Since the magnetic moment has a certain intensity and direction, the contrast of the magnetic force image is related not only to the magnetization but also to the direction of the magnetic moment. In conclusion, the larger the range of phase angle, the larger the detectable magnetic gradient range, the higher the sensitivity of the tip.

Figure 5 shows height difference of the film surface. The height difference increases with increasing iron content in $Fe_{100-x}Ga_x$ films.

Figure 6 shows the variation of height difference with the ratio of the pure iron slice areas to alloy target areas. It can be observed that the surface height difference of the $Fe_{100-x}Ga_x$ films decreases with increasing the value $R$.

The microstructure TEM images and diffraction image of $Fe_{100-x}Ga_x$ films are shown in Figure 7. There are some strip patterns in the films. Diffraction rings corresponding to polycrystalline appear, so the microstructure of film is crystal structure. However, diffraction rings of specimen no. (f) which iron content is high are not continuous and present a series of rings of dots.

The different diffraction patterns of sample $A$ and sample $F$ are caused by the different compositions in the films. Sample $A$ was sputtered by using an $Fe_{84}Ga_{16}$ target. The film is composed of polycrystalline Fe-Ga alloy grains and a small amount of amorphous Fe-Ga alloy particles. There is no extinction phenomenon during diffraction.

On the contrary, the sample $F$ sputtered films from $Fe_{84}Ga_{16}$ targets covered with Fe slices. The sputtering prod-

ucts have both $Fe_{84}Ga_{16}$ grains and pure iron grains. Due to the lower substrate temperature, the faster sputtering deposition rate, the slower diffusion of iron; not all iron dissolved into Fe-Ga alloy; the films are mainly composed of Fe-Ga alloy grains and a small amount of Fe grains.

Although Fe-Ga alloy grains and pure iron grains are both BCC ($A_2$), the lattice constants are different, and the diffraction ring is discontinuous because of the structure extinction.

*3.4. Magnetization and Coercivity.* Magnetization and coercivity results of $Fe_{100-x}Ga_x$ films are shown in Figure 8 and Table 2. The $Fe_{100-x}Ga_x$ films are ferromagnetic. The films with high iron content display large coercivity. The coercivity for the film of specimen no. (a) is 45.112 Oe; it is the minimum value.

It can be explain as follows: there are two factors influence on the coercivity results of $Fe_{100-x}Ga_x$ films, grain size, and film roughness, respectively [5]. Grain sizes are fine in the lower iron content films. The large interface regions can act as pinning centers for domain wall movement. On the other hand, as shown in Figure 5, the film roughness increases with decreasing of iron content. Finally, the coercivity decreases with decreasing iron content.

The larger the coercive force and saturation magnetization, the larger the magnetic loss. According to this principle, if we want to develop magnetostrictive microdevices, we need to prepare thin films with small coercivity.

# 4. Conclusions

We can conclude that compositions are the key factor that affects alloy phases, grain sizes, film surface roughness, and magnetic domains of the magnetron sputtered $Fe_{100-x}Ga_x$ films. Changing the ratio of the pure iron slice areas to alloy target areas, the desired film composition can be achieved by the improved Mosaic method. The desired film composition was achieved by changing the ratio of the pure iron slice areas to alloy target areas (i.e., the area ratio, $R$). EDS results of iron content in films are 83.25, 83.61, 84.35, 84.58, 84.95, and 85.58, separately.

The morphologies, magnetic domain structure, microstructure, and compositions of $Fe_{100-x}Ga_x$ films revealed by SEM-EDS, XRD, MFM, VSM, and TEM. The results show that there are $<1\,1\,0>$ texture in magnetron sputtered $Fe_{100-x}Ga_x$ films. The sharp peak attributed to the $A_2$ microstructure suggests that the film is crystalline.

The magnetic domain structure of $Fe_{100-x}Ga_x$ films presents a network form, and the domain width decreases with the decrease of gallium content. It is also found that the magnetic domains of the films are not uniform.

The TEM result shows that there are some strip patterns in the films. Diffraction rings corresponding to polycrystalline appear, so the film microstructure is crystal structure. However, diffraction rings of specimen no. (f) which iron content is high are discontinuous because of the structure extinction and present a series of rings of dots.

For a suitable candidate of microdevice applications in MEMS, the optimum composition film should be $Fe_{83.25}Ga_{16.75}$ film.

## Data Availability

The data used to support the findings of this study are available from the corresponding author upon request.

## Conflicts of Interest

There are no conflicts of interest to disclose for the publication of this paper.

## Acknowledgments

## References

[1] C. Wenzel, B. Adolphi, U. Merkel et al., "Resonant bending sensor based on sputtered Galfenol," *Sensors and Actuators A*, vol. 156, no. 1, pp. 129–133, 2009.

[2] J. W. Yan, J. Pan, and C. S. Zhang, "An overview of magnetostriction Fe-Ga alloy thin films," *Materials Review Supplement*, vol. 1, no. 1, pp. 108–110, 2013.

[3] T. Ueno, E. Summers, M. Wun-Fogle, and T. Higuchi, "Micro-magnetostrictive vibrator using iron-gallium alloy," *Sensor and Actuators A: Physical*, vol. 148, no. 1, pp. 280–284, 2008.

[4] A. Javed, N. A. Morley, and M. R. J. Gibbs, "Structure, magnetic and magnetostrictive properties of as-deposited Fe-Ga thin films," *Journal of Magnetism and Magnetic Materials*, vol. 321, no. 18, pp. 2877–2882, 2009.

[5] H. Basumatary, J. A. Chelvane, D. V. S. Rao, S. V. Kamat, and R. Ranjan, "Influence of substrate temperature on structure, microstructure and magnetic properties of sputtered Fe-Ga thin films," *Journal of Magnetism and Magnetic Materials*, vol. 384, no. 1, pp. 58–63, 2015.

[6] A. Butera, J. Gómez, J. A. Barnard, and J. L. Weston, "Magnetic anisotropy in $Fe_{81}Ga_{19}$/MgO (1 0 0) films sputtered at different powers," *Physica B: Condensed Matter*, vol. 384, no. 1-2, pp. 262–264, 2006.

[7] D. Seguin, M. Sunder, L. Krishna, A. Tatarenko, and P. D. Moran, "Growth and characterization of epitaxial $Fe_{0.8}Ga_{0.2}$/0.69PMN-0.31PT heterostructures," *Journal of Crystal Growth*, vol. 311, no. 12, pp. 3235–3238, 2009.

[8] T. L. Wang, S. S. Feng, and Y. P. Li, "Microstructure and magnetic properties of Fe-Ga thin films," *Rare Metal Materials and Engineering*, vol. 46, no. 2, pp. 406–410, 2017.

[9] A. Niesen, C. Sterwerf, M. Glas, J. M. Schmalhorst, and G. Reiss, "Structural and magnetic properties of sputter-deposited Mn-Fe-Ga thin films," *IEEE Transactions on Magnetics*, vol. 52, no. 7, pp. 1–4, 2016.

[10] J. W. Yan and J. C. Zhou, "Elemental diffusion in Ni-Cr thin films fabricated by double-targets magnetron sputtering," *International Journal of Modern Physics: B*, vol. 21, no. 12, pp. 1981–1996, 2007.

[11] J. W. Yan and J. C. Zhou, "Optimising of strain sensitivity and electric characteristics of Ni-Cr thin film fabricated by magnetron sputtering," *Journal of Material Science & Technology*, vol. 23, no. 2, pp. 195–202, 2007.

[12] D. A. Golosov, S. N. Melnikov, and A. P. Dostanko, "Calculation of the elemental composition of thin films deposited by magnetron sputtering of mosaic targets," *Surface Engineering and Applied Electrochemistry*, vol. 48, no. 1, pp. 52–59, 2012.

[13] J. Yan, R. Zhao, Y. Cha, and Q. Li, "Investigation on microstructures and phases of Fe-Ga alloy films deposited by magnetron sputtering," *International Journal of Nano and Biomaterials*, vol. 9, no. 1/2, p. 95, 2020.

[14] A. Javed, T. Szumiata, N. A. Morley, and M. R. J. Gibbs, "An investigation of the effect of structural order on magnetostriction and magnetic behavior of Fe-Ga alloy thin films," *Acta Materialia*, vol. 58, no. 11, pp. 4003–4011, 2010.

[15] H. LIU, H.-o. WANG, M.-x. CAO et al., "Magnetostriction and microstructure of melt-spun $Fe_{77}Ga_{23}$ ribbons prepared with different wheel velocities," *Transactions on Nonferrous Metal Society of China*, vol. 25, no. 1, pp. 122–128, 2015.

[16] F. Yang, W. D. Fei, and J. Q. Jiang, "Applications of X-ray diffraction technique in the residual stress measurement of films," *Journal of Functional Materials*, vol. 43, no. 11, pp. 1749–1752, 2007.

[17] J.-C. Shih, T.-S. Chin, Z.-G. Sun, H.-W. Zhang, and B.-G. Shen, "Domain structure of TbFe magnetostrictive films by MFM," *IEEE Transactions on Magnetics*, vol. 37, no. 4, pp. 2681–2683, 2001.

[18] H. Z. Song, Y. X. Li, J. T. Zeng, G. R. Li, and Q. R. Yin, "Observation of magnetic domain structure in Terfenol-D by scanning electron acoustic microscopy," *Journal of Magnetism and Magnetic Materials*, vol. 320, no. 6, pp. 978–982, 2008.

[19] Z. G. Sun, H. Kuramochi, M. Mizuguchi, F. Takano, Y. Semba, and H. Akinaga, "Magnetic properties and domain structures of FeSiB thin films prepared by RF- sputtering method," *Journal of Magnetism and Magnetic Materials*, vol. 272-276, pp. 1160-1161, 2004.

[20] Z. Tang, G. Zhao, and T. Ouyang, "Two-phase deep learning model for short-term wind direction forecasting," *Renewable Energy*, vol. 173, no. 72, pp. 1005–1016, 2021.

[21] X. Xu, C. Zhang, H. A. Derazkola, M. Demiral, A. M. Zain, and A. Khan, "UFSW tool pin profile effects on properties of aluminium-steel joint," *Vacuum*, vol. 192, p. 110460, 2021.

[22] X. L. Xu, C. W. Zhang, and H. A. Derazkola, "Dispersion of waves characteristics of laminated composite nanoplate," *Steel and Composite Structures*, vol. 40, no. 3, pp. 355–367, 2021.

[23] J. W. Yan, Y. P. Cha, and Q. P. LI, "The composition analysis and prediction of Fe-Ga alloy films deposited by magnetron sputtering," in *3rd International Conference on Applied*

*Mechanics and Mechanical Automation*, Phuket, Thailand, 2017.

[24] A. Javed, N. A. Morley, T. Szumiata, and M. R. J. Gibbs, "A comparative study of the microstructural and magnetic properties of textured thin polycrystalline Fe100−xGax ($10 \leq x \leq 35$) films," *Applied Surface Science*, vol. 257, no. 14, pp. 5977–5983, 2011.

[25] R. Q. Wu, "Origin of large magnetostriction in FeGa alloys," *Journal of Applied Physics*, vol. 91, no. 10, pp. 7358–7363, 2002.

[26] A. E. Clark, K. B. Hathaway, M. Wun-Fogle et al., "Extraordinary magnetoelasticity and lattice softening in bcc Fe-Ga alloys," *Journal of Applied Physics*, vol. 93, no. 10, pp. 8621–8623, 2003.

*Research Article*

# CAx Integration and Its Design Application Based on Feature Extension of Sensor Components

**Yaohong Tang** [ID],[1,2] **Mengmeng Song** [ID],[1,2] **Shungen Xiao** [ID],[1,2] **Xiangui Liu** [ID],[3] **and Guoxiang Liang** [ID][1]

[1]*School of Information and Mechanical & Electrical Engineering, Ningde Normal University, Ningde 352000, China*
[2]*New Energy Automobile Motor Industry Technology Development Base, Ningde Normal University, Ningde 352000, China*
[3]*School of Mechanical and Automotive Engineering, Xiamen University of Technology, Xiamen 361024, China*

Correspondence should be addressed to Yaohong Tang; 264572049@qq.com

In order to improve the information and product originality level of intelligent manufacturing industry based on sensor technology, this paper summarizes the current situation of CAx integration based on sensor technology and its design application and analyzes the shortcomings of existing CAx integration, aiming at accurate, complete, timely, and barrier-free transfer of sensor product data and information between CAx system and MRPII/ERP management information system. The concept and information model of feature extension of sensor components oriented to the whole process of sensor intelligent manufacturing is presented. Taking feature extension of sensor components as the integration link, CAx integration framework structure and its design application mode based on feature extension are established, while key technologies and implementation ideas to realize the integration and the design application are put forward, which provides an effective path to realize the sensor integration of CAx and management information systems such as MRPII/ERP.

## 1. Introduction

Sensor technology is one of the rapidly developing high and new technologies in today's world. It is also an important symbol of the development of contemporary science. Together with communication technology and computer technology, sensor technology forms the three pillars of information industry in the 21st century. If a computer is an extension of the human brain, then sensors are an extension of the human features. Therefore, each developed country regards sensor technology as the key technology of this century to try to develop. The application of sensors is also more and more extensive and has penetrated into various professional fields. However, the innovation of sensor technology and the ability of new product development are lagging behind the advanced level at home and abroad, which restricts the development of industrial automation and information technology.

The computer integrated manufacturing system (CIMS) based on sensor technology is a crucial technology for the informatization of manufacturing industry. CIMS requires fast, lossless, and distortionless communication of product information between computer aided X (CAx) systems and management systems such as manufacturing resource planning (MRPII) and enterprise resource planning (ERP). CAx integration technologies have been studied by researchers for decades, and commercial softwares such as Solidworks and Pro-E, which are typical computer aided design or computer aided manufacturing (CAD/CAM) integration, have been widely used in several industries. Fruitful research results oriented towards enterprises APPs have been achieved in unified platform integration technology for multisystem and cross-system. However, limitations still exist in these technologies, and integration requirements cannot be fully fulfilled.

The most concerning issue for the application of CAx system integration based on sensor technology is the

unblocked connection between CAD and other CAx systems [1–3]. Researchers have been made great effort on dealing with this issue, and several integration framework models have been proposed in different cases. CAD system and PDM system integration mode are studied [4]. 3D CAD software SolidWorks 2010 and the small PDM system are designed. CAD, CAPP, and CAM integrated system framework based on PDM is proposed, and the customization content and implementation technology involved in the implementation of the framework are researched in depth [5]. CAx systems are integrated with PDM system by adopting message-driven Hub Spoke integrated mode [6]. A new framework for the design of a CAx information management and integrated system (CAx-IMIS) based on product data management (PDM) techniques and STEP integration technologies is proposed [7]. Seamless integration of CAD/CAE was achieved, and the quality and efficiency of the shell nosing design were improved [8]. A knowledge-based integration system framework for mechanical product development is obtained [9]. The workflow of virtual modeling and simulation of CAx system is presented, and the design of new bicycle plastic bottle is introduced [10]. The future development and concept for CAx system structure affecting the auto companies and their suppliers are presented [11]. Researchers combined CAD, CAM, and computer-aided process planning (CAPP) with computer software on the product data management (PDM) platform, using the unified control program to realize the extraction, exchange, sharing, and manipulation of the information. This can guarantee not only unblocked information flow within the systems but also effective operation of the systems, thus, realizing the CAx integration goal [12]. Klocke et al. [13] proposed a method of extended function blocks to reduce data loss within adaptive process chains by introducing data port list, which realized the integration of CAx systems. Li et al. [14] presented a digital collaborative design model and investigated product design process integration technology based on Webservice. A new concept of closed-loop manufacturing process from numerical control machine to CAD/CAM systems based on STEP-NC was put forward [15].

To realize information integration in CAD/CAM, they introduced feature recognition technology in CAM programming and established the interaction of data management, manufacturing process management, and enterprise resource planning. Moreover, Ni et al. [16] proposed a heterogeneous system integration framework oriented to enterprise business cooperation and analyzed the key technologies related to the framework, such as ontology modeling, ontology mapping, and semantic interoperability mechanism, which provides a new architecture and method for business cooperation based heterogeneous system integration. A feature technology-based CAx integration system was presented [17–19]. The system realized the integration of subsystems CAD, CAM, and CAPP through the STEP interface and is adapted to product design and process planning of CAD system with different formats. Some researchers also studied ERP/CAx integration based on CORBA, COM/COM+, and JavaRMI component technology and PDM/CAx integration based on ontology/PLM, aiming to realize the connection between CAx and enterprise resource management systems, and support cooperative design.

Since the end of 1990s, the application of CAx integration has been focusing on enterprise APPs and enterprise knowledge. As a result, the integration application of CAx has gradually developed from the separate application of each unit technology system to the local connection of multiple CAx systems and finally to realize the overall integration [20–22]. In addition, deep learning platforms [23], dynamic system [24, 25], and fault diagnosis field [26] may be utilized for the design analysis of sensor parts and integration in engineering. From the previous work, it can be concluded that the existing CAx integration technologies mainly focus on STEP-based, PDM-based, and feature-based integration.

Nevertheless, there are still a lot of challenges in establishing the enterprise manufacturing integration system based on CAD/CAM/CAPP to meet the requirements of industrial informalization. First, STEP-based integration pattern use the neutral file to provide CAx systems with a "intermediate transformation" or "intermediate interface," which results in the loss of CAD design intention and cannot fully satisfy the integration requirements. Second, PDM-based integration technology only provides a platform for centralized management of product data. When data and information are transmitted between CAx systems through PDM platform, the intrinsic properties of the CAx single system expression will be lost and the integration requirement cannot be fully satisfied. Furthermore, even though the feature-based integration technology can solve the problem of the information exchange and sharing between CAx systems, this is confined within the CAx. Information exchange among subsystems as CAD, CAM, CAPP, and CAFD have to be supported by feature recognition and feature mapping technology. Therefore, the seamless integration of CAx system and management information systems such as CAQ and MRPII/ERP cannot be achieved. Meanwhile, the existing features are intrinsically CAD-based 3D geometries which do not contain the information including manufacturing features, fixture features, quality features, and resource features, thus, limiting the practical application of integration systems.

Focusing on the above limitations, this paper has investigated a feature extension technology and its information model thoroughly. Besides, a CAx integration framework based on information extension is established, and key technologies to achieve seamless integration are studied. This work can promote the development of CAx system towards the direction of high integration, networking, virtualization, and intelligence.

## 2. Principle of Feature Extension of Sensor Components and Its Information Modeling

General speaking, a feature should be with the multidomain property which includes the design, manufacture, quality, and the resource domain. This property makes the feature a complete knowledge for engineering applications, independent from a specific engineering system. The main idea

of the proposed feature extension is to construct a novel type of feature which has merits of independence, completeness, reusability, and revisability. Such type of feature can guarantee the integration of CAx and meet the requirement of feature's property mentioned above.

In the next pages of this section, the principles and the information modeling of the proposed feature extension method will be introduced in detail.

### 2.1. Definition and Expression of the Feature Extension of Sensor Components.

The feature extension is a geometrical unit which is adaptive to products'/components' lifetime and includes the complete information of products or components. The complete information (of design, manufacturing, clamping, quality, resource, and management) and its corresponding features are packaged in the feature extension. This property makes the proposed feature extension accessible for different application systems to obtain desired information.

According to the basic concept illustrated above, the feature extension can be expressed as a set of a series of features:

$$F = \{F_D, F_M, F_F, F_Q, F_E\}, \tag{1}$$

where $F$ is the feature extension (i.e., the unit geometrical entity); $F_D$ is the design features set in which all design information of $F$ is packaged, including feature ID, feature name, materials and thermal processing information, technical requirement, and geometrical topology; $F_M$ is the manufacturing feature of $F$, which is packaged with information concerning manufacturing details, such as manufacturing technologies, tools information, and manufacturing equipment; $F_F$ is the fixture features package of $F$, where assembling information including orientation, clamping, and guiding; $F_Q$ is packaged with the quality features of $F$, which is consisted of detection planning, detection standard, and detection method, etc.; $F_E$ is the resource and management feature set where the resource and management information (resource planning, logistics, delivery schedule, etc.) of $F$ is packaged.

The next, construction of the five features sets will be illustrated in detail.

#### 2.1.1. Expression of $F_D$: A Matrix.

The proposed feature extension requires the feasibility of interior features' labeling and matching. To meet such requirement and to make the expression more reasonable for the design features, the design features set $F_D$ can be designed as follows:

$$F_D = [\mathbf{f}_{ID}, \mathbf{f}_{NM}, \mathbf{f}_{GM}, \mathbf{f}_{SZ}, \mathbf{f}_{DV}, \mathbf{f}_{MR}, \mathbf{f}_{THM}]^T, \tag{2}$$

where each $f_X$ in $F_D$ is a column vector with $N$ elements, corresponding to $N$ samples of the feature extension. Among those, $f_{ID}$ is the label vector indicating the unique identification of the $N$ samples; $f_{NM}$ is the name vector storing the names of the $N$ samples; $f_{GM}$ is the geometrical vector, presenting the geometry entity of the $N$ samples; $f_{SZ}$ stores the geometrical size and tolerance of the feature extension; $f_{MR}$ and $f_{THM}$ are used to store the materials and thermal processing methods, respectively, of the $N$ samples.

It can be concluded from the above statement that the design feature $F_D$ has a form of matrix; each column of $F_D$ indicates the design feature of a certain feature extension.

#### 2.1.2. Construction of $F_M$: Tree-Structured Data.

The manufacturing feature $F_M$ is supposed to be extracted from design feature $F_D$, which acts as supplement (technical details) of relevant features packaged in $F_D$. Considering the constitution of manufacturing knowledge, the $F_M$ can be designed as tree-structured data, functioning as the core structure and information.

Based on the above analysis, the $F_M$ is designed as is shown in Figure 1.

#### 2.1.3. Expression of $F_F$: A Logical Rule Based on Relevance.

To comprehensively describe the fixture feature, $F_F$ is much easier that other features set since the $F_F$ can be treated as inheritance from $F_M$. Therefore, the $F_F$ packaged in a feature extension can be designed as a logical variable that indicates whether the feature extension is an $F_F$ or not, expressed as:

$$F_F = [0, 1]. \tag{3}$$

#### 2.1.4. Structure Design of $F_Q$.

The quality features set $F_Q$ includes the products' or the components' quality planning, quality strategy, detecting method, and detecting planning, etc. Those are tightly related to the $F_D$ and $F_M$. All necessary information must be included in the $F_Q$ so that the CAQ can access required message. Thus, the $F_Q$ can be structured into the one presented in Figure 2.

#### 2.1.5. Packaging of Resource and Management Feature Structure Design of $F_E$.

The resource and management features that set $F_E$ are usually determined by $F_D$ and $F_M$ which are tightly relevant to enterprises' management strategies. Therefore, a certain requirement (of a company) for resource management should be packaged in the feature extension. Following this concept, the packaging of the resource and management features can be designed including not only manufacturing but also management details, as is shown in Figure 3.

### 2.2. The Information Model of the Feature Extension of Sensor Components.

The feature extension proposed as (1) is to improve the design quality in manufacturing and to optimize the management operation of companies. More specifically, a feature extension is an improved type of feature set inherited from its original features. A feature extension extends the concept of "feature" by adding new properties (e.g., quality, fixture, and resource) into traditional features set. That means the core of a feature extension is a geometry entity in which all properties required by CAx and MRPII/ERP systems are packaged.

Following the discussion above, the information model of the proposed feature extension can be presented as Figures 4 and 5.
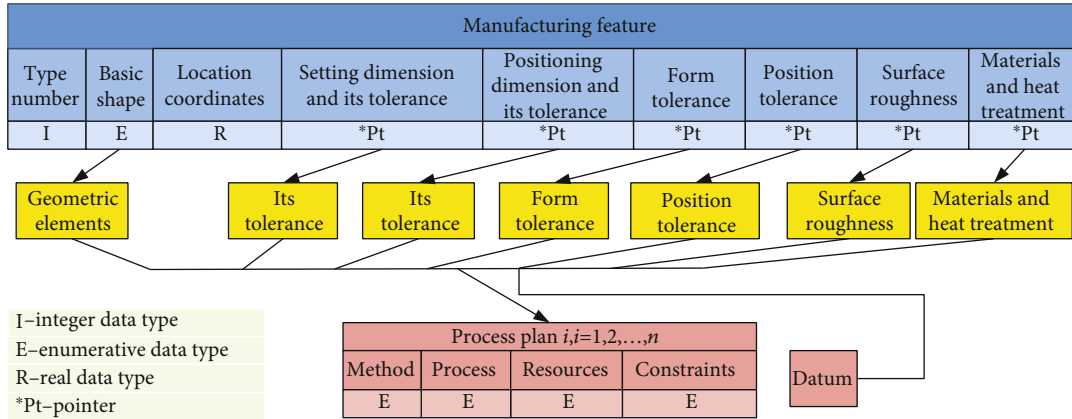
Figure 1: Tree structure of the manufacturing feature ($F_M$).



Figure 2: Structure of the quality feature.

## 3. Structure Design of the Integrated CAx System Based on the Feature Extension of Sensor Components

The main purpose to the proposed feature extension method is to accordingly establish an integrated platform face to enterprises which combines all the CAx systems, enterprise information management systems, and the work flows of those, together. This platform functions as an information hub system for all specific applications which is with properties of unified portal, feature-leading, and collaborative operation, whose core is the proposed feature extension.

The next, we shall illustrate the structure design of the integrated CAx system which is based on the proposed feature extension technology.

*3.1. Architecture Design of the Application Level for the Integrated System Using Sensor Technology.* The layers design of the application level of the integrated system is presented in Figure 6, which is consisted of four layers: the user interface (UI) layer, the controlling layer, the application integration layer, and the data support layer.

In the following content, the definition of the four layers will be introduced.

*3.1.1. The UI Layer.* This layer is designed to provide the users with a unified portal which permits users to operate and invoke the integrated CAx system.

*3.1.2. The Controlling Layer.* The main task of this layer is to control the information acquisition from the feature extension of every CAx or MPRII/ERP system in the integrated system. Meanwhile, the controlling layer grants each application authorities of accessing and obtaining the database, according to the logic of operation flow.

The controlling layer guarantees the cooperation (between the applications embedded in the integrated system, in the collaborative design stage) of processes, knowledge, and multidisciplinary optimization.

*3.1.3. The Application Integration Layer.* The application integration layer is embedded with CAx systems and other

As is shown in Figure 4, the proposed feature extension is designed to be a 3-layer structure, including support layer, property layer, and expression layer. The support layer is a set of feature mapping, feature knowledge, and feature rule, controlling the self-organization of the information included in it. As a result, the support layer finally map the design feature $F_D$ into manufacturing, fixture, quality, and resource & management feature, i.e., the $F_M$, $F_F$, $F_Q$, and $F_E$; the mapping constitutes the property layer.

Finally, after the mapping processing of the support layer, the expression layer which is presented as a geometry entity, by which the feature extension displays and expresses, is packaged with all properties provided by the property layer, serving the integrated systems with their required information.

We can conclude from the above illustration that the feature extension expresses explicitly as a special type of geometry entity which can be treated as an informational entity, serving as a bridge between CAx and other management applications. Figure 5 describes the packaged content and the informational structure of a feature extension. Obviously, a feature extension contains the whole features information of products or components indexed.

FIGURE 3: Structure of the resource and management feature.
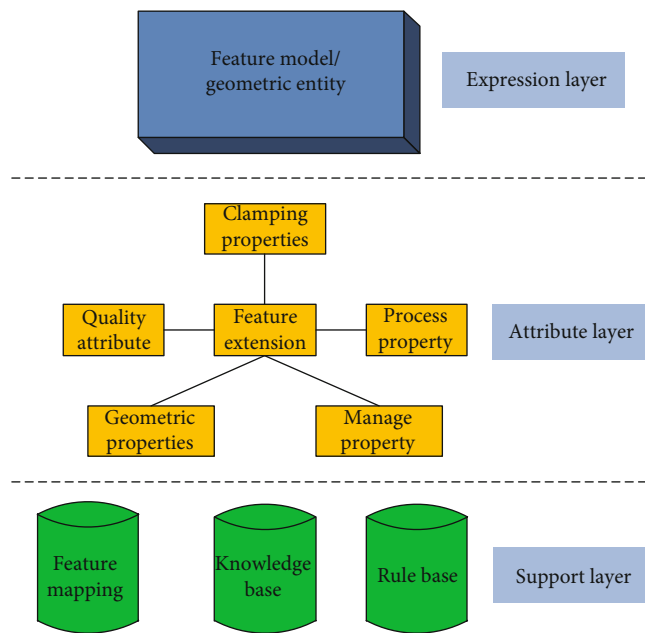


FIGURE 4: The layer structure of the feature extension.
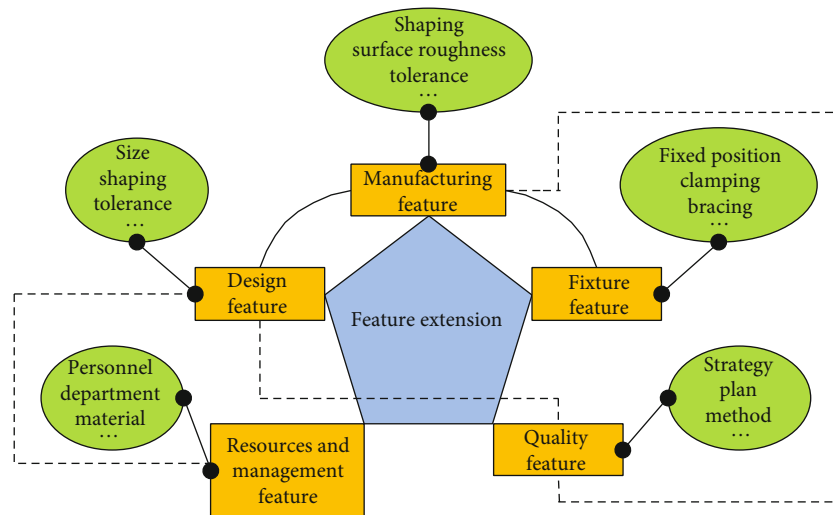


FIGURE 5: The information model of the feature extension.
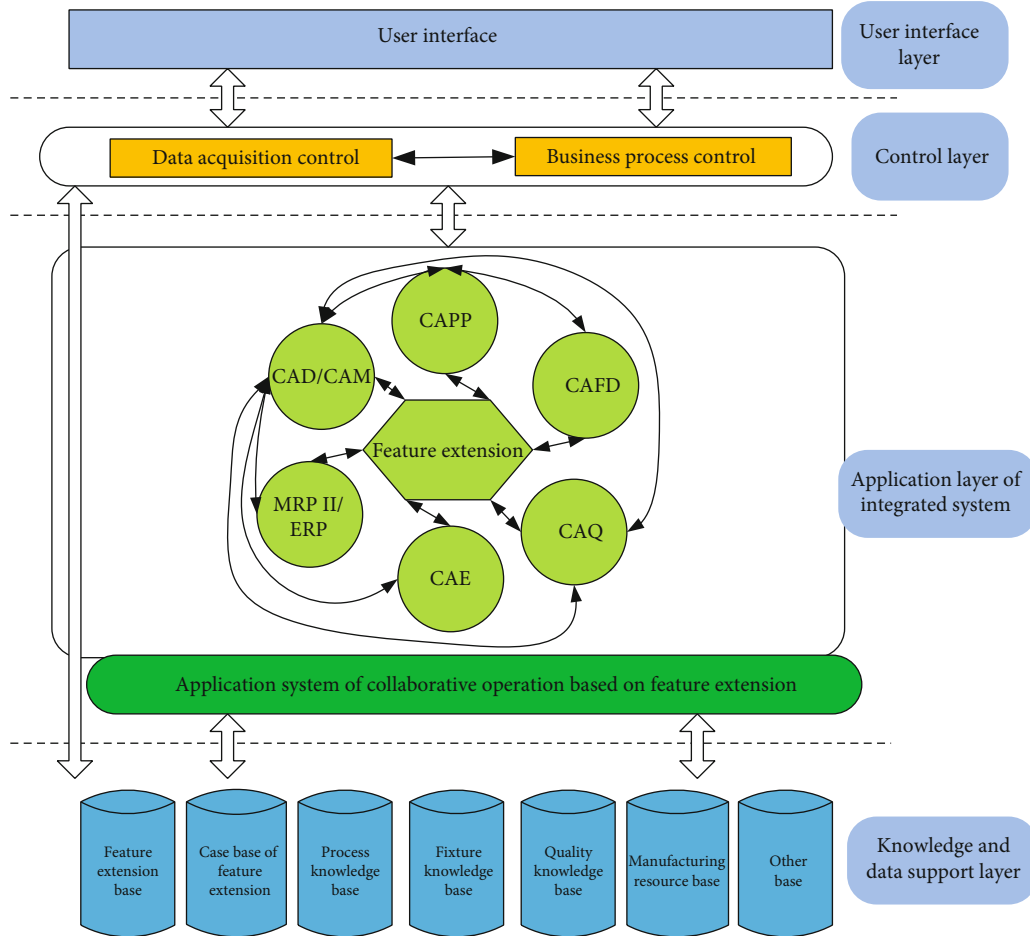
Figure 6: Structure of the integrated CAx system based on the feature extension.

management systems such as MRPII/ERP. In another words, the application integration layer is an integration of applications of CAD modeling, CAPP technology planning, CAFD fixture design, CAQ quality detection and controlling, CAE engineering analysis, and MRPII/ERP enterprise resource management, etc.

Among the integrated application described above, the CAD/CAM is in the key technology of the integration design. And the feature extension is the central component of this layer since the applications can be embedded in this layer by the different types of information packaged in the feature extension.

*3.1.4. The Data Support Layer.* The data support layer comprehensively manages different types of database (i.e., the extended features database, the feature extension samples database, and the technical knowledge database), so that the data presentation and the upper-layer operation of the feature extension can be supported.

*3.2. Key Issues in Feature Extension's Realization and Solutions Based on Sensor Components.* The previous section has introduced the 4-layer structure of the integrated CAx system proposed in this research. In this section, based on the definition of the feature extension and the structure

property of the 4-layer integration, we shall discuss the technical details on how a feature extension matches its corresponding CAD entity and how a combination of feature extensions forms a feature extension sample.

*3.2.1. The Realization of Feature Extension Based on API.* A numbers of commercial CAD softwares, such as Solidworks and Pro-E, provide users with an amount of APIs for secondary developing. Since, users can expediently define different feature extension via the APIs during geometry modeling.

More specifically, the APIs can be used to package a variety of information (including the design, manufacturing, fixture, quality, and resource and management information) in geometry entity when geometry modeling is carried out. Then, the integrated information and the geometry entity are bundled to be the unified feature extension.

The realization of feature extension using APIs demonstrated above has a remarkable merit that users are able to modify the properties packaged in a feature extension according to certain engineering requirements.

*3.2.2. The Matching between the Feature Extension and the CAD Entity.* Here, we shall introduce procedure that how to establish the matching between feature extension and CAD entities. The procedure has four steps:

(a)  (b)

(c)  (d)
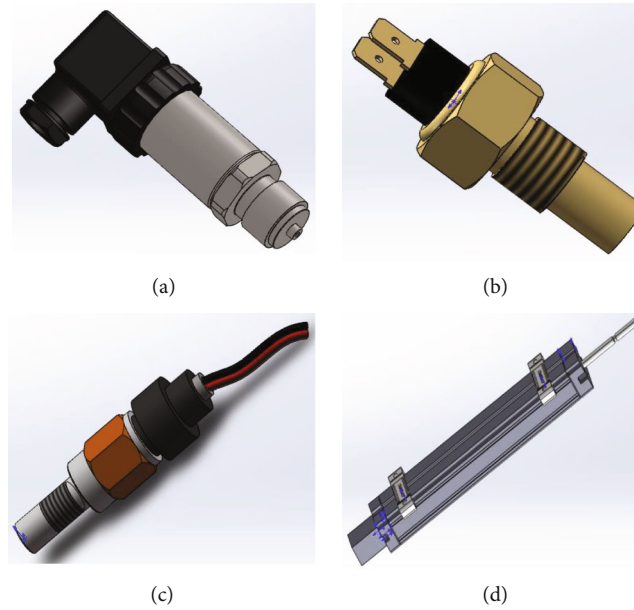
FIGURE 7: An example of feature extension based on (a) pressure sensor, (b) water temperature sensor, (c) speed sensor, and (d) GEFRAN displacement sensor.

*Step 1.* Obtain features constituting the feature extension from a CAD entity, using feature recognition technology.

*Step 2.* Compare the recognized features in Step 1 with the default members stored in the feature extension database and calculated the similarities. The member with the largest similarity becomes a candidate solution of the desired feature extension corresponding to the CAD entity.

*Step 3.* Modify the candidate solution obtained in Step 2 to make it the solution for the matching.

*Step 4.* Store the solution of Step 3 into the feature extension database, so that the database can include more matching examples with the matching procedure kept carrying out.

*3.2.3. The Assembling of the Feature Extension.* As is demonstrated before, the feature extension is in fact an extended features set. The feature extension is bundled with a corresponding geometry entity. Thus, the feature extension is expressed as a special geometry entity with other nonconventional features, i.e., a geometry entity with engineering semantics.

Different from simply bundling the features, the feature extension is determined by the features matching (as is illustrated in 2); the feature extension replaces the original features of its corresponding CAD model. Then, a novel type of entity model (of component) which is completely consisted with the feature extension solutions is obtained; such entity is embedded with all properties of the component's feature extension, realizing the advantages of CAx-independence and available to the proposed integrated CAx system.

Often, a component usually consisted of several structures. Obviously, according to the analysis above, the matching solution of each structure (of the component) needs to be assembled to be a feature extension entity.

Generally speaking, the relation between the solutions of a component can be determined by the original CAD model's topology and attachment details of structures. Assume that the component consisted of $n$ geometrical features and $\mathbf{A}$ denotes the feature relation matrix of the component's CAD model, and the matrix $A$ can be expressed as

$$\mathbf{A} = \begin{bmatrix} a_{11} & \cdots & a_{1n} \\ \vdots & \ddots & \vdots \\ a_{n1} & \cdots & a_{nn} \end{bmatrix}, \quad (4)$$

where $a_{ij}$ is the relation between the n geometrical features (such as the location and attachment relations). The elements where $a_{ij} \neq 0$ indicate that features $a_i$ and $a_j$ have certain relations, e.g., geometrical adjacency and form and location tolerance baseline. Whereas the elements where $a_{ij} = 0$ indicate features $a_i$ and $a_j$ are irrelevant.

Accordingly, the component expressed by the solutions of feature extension consisted of $n$ feature extension solutions. Now, assume $B$ is the relation matrix of the feature-extension-solution-expressed component, and the relation of $A$ and $B$ can be expressed as

$$\mathbf{B} = \mathbf{f}(\mathbf{A}), \quad (5)$$

where $f$ is a general matrix function. Equation (5) indicates $B$ is automatically generated by $A$, and the elements of $B$ are the replacement of $A$.

```
Private sub Cmdqueding_Click()
Dim part as object
Dim boolstatus as Boolean
Dim longstatus as long
Dim sql as string
Dim length as long
Dim filename as string
Dim rs as NewADODBRecordset
Dim cn as NewADOBConnection
If cn.State<>adStateCclosedThen cn.Close
Cn.Open "provider = SQLOLEDBl; persist security info = false; user ID = sa; Initial_Catalog = machine; data source = FORD4"
If rs.Status<>adStateClosedThen rs.Close
Rs.CursorLocation = adUseServer
…
End sub
```

ALGORITHM 1: A program fragment of developing A sensor feature extension.

```
…
Set swap = CreateObject("sldworks.Application")
Set part = swap.ActiveDoc
Set filename = PartGetTitle
Swap.LoadFile2 app.Path+"\" + "filename.Sldpart",""
…
Part.SelectByID"01D1@MaxC@filenameSLDPRT","DIMENSION",0.08775564,-0.00467529,0.017438243
Part.Parameter("@MaxC").SystemValue =01D1
Part.ClearSelection
…
End sub
```

ALGORITHM 2: A program fragment of modifying the feature extension attribute with user defined function fldtofile.

## 4. Design Application Strategy of the Applied Feature Extension

The definition and the development designs of the extended feature are two key issues for the integrated CAx system based on feature extension. One practical solution for the key issues mentioned above is to carry out a secondary development on widely-used commercial CAD softwares. This measure can sufficiently make use of the mainstream softwares' advantage and simplify the programming procedure. To solve the secondary development, this research offers an idea, as is concluded as the following four stages.

4.1. Define Feature Extension and Establish Extended Feature Library. The main task of this stage is classifying and coding the extended feature. Therefore, we can establish the information model for every type of extended feature and further develop a feature extension sample in a commercial CAD system. After that, the extended feature library and the feature extension sample library can be constructed accordingly.

4.2. Properties Packaging for the Extended Features. Noticing that the commercial CAD software offer abundant geometry modeling methods, other features, such as manufacturing, clamping, quality, and resource information, can be packaged with products' geometry feature. The benefit is that once done, the complete information of products during their lifetime can be generated in the geometry modeling stage.

4.3. Transformation from Products' Geometry Model to Feature Extension Entity. The main task of this stage is to construct a matching algorithm that relate the geometry and feature extension entities. This operation guarantees the visible models of products are not only geometry entities but also accessible general information entities for CAx and MRPII/ERP enterprise resource management systems.

4.4. Automatic Acquisition of Products' Information. It is necessary to provide the follow-up procedure with original information of products or components. For example, once the manufacturing information is obtained by the CAPP system, the technology planning can be generated automatically. Therefore, the CAx systems must be able to acquire the information of products or components automatically. One possible solution is to control the work flow and authority of each system.

## 5. An Example of Feature Extension of Sensor Components

In this paper, SolidWorks can be used as the development platform, visual basic, and SQL server are used as development tools, and SolidWorks API and user-defined functions are called to develop features extension and modify their properties. The following is a program fragment to develop a sensor feature extension (as shown in Figure 7) and modify its attributes.

## 6. Conclusions

To improve the design quality and product originality in manufacturing and to optimize the management operation of companies, this research develops a feature extension method that integrates CAx applications and MRPII/ERP together, so that the manufacturing and the management domains can be combined tightly. First, feature extension of sensor components is defined and extended feature library of sensor components is established. Classifying and coding are the main procedure. Second, feature extension properties of sensor components are packaging. Due to abundant geometry modeling methods by offering commercial software, manufacturing, clamping, quality, and resource information can be packaged. Then, the products' geometry model is transformed to feature extension entity based on sensor technology. Finally, sensor products' information is automatic acquisition.

The information model and the design application strategy have been studied in detail in this paper, which are constructive to researchers and engineers engaged in advanced manufacturing especially in sensor development. In the next step, we plan to apply the technology proposed in this research to a small-scale enterprise (a university company) to evaluate the performance and to further improve sensor research.

## Data Availability

These sensor model data in this paper comes from the secondary development of Solidworks API software.

## Conflicts of Interest

The authors declare no conflict of interest in this paper.

## Authors' Contributions

Yaohong Tang and Mengmeng Song contributed equally to this work and should be considered co-first authors.

## Acknowledgments

## References

[1] M. Philpotts, "An introduction to the concepts, benefits and terminology of product data management," *Industrial Management and Data Systems*, vol. 96, no. 4, pp. 11–17, 1996.

[2] Hsu-Pin Ben Wang and R. A. Wysk, "Intelligent reasoning for process planning," *Computers in Industry*, vol. 8, no. 4, pp. 293–309, 1987.

[3] K. K. Leong, K. M. Yu, and W. B. Lee, "A security model for distributed product data management system," *Computer in Industry*, vol. 50, no. 2, pp. 179–193, 2003.

[4] J. F. Gu and Z. L. Zhang, "Research on integration technology between SolidWorks and small PDM system," *Computer and Modernization*, vol. 11, pp. 214–217, 2011.

[5] Z. G. Li and Y. Gao, "Research on CAD/CAPP/CAM system integration technology based on PDM," *Electro-optic Technology Application*, vol. 35, no. 40, pp. 66–70, 2020.

[6] X. G. Yan, F. Zhang, Z. N. Chen, and H. Z. Bin, "PDM CAx product variant design system," *Journal of Computer-aided Design& Computer Graphics*, vol. 20, no. 1, pp. 124–127, 2008.

[7] J. M. Li, L. P. Huang, and H. L. Li, "CIMS oriented CAx information management and intergrated system," *Journal of Tsinghua University*, vol. 38, no. 10, pp. 65–69, 1998.

[8] Z. D. Zhao, C. L. Liu, and S. D. Huang, "Knowledge-based and CAX intelligent integration technology in shell nosing design and optimization," *Journal of Plasticity Engineering*, vol. 15, no. 3, pp. 81–85, 2008.

[9] H. Tang, "Application of CAx in mechanical product development and integration," *Electronics Design & Application*, vol. 47, no. 8, pp. 30–33, 2010.

[10] L. Chen, "Research on injection molding of bicycle plastic bottle holder based on CAx computer aided design," *China Plastics Industry*, vol. 47, no. 10, pp. 89–91, 2019.

[11] C. W. Dankwort, "CAx systems architecture of the future," *CAD Systems Development*, no. 27, pp. 20–31, 1997.

[12] B. S. Tong and J. M. Li, "Technologies of product data management," Tsinghua University Press, Beijing, 2000.

[13] F. Klocke, G. Spöcker, T. Huwer, T. Bobek, and K. Arntz, "Reducing data loss within adaptive process chains in the context of commonly-used CAx systems," *Production Engineering*, vol. 9, no. 3, pp. 307–316, 2015.

[14] S. Y. Li and T. F. Cai, "Collaborative product design process integration technology based on webservice," in *Global Design to Gain a Competitive Edge, Conference paper*pp. 231–240, Sanya, China, 2008.

[15] C. Danjou, J. le Duigou, and B. Eynard, "Closed-loop manufacturing process based on STEP-NC," *International Journal on Interactive Design and Manufacturing*, vol. 11, no. 2, pp. 233–245, 2017.

[16] Y. H. Ni, Y. Lu, H. B. Wang, and X. J. Gu, *Business Cooperation-Oriented Heterogeneous System Integration Framework and Its Implementation*, Enterprise Interoperability IV, 2010.

[17] W. Y. Zhang, S. B. Tor, and G. A. Britton, "Indexing and retrieval in case-based process planning for multi-stage non-axisymmetric deep drawing," *The International Journal of Advanced Manufacturing Technology*, vol. 28, no. 1-2, pp. 12–22, 2006.

[18] N. Wan, R. Mo, and Z. F. Chen, "Key technology of interoperability between CAD and digitizing systems," *Computer Integrated Manufacturing Systems*, vol. 14, no. 6, pp. 1085–1089, 2008.

[19] S. B. Su and W. K. Fan, "CAx research on integration of CAx and applied patterns," *Modern Manufacturing Engineering*, vol. 4, pp. 137–142, 2009.

[20] B. Babic, N. Nesic, and Z. Miljkovic, "A review of automated feature recognition with rule-based pattern recognition," *Computers in Industry*, vol. 59, no. 4, pp. 321–337, 2008.

[21] B. Zhao and Y. Yan, "Research on key technology of CAX design process integration," *Advanced manufacturing technology forum and manufacturing automation and information technology seminar*, vol. 11, pp. 181–188, 2007.

[22] X. F. Fang, W. W. Li, C. S. Zhu, and J. Wang, "Research on inference machine based on knowledge engineering in product configuration," *Machinery Design & Manufacture*, vol. 3, pp. 297–300, 2020.

[23] Z. Tang, G. Zhao, and T. Ouyang, "Two-phase deep learning model for short-term wind direction forecasting," *Renewable Energy*, vol. 173, pp. 1005–1016, 2021.

[24] S. Xiao, S. Liu, H. Wang, Y. Lin, M. Song, and L. Zhang, "Nonlinear dynamics of coupling rub-impact of double translational joints with subsidence considering the flexibility of piston rod," *Nonlinear Dynamics*, vol. 100, no. 2, pp. 1023–1229, 2020.

[25] S. Xiao, S. Liu, M. Song, N. Ang, and H. Zhang, "Coupling rub-impact dynamics of double translational joints with subsidence for time-varying load in a planar mechanical system," *Multibody System Dynamics*, vol. 48, no. 4, pp. 451–486, 2020.

[26] S. Xiao, S. Liu, F. Jiang, M. Song, and S. Cheng, "Nonlinear dynamic response of reciprocating compressor system with rub-impact fault caused by subsidence," *Journal of Vibration and Control*, vol. 25, no. 11, pp. 1737–1751, 2019.

*Research Article*

# Alignment Method of Combined Perception for Peg-in-Hole Assembly with Deep Reinforcement Learning

**Yongzhi Wang** [1], **Lei Zhao,**[1] **Qian Zhang,**[1,2] **Ran Zhou,**[1] **Liping Wu,**[1] **Junqiao Ma,**[1] **Bo Zhang,**[1] **and Yu Zhang** [1]

[1]*Department of Mechanical Engineering, Shenyang University of Technology, Shenyang 110000, China*
[2]*College of Science, Shenyang University of Chemical Technology, Shenyang 110000, China*

Correspondence should be addressed to Yu Zhang; zhangyu@sut.edu.cn

The method of tactile perception can accurately reflect the contact state by collecting force and torque information, but it is not sensitive to the changes in position and posture between assembly objects. The method of visual perception is very sensitive to changes in pose and posture between assembled objects, but they cannot accurately reflect the contact state, especially since the objects are occluded from each other. The robot will perceive the environment more accurately if visual and tactile perception can be combined. Therefore, this paper proposes the alignment method of combined perception for the peg-in-hole assembly with self-supervised deep reinforcement learning. The agent first observes the environment through visual sensors and then predicts the action of the alignment adjustment based on the visual feature of the contact state. Subsequently, the agent judges the contact state based on the force and torque information collected by the force/torque sensor. And the action of the alignment adjustment is selected according to the contact state and used as a visual prediction label. Whereafter, the network of visual perception performs backpropagation to correct the network weights according to the visual prediction label. Finally, the agent will have learned the alignment skill of combined perception with the increase of iterative training. The robot system is built based on CoppeliaSim for simulation training and testing. The simulation results show that the method of combined perception has higher assembly efficiency than single perception.

## 1. Introduction

It is an important challenge for the intelligent robot to fully observe environmental information in the complex unstructured environment. However, the perception capacity of the robot will directly affect the robot's performance in the task [1–5]. It is difficult to meet current complex work demands only relying on a single type of sensor to perceive the environment. Besides, traditional programming methods in assembly tasks require technicians with a high technical level and rich work experience to complete a large amount of code compilation and parameter deployment. This not only takes time and effort but also limits the flexibility of the production line. The traditional programming method in the structured environment can no longer meet the production

requirements that require frequent upgrades. The programming model of the robot has changed from hard coding to teaching-playback for the rapid changes in the production line [6–10]. The teaching-playback method greatly reduces the workload of programming. Nevertheless, the teaching method still requires a large number of parameter deployments like the traditional programming method. Therefore, more research has focused on training robots to acquire work skills independently with the learning-based method. The trained robot can autonomously interact with the environment to complete work. Robots mainly rely on visual and tactile perception methods to perceive the environment in the interacting process.

Tactile sensation is very important for humans to perceive the environment, and it is also one of the important

perception means for robots. The method based on force control is mostly used to solve the task of precision assembly. The force sensor, position sensor, and force/torque (F/T) sensor are the most commonly used sensors based on force control. They can accurately feedback the contact force when the assembly parts are in contact with each other. When three-point contact occurs in the peg-in-hole assembly, the three degrees of freedom of the peg are restricted by the hole, which makes it difficult to complete the insertion for the peg with the traditional method. A novel alignment method based on geometric and force analysis is developed to deal with this dilemma [11]. This method uses the F/T sensor to measure the contact force information to estimate the relative pose of the pile and hole.

The alignment between the peg and the hole is accomplished by compensating motion based on attitude estimation. To address the assembly failure caused by the large friction resistance and poor contact situations, a screw insertion method was developed for peg-in-hole assembly [12]. The proposed method analyzes the point contact and surface contact to reduce axial friction in the assembly process. And it is still valid in the case of transition fit. For high-precision assembly tasks, a large number of parameters often need to be deployed, which technicians need to spend a lot of time on programming deployment. Therefore, an easy to deploy teach-less method is proposed to complete precise peg-in-hole assembly [13]. Whereafter, an easy to deploy teach-less method is proposed to complete precise peg-in-hole assembly. The low accuracy of conventional programming is compensated without artificial parameter tuning by training based on deep reinforcement learning. Moreover, a variable compliance control method based on deep reinforcement learning is proposed for the peg-in-hole of the 7-DOF with torque sensor robot to improve the efficiency and robustness of the assembly task in the uncertain initial state and complex environment [14]. The trained robot can select passive compliance or active regulation to dispose of the current environment, which makes the variable compliance fewer adjustment steps than the fixed compliance. In addition, the method of combined learning-based algorithm and force control strategy is proposed [15]. It contains the hybrid force/position controller and the variable impedance controller. The hybrid force/position controller was designed to ensure the safe and stabilization of the searching hole. The variable impedance controller based on fuzzy Q-learning is used to conduct compliance action. The proposed method improves the stability and adaptability of the peg-in-hole assembly. Many high-precision assembly tasks mostly choose the method based on force control. However, the appearance characteristics and related location information of the environment cannot be well perceived for the force sensors.

Visual perception plays an important role in the robotic perception of the environment. Visual perception can quickly perceive the appearance characteristics and relative position information of the object. It is difficult for visual perception to process the occluded part when the target is partially occluded. Human beings often rely on touch, hearing, and smell to perceive the environment when their vision is obscured. And the visual perception is interfered with by environmental factors such as lighting, which leads to the robot needing to work in a specific working environment [16].

In recent years, the field of visual perception has also made numerous research progress with the vigorous development of deep learning and deep reinforcement learning. The robot of the combined system uses a two-level vision measurement method in robot automatic assembly [17]. This technique has developed an accurate coordinate transformation for the calibration of the dynamic coordinate system. Whereafter, the hole was 3D reconstructed for the hole edge point selection. This method makes the cost of the pose determination become lower. And it also extends the visual measurement range and improves the positioning accuracy. In addition, the method of uncalibrated visual servoing is used in peg-in-hole assembly, which is a three-phase assembly strategy [18].

The designed system first uses an eye-to-hand mono camera to perform attitude alignment, which makes the assembly object and the predefined transition location parallel to each other. Then, the system aligns the assembly object and the predefined transition position collinearly. Finally, the assembly object completed the longitudinal alignment. Besides, a learning-based visual servoing method was used to quicken the speed of the searching hole [19]. This method uses the concept of domain randomization based on deep learning to predict the position of the hole. The deep neural network uses synthetic data for training to predict the hole's quadrant. Whereafter, the peg moves towards the hole through visual servoing iteration. The diameter and the length of the assembly are, respectively, 10 mm and 70 mm. The assembly clearances between the peg and the hole are 0.4 mm. It still can quickly complete the peg-in-hole assembly when facing different surfaces with various colors and textures in the real world. And the assembly time is less than 70 s. Whereafter, in order to peg-in-hole alignment, a visual servoing based on learning was developed to faster align with the hole [20]. The deep neural network for peg and hole point estimates uses purely synthetic data to train. The assembly system is equipped with two cameras and a special lighting system, which can align the peg with the holes covered by different materials and then complete the insertion of the peg through compliance control with force-feedback. Moreover, the method of the dynamic position-based servo can perform the microassembly with the micropeg of diameter $80 \, \mu$m and the hole of $100 \, \mu$m [21].

The assembly system is equipped with encoders for position servo, light source, and three CCD cameras to automatically align, grasp, transport, and assemble. The process of the microassembly has not the contact adhesion force. The average time and the success rate of the assembly are 4 mins and 80%, respectively. In summary, the control method based on the vision for the assembly has higher assembly efficiency than force, but the assembly accuracy is not as good as the method based on force. If the system based on the vision method needs to improve the assembly accuracy, the system needs to be equipped with a high-precision vision sensor, a special lighting source, and spend more assembly time. The control methods based on vision or force have

their own advantages and disadvantages. If they can complement each other, the robot will have higher assembly efficiency while ensuring assembly accuracy.

Humans often use the means of visual observation and tactile perception to complete the peg-in-hole assembly. It is possible to complete the peg-in-hole assembly of the minuscule clearance under the condition of clear observation and sensitive tactile perception. On the one hand, we can also use only visual observation to complete the assembly. However, there needs to be sufficient clearance when the state of the peg and the hole can be clearly observed. Otherwise, it will cause the assembly to fail. On the other hand, we can also use only the tactile perception to achieve a successful assembly. However, it may take more time. So the assembly speed of a robot using multiple perception methods is often better than that of a single perception method. Therefore, the current research of peg-in-hole assembly mostly adopts the hybrid control method of visual observation and tactile perception [22–26]. For instance, a guidance algorithm based on geometrical information and force control is proposed to improve the success rate of the peg-in-hole assembling with complex shapes [7].

The proposed method makes a 6-DOF industrial robot with the eye-in-hand camera chooses assembly direction through spatial arrangement and geometric. And it determines the magnitude of force through kinesthetic teaching. Besides, the dual-arm coordination robot adopts a hybrid assembly strategy based on vision/force guidance for peg-in-hole assembly [27]. This method can be used in round, triangle, and square assembly parts with 0.5 mm maximum clearance. Baxter research robot has three vision sensors placed on the left hand and right hand head, respectively. The robot first uses visual guidance to achieve rough adjustment. Afterward, the robot uses the force feedback mechanism with the F/T sensor to perform precise adjustments. The proposed method can ensure a high assembly success rate for assembly parts of different shapes. Furthermore, the modalities with different characteristics were designed based on deep reinforcement learning for different geometry peg-in-hole tasks with tight clearance [28]. The robot has three sensors to collect the data of RGB images, F/T sensor, and end-effector as input.

Our technique uses multiple inputs to establish a compact multimodal representation to predict contact and alignment in the peg-in-hole assembly. And then, the robot controller with haptic and visual feedback was realized through the self-supervision training without the manual annotation. Moreover, a novel method was proposed to find the right inserting pose through trials with force feedback and vision [23]. The adjustment times of the assembly were minimized by the reinforcement learning training, which uses force and visual feature design. In addition, the combined method of learning-based algorithms and force control strategies were proposed to improve the efficiency and safety of the assembly process [15]. This method takes advantage of the MLP network to generate the action trajectories during the hole-searching and uses the force/position controller to ensure the safety and stability in the contact. The variable impedance controller based on fuzzy Q-learning was designed to insert the peg into the hole. The proposed method improves the efficiency and effectiveness of the assembly.

The current research of the peg-in-hole assembly uses mostly multiple perception methods, but most of them use a single perception method to adjust the alignment between the peg and the hole. However, humans often use the method of visual and tactile perception to complete this work. The robot's visual and force perception should be well combined to better intelligent performance and higher assembly efficiency.

In this paper, a hybrid control method of vision and tactility is proposed based on deep reinforcement learning to improve alignment efficiency for the peg-in-hole tasks. The mapping relationship between visual features and tactile signals will be established by trial and error with the self-supervised. Firstly, the RGB-D image is obtained by the visual sensor. Secondly, the deep neural network extracts visual features from the image and predicts the contact state. Thirdly, the agent receives the force signal by the tactile sensor to determine the current contact state as a visual prediction label. Finally, the network of the visual prediction uses this label to conduct the backpropagation calculation for correcting the network weights. We introduce the working principle of the peg-in-hole assembly in Section 2, and a quick hole-searching strategy is designed. In Section 3, the hybrid control method is proposed for the peg-in-hole assembly to improve assembly efficiency. In Section 4, the simulation results in CoppeliaSim and analysis results are presented. Section 5 elaborates the conclusions and future work.

## 2. Working Principles and Analysis of Peg-in-Hole Assembly

*2.1. Analysis of the Contact State between the Peg and the Hole.* The task of peg-in-hole assembly is mainly divided into the grasping stage, the hole-searching stage, the alignment stage, and the insertion stage. The task of the grasping stage is to grasp the peg and move it to the vicinity of the hole. The task of the hole-searching stage is to visually detect the edge and the center of the hole and then move the peg to the center position of the hole. The task of the alignment stage is to adjust the posture of the peg, so that the posture alignment is completed between the peg and the hole. The task of the insertion stage is to insert the peg into the hole after alignment. In the assembly process, there are three vital contact states as shown in Figure 1. The bottom of the peg makes surface contact with the upper surface of the hole after moving the peg. This contact is called surface contact, as illustrated in Figure 1(a). The point contact will occur between the inside of the hole and the surface of the peg if the peg is close enough to the center of the hole. Two-point contact and three-point contact are shown in Figures 1(b) and 1(c), respectively. The plane contact only occurs in the hole-searching stage. It means that the position of the hole has been found when the point contact has occurred. It means that the robot has completed the task of the hole-searching stage and entered the alignment stage.

(a)

(b)

(c)
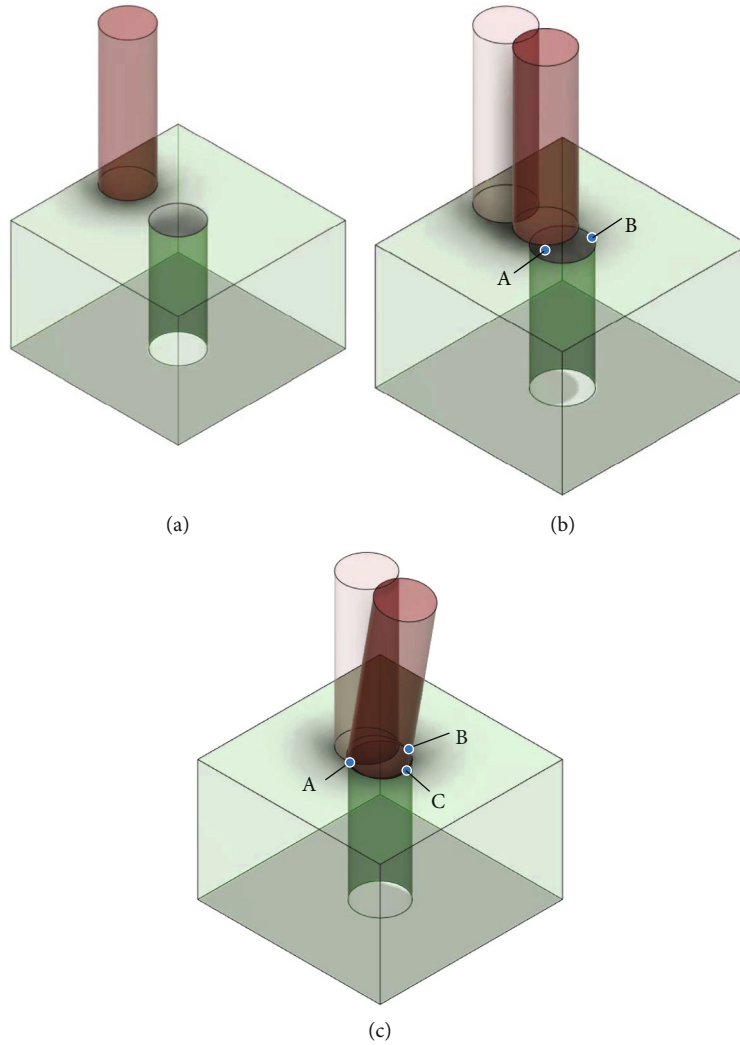
Figure 1: Schematic diagram of contact state based on (a) plane contact, (b) two-point contact, and (c) three-point contact.

The key stages that affect the efficiency of peg-in-hole assembly are the hole-searching stage and the alignment stage. Their details are introduced in Section 2.2 and Section 2.3, respectively.

## 2.2. Working Principles of Searching Hole

*2.2.1. The Method of Force-Based Searching Hole.* Firstly, the peg will be moved to the surface of the hole, which produces a plane contact state between the peg and the hole. At this time, the peg situates the outside of the hole. Subsequently, the peg searches for the position of the hole with an Archimedes spiral trajectory. During the search process, the center of the peg gradually approaches the center of the hole. The peg will be inserted into the hole or tilted in the inside of the hole under the action of the assembly force when the position of the shaft and the hole are close enough. The peg went into the inside of the hole by this time, that is, the work of the searching hole is completed and the adjustment phase is entered. The method of force-based searching hole often spends more time than the vision-based.

*2.2.2. The Method of Vision-Based Searching Hole.* The image data expressing the current environment information is obtained through the vision sensor. And then, it is applied edge detection with the Canny operator. But the edge detection is susceptible to interference from image noise. Therefore, image noise removal must be performed with Gaussian filtering before the edge detection. The image noises will be eliminated by the Gaussian smoothing filter, and the Gaussian kernel used by the filter is described as follows:

$$K = \frac{1}{273} \begin{bmatrix} 1 & 4 & 7 & 4 & 1 \\ 4 & 16 & 26 & 16 & 4 \\ 7 & 26 & 41 & 26 & 7 \\ 4 & 16 & 26 & 16 & 4 \\ 1 & 4 & 7 & 4 & 1 \end{bmatrix}. \tag{1}$$

And after that, the system calculates the intensity gradients and direction with the Sobel operator. The convolution

(a)



(b)
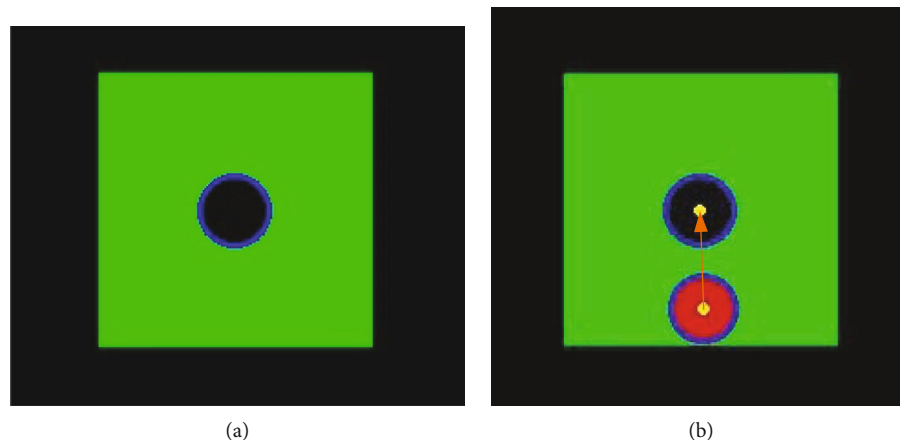
FIGURE 2: Schematic diagram of visual recognition with (a) edge detection of the hole and (b) position detection of the center for the hole.

arrays need to be applied to the $x$ and $y$ directions, respectively, to calculate the gradient magnitude and direction. The convolution arrays are shown as follows:

$$d_x = \begin{bmatrix} -1 & 0 & 1 \\ -2 & 0 & 2 \\ -1 & 0 & 1 \end{bmatrix}, \tag{2}$$

$$d_y = \begin{bmatrix} -1 & -2 & -1 \\ 0 & 0 & 0 \\ 1 & 2 & 1 \end{bmatrix}. \tag{3}$$

The intensity gradients $S$ determine whether the point is an edge point. The large gradient value indicates that the gray value around the point changes quickly and is an edge point. The small gradient value indicates that the point is not an edge point. The gradient direction $\theta$ indicates the direction of the edge. The calculation formula of the intensity gradients $S$ and direction $\theta$ is described as follows:

$$S = \sqrt{d_x^{\,2} + d_y^{\,2}}, \tag{4}$$

$$\theta = \arctan \frac{d_y}{d_x}. \tag{5}$$

Subsequently, the system performs the nonmaximum suppression operation for each pixel to filter out nonedge pixels. First of all, the gradient direction $\theta$ is approximated as one of 0, 45, 90, 135, 180, 225, 270, and 315. That is, the gradient direction $\theta$ is defined as eight directions in a two-dimensional space. And then, it compares the intensity gradients $S$ of each pixel. Finally, the pixel would be retained if the intensity gradients $S$ of the pixel is the largest; otherwise, it is suppressed to 0. The purpose of this process is to make the blurred boundary become sharp. There are still many image noises in the image after the process of nonmaximum suppression. This method is more sensitive to noise, so it is necessary to filter for image blurring and denoising. Thereafter,

the hysteresis threshold will be used to further process the noise. The method sets the upper bound and the lower bound of the threshold. It is considered to be an edge if the intensity gradients of the pixel are greater than the upper bound of the threshold, which is called a strong edge. It must not be an edge if its intensity gradients are less than the lower bound of the threshold, which will be removed. When the intensity gradients of the pixel are in threshold interval, it is considered as the weak edge. At this time, these pixels can only be considered as the candidate of the edge. They will be retained if it is connected to the edge; otherwise, it will be removed. The upper bound of the threshold is to distinguish the contour of the object from the environment, which determines the contrast between the object and the environment. The lower bound of the threshold is used to smooth the contour of the edge. The contour of the edge may be discontinuous or not smooth enough when the upper bound of the threshold is set too large. The detected edges of the contour may not be closed at this time. The lower bound of the threshold can make up for this; it can smooth the contour or connect the discontinuous parts.

In this way, a complete outline can be obtained, as illustrated in Figure 2(a). When the edge detection has been completed, the Hough gradient method is used to detect the center of the hole. This method will draw straight lines along the gradient direction of the pixels for all edge pixels. The straight line is perpendicular to the tangent line of the boundary pixel, which is the normal line.

The system will accumulate votes in the Hough two-dimensional accumulator space after the normal line of all contour pixels is drawn. The pixel with more votes is more likely to be the center of the hole. The robot gradually moves the peg to the inside from the outside of the hole after determining the center of the hole, as shown in Figure 2(b). However, during the peg approaches the center of the hole, it will slide down to the center of the hole under the action of the assembly force if the peg is close enough to the center of the hole. Subsequently, the peg will convert from plane contact to two-point contact or three-point contact. At this time, the work tasks of the hole-searching stage have been completed and the alignment stage has been entered.

(a)

(b)

(c)
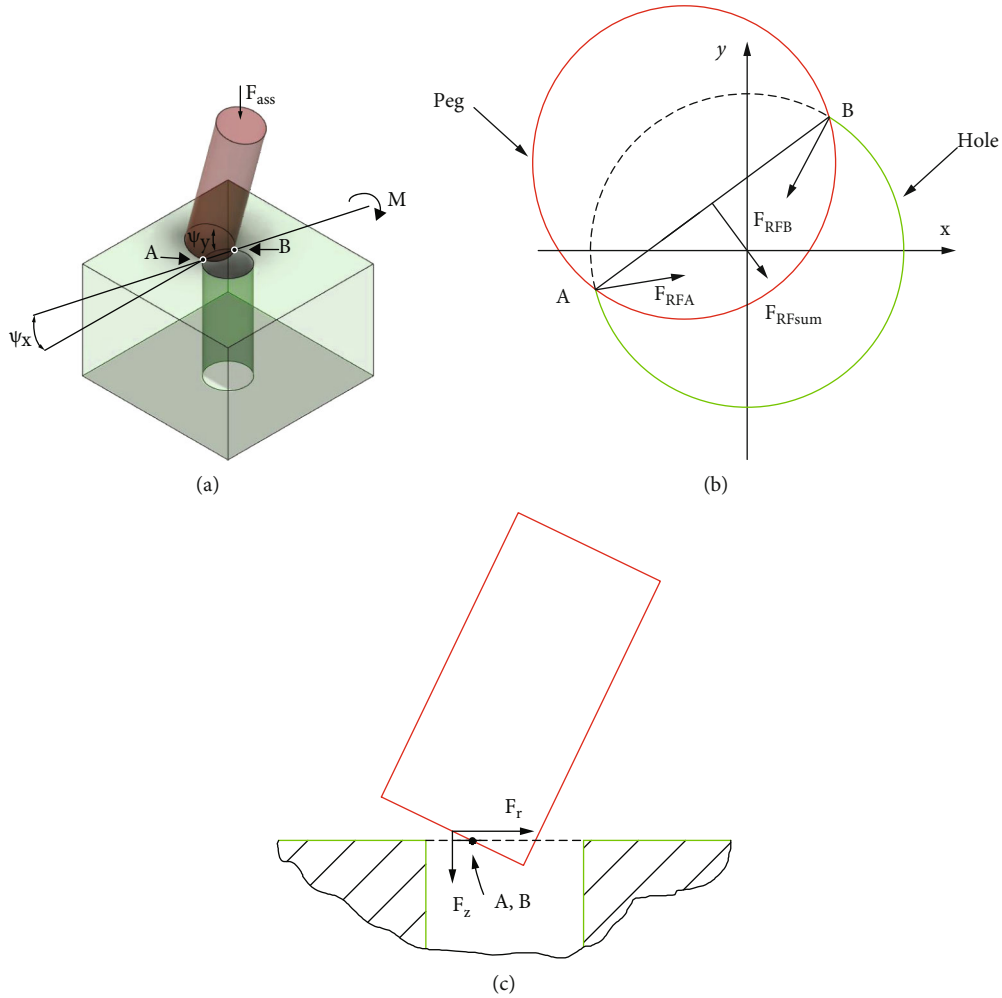
FIGURE 3: Schematic diagram of contact force analysis illustrating (a) contact force. (b) Top view of contact force analysis. (c) Side view of contact force analysis.

*2.3. Working Principles of Alignment.* The adjusting posture for the peg usually uses the method of compliance-based with force feedback to align the hole whether the assembly control method is force-based or hybrid control based on vision and force. When the point contact occurs, the peg will overcome the contact friction force between the peg and the hole under the action of the assembly force $F_{ass}$ and slide to the center of the hole, as shown in Figure 3(a).

This phenomenon of sliding to the center of the hole is called the "natural attraction" of compliance-based peg-in-hole assembly. For instance, the assembly force exerted by the robot on the peg causes a corresponding reaction force at the contact point A and B between the peg and the hole. The sum of the reaction forces $F_{RFsum}$ on the contact points always points to the center of the hole, as illustrated in Figure 3(b). The projections of the assembly force $F_{ass}$ on the $xy$-plane and the $z$-axis are $F_r$ and $F_z$, respectively, as shown in Figure 3(c). $F_z$ is always vertically downward, but the direction of $F_r$ is uncertain. They will counteract each other when the directions of $F_{RFsum}$ and $F_r$ are inconsistent. In this case, the peg cannot overcome the friction

at the contact point and will keep the peg stationary. When the direction of $F_{RFsum}$ and $F_r$ are consistent, the peg will overcome the friction at the contact point to slide to the center of the hole.

This adjustment method based on compliant control can smoothly complete the peg-in-hole assembly. However, it will also have some difficult situations, such as the peg slipping out of the hole and larger position errors or posture errors. Humans often rely on the cooperation of vision and tactile to deal with this dilemma. Therefore, this research improves the work efficiency of the peg-in-hole assembly by training the vision and tactile cooperation of the robot. The training details will be introduced in Section 3.

## 3. Alignment Method of Combined Perception for Peg-in-Hole

The assembly system for peg-in-hole is mainly composed of hole-searching module and alignment module. The performance of the alignment module determines the alignment efficiency. The current research usually uses alignment

(a)

(b)
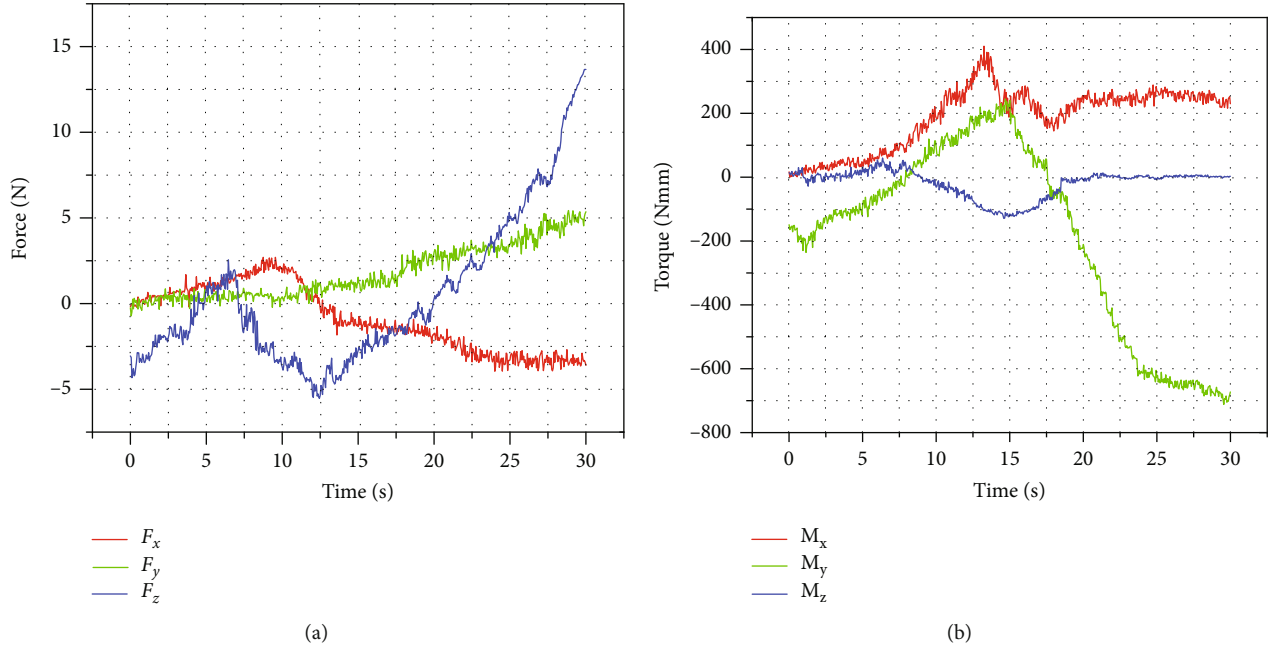
FIGURE 4: Interaction between peg and hole based on (a) contact forces and (b) contact torques.

methods based on force control. This method performs well when dealing with smaller position and posture errors, but it performs poorly when dealing with larger position and posture errors. This is because the force-based control method can only perceive the change of the contact state but cannot intuitively perceive the change of the spatial position and posture of the peg. Therefore, we propose a multiperception alignment method with vision and tactility based on the analysis in Section 2.3.

### 3.1. Working Principles of Combined Perception with Deep Reinforcement Learning.
Tactile perception with a force/torque sensor can accurately perceive the information of the contact state, but it is not sensitive to changes in spatial position and posture. Visual perception can intuitively reflect the change of spatial position and posture. However, when the perceived object is in contact with other objects, visual perception cannot accurately perceive the contact state. If visual perception and tactile perception can be combined, the intelligence of the robot will be further improved. In this work, the robot perceives the relative position and posture of the peg and the hole through the visual sensor to make adjustment action decisions. Then, the robot perceives the information of the contact state through the force/torque sensor, and the information of contact force and torque is shown in Figure 4.

Afterward, the robot gives the adjustment action based on tactile information as a prediction label of the current state [29]. Subsequently, if the predicted action is inconsistent with the label, the backpropagation calculation is performed on the neural network to modify the weight [30]. Finally, the robot can establish a mapping relationship between visual perception and tactile perception after training, so that the robot is sensitive to changes in position, pos-

ture, and contact force. The training process is shown in Figure 5.

The proposed method enables the robot to learn the alignment skills for peg-in-hole assembly through training based on self-supervised deep reinforcement learning. Thus, the decision-making problem of the alignment adjustment process is transformed into a probabilistic problem of the Markov decision processes. At the time $t$, the robot chooses action $a_t$ according to the observed environment state $s_t$. The environment state $s_t$ transitions to $s_{t+1}$, which has obtained the reward $R_{t+1} = r$. The transition probability of the state can be expressed as follows:

$$p(s_{t+1} \mid s_t, a_t) \doteq P_r\{s_{t+1} \mid s_t, a_t\} = \sum_{r \in R} p(s_{t+1}, R_{t+1} \mid s_t, a_t). \quad (6)$$

The state-action-reward chain is saved as a sample $D_i$:

$$D_i = (s_t, a_t, s_{t+1}, R_{t+1}). \quad (7)$$

The agent uses the strategy $\pi(s)$ to choose executable actions $a_t$ from action space $A(s)$. The process of training robots to learn skills can also be seen as maximizing the reward of the agent. The agent also obtains the optimal strategy $\pi^*(s)$ when the total reward $G_t$ is maximized.

$$G_t \doteq R_{t+1} + \gamma R_{t+2} + \gamma^2 R_{t+3} + \cdots = \sum_{k=0}^{\infty} \gamma^k R_{t+k+1}, \quad (8)$$

where $\gamma = 0.5$ is the future discount factor.

The proposed method uses off-policy Q-learning, and its action-value function is to evaluate the expected value $Q$ for the action in the current state:
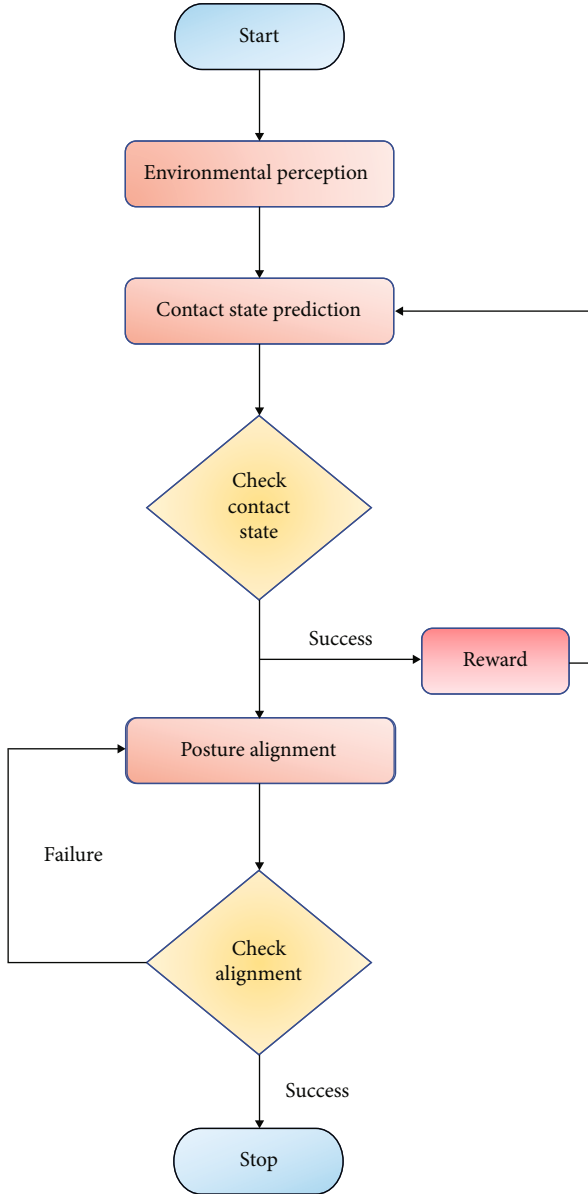
FIGURE 5: Flowchart of peg-in-hole procedure.

$$Q_\pi(s_t, a_t) \doteq \mathbb{E}_\pi[G_t \mid s_t, a_t] = \mathbb{E}_\pi\left[\sum_{k=0}^{\infty} \gamma^k R_{t+k+1} \mid s_t, a_t\right]. \quad (9)$$

This greedy strategy will select the optimal action $a^*{}_t$ with the highest $Q$ value; the agent obtains the optimal policy $\pi^*(s_t) = a^*{}_t = \underset{a \in A(s)}{\operatorname{argmax}} Q_{\pi^*}(s_t, a_t)$ and the optimal action-value function $Q_{\pi^*}(s_t, a_t)$ after the completion of training:

$$Q_{\pi^*}(s_t, a_t) = \mathbb{E}_\pi\left[R_{t+1} + \gamma \max_{a_{t+1}} Q_{\pi^*}(s_{t+1}, a_{t+1}) \mid s_t, a_t\right]$$

$$= \sum_{r \in R} p(s_{t+1}, R_{t+1} \mid s_t, a_t)\left[R_{t+1} + \gamma \max_{a_{t+1}} Q_{\pi^*}(s_{t+1}, a_{t+1})\right]. \quad (10)$$

3.2. Neural Network Architecture. The alignment module builds the neural network based on deep Q-networks by modeling Q-function. It has two convolutional neural networks with the same structure, namely, the target network and the evaluation network. The agent observes the environment to obtain RGB-D images as the input of the neural network. Initially, the RGB-D image is processed by the convolutional layer with the $5 \times 5$ convolution kernel and then performed batch normalization. Whereafter, it uses the ReLU activation function for nonlinear activation. Subsequently, max-pooling is used to reduce the deviation of the estimated mean value caused by the parameter error of the convolutional layer. The unit composed of convolutional layer, batch norm, ReLU, and max-pooling layer is defined as a convolution unit.

The network has six convolutional units, followed by three linear layers interleaved with two ReLU activation layers. Firstly, the target network outputs the adjustment action $a_t$ of the current state with softmax after inputting the RGB-D image. Then, the evaluation network evaluates the output of the target network. Afterward, the state $s_t$ transitions to $s_{t+1}$ after performing $a_t$ the action, and the reward value $R(s_t, a_t)$ is obtained. The evaluation network conducts the backpropagation calculation according to the reward $R(s_t, a_t) = r$ to update the parameters $\theta_i$ of the evaluation network:

$$\theta_{i+1} = \theta_i + \alpha\left[r + \gamma \max_{a_{t+1}} Q_\pi(s_{t+1}, a_{t+1}; \theta_i) - Q_\pi(s_t, a_t; \theta_i)\right]$$
$$\cdot \nabla Q_\pi(s_t, a_t; \theta_i), \quad (11)$$

where the learning rate $\alpha$ is set as $10^{-4}$.

The parameters $\theta_i$ of the evaluation network are updated in real-time; however, the parameters $\theta_i^-$ of the target network are fixed during a batch of iterative training. The target network does not conduct backpropagation calculations. The parameters $\theta_i^-$ of the target network are updated by copying parameters $\theta_i$ from the evaluation network after a batch of iterative training, that is, $\theta_i^- \longleftarrow \theta_i$. The predicted difference $\Delta Q = |Q_E^{\theta_i} - Q_T^{\theta_i^-}|$ gradually shrinks between the predicted value $Q_T$ of the target network and the predicted value $Q_E$ of the evaluation network as the number of iterative training increases. The Huber loss function $\mathscr{L}_i$ used for training is described as follows:

$$\mathscr{L}_i = \begin{cases} \frac{1}{2} \times \left(Q_E^{\theta_i} - Q_T^{\theta_i^-}\right)^2, & \text{for } \Delta Q = \left|Q_E^{\theta_i} - Q_T^{\theta_i^-}\right| < 1, \\ \left|\left(Q_E^{\theta_i} - Q_T^{\theta_i^-}\right) - \frac{1}{2}\right|, & \text{otherwise.} \end{cases}$$

$$(12)$$

The collected continuous sample in training with self-supervised deep reinforcement learning may always be correlated. However, the correlation of the continuous sample will make the variance of the parameter update relatively large. The prioritized experience replay is used to reduce

```
1:   Initialize replay buff D
2:   Initialize evaluation network parameters θ_i
3:   Initialize target network parameters θ_i^- = θ_i
4:   for episode=1, M do
5:      for t = 1, T do
6:         Obtain image s_t from environment
7:         With probability ε select a random adjustment action a_t
8:         otherwise select adjustment action a_t = argmaxQ(s_t, a_t ; θ_i^-)
9:         Execute adjustment action a_t in CoppeliaSim
10:        Obtain image s_{t+1} and reward R_{t+1} = r_t from environment
11:        Store transition (s_t, a_t, R_{t+1}, s_{t+1}) in D
12:        Sample random minibatch of transitions (s_t, a_t, R_{t+1}, s_{t+1}) from D
13:        Set Q_{Ej} = { r_j                                 , for terminal s_{j+1}
                        { r_j + γmaxQ̂(s_{j+1}, a_{j+1} ; θ_j^-)   , for non − terminal s_{j+1}
14:        Perform a gradient descent step on (Q_E^{θ_i} − Q_T^{θ_i^-})^2
15:     end for
16:  end for
```

ALGORITHM 1: System pipeline.

sample correlation and nonstationary distribution. Therefore, the training uses experience replay memory $D_i$ to store each transition $(s_t, a_t, s_{t+1}, R_{t+1})$. Afterward, the training samples a minibatch of transitions from the replay buffer to minimize the loss function. The pseudocode is described in Algorithm 1.

## 4. Simulation Results and Analyses

*4.1. Alignment Strategy Training with Visual and Tactile Perception.* The alignment training of peg-in-hole assembly with self-supervised deep reinforcement learning will be conducted in CoppeliaSim, as illustrated in Figure 6. The assembly system in simulation is equipped with a UR5 robotic arm and RG2 gripper. The working space fixedly places two RGB-D vision sensors. The force/torque sensor is installed between the RG2 gripper and the UR5 robotic arm. The diameter and length of the assembly peg are $\phi 30$ mm and 100 mm, respectively. The assembly clearance of the peg and the hole is 0.8 mm. The simulation workstation has configured the CPU of 3.80 GHz Intel(R) Xeon(R) Gold 522, the GPU of NVIDIA GeForce RTX 3090, and the RAM of 128 GB. The software version of CoppeliaSim on the Ubuntu 16.04 operating system is v4.0 with Bullet Physics 2.83 for dynamic and inverse kinematics modules.

The alignment strategy uses trial and error training based on self-supervised deep reinforcement learning. Firstly, the agent observes the environment through visual perception and obtains an RGB-D image. Then, the agent predicts the contact state and selects adjustment actions. Afterward, the robot recognizes the contact state based on the information of tactile perception, and it gives adjustment action as a prediction label for the visual prediction. Subsequently, visual prediction performs backpropagation calculations based on the prediction label.

Finally, the agent establishes the mapping relationship between visual perception and tactile perception through
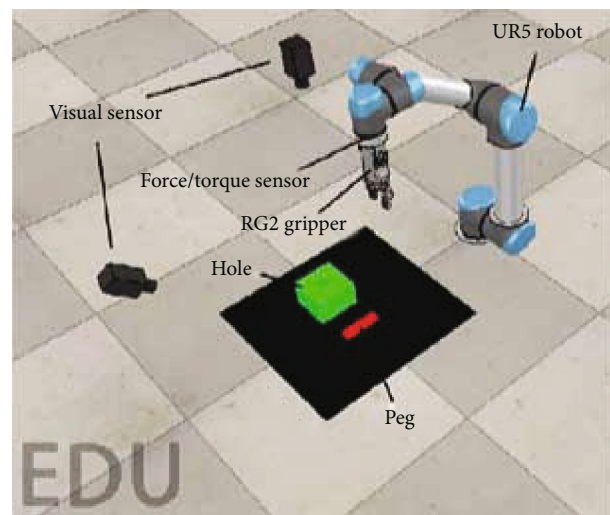


FIGURE 6: Schematic diagram of simulation scene.

the iteration of training. The agent will autonomously train 14,000 times without human intervention. The exploration strategy of the agent uses the $\varepsilon$-greedy strategy, in which its initial value is set to 0.5, and then gradually annealed to 0.1. The agent is more likely to select exploration actions in the early stages of training.

The purpose of exploration is that this can enable the robot to collect more contact state information at the beginning of training. Afterward, the agent selects the action with the highest Q value according to the strategy $\pi(s_t)$. As shown in Figure 7, the rewards obtained by the agent gradually increase to the convergence value as the accuracy of prediction increases.

*4.2. Simulation Results for Peg-in-Hole Assembly.* A series of simulation tests were performed to compare the performance
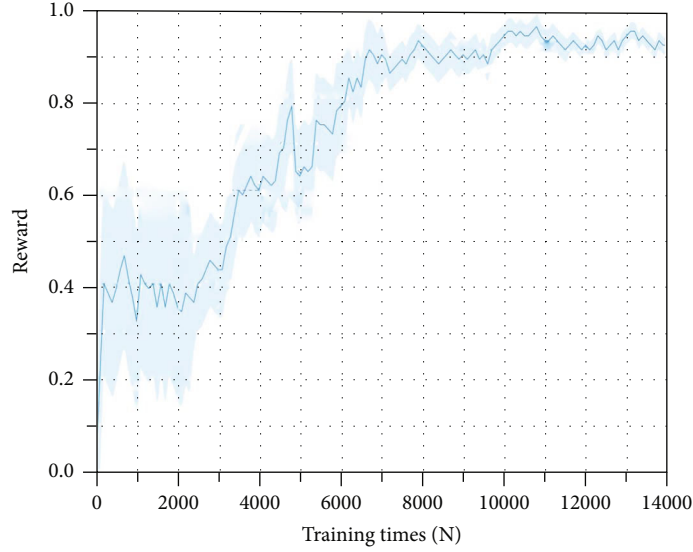
Figure 7: Iterative training reward for an agent.

of tactile perception, multiple perceptions in stages, and combined perceptions in peg-in-hole assembly. As analyzed in Section 2, the method of tactile perception (TP) refers to the peg-in-hole assembly using only the F/T sensor. The hole-finding stage uses visual perception, and the alignment stage uses tactile perception, and this method is called multiple perceptions in stages (MP). The proposed method in this work is called combined perceptions (CP). The robot will perform 1,000 peg-in-hole assembly tests after completing the training with self-supervised deep reinforcement learning. In addition, the robot will, respectively, use methods tactile perception and multiple perceptions in stages to perform 1,000 peg-in-hole assembly tests. The simulation test results are shown in Table 1.

The total time for peg-in-hole assembly using the method of tactile perception and multiple perceptions in stages is 38.46 hours and 34.31 hours, respectively. However, the total time of the combined perceptions is 32.15 hours. It can be seen that the method of combined perceptions takes 6.31 hours less than the method of tactile perception from the simulation results, and the assembly efficiency has improved by 16.41% compared with the method of tactile perception. Besides, the method of combined perceptions reduces 2.16 hours less than the method of multiple perceptions in stages, and the assembly efficiency has improved by 6.3% compared with the method of multiple perceptions in stages. This proves that the proposed method not only learns alignment skills but also improves assembly efficiency. Subsequently, 100 assembled samples are randomly selected for analysis and comparison, as illustrated in Figure 8.

Although the minimum assembly time and the maximum assembly time are relatively close among the three perception methods, the distribution area of the assembly time using the method of combined perceptions concentrates on a smaller time area. The total standard deviation of tactile perception (TP), multiple perceptions in stages (MP), and combined perceptions (CP) are 11.6926, 8.2279, and

Table 1: The total time of peg-in-hole assembly with three perception methods.

| Method | Total assembly time (h) |
| --- | --- |
| Tactile perception (TP) | 38.46 |
| Multiple perceptions in stages (MP) | 34.31 |
| Combined perceptions (CP) | 32.15 |
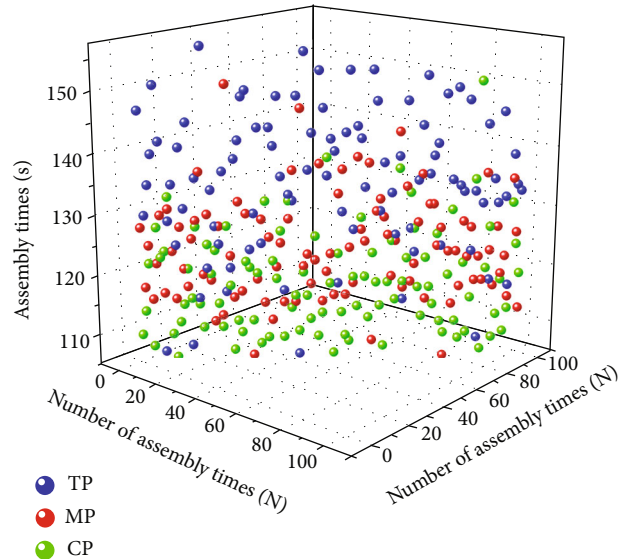


Figure 8: Scatter plot of assembly time.

5.1998, respectively. In addition, the standard error was also analyzed for the three methods, as shown in Figure 9. It can be seen that the method of the combined perceptions not only has better efficiency but also has smaller efficiency fluctuations.

Figure 9: Comparison results of standard error for assembly time.

## 5. Conclusions and Future Work

In this paper, we proposed an alignment method of combined perception for peg-in-hole assembly with self-supervised deep reinforcement learning. The proposed method has combined tactile perception and visual percept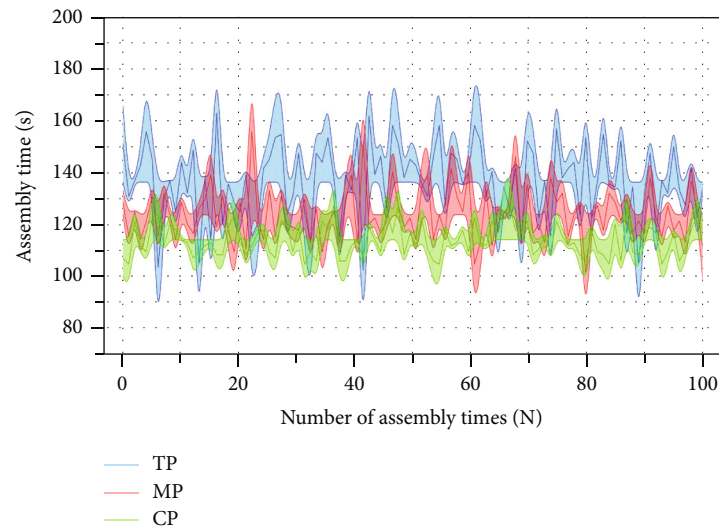ion to better perceive the environment information. The agent does not need human interference during the training process, which greatly reduces the difficulty and cost of data collection. In CoppeliaSim simulation, with the iterative training of the agent, visual perception and tactile perception have established a mapping relationship so that the robot can better perceive the changes of environmental information in the assembly.

From the simulation results, it can be seen that the assembly efficiency is improved after the agent learns the combined perception, and the stability of the assembly efficiency is better than the single perception method. The combined perception increases the perception ability of the robot, which will enable the robot to complete more complex tasks in an unstructured environment. In future research work, we hope to be able to apply the combined perception method to more tasks. In addition, we will still have committed to the research work about improving the efficiency of the peg-in-hole assembly.

## Data Availability

The data is available at https://github.com/Bensonwyz/Alignment-Method-of-Combined-Perception.

## Conflicts of Interest

We declare that we have no financial and personal relationships with other people or organizations that can inappropriately influence our work; there is no professional or other personal interest of any nature or kind in any product, service, and/or company that could be construed as influencing the position presented in, or the review of, the manuscript entitled.

## References

[1] A. Zeng, "Learning visual affordances for robotic manipulation[D]," Princeton University, 2019.

[2] Z. Tang, G. Zhao, and T. Ouyang, "Two-phase deep learning model for short-term wind direction forecasting," *Renewable Energy*, vol. 173, pp. 1005–1016, 2021.

[3] S. Fong, W. Song, K. Cho, R. Wong, and K. Wong, "Training classifiers with shadow features for sensor-based human activity recognition," *Sensors*, vol. 17, no. 3, p. 476, 2017.

[4] T. Li, S. Fong, K. K. L. Wong, Y. Wu, X. S. Yang, and X. Li, "Fusing wearable and remote sensing data streams by fast incremental learning with swarm decision table for human activity recognition," *Information Fusion*, vol. 60, pp. 41–64, 2020.

[5] K. Lan, S. Fong, L. S. Liu et al., "A clustering based variable sub-window approach using particle swarm optimisation for biomedical sensor data monitoring," *Enterprise Information Systems*, vol. 15, no. 1, pp. 15–35, 2021.

[6] F. J. Abu-Dakka, B. Nemec, A. Kramberger, A. G. Buch, N. Krüger, and A. Ude, "Solving peg-in-hole tasks by human demonstration and exception strategies," *Industrial Robot: An International Journal*, vol. 41, no. 6, pp. 575–584, 2014.

[7] H. C. Song, Y. L. Kim, and J. B. Song, "Guidance algorithm for complex-shape peg-in-hole strategy based on geometrical information and force control," *Advanced Robotics*, vol. 30, no. 8, pp. 552–563, 2016.

[8] L. Roveda, N. Iannacci, F. Vicentini, N. Pedrocchi, F. Braghin, and L. M. Tosatti, "Optimal impedance force-tracking control design with impact formulation for interaction tasks," *IEEE Robotics and Automation Letters*, vol. 1, no. 1, pp. 130–136, 2016.

[9] L. Roveda, N. Iannacci, and L. M. Tosatti, "Discrete-time formulation for optimal impact control in interaction tasks," *Journal of Intelligent & Robotic Systems*, vol. 90, no. 3, pp. 407–417, 2018.

[10] J. Yuan, R. Guan, L. Du, and S. Ma, "A robotic gripper design and integrated solution towards tunnel boring construction equipment," in *2020 IEEE/RSJ international conference on intelligent robots and systems (IROS)*, pp. 2650–2655, Las Vegas, NV, USA, Oct 2020.

[11] Te Tang, H.-C. Lin, Y. Zhao, W. Chen, and M. Tomizuka, "Autonomous alignment of peg and hole by force/torque measurement for robotic assembly," in *2016 IEEE international conference on automation science and engineering (CASE)*, pp. 162–167, Fort Worth, TX, USA, Aug 2016.

[12] Z. Liu, L. Song, Z. Hou, K. Chen, S. Liu, and J. Xu, "Screw insertion method in peg-in-hole assembly for axial friction reduction," *IEEE Access*, vol. 7, pp. 148313–148325, 2019.

[13] T. Inoue, G. De Magistris, A. Munawar, T. Yokoya, and R. Tachibana, "Deep reinforcement learning for high precision assembly tasks," in *2017 IEEE/RSJ international conference on intelligent robots and systems (IROS)*, pp. 819–825, Vancouver, BC, Canada, Sept 2017.

[14] T. Ren, Y. Dong, D. Wu, and K. Chen, "Learning-based variable compliance control for robotic assembly," *Journal of Mechanisms and Robotics*, vol. 10, no. 6, 2018.

[15] P. Zou, Q. Zhu, J. Wu, and R. Xiong, "Learning-based optimization algorithms combining force control strategies for peg-in-hole assembly," in *2020 IEEE/RSJ international conference on intelligent robots and systems (IROS).*, pp. 7403–7410, Las Vegas, NV, USA, 24 Oct.-24 Jan. 2021.

[16] J. Xu, Z. Hou, Z. Liu, and H. Qiao, "Compare contact model-based control and contact model-free learning: a survey of robotic peg-in-hole assembly strategies," arXiv preprint arXiv: 1904.05240, 2019.

[17] T. Jiang, H. Cui, X. Cheng, and W. Tian, "A measurement method for robot peg-in-hole prealignment based on combined two-level visual sensors," *IEEE Transactions on Instrumentation and Measurement*, vol. 70, pp. 1–12, 2021.

[18] Y. Liao, W. Chen, H. Wang, and R. Wu, "A peg-in-hole assembly strategy using uncalibrated visual servoing," in *2019 IEEE international conference on robotics and biomimetics (ROBIO),*, pp. 1845–1850, Dali, China, Dec 2019.

[19] J. C. Triyonoputro, W. Wan, and K. Harada, "Quickly inserting pegs into uncertain holes using multi-view images and deep network trained on synthetic data," in *2019 IEEE/RSJ international conference on intelligent robots and systems (IROS)*, pp. 5792–5799, Macau, China, Nov 2019.

[20] R. L. Haugaard, J. Langaa, C. Sloth, and A. G. Buch, "Fast robust peg-in-hole insertion with continuous visual servoing," arXiv preprint arXiv: 2011.06399, 2020.

[21] R. J. Chang, C. Y. Lin, and P. S. Lin, "Visual-based automation of peg-in-hole microassembly process," *Journal of Manufacturing Science and Engineering*, vol. 133, no. 4, 2011.

[22] Y. Liu, D. Romeres, D. K. Jha, and D. Nikovski, "Understanding multi-modal perception using behavioral cloning for peg-in-a-hole insertion tasks," ar Xiv preprint ar Xiv: 2007.11646, 2020.

[23] J. Ding, C. Wang, and C. Lu, "Transferable trial-minimizing progressive peg-in-hole model," in *2019 IEEE/RSJ international conference on intelligent robots and systems (IROS)*, pp. 5862–5868, Macau, China, Nov 2019.

[24] A. Owens and A. A. Efros, "Audio-visual scene analysis with self-supervised multisensory features[C]," in *Proceedings of the European Conference on Computer Vision (ECCV)*, pp. 631–648, Munich, Germany, 2018.

[25] C. Finn and S. Levine, "Deep visual foresight for planning robot motion," in *2017 IEEE international conference on robotics and automation (ICRA)*, pp. 2786–2793, Singapore, 29 May-3 June 2017.

[26] J. Sinapov, C. Schenck, and A. Stoytchev, "Learning relational object categories using behavioral exploration and multimodal perception," in *2014 IEEE international conference on robotics and automation (ICRA),*, pp. 5691–5698, Hongkong, China, 31 May-7 June 2014.

[27] Y. Zheng, X. Zhang, Y. Chen, and Y. Huang, "Peg-in-hole assembly based on hybrid vision/force guidance and dual-arm coordination," in *2017 IEEE international conference on robotics and biomimetics (ROBIO),*, pp. 418–423, Macau, Macao, Dec 2017.

[28] M. A. Lee, Y. Zhu, K. Srinivasan et al., "Making sense of vision and touch: self-supervised learning of multimodal representations for contact-rich tasks," in *2019 international conference on robotics and automation (ICRA)*, pp. 8943–8950, Montreal, QC, Canada, May 2019.

[29] X. Zhang, Y. Zheng, J. Ota, and Y. Huang, "Peg-in-hole assembly based on two-phase scheme and f/t sensor for dual-arm robot," *Sensors*, vol. 17, no. 9, p. 2004, 2017.

[30] C. Olah, "Calculus on computational graphs: backpropagation," 2015, http: //colah. github.io/posts/2015-08-Backprop/.

*Research Article*

# Application of Multiscale Facial Feature Manifold Learning Based on VGG-16

**Huilin Ge ⓘ, Zhiyu Zhu, Runbang Liu, and Xuedong Wu ⓘ**

*School of Electronic Information, Jiangsu University of Science and Technology, Zhenjiang 212003, China*

Correspondence should be addressed to Huilin Ge; ghl1989@just.edu.cn

*Purpose*. In order to solve the problems of small face image samples, high size, low structure, no label, and difficulty in tracking and recapture in security videos, we propose a popular multiscale facial feature manifold (MSFFM) algorithm based on VGG16. *Method*. We first build the VGG16 architecture to obtain face features at different scales and construct a multiscale face feature manifold with face features at different scales as dimensions. At the same time, the recognition rate, accuracy rate, and running time are used to evaluate the performance of VGG16, LeNet-5, and DenseNet on the same database. *Results*. From the results of comparative experiments, it can be seen that the recognition rate and accuracy of VGG16 are the highest among the three networks. The recognition rate of VGG16 is 97.588%, and the accuracy is 95.889%. And the running time is only 3.5 seconds, which is 72.727% faster than LeNet-5 and 66.666% faster than DenseNet. *Conclusion*. The model proposed in this paper breaks through the key problem in the face detection and tracking problem in the public security field, predicts the position of the face target image in the time dimension manifold space, and improves the efficiency of face detection.

## 1. Introduction

Face recognition [1–5], as a biometric recognition technology, is one of the hot topics in the research fields of pattern recognition, image processing, machine vision, neural networks, and cognitive science in recent years. At the same time, face recognition, as a biometric identification technology with high stability, high accuracy, difficult to copy, and easy to be accepted by humans [6–9], has a wide range of application prospects in the fields of identity authentication, security monitoring, human-computer interaction, etc. With the increasing innovation of information technology, the processing of images by face recognition technology has become more and more complex. With sufficient samples, single background, and stable ambient light, most algorithms can achieve higher recognition rates.

In practical applications, how to solve the influence of environmental factors, human sentiments, and posture changes has become a difficult problem in testing various algorithms. The face recognition algorithm based on eigenface extracts face features by way of dimensionality reduction. Although the computational complexity is reduced, some effective features will be lost while reducing the dimensionality.

In order to reflect the nonlinear structure of image features, two classical manifold learning methods have been proposed by previous researchers, which are ISO metric mapping (ISOMAP) [10–12] and local linear embedding (LLE) [13–15]. By learning the mapping from environmental space to eigenspace, the structure between adjacent points after projection can be preserved. Although such manifold learning methods can model the manifold structure of the data, they require a large amount of dense data as training samples, which is not applicable to some practical applications. Therefore, this paper constructs convolutional neural network (CNN) architecture to obtain face features at different scales, so as to solve the problem of insufficient sample size.

In recent years, CNN [16–20] has become a research hotspot in the field of speech analysis and image recognition, especially in the field of face recognition. The CNN makes full use of the locality of the data itself by combining the local perception area of the face image, sharing the weight, and spatially. This feature has a certain degree of robustness to illumination changes, posture, and occlusion.

224×224×3

112×112×128

224×224×64

56×56×256

28×28×512

14×14×512

7×7×512

1×1×4096

1×1×1000

■ Convolution+ReLU                    ■ Max pooling

■ Fully connected+ReLu                ■ Softmax
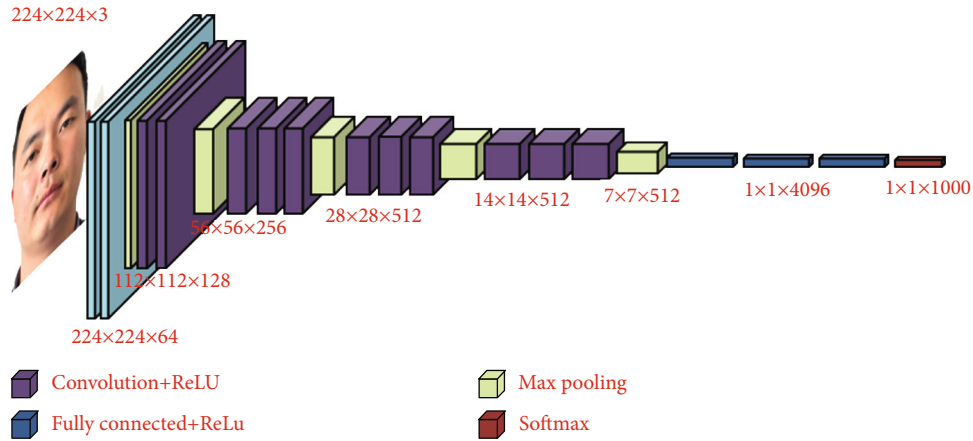
Figure 1: Network structure of VGG16.
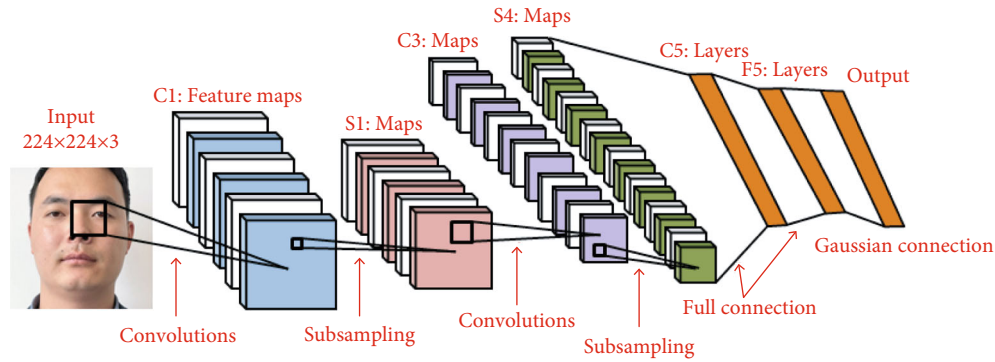


Figure 2: The network structure of LeNet-5.

Previously, there have been many studies on face recognition, such as methods based on statistical manifolds [21–24] and methods combined with deep neural networks. It can be seen that the image classification method based on the manifold will still maintain considerable research enthusiasm for a long time in the future.

In this paper, a CNN is used to construct a face recognition system. First, the VGG16 model [25–29] is used to extract facial features, and then multiscale facial feature manifold (MSFFM) [30, 31] is used for classification and tested in the actual environment.

## 2. Methodology

### 2.1. CNN Architecture

*2.1.1. VGG16.* VGGNet was proposed by the Oxford Visual Geometry Group of Oxford University [32]. It explored the relationship between the depth of CNN and its performance. By repeatedly stacking 33 small convolution kernels and 22 maximum pooling layers, it successfully constructed CNN with 16 to 19 layers deep. VGGNet is a modification based on AlexNet [33]; the training image size is $224 \times 224$. All images are subtracted from the mean of all training images. VGGNet contains many levels of networks, ranging in depth from 11 to 19 layers. The more commonly used ones are

VGGNet-16 and VGGNet-19. VGGNet divides the network into 5 segments, and each segment connects multiple $3*3$ convolutional networks in series. Each segment of convolution is followed by a maximum pooling layer, and the last is 3 fully connected layers and a softmax layer. The network structure of VGG16 is shown in Figure 1.

*2.1.2. LeNet-5.* LeNet-5 [34] is a classic structure of CNN, the pioneering work of CNN, mainly used for handwritten font recognition. Although the network is simple, the structure is complete, and the convolutional layer, pooling layer, and full link layer have been used until now. The number of layers is very shallow, and the size of the kernel is single. The kernel sizes used by the three convolutional layers of C1, C3, and C5 are all $5 \times 5$. The feature map size of C5 is $1 \times 1$ because the feature map size of S4 is $5 \times 5$ and the kernel size is the same, so the result size of the convolution is $1 \times 1$. The window size used by the two pooling layers of S2 and S4 is $2 \times 2$, and there are two types of pooling here. F6 is a fully connected layer with 84 neurons. The network structure of LeNet-5 is shown in Figure 2.

*2.1.3. DenseNet.* DenseNet [35] breaks away from ResNet's shortcomings of deepening the number of network layers [36] and Inception's shortcomings of widening network structure to improve network performance [37]. From the

Figure 3: DenseNet's network structure.

perspective of features, through feature reuse and bypass settings, it has greatly reduced the parameter quantity of the network alleviates the emergence of gradient vanishing problem to a certain extent. Combining the assu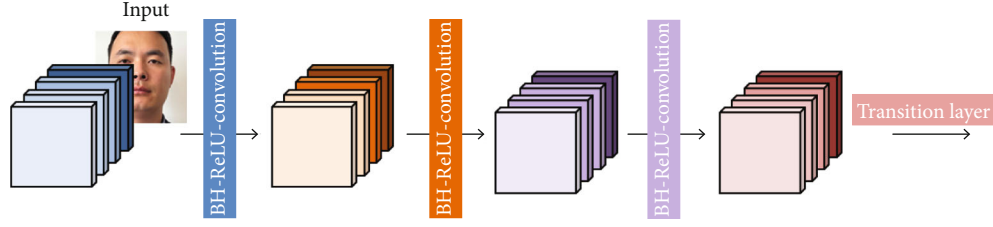mptions of information flow and feature reuse, DenseNet deserves to be the best paper of the year at the 2017 Computer Vision Conference. DenseNet has absorbed the most essential part of ResNet and has done more innovative work on this, which further improves the network performance.

DenseNet is a CNN with dense connections. In this network, there is a direct connection between any two layers, that is, the input of each layer of the network is the unions of the outputs of all the previous layers, and the feature map learned by this layer will also be directly passed to all subsequent layers that are used as input. The network structure of DenseNet is shown in Figure 3.

### 2.2. Manifold Learning

*2.2.1. Manifold Types Commonly Used in Image Classification.* In the field of computer vision, the covariance matrix conforming to the manifold geometry of the symmetric positive definite matrix has been proven to have very good effects in image classification tasks. Because the covariance matrix can better adapt to various types of image changes, it has become a mainstream image feature representation method in image classification based on Riemannian manifolds. Commonly used manifold types for image classification are symmetric positive definite matrix manifold and Gmssmami manifold.

*2.2.2. Kernel Function on Manifold.* In the field of machine learning, the kernel method is a type of learning algorithm used to solve pattern recognition problems. The most classic example is the support vector machine (SVM). The main idea is to embed the data in the original space into a specific high-dimensional space through some kind of implicit non-linear mapping, so that the linearly inseparable data in the original space becomes linearly separable after being mapped to the high-dimensional space.

Literature [18] presents a kernel function on the manifold of a symmetric positive definite matrix. According to the Frobenius norm and polarization formula, the inner product of two $n$-dimensional symmetric positive definite matrices $X_1$ and $X_2$ in the tangent space Tr Symn is defined as Equation (1).

$$\{\log (X_1), \log (X_2)\} = Tr\{\log (X_1) \log (X_2)\}. \quad (1)$$

It can be seen that the corresponding kernel function on Symn is defined as Equation (2).

$$k_L(X_1, X_2) = Tr\{\log X_1 \log X_2\}. \quad (2)$$

*2.2.3. Face Super-Resolution Algorithm Based on Sparse Representation.* The SR method adds sparse representation theory on the basis of manifold learning, uses a subset of the training sample block to linearly represent the input low-resolution image block, and uses the L1 norm to solve the optimal weight coefficient. We use the most similar face training sample block to represent the effect of the input image block.

For each image block $X(i, j)$ of the input low-resolution image, all training sample blocks at the same position in the low-resolution sample space are sparsely learned to reconstruct the representation coefficients, and the objective function is expressed as Equation (3).

$$argmin\|w(i, j)\| \; s.t. \left\| X(i, j) - \sum_{m=1}^{M} Y^m(i, j)w_m(i, j) \right\|_2^2. \quad (3)$$

Then, the objective function is transformed into Equation (4) for solving.

$$argmin \left\| X(i, j) - \sum_{m=1}^{M} Y^m(i, j)w_m(i, j) \right\|_2^2 + \rho\|w(i, j)\|_1. \quad (4)$$

We linearly weigh the representation coefficient obtained by Equation (4) and the corresponding high-resolution training sample block to obtain the high-resolution prediction image block. This algorithm solves the problem that the solution is not unique in the location-based image block algorithm.

### 2.3. Data Set

*2.3.1. Data Sources.* In practical applications, the biggest challenge of the face recognition system is that the recognition effect is not ideal when there are pose changes and occlusions. Therefore, this paper collects many types of face images in practical applications as experimental samples. The normal face sample is basically aligned or inclined at a small angle, without occlusion, and single expression, as shown in Figure 4(a). The face samples with posture changes have a variety of expressions and side faces as shown in Figure 4(b). A sample of an occluded face is shown in Figure 4(c). In the system test, 20 face images of each of 36

(a)                                          (b)                                          (c)
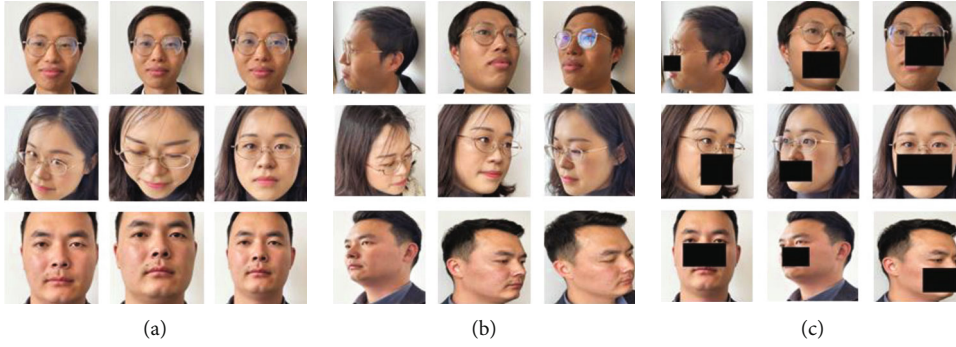
FIGURE 4: Face samples in various situations based on (a) the normal face sample, (b) the face samples with posture changes, and (c) the face samples with an occluded face.

humans were collected, and a total of 720 images were collected. The classification and pixels of the data set are shown in Table 1.

*2.3.2. Experimental Environment.* The software platform, processor, and operating system of the experimental environment are shown in Table 2. In order to ensure the fairness of the experimental results, all methods are implemented using the source code provided by the original author as much as possible, and the main parameters are adjusted and set according to the instructions in the original document.

*2.4. Evaluation Criteria.* This paper uses recognition rate, accuracy rate, and running time to evaluate the performance of VGG16, LeNet-5, and DenseNet.

First of all, the recognition rate refers to the ratio of the number of all recognized images to the total images, and the calculation method is as shown in Equation (5).

$$\text{Recognition rate} = \frac{n_R}{N}. \tag{5}$$

In Equation (5), $n_R$ refers to the number of all recognized images, and $N$ knows that it is the total number of images.

Second, accuracy refers to the ratio of the number of correctly identified images to the total number. The calculation method is as shown in Equation (6).

$$\text{Accuracy} = \frac{n_A}{N}. \tag{6}$$

In Equation (6), $n_A$ refers to the number of correctly identified images, and $N$ refers to it is the total number.

## 3. Experimental Results

*3.1. Recognition Rate.* Figure 5 shows the comparison curve of the recognition rate of VGG16, LeNet-5, and DenseNet.

It can be seen from Figure 5 that the recognition rate is proportional to the number of samples, and the recognition rate of MSFFM based on VGG16 is the highest. When the number of samples is 240, the recognition rate is 97.588%.

*3.2. Accuracy.* Figure 6 shows the accuracy comparison curve of VGG16, LeNet-5, and DenseNet. It can be seen from the

TABLE 1: Classification and pixels of the data set.

| Normal | Posture change | Covered | Pixel |
| --- | --- | --- | --- |
| 240 | 240 | 240 | $224 \times 224$ |

TABLE 2: Software platform, processor, and operating system of the experimental environment.

| Software platform | Processor | Operating system |
| --- | --- | --- |
| Matlab 2020a | Intel E7-2684 v5 | IOS |

comparison result that the accuracy rate of the face recognition algorithm based on VGG16 is 95.889%.

*3.3. Computational Time.* By comparing the data in Table 3, it can be seen that on the database, the time required for the three network pairs to complete an operation is about 3.5 seconds, 9.1 seconds, and 11.6 seconds, respectively, and the model we proposed can shorten the calculation time by nearly half. In contrast, our proposed VGG16 has achieved excellent results in reducing computational complexity. In general, VGG16 can effectively reduce the computational complexity, so it has better feasibility in practical applications.

## 4. Discussion

This paper introduces a CNN that integrates manifold learning. It uses the spatial manifold information of the image as an additional feature and integrates it into the improved CNN model, so as to improve the pertinence of the model to the data and improve the accuracy. The model proposed in this paper makes up for the lack of generalization ability.

Facial super-resolution is a specific scene application of image super-resolution technology, and facial super-resolution has attracted widespread attention from scholars. In actual scenes, the acquired face images are usually blurry and low quality, which is caused by a variety of reasons.

First, the location of the surveillance camera is high, the shooting range is large, and the target face image is small; second, the surveillance equipment is limited by storage space, and the video image is highly compressed, so the image loses
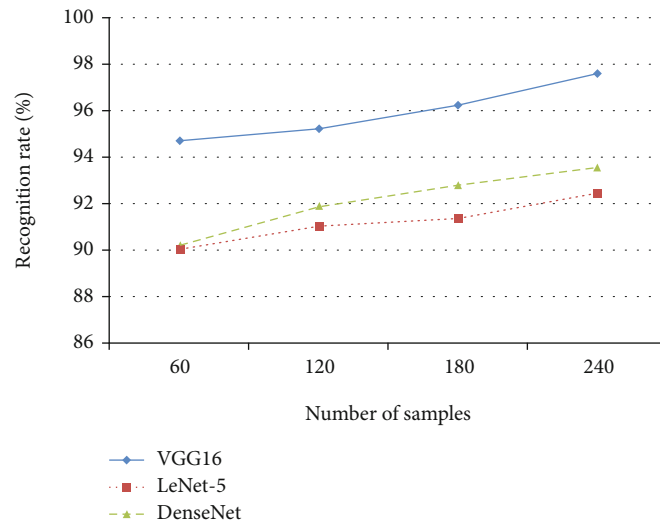
Figure 5: The recognition rate of VGG16, LeNet-5, and DenseNet.
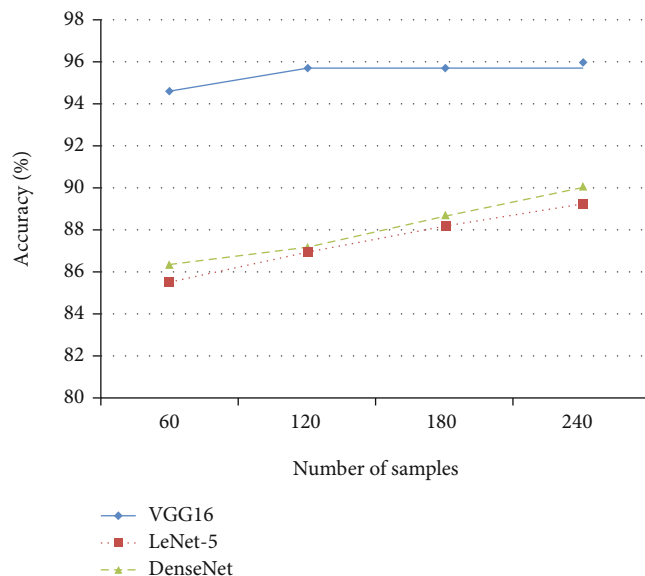


Figure 6: The accuracy comparison curve of VGG16, LeNet-5, and DenseNet.

Table 3: The time required for the three types of networks to complete an operation.

| VGG16 (s) | LeNet-5 (s) | DenseNet (s) |
| --- | --- | --- |
| 3.5 | 9.1 | 11.6 |

detailed information; third, the external environment is rainy weather and low light at night will further reduce the quality of the captured images.

The existing image feature representation methods focus on matrix-type manifolds. How to fuse multiple types of Riemannian manifolds, such as linear subspaces, probability distributions to form a multimodel representation method, and perform different manifolds the effective unification of the characteristic information will be a problem worthy of attention.

With the continuous deepening of research on CNN, vector-based convolution and pooling processing have been fully studied. In fact, in a network, we can apply Riemannian manifold geometry to the data in the middle layer for processing. This pooling and iterative process in the form of a matrix can have a positive effect on the final output of the network. For future implementation, we will continue to carry out related research in this direction.

## 5. Conclusion

We researched and adopted a popular multiscale facial feature algorithm based on VGG16 and designed and implemented face recognition on this basis. The system first intercepts each frame of image in the video stream for face detection and then recognizes the detected faces. The actual test results show that the system has a high recognition rate for face pose, expression, and occlusion changes when the training samples are sufficient. There is still a lot of research space for the algorithms based on manifold learning in face recognition and the application of these algorithms in face recognition systems.

## Data Availability

The [face image] data used to support the findings of this study have not been made available because [we collected face images on our own which includes faces of members from our project. They are not willing to give their information to the public].

## Conflicts of Interest

The authors declare that there is no conflict of interests.

## Acknowledgments

## References

[1] J. H. Lai, P. C. Yuen, and G. C. Feng, "Face recognition using holistic Fourier invariant features," *Pattern Recognition*, vol. 34, no. 1, pp. 95–109, 2001.

[2] J. Wright, A. Y. Yang, A. Ganesh, S. S. Sastry, and Y. Ma, "Robust face recognition via sparse representation," *IEEE Transactions on Pattern Analysis & Machine Intelligence*, vol. 55, no. 1, pp. 307–316, 2009.

[3] P. J. Phillips, Hyeonjoon Moon, S. A. Rizvi, and P. J. Rauss, "The FERET evaluation methodology for face-recognition algorithms," *IEEE Transactions on pattern analysis and machine intelligence*, vol. 22, no. 10, pp. 1090–1104, 2000.

[4] X. Tan and B. Triggs, "Enhanced local texture feature sets for face recognition under difficult lighting conditions," *Asahimas Flat Glass*, vol. 4778, no. 6, pp. 1635–1650, 2007.

[5] P. J. Phillips, H. Wechsler, J. Huang, and P. J. Rauss, "The FERET database and evaluation procedure for face-recognition algorithms," *Image and Vision Computing*, vol. 16, no. 5, pp. 295–306, 1998.

[6] T. Grüter, M. Grüter, and C. C. Carbon, "Neural and genetic foundations of face recognition and prosopagnosia," *Journal of Neuropsychology*, vol. 2, no. 1, pp. 79–97, 2008.

[7] D. Masip, G. Lapedriza, and J. Vitria, "Boosted online learning for face recognition," *IEEE Transactions on Systems, Man, and Cybernetics, Part B (Cybernetics)*, vol. 39, no. 2, pp. 530–538, 2009.

[8] N. Pinto and D. Cox, "An evaluation of the invariance properties of a biologically-inspired system for unconstrained face recognition," in *ICST Conference on Biologically Inspired Network, Information, and Computing Systems*, pp. 505–518, Berlin, Heidelberg, 2010.

[9] B. Tistarelli, E. Grosso, and Y. Grosso, "Identity management in face recognition systems," *Lecture Notes in Computer Science*, vol. 5372, pp. 67–81, 2008.

[10] S. Weng, C. Zhang, and Z. Lin, "Exploring the structure of supervised data by Discriminant Isometric Mapping," *Pattern Recognition*, vol. 38, no. 4, pp. 599–601, 2005.

[11] X. H. Fu, "The isometric extension of the into mapping from the unit sphere $S_1(E)$ to $S_1 l^\infty(\Gamma)$," *Acta Mathematica Sinica*, vol. 24, no. 3, pp. 87–92, 2008.

[12] N. Zhang and X. M. Tian, "Nonlinear dynamic fault detection method based on isometric mapping," *Journal of Shanghai Jiaotong University*, vol. 45, no. 8, pp. 1202–1206, 2011.

[13] G. Wen and L. Jiang, "Globalizing local neighborhood for locally linear embedding," in *2006 IEEE International Conference on Systems, Man and Cybernetics*, pp. 3491–3496, Taipei, Taiwan, 2006.

[14] X. Teng, B. Wu, W. Yu, and C. Liu, "A hand gesture recognition system based on local linear embedding," *Journal of Visual Languages & Computing*, vol. 16, no. 5, pp. 442–454, 2005.

[15] S. F. Daniel, A. Connolly, J. Schneider, J. Vanderplas, and L. Xiong, "Classification of stellar spectra with local linear embedding," *The Astronomical Journal*, vol. 142, no. 6, p. 203, 2011.

[16] L. Shang, Q. Yang, J. Wang, S. Li, and W. Lei, "Detection of rail surface defects based on CNN image recognition and classification," in *2018 20th International Conference on Advanced Communication Technology (ICACT)*, pp. 45–51, Chuncheon, Korea (South), 2018.

[17] G. Zheng, M. Tan, J. Yu, Q. Wu, and J. Fan, "Fine-grained image recognition via weakly supervised click data guided bilinear CNN model," in *2017 IEEE International Conference on Multimedia and Expo (ICME)*, pp. 661–666, Hong Kong, China, 2017.

[18] Y. Chen and R. Qu, "Study on infringement identification of art works based on CNN image recognition technology," *Journal of Physics: Conference Series*, vol. 1802, no. 3, article 032084, 2021.

[19] R. Kumar, S. Joshi, and A. Dwivedi, "CNN-SSPSO: a hybrid and optimized CNN approach for peripheral blood cell image recognition and classification," *International Journal of Pattern Recognition and Artificial Intelligence*, vol. 47, no. 1, pp. 202–209, 2020.

[20] W. Hao, R. Bie, J. Guo, X. Meng, and S. Wang, "Optimized CNN based image recognition through target region selection," *Optik (Stuttg)*, vol. 156, pp. 772–777, 2018.

[21] P. Turaga, A. Veeraraghavan, A. Srivastava, and R. Chellappa, "Statistical computations on Grassmann and Stiefel manifolds for image and video-based recognition," *IEEE Transactions on Pattern Analysis & Machine Intelligence*, vol. 33, no. 11, pp. 2273–2286, 2011.

[22] P. K. Turaga, A. Veeraraghavan, and R. Chellappa, "Statistical analysis on Stiefel and Grassmann manifolds with applications in computer vision," in *2008 IEEE computer society conference on computer vision and pattern recognition (CVPR 2008)*, Anchorage, Alaska, June 2008.

[23] C. Cafaro, "Information-geometric indicators of chaos in Gaussian models on statistical manifolds of negative Ricci curvature," *International Journal of Theoretical Physics*, vol. 47, no. 11, pp. 2924–2933, 2008.

[24] J. Verbeek, "Learning nonlinear image manifolds by global alignment of local linear models," *IEEE Transactions on Pattern Analysis & Machine Intelligence*, vol. 25, no. 1, p. 335, 2006.

[25] M. Valan, K. Makonyi, A. Maki, D. Vondráček, and F. Ronquist, "Automated taxonomic identification of insects with expert-level accuracy using effective feature transfer from convolutional networks," *Systematic Biology*, vol. 68, no. 6, pp. 876–895, 2019.

[26] N. V. Hieu and N. Hien, "Automatic plant image identification of Vietnamese species using deep learning models," *International Journal of Emerging Trends & Technology in Computer Science*, vol. 68, no. 4, pp. 25–31, 2020.

[27] J. Qiu, X. Lu, X. Wang, and X. Hu, "Research on rice disease identification model based on migration learning in VGG network," *IOP Conference Series: Earth and Environmental Science*, vol. 680, no. 1, article 012087, 2021(10pp).

[28] U. B. Patayon and R. V. Crisostomo, "Automatic identification of abaca bunchy top disease using deep learning models," *Procedia Computer Science*, vol. 179, no. 1, pp. 321–329, 2021.

[29] J. Hagenah, M. P. Heinrich, and F. Ernst, "Deep transfer learning for aortic root dilation identification in 3D ultrasound images," *Current Directions in Biomedical Engineering*, vol. 4, no. 1, pp. 71–74, 2018.

[30] M. Cadoni, E. Grosso, A. Lagorio, and M. Tistarelli, "Interpreting 3D faces for augmented human-computer interaction," in *International Conference on Universal Access in Human-computer Interaction: Users Diversity*, pp. 535–544, Berlin, Heidelberg, 2011.

[31] B. Mandal, X. D. Jiang, and A. Kot, "Multi-scale feature extraction for face recognition," in *2006 1ST IEEE Conference on Industrial Electronics and Applications*, Singapore, 2006.

[32] X. Zhen, J. Chen, Z. Zhong et al., "Deep convolutional neural network with transfer learning for rectum toxicity prediction in cervical cancer radiotherapy: a feasibility study," *Physics in Medicine & Biology*, vol. 62, no. 21, p. 8246, 2017.

[33] A. V. Vedalankar, S. S. Gupta, and R. R. Manthalkar, "Addressing architectural distortion in mammogram using AlexNet and support vector machine," *Informatics in Medicine Unlocked*, vol. 4, article 100551, 2021.

[34] G. Wei, G. Li, J. Zhao, and A. He, "Development of a LeNet-5 gas identification CNN structure for electronic noses," *Sensors*, vol. 87, no. 2, pp. 147–156, 2019.

[35] E. Y. Huan and G. H. Wen, "Transfer learning with deep convolutional neural network for constitution classification with face image," *Multimedia Tools and Applications*, vol. 79, no. 4, pp. 110–119, 2020.

[36] W. E. Lawson, "Multi-attribute residual network (MAResNet) for soft-biometrics recognition in surveillance scenarios," in *2017 12th IEEE International Conference on Automatic Face & Gesture Recognition (FG 2017)*, Washington, DC, USA, 2017.

[37] A. Satapathy and L. Livingston, "A lite convolutional neural network built on permuted Xceptio-inception and Xceptio-reduction modules for texture based facial liveness recognition," *Multimedia Tools and Applications*, vol. 80, no. 2, pp. 10441–10472, 2020.

*Research Article*

# Lowering Nitrogen Oxide Emissions in a Coal-Powered 1000-MW Boiler

**Xiaojuan Chen** [ID],[1] **Haiyang Zhang** [ID],[1] and **Hongwu Qin**[2]

[1]*School of Electronic Information Engineering, Changchun University of Science and Technology, Changchun 130022, China*
[2]*School of Electronic Information Engineering, Changchun University, Changchun 130022, China*

Correspondence should be addressed to Xiaojuan Chen; cxj001@cust.edu.cn

Burning of coal in power plants produces excessive nitrogen oxide ($NO_x$) emissions, which endanger people's health. Proven and effective methods are highly needed to reduce $NO_x$ emissions. This paper constructs an echo state network (ESN) model of the interaction between $NO_x$ emissions and the operational parameters in terms of real historical data. The grey wolf optimization (GWO) algorithm is employed to improve the ESN model accuracy. The operational parameters are subsequently optimized via the GWO algorithm to finally cut down the $NO_x$ emissions. The experimental results show that the ESN model of the $NO_x$ emissions is more accurate than both of the LSTM and ELM models. The simulation results show $NO_x$ emission reduction in three selected cases by 16.5%, 15.6%, and 10.2%, respectively.

## 1. Introduction

The energy statistics in China show that 59.2% of electrical energy comes from thermal electricity. This figure is just one percentage point lower than it was a year ago. The proportion of nonfossil energy sources (such as wind power, photoelectricity, and nuclear power) have increased recently, accounting now for nearly 41% of the total energy. In fact, the rapid development of new energy sources greatly affects the modes of operation of thermal power plants. Because of the uncertainty in energy supplies from wind and solar sources, thermal power plants must compensate for any failure in meeting grid demand. However, constant load changes pose a great challenge for energy conservation and emission reduction. According to new environmental standards in China, the emission of nitrogen oxide ($NO_x$) pollutants from boilers fueled by burning coal must be below 50 milligrams (mg) per standard or normal cubic meters ($Nm^3$) with a reference oxygen ($O_2$) content of 6%. Therefore, a new operation mode for reducing $NO_x$ emissions should be proposed. Most of the coal-fueled power plants have already been equipped with selective catalyst reduction (SCR) modules. With the help of a catalyst, such modules turn $NO_x$ into diatomic nitrogen ($N_2$) and water ($H_2O$). However, too little catalytic material will not adequately reduce the emissions, while too much catalytic material will increase ammonia escape and even block the air preheater [1]. Alternatively, combustion optimization is typically used as a key process for guaranteeing lower $NO_x$ emissions with no additional modifications. Generally, an optimization method consists of two parts: constructing a prediction model and optimizing the operational parameters. However, the $NO_x$ emissions are interrelated with many operational parameters because of the complexity of the combustion process. Accurate modeling of $NO_x$ emissions can be hardly established with conventional methods. Fortunately, the emergence of machine learning techniques presents an alternative effective way for building $NO_x$ emission models. Several $NO_x$ modeling methods have been recently proposed. For instance, Zhou et al. [2] created a $NO_x$ emission model utilizing artificial neural networks (ANNs) and genetic algorithms (GA) for a pulverized coal-fired boiler of a large capacity. Ilamathi et al. [3] combined ANN and GA techniques and optimized the operational parameters for $NO_x$ emission prediction and reduction in a pulverized coal-fired boiler of a 210 MW capacity. Chu et al. [4] established an ANN model that enabled a reduction

of $NO_x$ production. Unfortunately, an ideal ANN model should be trained with highly diverse examples, and ANN is vulnerable to overfitting and poor generalization. Three decades ago, support vector regression (SVR) methods started to compete with the ANN ones in modeling. In particular, the least-square support vector machines (LSSVM) emerged as a more effective variant of the standard support vector machines (SVM). In recent years, SVM and the LSSVM methods have been introduced as effective tools for modeling $NO_x$ emissions. Wu et al. [5] employed SVR for modeling the emissions of nitrogen oxides as well as carbon burnout of a coal-fired boiler of a 300 MW capacity. Tang et al. [6] employed the LSSVM for modeling the emissions of nitrogen oxides and utilized particle swarm optimization (PSO) to improve model accuracy. Lv et al. [7, 8] introduced a novel LSSVM model for $NO_x$ emission prediction and obtained results showing that this LSSVM model maintains good prediction accuracy. Li et al. [9] applied the SVM to establish a $NO_x$ emission prediction model, whose parameters were optimized by an enhanced PSO algorithm. Wang et al. [10] employed a LSSVM to model the emissions of nitrogen oxides for a 1000-MW once-through boiler. Fan et al. [11] fused a continuous restricted Boltzmann machine (CRBM) with SVR to model $NO_x$ emissions. Zhen et al. [12] addressed this modeling problem by integrating the LSSVM with a whale optimization algorithm (WOA). The WOA is used to optimize the kernel function width and penalty factor of the LSSVM. The simulation results showed that this method had stable, high-precision simulation performance. Apart from ANNs and SVMs, extreme learning machines (ELMs) have also been employed for modeling the emissions of nitrogen oxides. Li et al. [13] introduced ELMs as a tool for building a model for the emissions of nitrogen oxides, and they proposed an enhanced algorithm of teaching-learning-based optimization (I-TLBO), in order to fine-tune the ELM parameters and improve the modeling accuracy. Dong et al. [14] proposed the combination of partial least squares (PLS) and ELMs to assess $NO_x$ emissions of a 1000-MW once-through boiler. Recently, deep learning has been applied in image diagnosis [15], human activity recognition [16], and 5G networks [17]. The emergence of deep learning has led to the use of the long short-term memory (LSTM) architectures in modeling $NO_x$ emissions. Yang et al. [18] adopted the LSTM neural network to predict $NO_x$ emissions. Compared with the recurrent neural network (RNN) model, the LSTM model generally demonstrated a higher accuracy. Tan et al. [1] applied the LSTM approach for dynamic modeling of the $NO_x$ emissions of a 660-MW coal-fired boiler. They asserted that the LSTM model outperforms the SVM approach. Xie et al. [19] introduced a novel LSTM method with a new attention mechanism to model the $NO_x$ emissions, and the results demonstrated a superior prediction accuracy of the $NO_x$ emissions.

Additionally, any desirable combustion optimization algorithm should exhibit rapid convergence and high-quality solutions. Indeed, the past two decades witnessed a dramatic increase in the popularity of metaheuristic optimization techniques, and especially the application of these techniques in combustion optimization. For example, Zhou et al. [20] employed a PSO algorithm to optimize the parameters of a SVR model of $NO_x$ emissions. The emissions could be reduced by 32.67% and 16.3%, respectively, when the model was exploited with and without optimization. Wei et al. [21] utilized quantum genetic algorithms (QGA) together with simulated-annealing genetic algorithms (SAGA) for the optimization of the operating parameters, and hence the reduction of the emissions of nitrogen oxides. An improved flower pollination algorithm (IFPA) [22] was used to optimize hyper-parameters. An artificial bee colony (ABC) algorithm [23, 24] was also used for modeling and optimization of coal-fired boilers.

Notwithstanding the dramatic success achieved so far by methods for combustion optimization in lowering the emissions of nitrogen oxides, more improvements are still needed. A candidate for achieving such improvements is a novel variant of recurrent networks, namely, the echo state networks (ESNs). These networks enjoy the advantages of simplicity and high accuracy, which enable them to find diverse applications such as the prediction of the remaining useful life (RUL) [25], energy prediction [26], and anomaly detection [27]. Nevertheless, ESNs have been hardly applied for modeling the emissions of nitrogen oxides. Moreover, the grey wolf optimization (GWO) method has been introduced and subsequently employed in tackling real-world optimization problems [28–30]. In this work, the GWO method is used to optimize both the ESN model parameters and the operational parameters with the target of lowering the emissions of nitrogen oxides.

In summary, we introduce a combustion optimization method to lower the emissions of nitrogen oxides for a coal boiler that has a 1000-MW capacity. We introduced the ESN for modeling the $NO_x$ emissions and compared the ESN model against the ELM and LSTM ones. Meanwhile, we used the GWO algorithm for optimizing the operational parameters and lowering the emissions of nitrogen oxides based on an earlier $NO_x$ emission model. For validating the proposed method, we selected three typical values of the boiler maximum continuous rating (BMCR), namely, 100%, 90%, and 80%, for optimization by the GWO algorithm.

## 2. Methodology

*2.1. Echo State Networks.* An echo state network (ESN) is a variant of recurrent neural networks (RNN), basically distinguished via its dynamic reservoir (DR) within its sparsely connected hidden layer. The purpose of this reservoir is to allow the input sequence to expand nonlinearly. The ESN essentially has an RNN architecture, where the input and output layers are detached from each other by recurrent connected units. The network is trained through an initial random choice of both the input and the reservoir weights, followed by fixing these weights through the overall training process. Any feedback signals from the outputs to the reservoir are initially set randomly and then kept fixed in a similar fashion. The supervised training of the network updates only the readout weights. The basic architecture of an ESN is depicted in Figure 1.
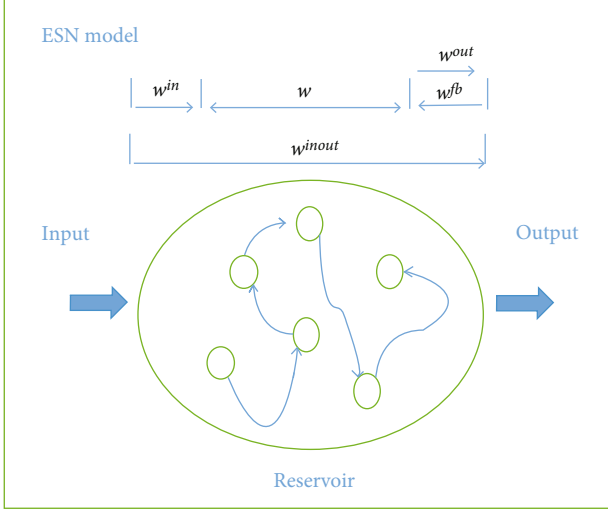
Figure 1: Architecture of an ESN.

We use the symbols $W^{\text{in}}$, $W$, and $W^{\text{fb}}$ to denote the backward weight matrices of the input, the reservoir, and the output of the ESN, respectively. We also use the symbols $W^{\text{inout}}$ and $W^{\text{out}}$ to refer to the readout matrices, and employ $u(t)$, $x(t)$, and $y(t)$ to designate the ESN inputs, reservoir states, and outputs, respectively. The number of training patterns is denoted by $t$. The following two equations define the general dynamics of a standard echo state network.

$$x(t+1) = f\left(W^{\text{in}}u(t+1) + Wx(t) + W^{\text{fb}}y(t)\right), \quad (1)$$

$$y(t+1) = f^{\text{out}}\left(W^{\text{out}}x(t+1) + W^{\text{inout}}u(t+1)\right). \quad (2)$$

The two functions, $f$ and $f^{\text{out}}$, are activation functions that can be either of the hyperbolic tangent (tanh) or linear types. As we have formerly asserted, the backward weights and those of the input and the reservoir are initially set randomly and then kept fixed. In order to define these weight matrices, we should consider certain metrics. In particular, we should carefully define the input scaling and the connectivity rate from the outset. Here, the term "input scaling" refers to the weight value range, while the term "connectivity" indicates how many connections we need to define for each matrix. We can guarantee that the network will not be driven by the internal or reservoir dynamics, provided the aforementioned factors are well set.

*2.2. Grey Wolf Optimizer.* The grey wolf optimizer (GWO) is a nature-inspired algorithm that mimics the hierarchy of leadership and the mechanism of hunting in grey wolves [31]. These wolves are apex predators that live in packs of four possible types: alpha, beta, delta, or omega. The leaders of the pack (called alphas) make decisions about daily activities for the entire pack. The alpha or dominant wolf is distinguished by the best management skills rather than the strongest body. As the second-ranking wolf in the pack hierarchy, the beta wolf provides feedback and helps the alpha one in decision-making. An omega wolf has the lowest rank

in the pack, but it has a key role in maintaining the dominance structure. A delta wolf is inferior to both the alpha and beta ones but superior to the omega wolf in the aforementioned hierarchy. The delta wolves might be scouts, sentinels, elders, hunters, or caretakers. Group hunting in wolf packs has three major stages: tracking or searching, prey encirclement, and prey attack. The GWO algorithm is designed based on this hierarchy of leadership and mechanism of hunting. The prey encirclement behavior can be mathematically expressed as

$$\vec{D} = \left| C \cdot \vec{X_p}(t) - \vec{X}(t) \right|, \quad (3)$$

$$\vec{X}(t+1) = \vec{X_p}(t) - A \cdot \vec{D}. \quad (4)$$

The symbol $t$ denotes the present iteration, $\vec{X_p}$ denotes the prey position vector, and $\vec{X}$ designates the wolf position vector, while $A$ and $C$ stand for two coefficients, whose values are computed via

$$A = 2a \cdot r_1 - a, \quad (5)$$

$$C = 2 \cdot r_2. \quad (6)$$

The value of $a$ is iteratively decreased in a linear fashion from 2 to 0, and $r_1$ and $r_2$ are numbers randomly generated from the unit interval [0,1]. Equations (3) and (4) describe how grey wolves update their positions, while still encircling their preys.

The wolf pack hunting pattern is led by the alpha wolves and often also by the beta and delta ones. These patterns can be mathematically modeled as follows:

$$\vec{D_\alpha} = \left| C_1 \cdot \vec{X_\alpha} - \vec{X} \right|,$$
$$\vec{D_\beta} = \left| C_2 \cdot \vec{X_\beta} - \vec{X} \right|, \quad (7)$$
$$\vec{D_\delta} = \left| C_3 \cdot \vec{X_\delta} - \vec{X} \right|,$$

$$\vec{X_1} = \left| \vec{X_\alpha} - A_1 \cdot \vec{D_\alpha} \right|,$$
$$\vec{X_2} = \left| \vec{X_\beta} - A_2 \cdot \vec{D_\beta} \right|, \quad (8)$$
$$\vec{X_3} = \left| \vec{X_\delta} - A_3 \cdot \vec{D_\delta} \right|,$$

$$\vec{X}(t+1) = \frac{\left( \vec{X_1} + \vec{X_2} + \vec{X_3} \right)}{3}. \quad (9)$$

*2.3. A Hybrid Optimization Technique Integrating ESN and GWO.* For applying the ESN model, we must properly specify network parameters and designations such as the infrastructure of the reservoir, and also the network weights and connections. However, even if we apply the settings recommended by Jaeger [32] for the reservoir initialization stage, we cannot guarantee that the ESN model will suit the

intended application. We should realize that the ESN performance is essentially associated with the reservoir design, and if we conceive this well, then we can aspire to obtain satisfactory results. We might repeat the tests hoping to acquire good design scenarios. However, we can never be certain about achieving optimal scenarios. Anyhow, the design procedure should involve a few parameters, including the number of neurons within the network (NN), the connectivity rate of the network (RR), the feedback rate (FR), and the input connectivity rate (IR). Meanwhile, since not all the weights are being updated as part of the training process, pretraining is needed to suit the targeted task. The GWO algorithm should be used in such a way that it serves as an optimization algorithm. Figure 2 shows a flowchart of the proposed model for nitrogen oxide emissions. The following steps describe the specific modeling procedure:

*Step 1.* Enter the input data.

*Step 2.* Initialize the $a$, $A$, and $C$ parameters of the GWO algorithm.

*Step 3.* Set the initial architecture parameters including NN, RR, FR, and IR.

*Step 4.* Use the architecture parameters to establish the ESN model.

*Step 5.* Calculate the emissions of nitrogen oxides for different architecture parameters and use the mean absolute error as the corresponding fitness measure.

*Step 6.* Obtain the minimum fitness values for all architecture parameters.

*Step 7.* If the obtained minimum fitness values satisfy the requirements of model accuracy, then jump to Step 9. Otherwise, continue.

*Step 8.* Use Equation (9) to update the positions, increment the counter for the number of iterations, and then return to Step 4.

*Step 9.* Output the parameters of the optimal architecture.

*Step 10.* Initialize $a$, $A$, and $C$ parameters in the GWO and ESN weights.

*Step 11.* Select the weights to be optimized.

*Step 12.* Train the ESN model.

*Step 13.* Compute the error.

*Step 14.* If the error satisfies the model accuracy requirement, then jump to Step 16. Else, continue.

*Step 15.* Use Equation (9) to update the positions, increment the counter for the number of iterations, and then return to Step 12.

*Step 16.* Output the ESN model.

*2.4. Optimizing the Operational Parameters Using GWO.* We seek to establish a model for nitrogen oxide emissions, through which we can assess how the operational parameters are relevant to these emissions. As a bonus, emission reduction can be achieved by fine-tuning the operational parameters of the aforementioned model. We selected two of the most sensitive sets of operational parameters herein as candidates for potential change. These are parameters of the separated overfire air (SOFA) flow rate (four parameters) and the secondary air-damper opening percentage (six parameters). We carefully identified ranges for possibly adjusting these changeable parameters. We based our range selections on the standard operation habits and the accumulated experience of the operators and engineers. The following steps describe our procedure in detail:

*Step 1.* Enter the input data.

*Step 2.* Obtain the initial values for the $a$, $A$, and $C$ parameters in the GWO algorithm.

*Step 3.* Generate the initial operational parameters.

*Step 4.* Calculate the nitrogen oxide emissions for the different operational parameters and the corresponding errors.

*Step 5.* If the minimum error values satisfy the production requirements, then jump to Step 7, or else continue.

*Step 6.* Use Equation (9) to update the positions, increment the counter for the number of iterations, and then return to Step 4.

*Step 7.* Produce the optimal operational parameters as the final output.

## 3. Experimental Setup, Results, and Discussion

We obtained more than 5,000 patterns from the distributed control system (DCS) of the coal-fueled boiler (the power plant) and employed a sampling interval of 1 minute. Table 1 lists the properties of the coal fueling the power plant.

The model employed twenty variables that can be detailed as follows: unit load, total coal flow rate, total airflow rate, feed-water flow, main steam pressure, main steam temperature, water coal ratio, boiler tail flue temperature, separated overfire air (SOFA) flow rate (four variables), secondary air damper opening percentage (six variables), flue gas oxygen content, and $NO_x$ emissions. The input variables were selected according to basic boiler knowledge and the engineers' suggestions. In this work, all data of nitrogen oxide emissions is presented on the basis of a dry gas at 6% $O_2$. Data preprocessing was conducted prior to the modeling
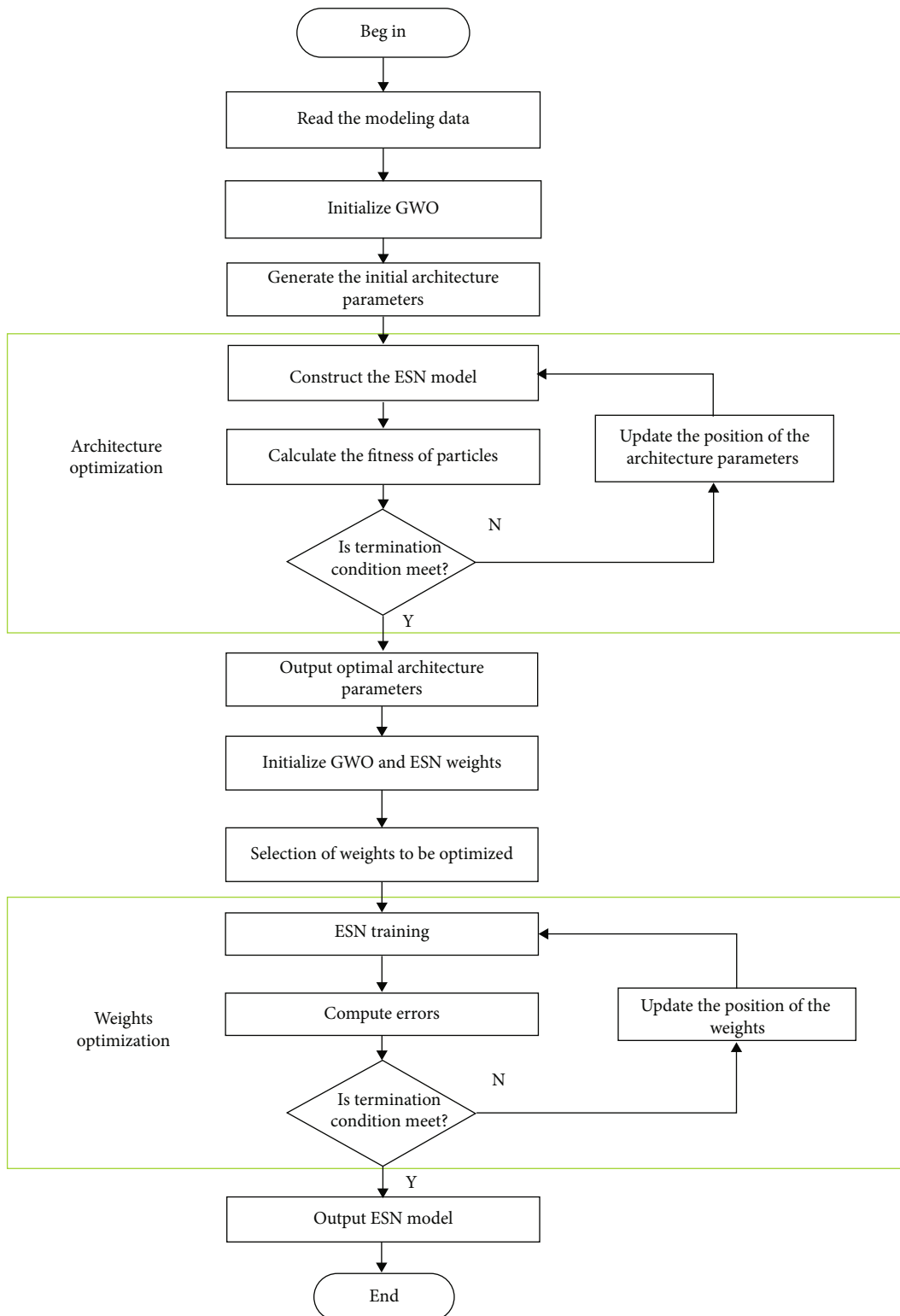
Figure 2: A flowchart of the proposed NO$_x$ modeling approach.

TABLE 1: Coal properties.

| Explanation | Unit | Value |
| --- | --- | --- |
| Carbon | % | 61.7 |
| Oxygen | % | 8.56 |
| Hydrogen | % | 3.67 |
| Nitrogen | % | 1.12 |
| Sulfur | % | 0.60 |
| Ash | % | 8.80 |
| Moisture | % | 15.55 |
| Volatile component | % | 26.50 |
| Quantity of produced heat | KJ/kg | 23442 |

process. First, noise and outlier removal operations were conducted to enhance the quality of the coarse or raw sampling data. Then, we removed all operational variables that do not experience any change during sampling. We also calculated the average values for variables with multiple measurements.

3.1. Performance Indices. To evaluate the developed model of nitrogen oxide emissions, we utilized four standard indices: the mean absolute error (MAE), the mean absolute percentage error (MAPE), the root-mean-square error (RMSE), and the coefficient of determination ($R^2$). These indices are defined as follows:

$$\text{MAE} = \frac{1}{M} \sum_{j=1}^{M} \left| y_j - \widehat{y}_j \right|, \tag{10}$$

$$\text{MAPE} = \frac{1}{M} \sum_{j=1}^{M} \left| \frac{y_j - \widehat{y}_j}{y_j} \right|, \tag{11}$$

$$\text{RMSE} = \sqrt{\frac{1}{M} \sum_{j=1}^{M} \left( y_j - y\wedge_j \right)^2}, \tag{12}$$

$$R^2 = 1 - \frac{\sum_{j=1}^{M} \left( y_j - y\wedge_j \right)^2}{\sum_{j=1}^{M} \left( y_j - \bar{y}_j \right)^2}. \tag{13}$$

3.2. Modeling of $NO_x$ Emissions. Figure 3 illustrates both the predicted and measured training data samples for the emissions of the nitrogen oxides according to the established ESN model. The dotted red straight line is the perfect line which indicates the equivalence of the predicted and measured values. The blue points indicate the ESN prediction results, associated with the measurements. All data points are almost distributed or scattered along the perfect line. Based on our calculations, the MAPE for the training dataset was only 4%, while the coefficient of determination ($R^2$) was 0.91. This shows that the ESN is highly suitable for modeling the nitrogen oxide emissions.

After we trained the $NO_x$ model on a part of the dataset, we employed the remaining part of the dataset to assess the performance of the model. Figure 4 presents the prediction results of 1000 test cases. Like the situation in Figure 3, the points in Figure 4 are also nearly aligned with the perfect line. This means that the prediction results are in good agreement with the measurements. Figure 5 shows the ESN-based distribution of the relative test errors. Among 1000 test samples, 74% of the relative errors were below 5%. The RMSE and $R^2$ were also calculated and were found to be 10.527 and 0.86, respectively. These results enable us to conclude that the proposed ESN model is accurate in its $NO_x$ emission prediction.

3.3. Performance Comparison with LSTM and ELM. To further demonstrate the superiority of the performance of the ESN model, we compared the ESN model outcomes with those of the widely used ELM model and the LSTM model.

The ELM model is an effective machine learning method, which generally demonstrates superior accuracy and generalization performance in comparison with the conventional SVM and LS-SVM methods. To realize the actual modeling process, we employed a Matlab implementation of the ELM algorithm with a sigmoidal transfer function. A trial-and-error scheme was followed to set the number of neurons. The LSTM architecture is a RNN variant, which includes a single input layer, a single hidden layer, and also a single output layer, such that the dropout is set after the hidden LSTM layer.

Figures 5 and 6 and Table 2 provide a brief outline of the performance of each of the aforementioned three different models. Figure 6 asserts that each of the three prediction curves follows the real-data direction and that each of the three algorithms can be employed to successfully predict the emissions of nitrogen oxides. However, the results in Table 2 suggest that the prediction accuracy of either LSTM or ESN exceeds that of ELM. This indicates that the RNN prediction accuracy strongly exceeds that of a conventional model. Figure 5 illustrates the relative test error distributions, showing that the majority of the ESN errors are within 5%. Table 2 lists the MAPE, MAE, RMSE, and $R^2$ indicators for the test dataset with different models. The ELM model, which represents a conventional machine learning approach, is clearly underperformed by the ESN and LSTM models. Indeed, the ELM produces the most inaccurate results on three of the four criteria. The MAPE, MAE, and $R^2$ of the LSTM are better than those of the ELM, but the RMSE of the LSTM is slightly inferior to the RMSE of the ELM. The MAPE, MAE, RMSE, and $R^2$ criteria of the ESN model are better than the performance indices of the other two models. This indicates that the ESN model is a promising alternative for achieving the required accuracy when dealing with models of nitrogen oxide emissions.

3.4. Combustion Optimization with the GWO Algorithm. In this paper, we selected three standard optimization cases according to the boiler maximum continuous rating (BMCR). The values for this rating were 100% BMCR (Case 1), 90% BMCR (Case 2), and 80% BMCR (Case 3). The original nitrogen oxide emissions for these three selected cases were, respectively, 303, 270, and 216 mg/Nm³. We also
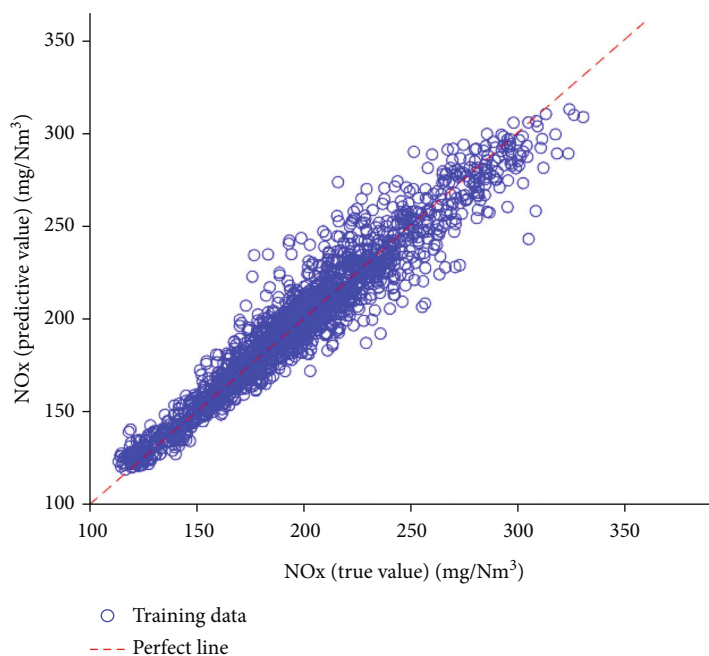
FIGURE 3: The measured and predicted ESN training data for nitrogen oxide emissions.
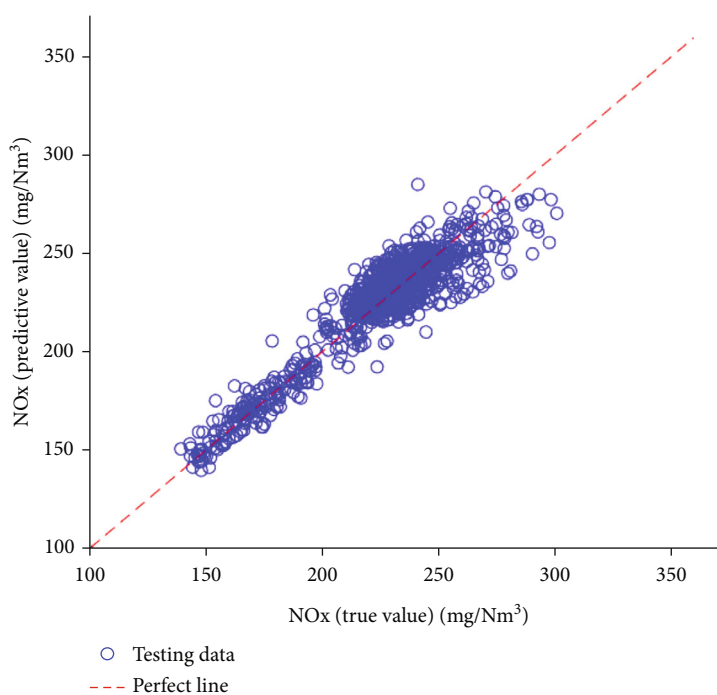


FIGURE 4: The measured and predicted ESN test data for nitrogen oxide emissions.

selected two sets of parameters (namely, the secondary air damper opening percentage ($x_1$, $x_2$, $x_3$, $x_4$, $x_5$, $x_6$) and the SOFA flow rate ($x_7$, $x_8$, $x_9$, $x_{10}$) as design variables to be optimized by the GWO algorithm. We determined these variables and their ranges to be conforming to the regular operation habits and the accumulated experience of operators and engineers. Figure 7 illustrates the search process employed in Case 1. This search process is a convergent one with an extremely fast speed of convergence. The simulation results indicate that the predicted emissions of nitrogen oxides were lowered to approximately 253, 228, and 194 mg/Nm$^3$ from their original values of 303, 270, and 216 mg/Nm$^3$, respectively. Therefore, the ratios of reduction amounted to percentages of 16.5%, 15.6%, and 10.2%, respectively. Table 3 lists both the original and optimized parameters. In order to verify the GWO performance, we
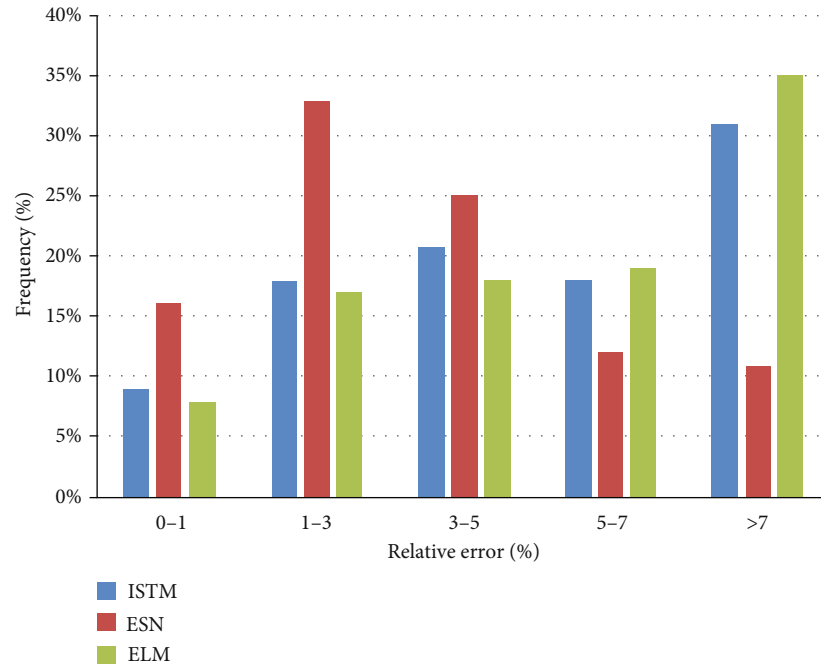
FIGURE 5: Relative test error distributions for the considered models.
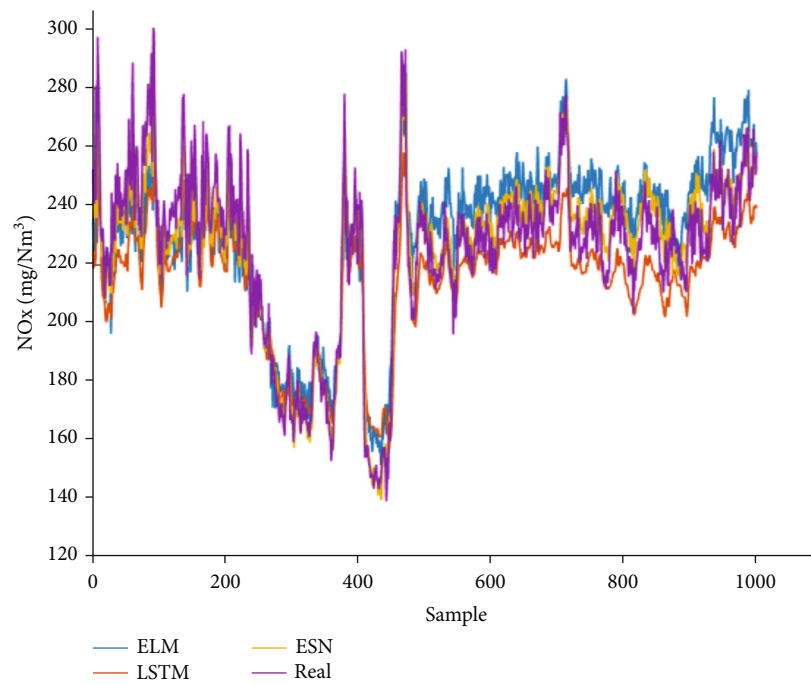


FIGURE 6: Prediction results for the considered algorithms.

TABLE 2: Comparison results with different evaluation criteria.

| Model | MAPE | MAE | RMSE | $R^2$ |
|---|---|---|---|---|
| ESN | 0.0353 | 8.052 | 10.527 | 0.868 |
| LSTM | 0.0559 | 12.89 | 16.042 | 0.867 |
| ELM | 0.0589 | 13.23 | 15.853 | 0.735 |

compared the widely used PSO algorithm and the present GWO algorithm. To achieve this comparison, we repeated both algorithms thirty times with an eye to optimize Case 1. Figure 7 indicates that both the PSO and GWO algorithms can dramatically lower the emissions of the nitrogen oxide pollutants. On average, the GWO optimization results are superior to those of the PSO one. This means that the
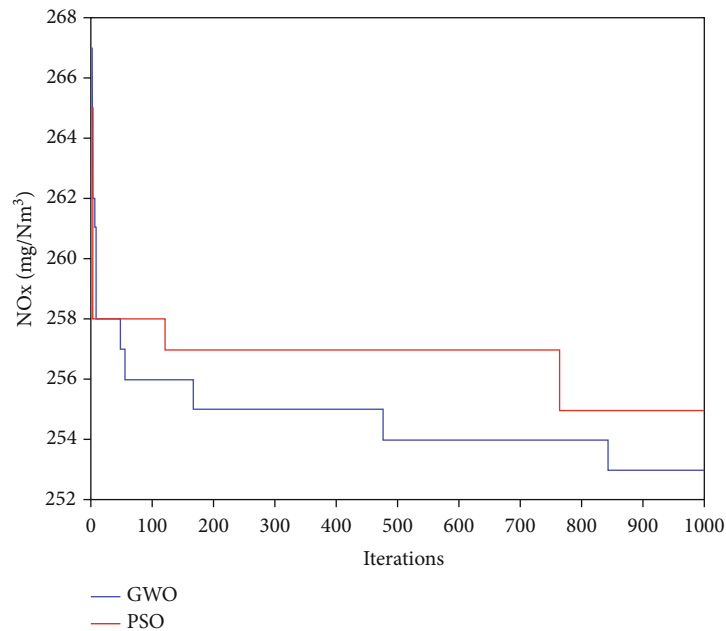
FIGURE 7: The search process by the two competing algorithms for 100% BMCR (Case 1).

TABLE 3: The initial and optimized operational parameters and the concentrations of the emissions of nitrogen oxides.

|  |  | x1 (%) | x2 (%) | x3 (%) | x4 (%) | x5 (%) | x6 (%) | x7 (t/h) | x8 (t/h) | x9 (t/h) | x10 (t/h) | $NO_x$ (mg/Nm$^3$) |
|---|---|---|---|---|---|---|---|---|---|---|---|---|
| Case 1 | Original | 14 | 59 | 37 | 60 | 41 | 70 | 101 | 95 | 129 | 77 | 303 |
|  | Optimized | 15 | 53 | 38 | 66 | 42 | 75 | 127 | 110 | 147 | 90 | 253 |
| Case 2 | Original | 14 | 65 | 31 | 65 | 32 | 72 | 141 | 101 | 141 | 82 | 270 |
|  | Optimized | 14 | 54 | 28 | 79 | 39 | 86 | 204 | 137 | 186 | 116 | 228 |
| Case 3 | Original | 14 | 79 | 49 | 79 | 49 | 79 | 153 | 128 | 173 | 105 | 216 |
|  | Optimized | 15 | 73 | 50 | 84 | 54 | 81 | 179 | 139 | 181 | 114 | 194 |

GWO algorithm can offer solutions of a higher quality and better stability. In short, the GWO algorithm may offer a better alternative for combustion optimization.

## 4. Conclusions

We consider two important steps towards optimizing combustion processes to achieve low emissions of nitrogen oxides. These steps are modeling of $NO_x$ emissions and optimization of the pertinent operational parameters. In this work, we introduce a novel approach, which combines the ESN and GWO algorithms to model the emissions of nitrogen oxides and optimize the pertinent operational parameters in a coal-fueled boiler of a 1000 MW capacity. We utilized the ESN algorithm to model the $NO_x$ emissions of this boiler and, further, utilized this model to optimize the relevant operational parameters through the application of the GWO algorithm. We finally managed to lower the nitrogen oxide emissions through the adjustment of the pertinent parameters to their optimal values. We found the values predicted by the ESN model for the $NO_x$ emissions to be consistent with their measured values. We obtained a mean absolute error (MAE) of the test data that was as low as

3.5%. In comparison with the LSTM and the ELM algorithms, the ESN algorithm is more successful in the modeling of nitrogen oxide emissions due to its strong generalization capability. We selected a secondary opening percentage and a separated overfire air (SOFA) flow rate from three typical cases for optimization by the GWO algorithm. Our simulation results for the three selected cases indicated that the nitrogen oxide emissions were lowered by 16.5%, 15.6%, and 10.2%, respectively. Compared with the widely used PSO, our approach lowers the nitrogen oxide emissions within any specified time and increases the solution stability. In summary, our proposed combination of the ESN and GWO algorithms can model and lower the emissions of nitrogen oxides for coal-fired boilers. Our approach is more powerful and effective than other modeling approaches such as the LSTM and ELM algorithms and other optimization approaches such as the PSO algorithm.

## Data Availability

The data employed in creating our model pertain to a 1000 MW ultra-supercritical once-through boiler with variable pressure and octagonal-inverse double tangential firing.

## Conflicts of Interest

The authors declare no conflict of interest.

## Authors' Contributions

X. J. Chen designed the research and the article structure and revised the manuscript. H. Y. Zhang carried out the experiments and revised the manuscript. H. W. Qin revised the manuscript. All authors read and approved the final paper.

## References

[1] P. Tan, B. He, C. Zhang et al., "Dynamic modeling of $NO_X$ emission in a 660 MW coal-fired boiler with long short-term memory," *Energy*, vol. 176, pp. 429–436, 2019.

[2] H. Zhou, K. Cen, and J. Fan, "Modeling and optimization of the NOX emission characteristics of a tangentially fired boiler with artificial neural networks," *Energy*, vol. 29, no. 1, pp. 167–183, 2004.

[3] P. Ilamathi, V. Selladurai, K. Balamurugan, and V. T. Sathyanathan, "ANN-GA approach for predictive modeling and optimization of NOX emission in a tangentially fired boiler," *Clean Technologies and Environmental Policy*, vol. 15, no. 1, pp. 125–131, 2013.

[4] J. Chu, S. Shieh, S. Jang, C. I. Chien, H. P. Wan, and H. H. Ko, "Constrained optimization of combustion in a simulated coal-fired boiler using artificial neural network model and information analysis," *Fuel*, vol. 82, no. 6, pp. 693–703, 2003.

[5] F. Wu, H. Zhou, T. Ren, L. G. Zheng, and K. F. Cen, "Combining support vector regression and cellular genetic algorithm for multi- objective optimization of coal-fired utility boilers," *Fuel*, vol. 88, no. 10, pp. 1864–1870, 2009.

[6] Z. H. Tang, X. Y. Wu, S. X. Cao, and M. X. Yang, "Modeling of the boiler NOx emission with a data driven algorithm," *Journal of Chemical Engineering of Japan*, vol. 51, no. 8, pp. 695–703, 2018.

[7] Y. Lv, J. Z. Liu, T. T. Yang, and D. L. Zeng, "A novel least squares support vector machine ensemble model for $NO_x$ emission prediction of a coal-fired boiler," *Energy*, vol. 55, pp. 319–329, 2013.

[8] Y. Lv, T. T. Yang, and J. Z. Liu, "An adaptive least squares support vector machine model with a novel update for NOx emission prediction," *Chemometrics and Intelligent Laboratory Systems*, vol. 145, pp. 103–113, 2015.

[9] Q. W. Li, K. Y. Zhou, and G. H. Yao, "Combustion optimization model for NO x reduction with an improved particle swarm optimization," *Journal of Shanghai Jiaotong University (Science)*, vol. 21, no. 5, pp. 569–575, 2016.

[10] Y. L. Wang, Z. Y. Ma, H. H. You et al., "Development of a NO x emission model with seven optimized input parameters for a coal-fired boiler," *Journal of Zhejiang University, SCIENCE A*, vol. 19, no. 4, pp. 315–328, 2018.

[11] W. Fan, F. Q. Si, S. J. Ren, C. Yu, Y. F. Cui, and P. Wang, "Integration of continuous restricted Boltzmann machine and SVR in NOx emissions prediction of a tangential firing boiler," *Chemometrics and Intelligent Laboratory Systems*, vol. 195, p. 103870, 2019.

[12] C. G. Zhen and H. Y. Liu, "Model for predicting NOx emission from boilers based on MWOA-LSSVM integration," *Journal of Chemical Engineering of Japan*, vol. 52, no. 8, pp. 702–709, 2019.

[13] X. Li, P. F. Niu, J. P. Liu, and Q. Liu, "Improved teaching-learning-based optimization algorithm for modeling NOX emissions of a boiler," *CMES-Computer Modeling in Engineering and Sciences*, vol. 117, no. 1, pp. 29–57, 2018.

[14] Z. Dong, N. Ma, and C. Q. Li, "NOx emission model for coal-fired boilers using partial least squares and extreme learning machine," *Journal of Southeast University*, vol. 32, no. 2, pp. 179–184, 2019.

[15] K. K. L. Wong, G. Fortino, and D. Abbott, "Deep learning-based cardiovascular image diagnosis: a promising challenge," *Future Generation Computer Systems*, vol. 110, pp. 802–811, 2020.

[16] T. Li, S. Fong, K. K. L. Wong, Y. Wu, X. S. Yang, and X. Li, "Fusing wearable and remote sensing data streams by fast incremental learning with swarm decision table for human activity recognition," *Information Fusion*, vol. 60, pp. 41–64, 2020.

[17] T. Li, M. Zhao, and K. K. L. Wong, "Machine learning based code dissemination by selection of reliability mobile vehicles in 5G networks," *Computer Communications*, vol. 152, pp. 109–118, 2020.

[18] G. T. Yang, Y. N. Wang, and X. L. Li, "Prediction of the NOx emissions from thermal power plant using long short term memory neural network," *Energy*, vol. 192, pp. 1–13, 2020.

[19] P. R. Xie, M. M. Gao, H. F. Zhang, Y. G. Niu, and X. W. Wang, "Dynamic modeling for NOx emission sequence prediction of SCR system outlet based on sequence to sequence long short-term memory network," *Energy*, vol. 190, pp. 1–12, 2020.

[20] H. Zhou, L. G. Zheng, and K. F. Cen, "Computational intelligence approach for NOx emissions minimization in a coal-fired utility boiler," *Energy Conversion and Management*, vol. 51, no. 3, pp. 580–586, 2010.

[21] Z. B. Wei, X. L. Li, L. J. Xu, and Y. T. Cheng, "Comparative study of computational intelligence approaches for NOx reduction of coal-fired boiler," *Energy*, vol. 55, pp. 683–692, 2013.

[22] Z. H. Tang, G. N. Zhao, and T. H. Ouyang, "Two-phase deep learning model for short-term wind direction forecasting," *Renewable Energy*, vol. 173, pp. 1005–1016, 2021.

[23] J. G. Song, C. E. Romero, Z. Yao, and B. He, "Improved artificial bee colony-based optimization of boiler combustion considering $NO_X$ emissions, heat rate and fly ash recycling for on-line applications," *Fuel*, vol. 172, pp. 20–28, 2016.

[24] G. Q. Li, P. F. Niu, Y. P. Ma, H. Wang, and W. Zhang, "Tuning extreme learning machine by an improved artificial bee colony to model and optimize the boiler efficiency," *Knowledge-Based Systems*, vol. 67, pp. 278–289, 2014.

[25] J. X. Pei and J. Wang, "Multisensor prognostic of RUL based on EMD-ESN," *Mathematical Problems in Engineering*, vol. 2020, 12 pages, 2020.

[26] K. He, L. Mao, J. B. Yu, W. G. Huang, Q. B. He, and L. Jackson, "Long-term performance prediction of PEMFC based on LASSO-ESN," *IEEE Transactions on Instrumentation and Measurement*, vol. 70, pp. 1–11, 2021.

[27] S. T. Zhang, X. B. Lin, L. Wu, and Y. Q. Song, "Network traffic anomaly detection based on ML-ESN for power metering system," *Mathematical Problems in Engineering*, vol. 2020, Article ID 7219659, 21 pages, 2020.

[28] P. Madhusmita, D. Bikramaditya, and P. Bhusan, "Global path planning for multiple AUVs using GWO," *Archives of Control Sciences*, vol. 30, no. 1, pp. 77–100, 2020.

[29] S. Ahmet and G. Fatih, "A novel hybrid PSO-GWO algorithm for optimization problems," *Engineering with Computers*, vol. 35, no. 4, pp. 1359–1373, 2019.

[30] A. Madadi and M. Motlagh, "Optimal control of DC motor using grey wolf optimizer algorithm," *Technical Journal of Engineering and Applied Science*, vol. 4, no. 4, pp. 373–379, 2014.

[31] S. Mirjalili, S. M. Mirjalili, and A. Lewis, "Grey wolf optimizer," *Advances in Engineering Software*, vol. 69, pp. 46–61, 2014.

[32] H. Jaeger and H. Haas, "Harnessing nonlinearity: predicting chaotic systems and saving energy in wireless communication," *Science*, vol. 304, no. 5667, pp. 78–80, 2004.

*Research Article*

# A Visual Grasping Strategy for Improving Assembly Efficiency Based on Deep Reinforcement Learning

**Yongzhi Wang** [iD],[1] **Sicheng Zhu,**[2] **Qian Zhang,**[1,3] **Ran Zhou,**[1] **Rutong Dou,**[1] **Haonan Sun,**[4] **Qingfeng Yao,**[5] **Mingwei Xu,**[1] **and Yu Zhang** [iD][1]

[1]*Department of Mechanical Engineering, Shenyang University of Technology, Shenyang 110000, China*
[2]*College of Information Science and Engineering, Zhejiang University, Hangzhou 310058, China*
[3]*Department of Robotics, Ritsumeikan University, Shiga 525-8577, Japan*
[4]*Department of Digital Factory, Chinese Academy of Sciences, Shenyang 110000, China*
[5]*College of Science, Shenyang University of Chemical Technology, Shenyang 110000, China*

Correspondence should be addressed to Yu Zhang; zhangyu@sut.edu.cn

The adjustment times of the attitude alignment are fluctuated due to the fluctuation of the contact force signal caused by the disturbing moments in the compliant peg-in-hole assembly. However, these fluctuations are difficult to accurately measure or definition as a result of many uncertain factors in the working environment. It is worth noting that gravitational disturbing moments and inertia moments significantly impact these fluctuations, in which the changes of the peg concerning the mass and the length have a crucial influence on them. In this paper, a visual grasping strategy based on deep reinforcement learning is proposed for peg-in-hole assembly. Firstly, the disturbing moments of assembly are analyzed to investigate the factors for the fluctuation of assembly time. Then, this research designs a visual grasping strategy, which establishes a mapping relationship between the grasping position and the assembly time to improve the assembly efficiency. Finally, a robotic system for the assembly was built in V-REP to verify the effectiveness of the proposed method, and the robot can complete the training independently without human intervention and manual labeling in the grasping training process. The simulated results show that this method can improve assembly efficiency by 13.83%. And, when the mass and the length of the peg change, the proposed method is still effective for the improvement of assembly efficiency.

## 1. Introduction

The application and development of robots in the industrial field have been developed by leaps and bounds in the past two decades [1–9]; thus, they are gradually integrated into people's daily live. Robots are used to replace humans for completing work in many scenes. The traditional control methods of the robot are the patterns of hard coding in a structural environment. These methods limit robotics' adaptability and manufacturing flexibility, which increases the labor cost and reduces the suitable range of robotic application situations. Moreover, the traditional robot control methods have a huge gap with human intelligence when sensing the environment or learning some skills. Therefore, it becomes the main development direction in the field of

robot control that robots were trained to learn skills. The ways of perceiving the environment of humans are gradually implemented on robots through bionic means, such as visual sensors and force sensors [10–15]. The motion accuracy of robotic control has surpassed humans, such as speed, distance, and angle. Nevertheless, robotic intelligence has not yet met the demands of humans in the work of learning skills. In order to enable robots to acquire new knowledge or skills autonomously, researchers use the methods of machine learning to continuously improve robotic performance by training. Ultimately, robots can imitate or realize the learning behavior of humans [16–21].

The grasping function is the most basic manipulating function of robots in industry and daily life, and it is also the foundation of many complex manipulating actions [22–

26]. The assembly task is a complex robotic task, which often requires the grasping function. Therefore, researchers have been conducted much research in the field of grasping in recent years. The feature algorithm of deep learning based on multimodal group regularization has been able to do not rely on the hand design of features in the task of RGB-D image detection for robot grasping [27]. And it got better performance than the previous hand design of the features. The eye-hand coordination system with deep learning can perform real-time servo compensation, which does not depend on camera calibration and robot posture [28]. The deep learning method can solve the problem of grasping prediction well and has been able to be designed without relying on artificial features, which has greatly reduced the cost of learning. However, deep learning methods often require a large number of data sets to complete the analysis, and the results after training are very dependent on the quality of the data sets. This limits its range of application to a certain extent. Deep learning has good analysis and perception skills, but it lacks decision-making skills. This also limits the usage scenarios of grasping strategies based on deep learning. Deep learning needs an expensive cost to build a large number of data sets in practice, and even difficult to achieve it. Therefore, it is a good solution to use the trial and error method based on reinforcement learning to make the robot collect data sets autonomously. Therefore, the grasping method based on reinforcement learning has been widely studied. For example, the viewpoint optimization strategy based on reinforcement learning uses active vision to optimize the visual sensor viewpoint [29], which can make the grasping decisions with some information missing through the trial and error of reinforcement learning without relying on multiangle image acquisition. And this method relaxes the assumption of the sensor viewpoint and improves the grasping success rate. In addition, the hierarchical strategy of reinforcement learning can automatically learn multiple grasping strategies to solve the limitation of a single grasping type for the robot system [30]. Low-level strategies learn how to grasp specific locations with specific grasping types, and high-level strategies learn how to choose grasping types and locations. This strategy can generate a grasping strategy from a given grasping position. Although reinforcement learning has good decision-making ability, it is limited to discrete action space due to the limitation of computing power, which limits its application range and makes it difficult to deal with the problems related to continuous action space. But many practical problems are working in continuous action space. Hence, scholars have carried out numerous studies with regard to deep reinforcement learning, which combines the perception ability of deep learning and the decision-making ability of reinforcement learning [31, 32]. And it achieves direct control from the original input to output through the end-to-end learning method. Subsequently, researchers proposed many grasping methods based on deep reinforcement learning. The visual grasping method based on deep reinforcement learning can output the predicted reward of all possible actions in the current state just by inputting the observation image and, then, choose the optimal action [33, 34]. The robot is entirely self-supervised to improve the success rate for grasps by trial and error. Besides, in the real environment, the visual grasping method based on deep reinforcement learning does not need fine-tuning to successfully grasp previously seen objects, and even it can successfully grasp previously unseen semicompliant objects [35]. Therefore, deep reinforcement learning is more suitable to deal with the grasping problem for assembly in continuous action space.

The task of peg-in-hole is a classic assembly task. It is one of the basics for many complex assembly tasks [36]. In recent years, the research of the peg-in-hole assembly has also made many novel methods. For example, the automatic alignment method based on force/torque establishes a three-point contact model, which analyzes the autonomous correction before insertion through force analysis and geometric analysis [37]. In addition, the screw insertion method in the peg-in-hole assembly reduces the axial friction force by rotating shaft compensation and improves the collision contact of the peg and the hole during assembly [38]. Moreover, the compliance control method without force feedback can analyze the current contact state between the hole and the peg, which overcomes the unavoidable positional uncertainty in the identification process [39]. And the peg-in-hole assembly can be completed without relying on expensive force sensors or remote compliance machinery. Additionally, the assembly strategy of the variable compliance center has designed an elastic displacement device [40]. This method combines the advantages of active compliance and passive compliance without force/torque sensors, which simplifies the control system. This method can well solve alignment errors. The traditional control method in the peg-in-hole assembly has obtained many research results, but the traditional control method is limited to the specific working environment. Traditional assembly robots require a great number of parameters to be deployed before work. Therefore, the research of peg-in-hole assembly in a nonstructural environment is still a challenge. However, the method of intelligent assembly robots based on deep reinforcement learning can greatly reduce the work of related manual parameters deployment [41]. It uses the robot's sensor to perceive the environment and then analyzes the system state. This method can obtain better control accuracy and robustness. Furthermore, an assembly training method with deep reinforcement learning has been designed to dispose of the uncertainty in the complicated assembly process of circuit breakers [42]. It enables the robot to autonomously learn the skill of orientation and pose adjustments in the assembly training. This method has obtained a high assembly success rate.

The core work of the peg-in-hole is to align the peg with the hole, namely, adjusting the attitude and position of the peg. The assembly alignment efficiencies are affected by many uncertain factors in the real environment during the alignment adjustment. In order to solve this problem, this article has conducted the following research:

(1) To analyze the relationship between the grasping position and the adjustment time of the assembly alignment

(2) To investigate the impact of assembly efficiency when the length and mass of the peg have changed

(3) To verify the effectiveness of the proposed method in improving assembly efficiency

The remainder of this paper is organized as follows: in the Section 2, the working principle of the device is introduced, and the relationship between grasping position and assembly efficiency is analyzed. The Section 3 puts forward the visual grasping strategy and explains the details of the assembly. The simulation results and analysis results are presented in Section 4. The last section introduces the conclusion of this paper and the future work.

## 2. Working Principles and Analyses

*2.1. Working Principles and Analyses of Assembly.* Peg-in-hole is divided into search phase, alignment phase, and insertion phase. Firstly, the job of the search phase is to find the location of the hole. And then, the alignment phase is to adjust the assembly attitude of the peg to align with the hole. Finally, the insertion phase is to insert the peg into the hole to complete the assembly tasks. It is often assumed, at the early research for peg-in-hole assembly, that the peg and the hole can be well aligned before insertion. In fact, the peg may not be well aligned with the hole, which needs to adjust the position and attitude of the peg to complete the alignment with the hole. The assembly time is also prolonged as the number of adjustments increases to reduce the assembly efficiency.

There is often an inclination angle between the peg and the hole during the assembly alignment phase early. This inclination angle is a key parameter of the assembly alignment, as shown in Figure 1. It is still possible to complete the assembly when there is an inclination angle between the peg and the hole if the assembly work has an assembled clearance. This inclination angle is the maximum inclination angle $\delta$ allowed by the assembly. The formula of the maximum inclination angle $\delta$ for assembly is described as follows:

$$\delta = \arctan \frac{\zeta}{K}, \tag{1}$$

where $\zeta$ is the peg-in-hole assembled clearance and $K$ is the assembly insertion distance.

There are three contact states during the assembly of peg-in-hole, as illustrated in Figure 2. The robot moves the peg near the plane of the hole so that the bottom of the peg is in contact with the top of the hole. This contact state is defined as plane contact, as shown in Figure 2(a). The robot uses a spiral force to sweep the surface of the part to searching the hole. The peg will incline if the center of the peg is close enough to the center of the hole. The contact state becomes a two-point contact at this time, as illustrated in Figure 2(b). The peg slides along the edge of the hole while maintaining two-point contact. When the center of the peg approaches the center of the hole to a certain range, the contact state changes to a three-point contact, as shown in
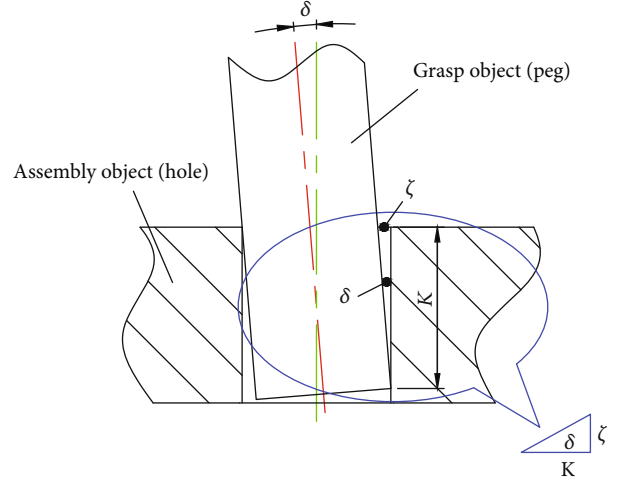


FIGURE 1: The schematic diagram of the assembly attitude angle. The red central line is the central line of the peg and the green central line is the hole's central line.

Figure 2(c). The peg needs to adjust attitude for alignment by this time.

The insertion action cannot be completed if the inclination angle is greater than the maximum inclination angle $\delta$. That is to say, the insertion distance $K$ is zero by this time. The training target of the robots is that the inclined angle can be faster adjusted to zero or less than the maximum inclination angle $\delta$ to insert the peg into the hole. This reduces the difficulty of assembly alignment but increases the difficulty of precise definition of the assembly model. The peg completes the alignment of adjusting attitude when the inclination angle $\psi$ of the current alignment is adjusted to be lower than the maximum inclination angle $\delta$ or zero. The peg is then inserted into the hole to complete the assembly task. Thus, the alignment adjustment time is one of the important indicators that affect assembly efficiency.

The downward assembly force will be generated when the robot tries to insert the peg into the hole in the two-point contact state, which will generate a corresponding reaction force at the contact point. The direction of the sum of reaction forces $F_{sum}$ always points to the center of the hole, as shown in Figure 3(a). The current inclination angle $\psi_y$ is the angle between the line connecting the two contact points A and B and the $y$-axis. The peg will spontaneously slide toward the center of the hole under the action of the sum of the reaction force if the friction at the contact point is ignored. This spontaneous sliding is due to natural attraction, which is also the core control principle of the compliance-based robotic peg-in-hole. The robot with this ability can deal with the uncertainty of the hole position. $F_r$ and $F_z$ are the projections of the assembly force on the $xy$-plane and the $z$-axis, and $F_z$ is consistent with the direction of gravity as illustrated in Figure 3(b). The assembly force of the peg is greater than the static friction force at the contact point if $F_r$ and the resultant of reaction force $F_{sum}$ are in the same direction. Thus, the peg and the hole generate relative sliding to each other, and then, the peg slides into
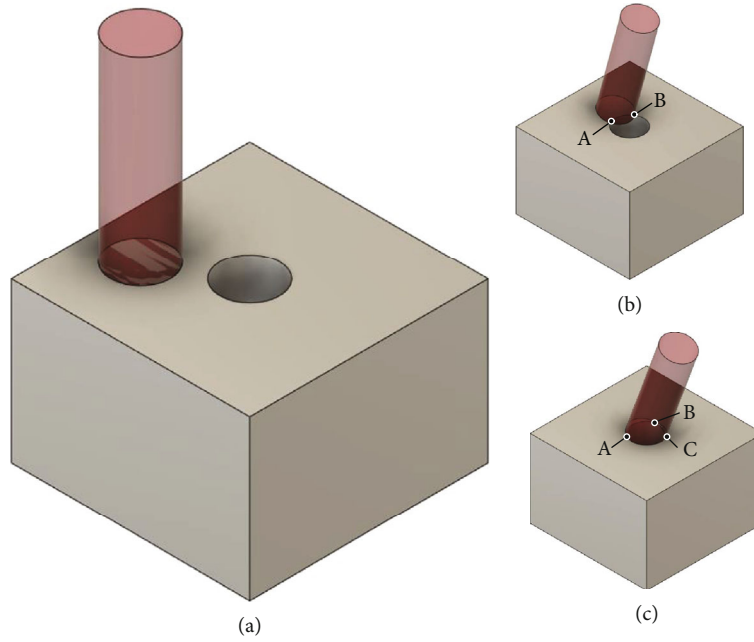
FIGURE 2: Schematic diagram of contact state. (a) Plane contact. (b)Two-point contact. (c) Three-point contact.
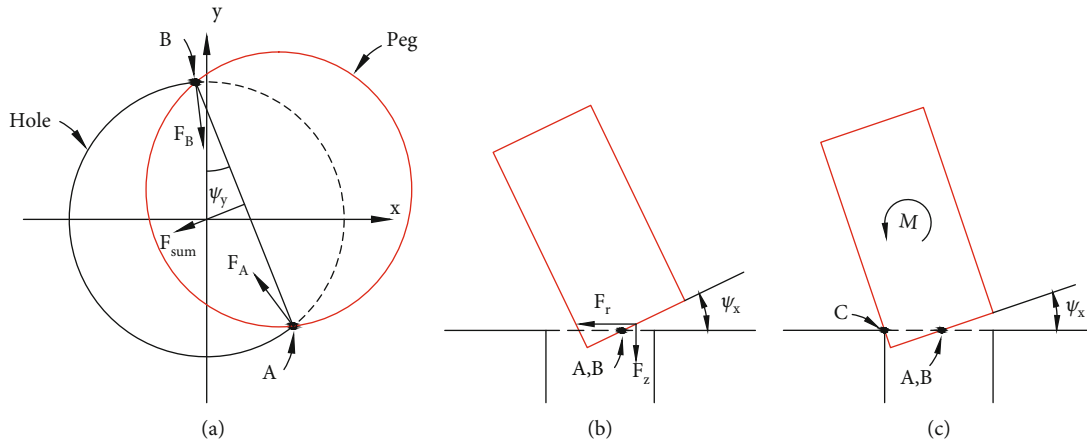


FIGURE 3: Schematic diagram of contact force. (a) Top view of two-point contact. (b) Side view of two-point contact. (c) Side view of three-point contact.

the hole. They cancel each other out if the direction of $F_r$ and $F_{\text{sum}}$ are opposite. The assembly force is less than the static friction force of the contact point at this time, and the peg and the hole will not slide relative to each other. It may cause the peg to miss the alignment position or slip out of the hole. The fluctuation of the disturbance moment will cause the assembly force to fluctuate suddenly, which makes the peg unable to complete the alignment. The robot then needs to readjust the alignment, which increases assembly time and reduces assembly efficiency. When the peg is attracted into the center of the hole, it can be inserted into the hole if the current inclination angle $\psi_x$ is zero. Otherwise, the contact state changes to the state of three-point contact. The turning moment $M$ is required to adjust the current inclination angle $\psi_x$ to insert the peg into the hole, as shown in Figure 3(c). The peg is inserted

into the hole to complete the assembly after fulfilling the alignment adjustment.

*2.2. Analyses of Disturbance for Assembly.* This research is focused on the grasping position to impact the efficiency of assembly alignment, thereby improving assembly efficiency. Therefore, the search phase and the insertion phase are not researched and discussed deeply. Different grasping positions produce different alignment times for the same current inclination angle $\psi$, as shown in Figure 4. Different motion trajectories and disturbing moments will be produced by the different grasping positions, which produce the difference in assembly time. Among these disturbing moments, the effects of gravitational disturbing moments and inertia moments are particularly significant for assembly, which will also emerge the fluctuation when the robot adjusts the peg to
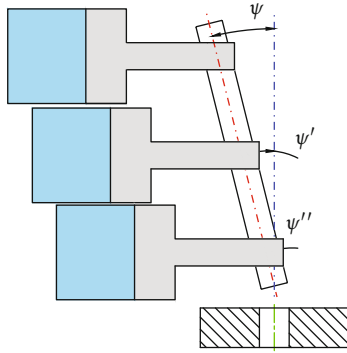
FIGURE 4: The schematic diagram of different gripping positions for adjustment alignment.

align the hole. In addition, it will be affected by the fluctuation of the disturbing moments that the robot adjusts the position and attitude of the peg. The signal fluctuations caused by disturbing moments will raise the difficulty of assembly alignment, which increases the adjustment time and reduces the efficiency of assembly work. Two special grasping positions are worth noting to reduce the influence of disturbing moments:

(1) The grasping position is the point where the center of mass and the center of rotation coincide, which can produce the smallest disturbing moments of gravity during the adjusting alignment. But there are still the inertia moments

(2) The grasping position is not only to coincide with the center of mass and the center of rotation but also to coincide with the inertial axis and the rotating axis, which produces minimum gravitational disturbing moments and inertia moments

The formula of gravitational disturbing moment $M_G$ is shown as follows:

$$M_G = mg|l| \sin \beta, \tag{2}$$

where $m$ is the mass of the peg, $g$ is the gravitational acceleration, $l$ is the distance from the rotation axis to the force functional point, and $\beta$ is the angle between the gravity moment and the vector (i.e., $\beta = 90° - \delta$).

The formula of the inertia couples $M_I$ generated by the moment of inertia $J$ is described as follows:

$$M_I = J \frac{d^2\beta}{dt^2} = \frac{1}{2} mr^2 \frac{d^2\beta}{dt^2}, \tag{3}$$

where $r$ is the vertical distance between the center of mass and the rotating axis and $d^2\beta/dt^2$ is the angular acceleration.

It can be seen from the above formula that the mass of the peg and the operating distance have an important influence on the gravitational disturbing moments and inertia moments. The position of the center of mass becomes uncertain due to the manufacturing error of the peg in the same

manufacturing batch. In addition, there are different coincidence degrees between the inertial axis and the rotating axis because of the different grasping positions. And the alignment process of adjusting attitude will move disparate distances and motion trajectories even when the peg has the same inclination angle. These factors have aggravated the uncertainty of the adjustment time. Therefore, selecting a suitable grasping position in the process of assembly can effectively reduce the fluctuation of the disturbing moments on the alignment adjustment, which is mainly caused by changes in mass, volume, and operating distance. The traditional control method for the robot cannot handle these complex and changeable assembly tasks. Hence, we hope to train the robot through the training method of deep reinforcement learning so that the robot can autonomously deal with these assembly tasks in an unstructured environment. Robots often need multiple times to adjust attitude in the alignment stage. The compliant control needs to constantly judge the current attitude based on the contact force. Some uncertain factors cause the fluctuation of the signal of contact force, which increases the difficulty of alignment. In particular, the gravitational disturbing moments and the inertia moments have a prominent influence on this fluctuation, which will lead to a prolonged time for alignment adjustment and ultimately reduce assembly efficiency. Therefore, the cost of time on the alignment stage can be reduced if the robot can reduce the fluctuation of the disturbing moments. Finally, the improvement of assembly efficiency is realized. Traditional control methods cannot handle these uncertain fluctuations of disturbing moments. However, artificial calibration of mechanical parameters or grasping positions is not only cumbersome, but also has certain errors, or even impossible to achieve. This difficulty can be avoided through trial and error learning based on deep reinforcement learning, which does not require artificial labels and prior knowledge of mechanical parameters. When the grasping position is restricted to a certain area with the proposed method, which is considered to improve assembly efficiency if the trained robot expends less assembly time than the untrained robot.

## 3. Assembly System with Deep Reinforcement Learning

The assembly task of peg-in-hole is divided into two branch tasks: grasping task and assembly task. Therefore, the robot is equipped with the grasping module and assembly module. The grasping task refers to the robot grasping the assembly peg before performing assembly. The assembly task is divided into three stages: searching, alignment, and insertion. This research proposes a visual grasping strategy to boost assembly efficiency by improving its grasping strategy based on the analysis in Section 2.2.

*3.1. Grasping Module with Visual Grasping Strategy.* The decision-making process of the grasping module is regarded as a Markov decision-making process. The grasping workflow is transformed into an interactive process that can be expressed in probabilistic form through the Markov decision process. Firstly, the robot observes the environmental state $s_t$

at time $t$ and selects the performing action $a_t$ from the available action set $A(s)$ through the strategy $\pi(s_t)$. And then the environmental state changes from $s_t$ to $s_{t+1}$, meanwhile, the reward $R(s_t, s_{t+1})$ is obtained. The state-action-reward chain in the grasping decision-making process can be expressed as follows:

$$\{s_0, a_0, R_1, s_1, a_1, \cdots, R_{t-1}, s_{t-1}, a_{t-1}, R_t, s_t\}. \tag{4}$$

The reward $R(s_t, s_{t+1})$ is composed of the grasping reward $r^G{}_{t+1}$ and the assembly reward $r^{AM}{}_{t+1}$. The robot obtains a grasping reward $r^G{}_{t+1} = 0.3$ after successfully grasping the peg each time. The grasping network will also obtain an assembly reward $r^{AM}{}_{t+1} = 0.7$ if the assembly time is less than the threshold. The reward $R(s_t, s_{t+1})$ is described as follows:

$$R(s_t, a_t) = R_t = r^G{}_{t+1} + r^{AM}{}_{t+1}. \tag{5}$$

The training purpose of deep reinforcement learning is to obtain the optimal strategy $\pi^*$, which can maximize the total reward $G_t$:

$$G_t = R_t + \gamma R_{t+1} + \gamma^2 R_{t+2} + \gamma^3 R_{t+3} + \cdots,$$
$$G_t = \sum_{t=0}^{\infty} \gamma^t R_t = \sum_{k=0}^{\infty} \gamma^t r_{t+k+1}. \tag{6}$$

The target of improving assembly efficiency is fulfilled if the robot can maximize the total reward $G_t$ by establishing the mapping relationship between the grasping position and the assembly time. Therefore, the robot trained a greedy deterministic policy $\pi(s_t)$ using off-policy Q-learning, which chooses action $a_t$ by maximizing the action-value function $Q_\pi(s_t, a_t)$:

$$Q_\pi(s_t, a_t) = \mathbb{E}_\pi[R_t \mid s_t = s, a_t = a]. \tag{7}$$

The optimal action-value function is expressed as follows:

$$Q^*(s_t, a_t) = \max_\pi Q_\pi(s_t, a_t) = R(s_t, a_t) + \gamma \max_{a \in A(s)} Q_\pi(s_{t+1}, a_{t+1}), \tag{8}$$

where $\gamma$ is the future discount, which is set to a constant $\gamma = 0.5$.

The optimal strategy $\pi^*$, which was obtained by training, can select the optimal action $a^*{}_t$ with the highest $Q$ value from the set of available action $A(s)$ in the current state $s_t$. The formula of optimal strategy $\pi^*$ is as follows:

$$\pi^*(s_t) = a^*{}_t = \underset{a \in A(s)}{\arg\max} Q^*(s_t, a_t). \tag{9}$$

The fully convolutional networks based on DQN and DenseNet are used to build the network of grasping decision-making in this paper. The networks take the height-map describing the observing environmental state $s_t$ as input, which outputs a dense pixel-wise map of $Q$ values with the

same size and resolution as the input. Any pixel point in the image has a $Q$ value, which predicts the future reward of performing the grasping action $a_t$ at the spatial position. To begin with, the agent observes the information of the environment to get the visual data, and then, it is reprojected onto the orthographic RGB-D heightmap. Whereafter, the color channel (RGB) and the clone depth channel (DDD) of the heightmap are input to two parallel 121-layer Dense-Nets to process the image features. And then, the image after channel-wise concatenation is sent to 3 additional $1 \times 1$ convolutional layers interleaved with ReLU activation functions and BatchNorm. Finally, the pixel-level probability map with $Q$ value is obtained after bilinearly upsampled processing, and it is the same as the input image resolution by $224 \times 224$. The robot will choose the performing action with the highest $Q$ value based on this probability map. The grasping strategy has two fully convolutional neural networks with the same structure: target network and evaluation network. They have the same network architecture and initial network parameters. Firstly, the target network selects the action $a_t$ with the highest $Q$ value according to the strategy $\pi(s_t)$. Afterward, the evaluation network will evaluate this action. And two networks output $Q_{tar}$ and $Q_{eva}$, respectively. The evaluation network updates the network parameters $\theta_i$ in real-time through the backpropagation operation according to the reward $R(s_t, a_t)$. But the target network only performs forward propagation operations, and it updates the network parameters $\theta_i'$ of the target network by copying the parameters $\theta_i$ of the evaluation network after completing a batch of iterative training, that is, $\theta_i' \longleftarrow \theta_i$. The robot is considered to have completed training when the difference $\Delta Q$ in the predicted $Q$ value between the target network and the evaluation network is less than the threshold through continuous iteration. $\Delta Q$ is described as follows:

$$\Delta Q = |Q_{tar} - Q_{eva}|. \tag{10}$$

The evaluation network uses the Huber loss function $\mathscr{L}_i$ as follows:

$$\mathscr{L}_i = \begin{cases} 0.5 \times \left(Q_{tar}{}^{\theta_i'} - Q_{eva}{}^{\theta_i}\right)^2, & \text{for} |Q_{tar} - Q_{eva}| < 1 \\ \left|\left(Q_{tar}{}^{\theta_i'} - Q_{eva}{}^{\theta_i}\right) - 0.5\right|, & \text{otherwise}. \end{cases} \tag{11}$$

### 3.2. Compliance-Based Assembly Module

The assembly module is based on compliant behavior control, which completes the peg-in-hole assembly by analyzing the contact state between the peg and hole to generate compliance behavior. The assembly module divides the assembly work into three stages: hole-searching stage, alignment stage, and insertion stage. The robot moves the peg to the surface of the hole after successfully grasping the peg. And the contact between the peg and the hole results in a plane contact state of the peg. The robot enters the hole-finding stage at the time. In order to simulate the uncertainty of the hole position during work, the initial position of the hole is randomly placed within a
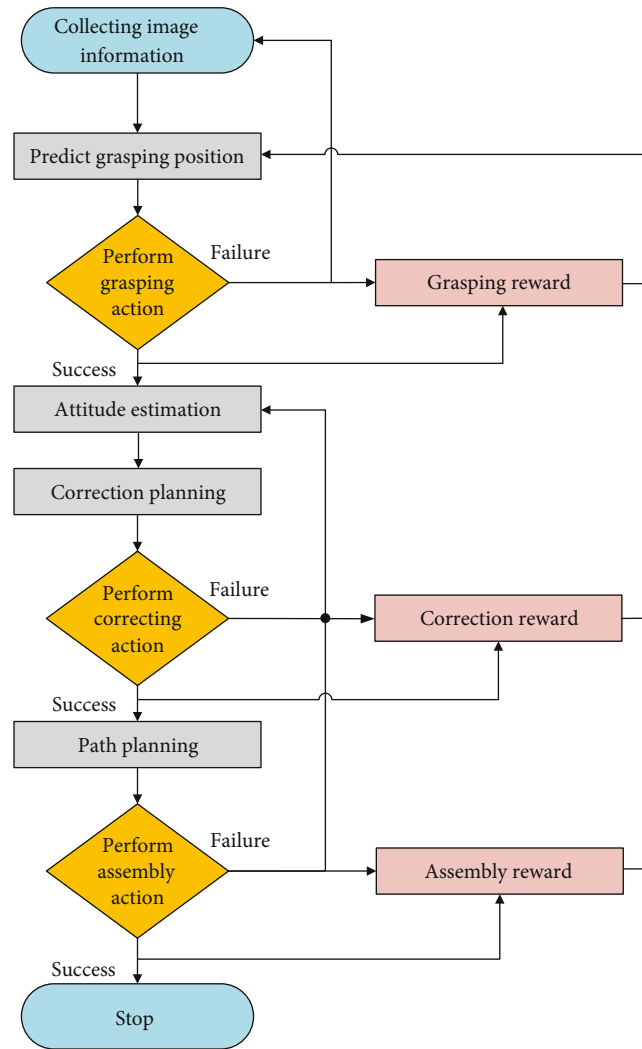
FIGURE 5: Flowchart of peg-in-hole procedure.

small range, which is equal to the area of the hole. Afterward, the robot searches holes on the surface through rubbing motion with the trajectory of Archimedes spiral. The peg will be inclined if the peg is close enough to the hole. And then, the contact state will change to two-point contact. Subsequently, the peg slides along the edge of the hole. There will be a three-point contact state when the peg is close enough to the center of the hole but still has an inclination angle. The alignment of the peg and the hole is completed by using the wiggling motion to adjust the error of the inclining angle. Finally, the assembly task is finished after performing the insertion action. The proposed method and baseline both use the same assembly module to ensure the fairness of the comparison in the assembly efficiency test. However, the grasp module of the baseline method is not equipped with an assembly reward $r^{AM}$. The effectiveness of the proposed method was proved if adding the assembly reward $r^{AM}$ for alignment in robot training can improve assembly efficiency. The process of peg-in-hole assembly is shown in Figure 5.

## 4. Simulation Results and Analyses

*4.1. Training of Visual Grasping Strategy.* The assembly system established in the simulation software V-REP, which uses a UR5 robotic arm with an RG2 gripper, as shown in Figure 6. And it is also equipped with the RGB-D vision sensor, force sensor, and position sensor. The length of the peg is 100 mm, and its weight is 0.55 kg. The diameter is $\phi 30$ mm, and the assembly clearance is 1 mm. The peg and the hole have not chamfered. The CPU of the simulation workstation is Intel(R) Xeon(R) Gold 5222 at 3.80 GHz, the GPU is NVIDIA GeForce RTX 3090, and it is equipped with 128 GB of RAM. The robot uses trial and error in training to explore the law of the difference in assembly alignment efficiency caused by different grasping positions. The method of stochastic gradient descent with momentum is used for the training of the grasping networks. The learning rate is a constant at $10^{-4}$, and the momentum is set as 0.9. The exploration strategy is a deterministic $\varepsilon$-greedy, and its initial value is set as 0.5 and then annealed overtraining to 0.1.
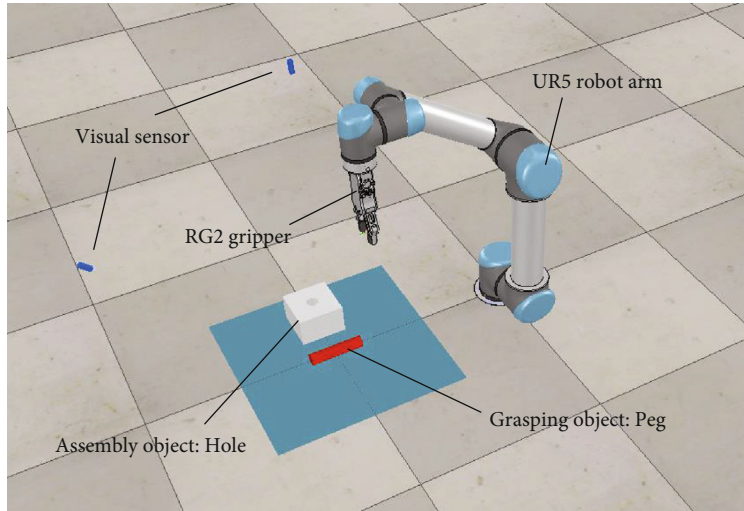
FIGURE 6: Schematic diagram of simulation system.

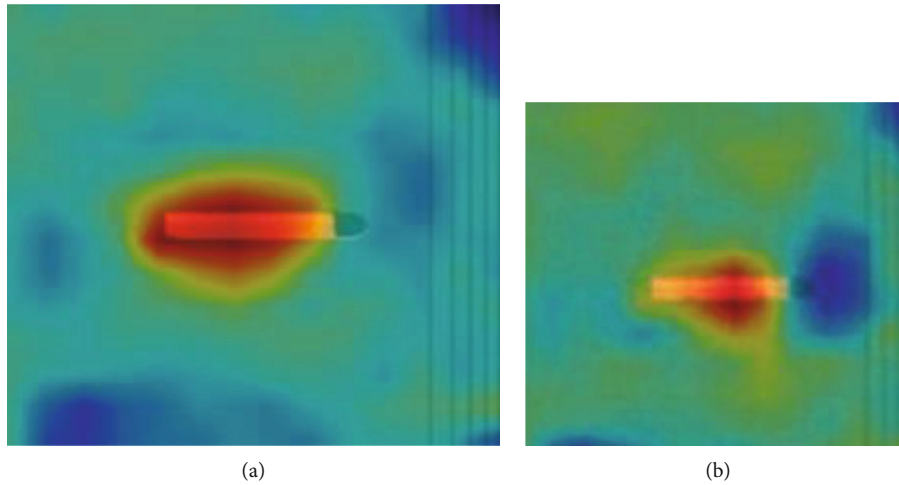

|        (a)        |        (b)        |

FIGURE 7: Heat maps of grasping decision-making. (a) Selection area of untrained grasping position. (b) Selection area of trained grasping position.

The first 1000 times of grasping training are to randomly select the grasping position. The purpose of random selection is to allow the robot to explore the impacts on the assembly efficiency for different grasping positions. The robot will choose the grasping position with the highest $Q$ value in the remaining times of 4000 training. The heat maps of the grasping decision-making are shown in Figure 7. The red area represents the grasping position with a higher predicted $Q$ value. The area where the untrained robot chooses the grasping position is spread over the whole peg, as illustrated in Figure 7(a). The robot will obtain the assembly reward $r^{AM}$ when the assembly time is less than the threshold. The selection area of the grasping position will gradually shrink as the number of training increases, as shown in Figure 7(b). The grasping position is restricted to a specific area smaller than the previously selected area by establishing the mapping relationship between the grasping position and the adjusting time of alignment.

4.2. Simulation Test for Assembly Efficiency. The simulation tests have the purposes to prove the following two problems:

(1) To verify whether the proposed grasping strategy can help robots improve assembly efficiency

(2) To test whether this strategy is still effective when qualities, lengths, and mechanical parameters of the peg have changed

The proposed method is a visual grasping strategy (VGS) for the peg-in-hole task. The robot used baseline and VGS to conduct 1000 peg-in-hole assembly simulation tests, respectively, to compare the difference in assembly efficiency. The total assembly time of the baseline method is about 38.46 hours, while the total assembly time of VGS is only about 33.14 hours, which improves the assembly efficiency by 13.83%. VGS compares the distribution of the assembly time with baseline, as shown in Figure 8. In the test, the shortest
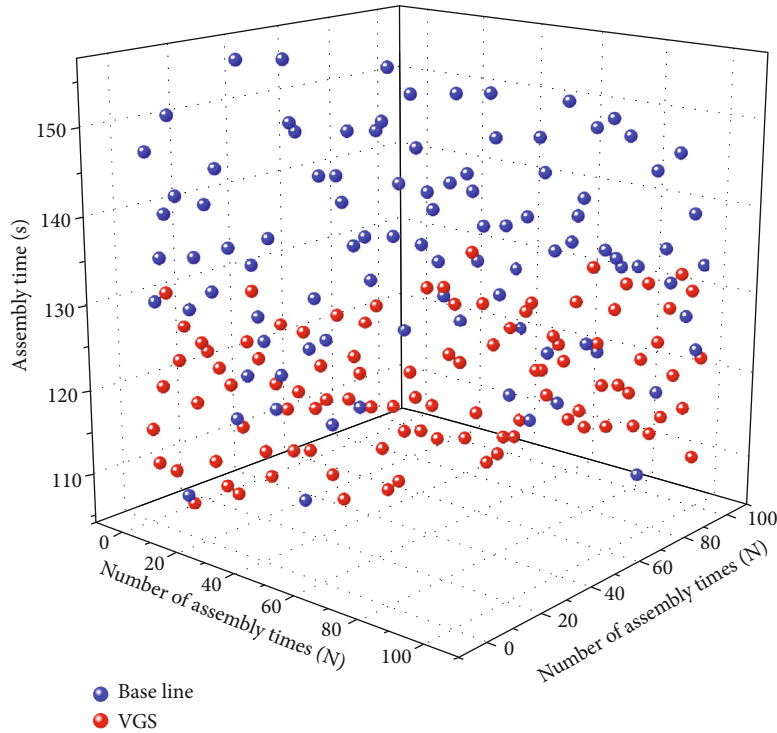
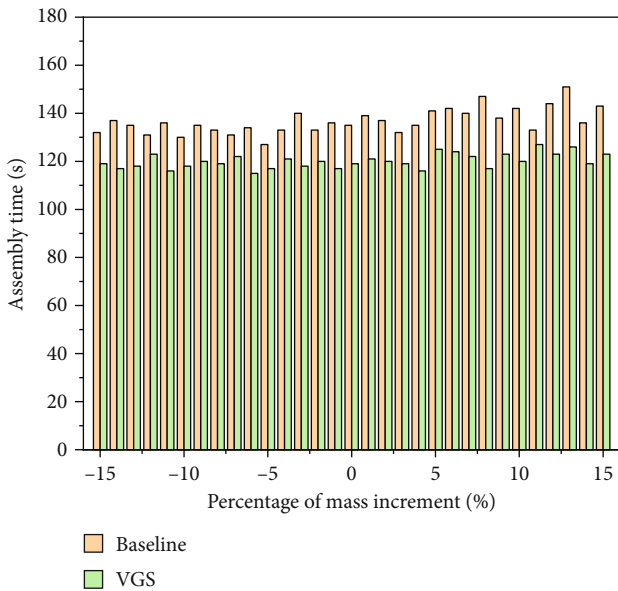Figure 8: Comparison chart of assembly time.



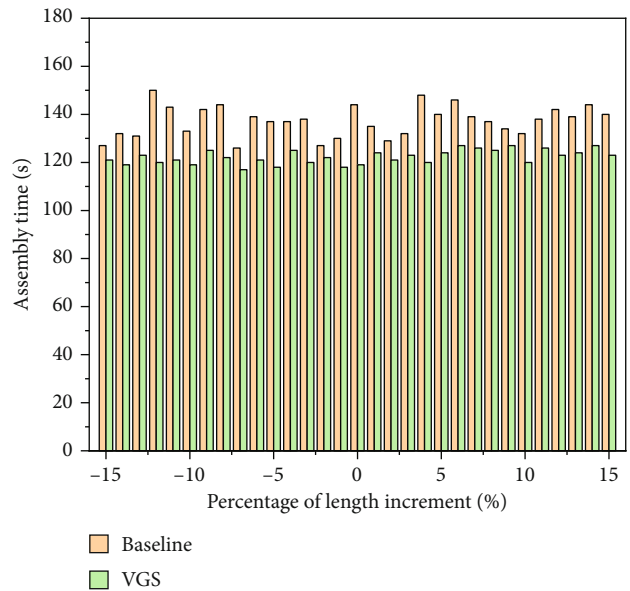Figure 9: Comparing assembly time of different mass.



Figure 10: Comparing assembly time of different length and mass.

assembly time for baseline and VGS methods is both 106 seconds. But the longest time of baseline is 157 seconds, and VGS is 135 seconds. Baseline takes 19 seconds of the average assembly time more than VGS. It can be seen that the robot using VGS has a relatively shorter assembly time. The results of the simulation prove that our method can effectively improve assembly efficiency.

The change in the diameter of the peg causes a change in its mass, and these changes have certain effects on the assembly alignment. It is very cumbersome to manually calculate

and mark changes in mechanical parameters caused by these changes. The mass of the peg is additionally reduced or increased by 15% based on initial mass to imitate the random changes of the mass in the actual conditions. The robot, respectively, using baseline and VGS conducts 1000 assembly tests for the different mass of the peg, as shown in Figure 9. It can be shown that VGS can still improve the assembly efficiency by 12.13% when the diameter and mass of the peg make some changes. In this simulation result, the standard deviation of the baseline is 5.1756, and the standard deviation

of VGS is 3.0133. It can be seen that VGS has better stability for assembly efficiency.

Subsequently, the length of the peg is changed between 85% and 115% based on the original length of the peg. Not only has its mass been changed but also its mechanical parameters have been changed when the length of the peg changes. The robot, respectively, using baseline and VGS conducts 1000 assembly tests for the different length and mass of the peg, as shown in Figure 10. The result shows that VGS can also improve the assembly efficiency by 10.92%, even if the length and mass of the peg have certain changes. When the length and mass have changed, the standard deviations of baseline and VGS are 6.2242 and 3.8508, respectively. Obviously, VGS has a smaller fluctuation of the assembly time, and the assembly efficiency is more stable.

## 5. Conclusions and Future Work

In this paper, a visual grasping strategy based on deep reinforcement learning is proposed, which can improve assembly efficiency. The fluctuation of the contact force signal caused by the disturbing moments in compliance-based assembly is analyzed, and the visual grasping strategy introduces the assembly reward to reduce the fluctuation. In V-REP, the simulations of peg-in-hole are carried out, it can be obtained from simulation results that the grasping area is restricted at a special area less than the previous area, and the trained robot spends less assembly time than the untrained robot. Furthermore, the proposed method improves the assembly efficiency by 13.83% compared to baseline.

The proposed visual grasping strategy can also effectively improve the assembly efficiency when the size and mechanical parameters of the peg have changed, which provides some guidance in peg-in-hole assembly. Future research work will focus on extending the proposed strategy to different assembly parts to complete more complex tasks. At the same time, finding effective ways to improve the efficiency of training samples, assisting agents to obtain better assembly capabilities, and realizing multiagent collaborative assembly are also future research work.

## Data Availability

The data used to support this study are available at https://github.com/Bensonwyz/A-Grasping-Strategy-for-Improving-Assembly-Efficiency-based-on-Deep-Reinforcement-Learning.

## Conflicts of Interest

We declare that we have no financial and personal relationships with other people or organizations that can inappropriately influence our work; there is no professional or other personal interest of any nature or kind in any product, service, and/or company that could be construed as influencing the position presented in, or the review of, the manuscript entitled.

## References

[1] T. Kamegawa, T. Akiyama, S. Sakai et al., "Development of a separable search-and-rescue robot composed of a mobile robot and a snake robot," *Advanced Robotics*, vol. 34, no. 2, pp. 132–139, 2020.

[2] L. el Hafi, S. Isobe, Y. Tabuchi et al., "System for augmented human–robot interaction through mixed reality and robot training by non-experts in customer service environments," *Advanced Robotics*, vol. 34, no. 3-4, pp. 157–172, 2020.

[3] D. Ferone, P. Festa, and M. G. C. Resende, "Hybridizations of GRASP with path relinking for the far from most string problem," *International Transactions in Operational Research*, vol. 23, no. 3, pp. 481–506, 2016.

[4] J. Dufek and R. Murphy, "Visual pose estimation of rescue unmanned surface vehicle from unmanned aerial system," *Frontiers in Robotics and AI*, vol. 6, p. 42, 2019.

[5] N. Vahrenkamp, E. Koch, M. Wachter, and T. Asfour, "Planning high-quality grasps using mean curvature object skeletons," *IEEE Robotics and Automation Letters*, vol. 3, no. 2, pp. 911–918, 2018.

[6] D. Watkins-Valls, J. Varley, and P. Allen, "Multi-modal geometric learning for grasping and manipulation," in *2019 International Conference on Robotics and Automation (ICRA)*, pp. 7339–7345, Montreal, QC, Canada, 2019.

[7] J. Deng, W. Dong, R. Socher, L.-J. Li, K. Li, and L. Fei-Fei, "Imagenet: a large-scale hierarchical image database," in *2009 IEEE Conference on Computer Vision and Pattern Recognition*, pp. 248–255, Miami, FL, USA, 2009.

[8] Y. Lin, S. Ren, M. Clevenger, and Y. Sun, "Learning grasping force from demonstration," in *2012 IEEE International Conference on Robotics and Automation*, pp. 1526–1531, Saint Paul, MN, USA, 2012.

[9] S. Ma, L. Du, E. Tsuchiya, and M. Fuchimi, "Paper-made grippers for soft food grasping," in *2020 17th International Conference on Ubiquitous Robots (UR)*, pp. 362–367, Kyoto, Japan, 2020.

[10] A. J. Choi, H. H. Yang, and J. H. Han, "Study on robust aerial docking mechanism with deep learning based drogue detection and docking," *Mechanical Systems and Signal Processing*, vol. 154, p. 107579, 2021.

[11] L. Gerez, G. Gao, and M. Liarokapis, "Employing magnets to improve the force exertion capabilities of adaptive robot hands in precision grasps," in *2019 IEEE/RSJ International Conference on Intelligent Robots and Systems (IROS)*, pp. 7630–7635, Macau, China, 2019.

[12] A. M. Schmidts, D. Lee, and A. Peer, "Imitation learning of human grasping skills from motion and force data," in *2011 IEEE/RSJ International Conference on Intelligent Robots and Systems*, pp. 1002–1007, San Francisco, CA, USA, 2011.

[13] M. Abdeetedal and M. R. Kermani, "Grasp synthesis for purposeful fracturing of object," *Robotics and Autonomous Systems*, vol. 105, pp. 47–58, 2018.

[14] M. Bianchi, G. Averta, E. Battaglia et al., "Touch-based grasp primitives for soft hands: applications to human-to-robot handover tasks and beyond," in *2018 IEEE International Conference on Robotics and Automation (ICRA)*, pp. 7794–7801, Brisbane, QLD, Australia, 2018.

[15] H. Merzić, M. Bogdanović, D. Kappler, L. Righetti, and J. Bohg, "Leveraging contact forces for learning to grasp," in *2019 international conference on robotics and automation (ICRA)*, pp. 3615–3621, Montreal, QC, Canada, 2019.

[16] G. A. Garcia Ricardez, N. Koganti, P. C. Yang et al., "Adaptive motion generation using imitation learning and highly compliant end effector for autonomous cleaning," *Advanced Robotics*, vol. 34, no. 3-4, pp. 189–201, 2020.

[17] X. Li, H. Cheng, H. Chen, and J. Chen, "Learning quasi-periodic robot motions from demonstration," *Autonomous Robots*, vol. 44, no. 2, pp. 251–266, 2020.

[18] X. Xie, C. Li, C. Zhang, Y. Zhu, and S.-C. Zhu, "Learning virtual grasp with failed demonstrations via bayesian inverse reinforcement learning," in *2019 IEEE/RSJ International Conference on Intelligent Robots and Systems (IROS)*, Macau, China, 2019.

[19] J. Zimmer, T. Hellebrekers, T. Asfour, C. Majidi, and O. Kroemer, "Predicting grasp success with a soft sensing skin and shape-memory actuated gripper," in *2019 IEEE/RSJ international conference on intelligent robots and systems (IROS)*, pp. 7120–7127, Macau, China, 2019.

[20] X. Tan, Y. Lee, C. B. Chng, K. B. Lim, and C. K. Chui, "Robot-assisted flexible needle insertion using universal distributional deep reinforcement learning," *International Journal of Computer Assisted Radiology and Surgery*, vol. 15, no. 2, pp. 341–349, 2020.

[21] D. Wang, Y. Hu, and T. Ma, "Mobile robot navigation with the combination of supervised learning in cerebellum and reward-based learning in basal ganglia," *Cognitive Systems Research*, vol. 59, pp. 1–14, 2020.

[22] J. Mahler, R. Platt, A. Rodriguez et al., "Guest editorial open discussion of robot grasping benchmarks, protocols, and metrics," *IEEE Transactions on Automation Science and Engineering*, vol. 15, no. 4, pp. 1440–1442, 2018.

[23] A. K. Tanwani, N. Mor, J. Kubiatowicz, J. E. Gonzalez, and K. Goldberg, "A fog robotics approach to deep robot learning: application to object recognition and grasp planning in surface decluttering," in *2019 international conference on robotics and automation (ICRA)*, pp. 4559–4566, Montreal, QC, Canada, 2019.

[24] B. Wu, I. Akinola, and P. K. Allen, "Pixel-attentive policy gradient for multi-fingered grasping in cluttered scenes," 2019, https://arxiv.org/abs/1903.03227.

[25] J. Mahler, M. Matl, V. Satish et al., "Learning ambidextrous robot grasping policies," *Science Robotics*, vol. 4, no. 26, article eaau4984, 2019.

[26] D. Kragic, A. T. Miller, and P. K. Allen, "Real-time tracking meets online grasp planning," in *Proceedings 2001 ICRA. IEEE International Conference on Robotics and Automation (Cat. No.01CH37164)*, vol. 3, pp. 2460–2465, Seoul, Korea (South), 2001.

[27] I. Lenz, H. Lee, and A. Saxena, "Deep learning for detecting robotic grasps," *The International Journal of Robotics Research*, vol. 34, no. 4-5, pp. 705–724, 2015.

[28] S. Levine, P. Pastor, A. Krizhevsky, J. Ibarz, and D. Quillen, "Learning hand-eye coordination for robotic grasping with deep learning and large-scale data collection," *The International Journal of Robotics Research*, vol. 37, no. 4-5, pp. 421–436, 2018.

[29] B. Calli, W. Caarls, M. Wisse, and P. Jonker, "Viewpoint optimization for aiding grasp synthesis algorithms using reinforcement learning," *Advanced Robotics*, vol. 32, no. 20, pp. 1077–1089, 2018.

[30] T. Osa, J. Peters, and G. Neumann, "Hierarchical reinforcement learning of multiple grasping strategies with human

instructions," *Advanced Robotics*, vol. 32, no. 18, pp. 955–968, 2018.

[31] V. Mnih, K. Kavukcuoglu, D. Silver et al., "Playing atari with deep reinforcement learning," 2013, https://arxiv.org/pdf/1312.5602/.

[32] V. Mnih, K. Kavukcuoglu, D. Silver et al., "Human-level control through deep reinforcement learning," *Nature*, vol. 518, no. 7540, pp. 529–533, 2015.

[33] A. Zeng, S. Song, S. Welker, J. Lee, A. Rodriguez, and T. Funkhouser, "Learning synergies between pushing and grasping with self-supervised deep reinforcement learning," in *2018 IEEE/RSJ international conference on intelligent robots and systems (IROS)*, pp. 4238–4245, Madrid, Spain, 2018.

[34] Z. Yang and H. Shang, "Robotic Pushing and Grasping Knowledge Learning via Attention Deep Q-learning Network," in *Knowledge Science, Engineering and Management. KSEM 2020*, G. Li, H. Shen, Y. Yuan, X. Wang, H. Liu, and X. Zhao, Eds., vol. 12274 of Lecture Notes in Computer Science, pp. 223–234, Springer, Cham, 2020.

[35] O. M. Pedersen, E. Misimi, and F. Chaumette, "Grasping unknown objects by coupling deep reinforcement learning, generative adversarial networks, and visual servoing," in *2020 IEEE international conference on robotics and automation (ICRA)*, pp. 5655–5662, Paris, France, 2020.

[36] K. Zhang, J. Xu, H. Chen, J. Zhao, and K. Chen, "Jamming analysis and force control for flexible dual peg-in-hole assembly," *IEEE Transactions on Industrial Electronics*, vol. 66, no. 3, pp. 1930–1939, 2018.

[37] T. Tang, H. C. Lin, Y. Zhao, W. Chen, and M. Tomizuka, "Autonomous alignment of peg and hole by force/torque measurement for robotic assembly," in *2016 IEEE international conference on automation science and engineering (CASE)*, pp. 162–167, Fort Worth, TX, USA, 2016.

[38] Z. Liu, L. Song, Z. Hou, K. Chen, S. Liu, and J. Xu, "Screw insertion method in peg-in-hole assembly for axial friction reduction," *IEEE Access*, vol. 7, pp. 148313–148325, 2019.

[39] H. Park, J. Park, D. H. Lee, J. H. Park, M. H. Baeg, and J. H. Bae, "Compliance-based robotic peg-in-hole assembly strategy without force feedback," *IEEE Transactions on Industrial Electronics*, vol. 64, no. 8, pp. 6299–6309, 2017.

[40] S. Wang, G. Chen, H. Xu, and Z. Wang, "A robotic peg-in-hole assembly strategy based on variable compliance center," *IEEE Access*, vol. 7, pp. 167534–167546, 2019.

[41] T. Inoue, G. De Magistris, A. Munawar, T. Yokoya, and R. Tachibana, "Deep reinforcement learning for high precision assembly tasks," in *2017 IEEE/RSJ international conference on intelligent robots and systems (IROS)*, pp. 819–825, Vancouver, BC, Canada, 2017.

[42] F. Li, Q. Jiang, S. Zhang, M. Wei, and R. Song, "Robot skill acquisition in assembly process using deep reinforcement learning," *Neurocomputing*, vol. 345, pp. 92–102, 2019.